Tracking control for mechanical systems experiencing simultaneous impacts

Chen, Hao Liang

Award date:
2018

Technische Universiteit
Eindhoven
University of Technology

Department of Mechanical Engineering
Dynamics and Control

Tracking control for mechanical systems experiencing simultaneous impacts

DC 2018.023

Author:
Hao Liang Chen 0799276

Project supervisor:
Prof. dr. ir. N. van de Wouw

Department of Mechanical Engineering
Research group Dynamics and Control
Eindhoven University of Technology

Coaches:
Dr. A. Saccon
Ir. M.W.L.M. Rijnen

Department of Mechanical Engineering
Research group Dynamics and Control
Eindhoven University of Technology

Master thesis

Eindhoven, January 2018

Abstract

Robotic systems interacting with other objects/the environment typically perform in a slow fashion. To increase the performance, one should also take into account impacts. Control strategies involving *single contact impacts* are well established in the literature. *Simultaneous impacts*, i.e., impacts occurring at multiple contacts at the same time instance, however, are typically neglected and thus form the center of attention in this work. A trajectory with simultaneous impacts tends to show more complex behavior in its neighborhood, as a perturbed trajectory may experience more jumps than the reference. This then results in the unwanted *peaking phenomenon*, which is even more complex due to the multiple jumps. Furthermore, a perturbed trajectory may continue in modes that are not specified in the reference trajectory, as a perturbed system may achieve a configuration with only one contact closed. The combination of these problems complicate the tracking problem considerably, and to our knowledge none have formally investigated generic aperiodic trajectories with simultaneous impacts.

In this work, these trajectories are investigated, and trajectory tracking is realized for a given benchmark example. To do so, the *mechanical system with unilateral constraints* is reformulated as a *nonlinear state-triggered hybrid system*. We then propose the hybrid control strategy *reference spreading control for simultaneous guard activation*, and via a *sensitivity analysis* we infer the local stability of these trajectories. From the *sensitivity analysis*, we obtain a *positively homogeneous time-triggered hybrid system* that is capable of describing the system behavior locally. The interesting part about this local model is that it combines the jumping and in-between flow effects of the nonlinear state-triggered hybrid system in a so-called *conewise constant jump gain*. The local modal are then able to describe the local system behavior, even when the jump times are different. Reference spreading control and the underlying sensitivity analysis are then used to achieve trajectory tracking of a given benchmark example, which is shown via numerical experiments.

As a benchmark example, we consider a mechanical system consisting of a fully actuated block and an unactuated plank with a spring and damper. The system is assumed to have no friction, thus we focus only on the normal impact phenomena. As a reference motion we consider a block experiencing simultaneous inelastic impacts on the flat surface of the plank. Using this case study, we validate numerically that the positive homogenization can provide first-order approximations of the dynamics of the nonlinear hybrid system, both in open- and closed- loop. We furthermore observe that uniform asymptotic stability of the closed-loop positive homogenization indicates trajectory tracking of the closed-loop benchmark example and thus expect that reference spreading control with the underlying sensitivity analysis can be used to realize trajectory tracking for mechanical systems experiencing simultaneous impacts in general.

Nomenclature

Roman symbols

b_P	Damping coefficient of rotational damper of plank
c	number of guard conditions/unilateral constraints
e	Basis vector
e_C	Euclidean error
e_R	Reference spreading error
E	Matrix of restitution coefficients
f	Vectorfield
g	Gravity acceleration
g	Jump map
G	(Conewise) constant jump gain
h	Contact distance
H	Column containing the centripedal, Coriolis and gravity terms
i	Macro discrete time of multi-scale hybrid time
$I_{(\cdot)}$	Hybrid time domain of a (subscript) trajectory
$\mathcal{I}$	Set of contact indices
j	Discrete time of classical hybrid time
J	Mass moment of inertia of object
k_P	Stiffness of rotational spring of plank
k	Micro discrete time of multi-scale hybrid time
l	Height of object
L	Length of object
m	Mass of object
M	mass matrix
O	Origin of frame
q	Generalized coordinates
Q^{nc}	Non-conservative generalized forces
s	Transition specific constraint indicator
S	Constraint indicator
S_s	Matrix containing the generalized directions of the actuator forces
t/t_i^k	Time/ k'th event time pertaining to i'th nominal even
T	Kinetic energy
u	Input
U	Internal energy
v	Generalised velocity
v	Perturbed input direction
V	Potential energy
W	Matrix containing the direction of contact forces in the generalized coordinates
x	State
x	The horizontal displacement of block
y	The vertical displacement of block
z	Positively homogeneous state/perturbed state direction

Greek symbols

α	Reference state
γ	(Transition specific) guard
Γ	Total guard vector
ϵ	Perturbation scaling parameter
ε	Restitution coefficient
$\kappa(i)$	Event complexity (impact complexity) at nominal event i
λ	Contact forces
Λ	Contact impulses
μ	Nominal input term
θ	Angle of block
σ	Mode of the system
$\sigma_k(i)$	transition specific mode
$\Sigma(i)$	Set of relevant transition specific modes in multi-scale hybrid time
τ	Nominal event time
τ_{rot}	Torque given to the block
ϕ	Angle of plank with respect to inertial frame
ψ	Angle of the normal cone
ξ	Normal contact velocity
ω	Angular velocity
Ω	Angular momentum

Subscripts

B	block variable
d	Damping
f	Final
ϵ	Perturbed
g	Global coordinates (frame)
g	Gravity
l	Local coordinates (frame)
P	Plank variable
ref	Reference
R	Reduced
s	Full impact seqeunce

Left upperscripts

σ	Current mode/sequence of modes

Right upperscripts

a	Ante-event
k	The k'th micro counter
p	Post-event

Miscellaneous

Df	Linear map
$\vec{(\cdot)}$	Vector notation
$\mathbf{(\cdot)}$ [bold]	Column/row/matrix notation
$\dot{(\cdot)}$	Velocity notation
$\ddot{(\cdot)}$	Acceleration notation
$\mathbb{R}$	Real numbers
$\mathbb{N}$	Integer numbers
$\bar{(\cdot)}$	Extended
$\emptyset$	Empty set
$num1(\cdot)$	Operator counting the number of 1's in a binary numbering convention.

Contents

Chapter 1

Introduction

1.1 Physical robot-environment interaction

The analysis and control of mechanical systems with contact is an active field of research. Many examples of such systems is found in the field of robotics. One can think about assembly line robots, handling objects using a gripper, or bipedal humanoid robots, having feets and arms that interact with the environment. Although control strategies exist for such systems, a common approach to handle changes during contact conditions, i.e., impact and detachment, is still to enforce that these changes occur at negligible speed. This, however, leads to the robot performing the task in a slow fashion. Quickening the task consequently increases the effect of impacts, complicating tracking control due to velocity discontinuities. Faster robots, however, may be desired, as factories may realize greater throughputs, and robots may be deployed in more challenging environments. One could, for instance, think about deploying robots in rescue operations for which a fast response is desired.

Recently, there has been an increase of research efforts directed towards elimination of such a performance-restricting condition, i.e., establishing contact at negligible speed. Most of these studies consider the scenario of a fixed sequence where only one contact is established or lost at a time. In this work instead, we consider the case of *simultaneous impacts*. The term *simultaneous impacts* refers to impacts for which multiple contact points of the mechanical system participates. This will further elevate restrictions on the system and in that way increase potential performance. The problem under study in this thesis, is to make a mechanical system perform a desired motion with simultaneous contact changes. This is essentially complicated by the fact that trajectories nearby the reference trajectory tend to experience a different sequence of contact changes. Consequently, a control strategy that can deal with this aspect needs to be constructed.

1.2 Control of multi-contact robotical systems

Control strategies that deal with multi-contact mechanical systems already exist. These strategies, however, prevent or ignore the occurrence of simultaneous impacts. An example is the control strategy in [1], in which the authors make the quadruped robot MIT CHEETAH 2, see Figure 1.1[1], run with the bounding gait specified in [2]; the pair of rear and front legs strike the ground alternately. Instead of a four-legged model, a two-legged model is used, and it is assumed that the pair of front and hind legs act in synchrony; the authors do not explicitly consider multi-contact situations. The bounding gait in [2], additionally, only performs well when the considered system has met certain requirements, which in turn limits the application of the control strategy in [1]. Furthermore, the authors do not incorporate impacts in the modeling process.

[1] https://biomimetics.mit.edu/research/dynamic-locomotion-mit-cheetah-2

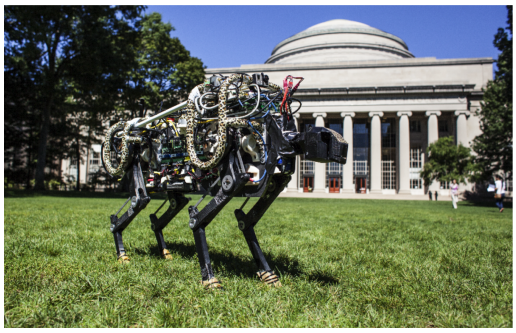

Figure 1.1: A picture of the quadruped robot MIT Cheetah 2.

Other examples can be found in the locomotion of bipedal robots, see Figure 1.2[2]. In [3], the authors mention some methods to control the walking behavior of a bipedal robot, e.g., via a Zero Moment Point (ZMP) based approach. This method focuses on the dynamic stability of the robot, cf. [4]. By the usage of the ZMP, one assumes zero impacting velocities as they tend to keep the upper bodies - which have the most mass - relatively still with respect to the moving leg. This is also noticed in [5], where the robot moves in a similar manner. As it does walk on uneven ground, an angular momentum based controller is implemented for when the robot is out of balance. The authors, though, consider no impacts, as one can find no state jumping expressions in [5].

In [6], the authors use the concept of hybrid zero dynamics and human-inspired control. For this, impacts are also considered to take place when the displacing foot hits the ground, whereas with the previous strategies this was neglected. Nevertheless, simultaneous impact is neglected as the authors consider the flat foot as a *single contact object* instead of a more realistic *multi-contact object*, cf. [7] and [8]. In [9], the authors extended the theory in [6] to incorporate more anthropomorphic gaits by having a walking pattern where the foot does not land flat on the ground. Herein, the foot is regarded as a two-contact body with a heel and a toe. The authors, however, generate a trajectory in which there is always a sequence of *single contact impacts*, i.e., *heel strike* $\rightarrow$ *toe strike* $\rightarrow$ *heel lift*, and *simultaneous impacts* are thus avoided.

Figure 1.2: A picture of the bipedal humanoid robot HRP-4.

[2] http://www.plasticpals.com/?attachment_id=24543

One can also look at tracking control of industrial robots, for which we refer to [10]. Herein, the robot tries to insert a complex shaped planar part into a board like a puzzle piece. To achieve the highest rate of convergence, the authors analyze multiple reference trajectories in which they insert the planar part via different contact sequences, similar to how we complete a puzzle. Although the approach does work, see [11], one may rather prefer stating only one trajectory with simultaneous contact and just look at the end result; we are not interested in what happens during simultaneous contact.

Even though there are many control strategies present, none investigates formally the stability of trajectories with simultaneous impacts. One reason may be that the authors expected insignificant changes to the performance of their control strategies when considering simultaneous impacts. In the case of a flat walking robot, assuming that a foot, although impacting in a slightly rotated fashion, will still land flat on the ground, is a reasonable one and should also occur in almost all situations; one should only be careful when walking with fast speeds on edges. Another reason may be the difficulty of investigating the stability of these motions, as we explain in the next section.

1.3 Main challenge

The tracking problem for single-contact impacts is already treated extensively in the literature, and solutions have been found for it. Nonetheless, we give a short description of this tracking problem to give the reader a sense that even the *simpler* case is quite challenging to solve. After that, the tracking problem for simultaneous impacts is worked out, defining the main challenges of this work.

Tracking problem single-contact impacts

Due to the state-triggered nature of the impacts, the times at which jumps occur for a trajectory near a reference trajectory will, in general, not coincide with the jump times of the reference, cf. [12] - [25]. Defining the classical notion of error as the difference between the system state and reference state, i.e., the Euclidean error, results in so-called *peaking phenomenon*, cf. [12] - [25]. This peaking phenomenon is visible as high discontinuous error values and is undesired due to the complication of describing stability, even when the error trajectory may show desirable results. Consequently, the number of stabilizing control strategies that can achieve trajectory tracking are limited. Furthermore, one may achieve poor tracking performance when designing a tracking controller based on the Euclidean error as mentioned in [16].

Tracking problem for simultaneous impacts

Considering a reference trajectory with simultaneous impacts, a nearby state trajectory will not only jump sooner or later than the reference, but will also show more jumps than the reference. Figure 1.3 illustrates a mechanical example, in which the upper drawing depicts a reference motion with simultaneous impacts, and the lower drawing a perturbed motion with a sequence of single-contact impacts. Consequently, the Euclidean error shows two peaks of high error values, in contrast to one peak for the single-contact case. To our knowledge, no control strategy exists to deal with this mismatch of number of jumps, i.e., the reference trajectory jumps only once, whereas the perturbed trajectory jumps twice (or more).

Another problem is the occurrence of modes which are not specified in the reference trajectory. These modes can, for instance, be interpreted as the different contact states of the mechanical system. Considering Figure 1.3, one can observe that the perturbed motion experiences continuous dynamics which do not occur in the reference motion, i.e., the dynamics with only one contact established. Furthermore, depending on the perturbation, a different contact may be established,

and one may subsequently conclude another mode that is not present in the reference trajectory. For example, rotating the block in Figure 1.3 anti-clockwise may result in a perturbed motion with the left-contact impacting first. This, consequently, may result in vastly different behavior of the perturbed motion. Stabilizing the reference trajectory thus becomes more challenging, as one not only needs to take into account the multiple jumps of the perturbed motion, but also the perturbed motion behaving differently for different perturbations.

1.4 Control of hybrid systems with state-triggered jumps

In this work, the *mechanical system with unilateral constraint* is reformulated as a *nonlinear state-triggered hybrid system*. In the literature, it is found that formulating the dynamics in a hybrid system framework allows for viable descriptions and control methods of mechanical systems experiencing impacts, cf. [6, 9, 12, 13, 14, 15, 16, 17, 18]. The continuous dynamics are described using ordinary differential equations, whereas the impact phenomena are captured using a jump map that is triggered by a condition on the state itself. In this section, the approach is formulated to which we solve the tracking problem for simultaneous impacts. Before doing so, a literature review is given about the available strategies for the single-contact case. This then further supports the strategy taken in this work.

Control for single-contact impact

Several approaches exist to deal with the non-coinciding jumping times and the resulting peaking phenomenon. In [19], the authors try to make the jump times coincide by also actuating the impacting surface. The issue with this approach, is that it will only work when the state of the system and its environment are known exactly, and an actuatated surface is available. The first is never the case in practice, and the second is not always present. In [20] instead, a reference trajectory is set up with periodic jump times, and the error is simply not defined for a small time interval about the jump times of the reference trajectory. This approach will only work with periodic reference trajectories, which is not applicable to our analysis as we also consider generic aperiodic trajectories.

In [21], the authors consider an extra mirrored reference trajectory to avoid the peaking error. They track either the original reference trajectory or the mirrored trajectory depending on the jumps of either the perturbed or the reference trajectory. In this way, the directions of the motion of the system and reference will always be the same, which causes these error peaks to dissapear. In [12, 13, 14, 22], a novel method to quantify the error is defined which they call a distance function. This distance function deals with such non-coinciding jump times by implicitly incorporating the state jump map in its definition. The result is that the distance function will not be affected by jumps, as it applies the jump map to the trajectory which has not jumped when the other has. Both methods are, however, not equipped to handle inelastic impacts and phases of intermittent contact.

Finally, there is the Reference Spreading (RS) based hybrid control as discussed in [15, 16, 17, 18, 23, 24], which is used in this work. This approach can deal with aperiodic signals and situations where the system experiences inelastic impacts, see [15, 17]. It is based on extending the reference trajectory about the times of jump by forward and backward integration of the dynamics, such that at every point in time multiple reference branches are found. A switch from one branch to the next is then triggered by a jump of the system, enforcing the jumps in the state and reference to occur at the same time.

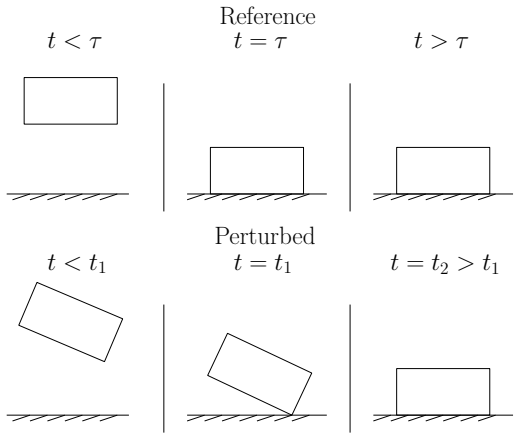

Figure 1.3: A graphical representation of a planar block with a reference motion with simultaneous impacts in the upper drawing and a perturbed motion with single-contact impacts in the lower drawing. The reference motion experiences simultaneous impacts at $t = \tau$, while the perturbed motion experiences single contact impacts at $t = t_1$ and $t = t_2$ with $t_1 < t_2$.

Control for simultaneous impacts

We propose to use RS control to deal with the tracking problem. The methodology is, however, currently still limited to trajectories with single-contact impacts. The adaptation of the strategy to track trajectories with simultaneous impacts is one of the points of interest in this work. We furthermore perform a *sensitivity analysis*, cf. [23], to gain insight about the local behavior of the nonlinear state-triggered hybrid system. Subsequently, a tool may be developed via this analysis that helps us in designing a tracking controller with RS control. The sensitivity analysis is, nevertheless, also currently limited to trajectories with single-contact impacts, and the extension of the analysis to trajectories with simultaneous impacts is another point of focus in this work. To our knowledge, this has not been done before and the closest to what we find is [26].

1.5 Research objective

The research objective of this work is to investigate whether the RS control and the underlying sensitivity analysis can be used to stabilize motions of mechanical systems experiencing simultaneous inelastic impacts. To achieve this goal, we formulate the following subgoals:

- Extend the RS control framework to dynamical systems experiencing jumps by satisfaction of two (or more) guards, i.e., when two or more contacts get closed.
- Extend the sensitivity analysis in [23] to be applicable to trajectories with jumps due to the satisfaction of two (or more) guards.
- Define a proper benchmark example for which we can design a reference trajectory with simultaneous inelastic impacts, and to which we can apply the sensitvity analysis.
- Analyze how well the local description of the dynamics, resulting from the sensitivity analysis, approximates the original mechanical system near a reference trajectory, both for open- and closed- loop conditions.

1.6 Outline of the report

The remainder of this report is structured as follows. In Chapter 2, we define the multi-contact mechanical system in the framework of non-smooth dynamics. We formulate the continuous and impact dynamics, and with an impact law the occurrence of simultaneous inelastic impacts. We then reformulate the mechanical system within a hybrid system framework, allowing us to perform RS control and sensitivity analysis on.

In Chapter 3, we first discuss the RS control for the single guard cases, i.e., single-contact impacts, as performed in [15, 16, 17, 18, 23, 24]. We then extend this control strategy to be applicable to trajectories with jumps due to the simultaneous activation of multiple guard conditions, i.e., simultaneous impacts. For sake of brevity, we will just state *trajectories with simultaneous guard activation* in the future.

A sensitivity analysis is performed in Chapter 4, where we also introduce new hybrid notations to ease the description of dynamical systems with multiple guard conditions. From the sensitivity analysis, we derive a tool, i.e., a local model, that potentially can be used to analyze the stability of a trajectory with simultaneous guard activation. We validate this numerically in Chapter 5.

In Chapter 5, we first explain the benchmark example on which we apply the RS control and sensitivity analysis. We then show from numerical experiments that the local model, derived from the sensitivity analysis, can describe the local behavior of our benchmark example well. We furthermore show that uniform asymptotic stability of our closed-loop local model seems to indicate trajectory tracking for our closed-loop benchmark example. This then gives the indication that the tool developed from senstivity analysis may indeed be used to stabilize a trajectory with simultaneous impacts.

Chapter 6 then summarizes the main conclusions derived throughout the report, and furthermore gives recommendations for future work.

Chapter 2

Modeling mechanical system with unilateral constraints

This chapter reviews the modeling of mechanical systems with unilateral constraints. Unilateral constraints characterize constraints on the distance between two rigid bodies. The occurrence of impacts is induced by these constraints, where we assume that impacts are instantaneous and the accompanying forces are impulsive. These assumptions are typically used in literature to analyze and control physical systems with impacts and have resulted in satisfying results in practice, cf. [6, 9, 15, 17, 18, 25, 27, 28, 29, 30, 31, 32]. To describe the impact dynamics, we resort to the framework of *non-smooth mechanics*, see [25]. In [25], a *measure differential inclusion (MDI)* is used to describe the dynamics of the mechanical system with unilateral constraints, and from it we derive an *impact equation*. Note that the impact equation does not necessarily have to be derived from an MDI, but that we do so in this work. The impact dynamics are described via the combination of the *impact equation* and *impact law*. The impact equation relates the momentum of the impact force to the change of momentum (associated to the difference of the pre- and post- impact velocity), and the impact law relates the pre-impact velocities to the post-impact velocities. The continuous and impact dynamics are then used in Chapter 5 to perform numerical experiments.

To describe the trajectories that we are interested in stabilizing, and to perform the sensitivity analysis, we formulate the dynamics in the framework of hybrid systems. In the literature, it is found that the hybrid system formalism is a viable method in describing and controlling mechanical systems experiencing impacts, cf. [6, 9, 12, 13, 14, 15, 16, 17, 18]. This hybrid system formalism is then further used in Chapter 3 and Chapter 4. One has to take into account that the two frameworks of non-smooth mechanics and hybrid system are not equivalent, and that the first one can describe the dynamics in all possible situations, while the second one is more interesting to support the stability and sensitivity analysis.

The chapter starts by discussing the dynamics in the framework of non-smooth mechanics. As the main focus of this work is the stability and sensitivity analysis, several simplifications have been made to model multi-contact mechanical systems. after that, the dynamics in the framework of hybrid systems are formulated.

2.1 Dynamics in the framework of non-smooth mechanics

In this section, the behavior of the mechanical system with unilateral constraints is formulated in the framework of non-smooth mechanics. The continuous dynamics are deduced via *constrained Euler-Lagrange equations*, see [33, Section 2, p.21-41], and the impact dynamics via the combination of an impact equation and impact law.

2.1.1 Continuous dynamics

A mechanical system with c unilateral constraints is considered, and the occurrence of friction is neglected. The latter is done, as formulating the impact dynamics without friction proves to be a challenging enough matter. Away from impact events, the dynamics of the system satisfy the constrained Lagrange equations

$$\begin{aligned} \frac{d}{dt}(T_{,\mathbf{v}}) - T_{,\boldsymbol{q}} + V_{,\boldsymbol{q}} &= (\boldsymbol{Q}^{nc})^T + (\boldsymbol{W}(\boldsymbol{q})\boldsymbol{\lambda})^T, \\ 0 \leq \boldsymbol{h}(\boldsymbol{q}) &\perp \boldsymbol{\lambda} \geq 0, \end{aligned} \tag{2.1}$$

with $\boldsymbol{q} \in \mathbb{R}^n$ being the n generalized coordinates, $\mathbf{v} \in \mathbb{R}^n$ the n generalized velocities, $T \in \mathbb{R}$ the kinetic energy, $V \in \mathbb{R}$ the potential energy, $\boldsymbol{Q}^{nc} \in \mathbb{R}^n$ the generalized non-conservative forces, due to damping or actuation, $\boldsymbol{h}(\boldsymbol{q}) \in \mathbb{R}^c$ the contact distance functions, and $\boldsymbol{W}(\boldsymbol{q}) \in \mathbb{R}^{n\times c}$ the matrix containing the generalized force directions of the contact forces $\boldsymbol{\lambda} \in \mathbb{R}^c$ (Lagrange multipliers). Note that we denote columns/rows/matrices with a bolded font, and that in (2.1), $(\cdot)_{,\boldsymbol{q}}$ for instance denotes the partial derivative with respect to $\boldsymbol{q}$. Furthermore, we use the notation $\perp$ to indicate a complementarity condition, i.e., either $\boldsymbol{h}(\boldsymbol{q})$ or $\boldsymbol{\lambda}$ is zero, or both are zero, by satisfying

$$\boldsymbol{h}(\boldsymbol{q}) \geq 0, \qquad \boldsymbol{\lambda} \geq 0, \qquad \boldsymbol{h}^T(\boldsymbol{q})\boldsymbol{\lambda} = 0. \tag{2.2}$$

In (2.1), the first two terms are derived from the kinetic energy T, composed of the translational and rotational energy of a rigid mass. The third term is determined from the potential energy V, typically containing elastic energy from springs and gravitational energy, and the fourth term from the generalized non-conservative forces. The final and most interesting term is obtained from the unilateral constraints $\boldsymbol{h}(\boldsymbol{q}) \geq 0$, assumed to be ideal and therefore only contributing with normal, but no tangential, forces. Figure 2.1 illustrates two unilateral constraints, i.e., $h_1(\boldsymbol{q}) \geq 0$ and $h_2(\boldsymbol{q}) \geq 0$, representing, respectively, the impenetrability (or distance) between *point A and the ground* and *point B and the ground*. The impenetrability condition is realized via the complementarity condition (2.1), stating that a contact force $\lambda_i \geq 0$ exists when the corresponding contact is closed, i.e., $h_i(\boldsymbol{q}) = 0$ with $i \in \{1, 2\}$. The matrix $\boldsymbol{W}(\boldsymbol{q})$ in (2.1) is derived from the unilateral constraint function $\boldsymbol{h}(\boldsymbol{q})$ giving

$$\boldsymbol{W}^T(\boldsymbol{q}) = \frac{\partial \boldsymbol{h}(\boldsymbol{q})}{\partial \boldsymbol{q}} \in \mathbb{R}^{c\times n}. \tag{2.3}$$

Equation (2.1) is then written in a compact form as

$$\begin{aligned} \boldsymbol{M}(\boldsymbol{q})\dot{\mathbf{v}} - \boldsymbol{H}(\boldsymbol{q}, \mathbf{v}) &= \boldsymbol{S}_s(\boldsymbol{q})\boldsymbol{u} + \boldsymbol{W}(\boldsymbol{q})\boldsymbol{\lambda}, \\ 0 \leq \boldsymbol{h}(\boldsymbol{q}) &\perp \boldsymbol{\lambda} \geq 0, \end{aligned} \tag{2.4}$$

with $\boldsymbol{M} \in \mathbb{R}^{n\times n}$ being the symmetric positive definite mass matrix, $\boldsymbol{H} \in \mathbb{R}^n$ a vectory typically containing the centripedal, Coriolis, damping, and gravity terms, and $\boldsymbol{S}_s \in \mathbb{R}^{n\times m}$ a matrix of the generalized force directions for the actuation vector $\boldsymbol{u} \in \mathbb{R}^m$.

2.1.2 Impact dynamics

In the framework of non-smooth mechanics, there is the idealization that impacts are instantaneous events associated with impulsive forces. Consequently, velocity discontinuities are allowed in the system. These systems are in turn characterized as *non-smooth dynamical systems* [25, Section 1.3, p. 9-11]. Due to this idealization, a more elaborate modeling framework is required that is simply not an ODE or DAE as equation (2.4) to describe the impact dynamics. Therefore, we use the formulation of an MDI, cf. [25, 34], to obtain a so-called impact equation. The impact effect is then captured by the combination of the impact equation and the impact law. The impact equation relates the momentum of the impact force to the change of momentum (associated to the difference of the pre-impact and post-impact velocity), and the impact law relates the pre-impact (normal contact) velocities to the post-impact (normal contact) velocities.

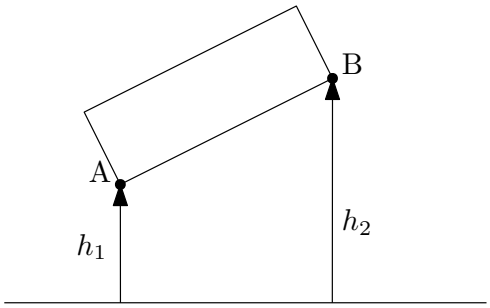

Figure 2.1: Planar example of a rigid block over a rigid surface. The unilateral constraint is formulated as the inequalities $h_1 \geq 0$ and $h_2 \geq 0$, where h_1 and h_2 denote, respectively, the distance between block corner A and the ground, and block corner B and the ground.

Remark 2.1 *It is not necessary to formulate an MDI in order to derive the impact equation. The main advantage of an MDI is the capability of describing both continuous and impact dynamics in one model. This proves to be useful when performing a time-stepping scheme, cf. [34]. This time-stepping scheme is, however, not practical when performing numerical experiments with the considered control strategy in Chapter 3, which is further clarified in Chapter 5. We thus prefer to use two separate models, one for the continuous dynamics and one for the impact dynamics.*

Impact equation

To include the effects of impulsive forces, (2.4) is generalized to the MDI

$$\boldsymbol{M}(\boldsymbol{q})d\mathbf{v} - \boldsymbol{H}(\boldsymbol{q},\mathbf{v})dt = \boldsymbol{S}_s(\boldsymbol{q})\boldsymbol{u}dt + \boldsymbol{W}(\boldsymbol{q})d\boldsymbol{\Lambda} \tag{2.5}$$

with $d\boldsymbol{\Lambda}$ being the differential measure of the momenta due to contact and $d\mathbf{v}$ the differential measure of $\mathbf{v}$, where it is assumed that $\boldsymbol{q}$ is an *absolutely continuous function of time* and $\mathbf{v}$ is of *locally bounded variation*. These defintions follow from [25] as:

Definition 2.1 (Absolute continuity) *a function $\boldsymbol{f} : I \to \mathbb{R}^n$ is absolutely continuous on $I \subset \mathbb{R}$ if for every $\epsilon > 0$ there exists a $\delta(\epsilon) > 0$ such that*

$$\sum_{i=1}^{n} ||\boldsymbol{f}(b_i) - \boldsymbol{f}(a_i)|| < \epsilon \tag{2.6}$$

for any n and any disjoint collection of intervals $[a_i, b_i] \in I$ satisfying

$$\sum_{i=1}^{n} (b_i - a_i) < \delta, \tag{2.7}$$

Definition 2.2 (Variation) *let $\boldsymbol{f} : I \to X$ (with I being the real interval and X an Euclidean space with the norm $||.||$) and let $[a, b]$ be a subinterval of I. The variation of $\boldsymbol{f}$ on $[a, b]$, denoted with $var(\cdot)$, is the nonnegative extended real number*

$$var(\boldsymbol{f}, [a, b]) = sup \sum_{i=1}^{n} ||\boldsymbol{f}(x_i) - \boldsymbol{f}(x_{i-1})||, \tag{2.8}$$

where the supremum is taken over all strictly increasing finite sequences $x_1 < x_2 < \cdots < x_n$ of points on $[a, b]$. Here n denotes the number of points.

Definition 2.3 (Locally Bounded Variation) *the function $\boldsymbol{f} : I \to X$ is said to be of locally bounded variation, $\boldsymbol{f} \in lbv(I, X)$, if and only if*

$$var(\boldsymbol{f}, [a, b]) < \infty \tag{2.9}$$

for every compact subinterval $[a, b]$ of I.

One can interpret (2.5) as an equation at the level of momenta, i.e., as integrals of forces. While the second and third terms denote standard integrands of an integral over time, the first and fourth terms in (2.5) allow for, respectively, the generalized velocity to have jumps and the constraint forces to be impulsive, and therefore cannot be written simply as $\mathbf{v}dt$ and $\boldsymbol{\lambda}dt$. The interested reader is referred to [34, Section 1, p.1-5] and [25, Section 5.4, p.99-106] for a more complete and exhaustive description.

By stating $\mathbf{v}$ of local bounded variation, we can define for $\mathbf{v}$ a left and right limit at each time instance $t_i \in \mathbb{R}_{\geq 0} = I$, with $i \in \mathbb{N}$, denoted $\mathbf{v}^-(t_i)$ and $\mathbf{v}^+(t_i)$, respectively, and defined as

$$\mathbf{v}^-(t_i) = \lim_{t \uparrow t_i} \mathbf{v}(t), \qquad \mathbf{v}^+(t_i) = \lim_{t \downarrow t_i} \mathbf{v}(t). \tag{2.10}$$

Defining a set $D \subset I$ as the collection of time instances t_i where $\mathbf{v}(t_i)$ is discontinuous, we consequently state that $\mathbf{v}^- = \mathbf{v}^+$ for all $t_i \notin D$ and $\mathbf{v}^- \neq \mathbf{v}^+$ for all $t_i \in D$. The differential measures are then defined as

$$\begin{aligned} d\boldsymbol{\Lambda} &= \boldsymbol{\lambda}dt + \boldsymbol{\Lambda}d\eta, \\ d\mathbf{v} &= \dot{\mathbf{v}}dt + (\mathbf{v}^+ - \mathbf{v}^-)d\eta, \end{aligned} \tag{2.11}$$

in which two components are present, namely the *Lebesgue measurable part*, e.g., $\boldsymbol{\lambda}dt$, and the *atomic part*, e.g., $\boldsymbol{\Lambda}d\eta$. The time integral of the atomic measure over a single time instance results in

$$\int_{t_i}^{t_i} d\eta = \begin{cases} 1, & \forall t_i \in D, \\ 0, & \forall t_i \notin D, \end{cases} \tag{2.12}$$

whereas the time integral of the Lebesgue part result in

$$\int_{t_i}^{t_i} dt = 0, \qquad \forall t_i \in I. \tag{2.13}$$

The impact equation then results from the MDI formulation by taking the time integral of (2.5) with (2.11) over a discontinuous time instance $t_i \in D$ as

$$\int_{t_i}^{t_i} \boldsymbol{M}(\boldsymbol{q})\Big(\dot{\mathbf{v}}dt + (\mathbf{v}^+ - \mathbf{v}^-)d\eta\Big) - \int_{t_i}^{t_i} \boldsymbol{H}(\boldsymbol{q}, \mathbf{v})dt = \int_{t_i}^{t_i} \boldsymbol{S}_s(\boldsymbol{q})\boldsymbol{u}dt + \int_{t_i}^{t_i} \boldsymbol{W}(\boldsymbol{q})\Big(\boldsymbol{\lambda}dt + \boldsymbol{\Lambda}d\eta\Big), \tag{2.14}$$

simplifying, under consideration of (2.12) and (2.13), to

$$\boldsymbol{M}(\boldsymbol{q})\Big(\mathbf{v}^+ - \mathbf{v}^-\Big) = \boldsymbol{W}(\boldsymbol{q}, t)\boldsymbol{\Lambda}, \tag{2.15}$$

or, equivalently, as

$$\mathbf{v}^+ = \boldsymbol{M}(\boldsymbol{q})^{-1}\Big(\boldsymbol{W}(\boldsymbol{q}, t)\boldsymbol{\Lambda} + \boldsymbol{M}(\boldsymbol{q}, t)\mathbf{v}^-\Big). \tag{2.16}$$

Equation (2.16) is called the impact equation associated to the MDI (2.14), and it allows to compute the post-impact velocities once the configuration, the pre-impact velocities, and the impulsive momentum $\boldsymbol{\Lambda}$ are known. The impact equation has to be complemented with a (yet to be specified) impact law to determine the value of $\boldsymbol{\Lambda}$ as a function of $\boldsymbol{q}$ and $\mathbf{v}^-$. This impact law is discussed next.

Impact law

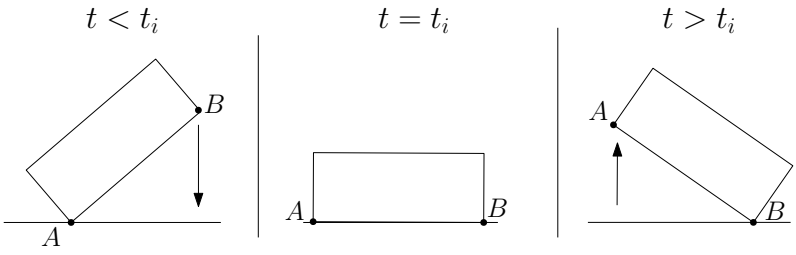

Figure 2.2: Graphical illustration of the effects of a superfluous contact. A planar block is considered with corner points A and B. Before time of impact, at $t < t_i$ with $t_i \in D$, the block is in contact with the ground at the corner A, and corner B is in the air. At $t = t_i$ the block experiences impact at corner B, after which the superfluous contact A experiences detachment on the right drawing.

Two well known impact laws for multi-contact mechanical systems are the *generalized Newton's impact law* and the *generalized Poisson's impact law*, cf. [25, 35, 36, 37]. The first gives a relation on the velocity level of the contact distance $\boldsymbol{h}(\boldsymbol{q})$, whereas the second gives a relation on the level of momenta. One can look further as in [38] and even consider an impact law that gives a relation on (potential and kinetic) energy. In this work, we use the simpler impact law, namely the generalized Newton's impact law. Therefore, we only elaborate on this specific impact law next.

The generalized Newton's impact law is given as

$$\xi_i^+ \geq \varepsilon_i \xi_i^-, \qquad \forall i \in \mathcal{I}_c, \tag{2.17}$$

with $\boldsymbol{\xi} = \boldsymbol{W}^T(\boldsymbol{q})\mathbf{v} + \frac{\partial \boldsymbol{h}}{\partial t}$ being the normal velocities of the contact distances $\boldsymbol{h}$, ε_i a Newtonian restitution coefficient related to the contact distance h_i, and $\mathcal{I}_c = \{i | h_i = 0\}$ a set of closed contact indices with $i \in \mathcal{I} = \{1, 2, \cdots, c\}$ denoting the full set of contact indices. Notice that the formulation in (2.17) allows the post-impact velocity to be *larger* than 0, even when there is no pre-impact velocity, i.e., $\xi_i^- = 0$. Contacts for which this occur are called *superfluous contacts*, cf. [25], and should be taken into account when dealing with multi-contact mechanical systems.

Superfluous contacts do not transmit a contact impulse, i.e., it does not participate in the impact, but may experience a jump in the normal contact velocity due to transmitted impacts at other contacts. The presence of these contacts is dependent on factors such as the property of the impacting object, and the impacting configuration and speed. Figure 2.2 illustrates an example of the influence of a superfluous contact, where we consider the same block as in Figure 2.1. On the left drawing of Figure 2.2, point A is at rest, i.e., $h_1 = 0$ and $\xi_1 = 0$, and point B undergoes a falling motion, i.e., $\xi_2 < 0$. In the middle drawing, the block experiences an inelastic impact at point B, after which $h_2 = 0$ and $\xi_2 = 0$. Point A, however, may experience a jump in its contact velocity, i.e., $h_1 = 0$ and $\xi_1 > 0$, due to the transmitted impact at point B. This results in the right drawing where point A detaches from the ground, and consequently point A is considered a superfluous contact.

Combining the impact equation (2.15) and the generalized Newton's impact law (2.17) results in the impact dynamics

$$\begin{aligned} \boldsymbol{M}(\boldsymbol{q})(\mathbf{v}^+ - \mathbf{v}^-) &= \boldsymbol{W}(\boldsymbol{q})\boldsymbol{\Lambda}, \\ 0 \leq \boldsymbol{\zeta} \perp \boldsymbol{\Lambda} &\geq 0, \end{aligned} \tag{2.18}$$

where $\boldsymbol{\zeta} = \boldsymbol{\xi}^+ - \boldsymbol{E}\boldsymbol{\xi}^- \in \mathbb{R}^p$ is a column of the size of p closed contacts, and $\boldsymbol{E} := \mathrm{diag}(\varepsilon_i) \in \mathbb{R}^{p \times p}$, with $i \in \mathcal{I}_c$, a diagonal restitution coefficient square matrix. Moreover, a global resitution

coefficient of $\varepsilon = \varepsilon_i = 0$, with $i \in \mathcal{I}_c$, is chosen to model the inelastic impacts. Note that one could also consider non-diagonal restitution matrices and additionally a non-global restitution coeffient, cf. [36, 39]. Doing so, results in more complex impact dynamics, whereas the aim is to have at hand an (simple) impact model to demonstrate via numerical simulations the formulas, derived in Chapter 4, for the sensitivity analysis about a reference trajectory jumping due to simultaneous impacts. These formulas can be applied to any specific impact laws, but choosing the generalized Newton's impact law results in simple expressions that are simple to present analytically. If things are done automatically via a computer program, then other impact laws (that might be more accurate for the use case at hand) are straightforward to be implemented.

Conditions superfluous contact

The complementarity condition (2.18) allows to treat the following cases:

- the contact is actively participating in the impact process, i.e., $\Lambda_i > 0$ and $\xi_i^+ = \varepsilon_i \xi_i^-$ for $i \in \mathcal{I}_c$,
- the contact is superfluous, i.e., $\Lambda_i = 0$ and $\xi_i^+ \geq \varepsilon_i \xi_i^+$ for $i \in \mathcal{I}_c$.

Equation (2.18), however, does not indicate explicitly under what circumstances superfluous contacts will be present. We want to eliminate the occurrence of these contacts, as these will make the considered trajectories and sensitivity analysis in, respectively, Chapter 3 and Chapter 4 more complicated. Taking the motion in Figure 2.2 as an example, one concludes that the perturbed system experiences at least two impacts (and detachments), instead of only one impact when no superfluous contacts are present. This perturbed motion is typically referred to as *rocking* and will most likely make the stability analysis of our reference trajectory more difficult. As will be elaborated in Chapter 4 more, the sensitivity analysis considers *all* perturbed motions of the mechanical system. This analysis is challenging enough without rocking (superfluous contacts), and taking into account rocking increases the number of possible motions, and thus make our analysis more extensive.

To prevent superfluous contacts, the impact dynamics are analyzed in more detail in Appendix A. From it, we obtain a condition that should prevent superfluous contacts, and thus rocking, for planar cases with two contacts. This condition is formulated as

$$\arccos\left(\frac{\nabla h_1^T \boldsymbol{M} \nabla h_2}{\sqrt{\nabla h_1^T \boldsymbol{M} \nabla h_1}\sqrt{\nabla h_2^T \boldsymbol{M} \nabla h_2}}\right) \geq \frac{\pi}{2} \tag{2.19}$$

with $\nabla h_i(\boldsymbol{q}) = \boldsymbol{M}^{-1}(\boldsymbol{q})\frac{\partial h_i}{\partial \boldsymbol{q}}$ for $i \in \{1, 2\}$. We assume that this is always satisfied in our work, such that we state the following:

Assumption 2.1 (No-superfluous contact) *The planar system with two contacts considered in this work does not have superfluous contacts.*

Consequently, the impact dynamics simplify to

$$\begin{aligned} \boldsymbol{M}(\boldsymbol{q})(\mathbf{v}^+ - \mathbf{v}^-) &= \boldsymbol{W}(\boldsymbol{q})\boldsymbol{\Lambda}, \\ 0 \leq \boldsymbol{\xi} \perp \boldsymbol{\Lambda} &\geq 0, \end{aligned} \tag{2.20}$$

where the complementarity condition consists of the normal contact velocity $\boldsymbol{\xi}$ instead of $\boldsymbol{\zeta}$. The continuous and impact dynamics are then formulated as, respectively, (2.4) and (2.20). These dynamics are used to perform numerical simulations in Chapter 5. In the next section, these dynamics are reformulated in a hybrid system framework, such that we can apply the control strategy and sensitivity analysis, treated in Chapter 3 and Chapter 4, on the considered mechanical system.

2.2 Dynamics in the framework of hybrid system

A hybrid system has both continuous and discrete dynamics. In a mode, the dynamics are continuous till a transition condition, so-called *guard*, is fulfilled. The dynamics then experience a discrete change as mode transitions (and state jumps), after which it flows continuously till the next guard is fulfilled. Mechanical systems also fit to a certain extent[1] in this framework. The guards are described using unilateral constraints, which upon activation, i.e., at impacts, let a velocity jump occur as in (2.18). This velocity jump is described via a so-called *jump map*. The continuous dynamics are obtained by the ODE (2.4), changing when different constraints are active. Note that in our case with no friction, these modes are simply related to the different contact situations, i.e., the combination of closed and open contacts. In the case when friction plays a role, one may obtain extra modes to describe stick-slip behavior.

We use the hybrid systems framework as in [15], cf. [40, Section 1.5.2, p.11-13], and illustrate the hybrid scheme in Figure 2.3. The associated variables can be described as follows:

- $\sigma = \{1, 2, \cdots, N\}$ is a finite set of N modes.
- $\boldsymbol{x} \in X = \mathbb{R}^{n_\sigma}$ for which X is the state space in mode σ, and n_σ implies the number of corresponding state elements with $\boldsymbol{x} = \begin{pmatrix} \boldsymbol{q}, & \mathbf{v} \end{pmatrix}^T$.
- $\boldsymbol{u} \in U = \mathbb{R}^{m_\sigma}$ for which U is an input set with m being the number of input terms. Note that the number of input terms is also dependent on the current mode, for which we use the symbol m_σ.
- ${}^{\sigma}\boldsymbol{f} : X \times U \times \mathbb{R} \times \mathbb{N} \to X$ being a vector field for the current mode σ. Note that this originates from ${}^{\sigma}\boldsymbol{f}(\boldsymbol{x}, \boldsymbol{u}, t, j)$, where $t \in \mathbb{R}$ is the time, and $j \in \mathbb{N}$ the discrete time that goes up for every transition between modes. The reason for using this discrete time is explained in Chapter 3.
- ${}^{\sigma_p \leftarrow \sigma_a}\gamma : X_a \times U \times \mathbb{R} \to \mathbb{R}$ being the guard function for transitioning from an ante-event mode σ_a to a post-event mode σ_p. Here, we denote X_a as the state space in mode σ_a.
- ${}^{\sigma_p \leftarrow \sigma_a}\boldsymbol{g} : X_a \times \mathbb{R} \times \mathbb{N} \to X_p$ being a jump map. Here, we denote X_p as the state space in mode σ_p.

The components of the hybrid system and their notation will be elaborated on, and modified slightly, to specifically consider simultaneous impacts, in Chapter 4.

[1] As long as we consider the trajectories in a neighborhood of a sufficiently regular one. The hybrid system framework can, for instance, not deal with *Zeno-behavior*, whereas the non-smooth mechanics framework is able to treat such cases by using a *time-stepping* scheme with an MDI, see [34].

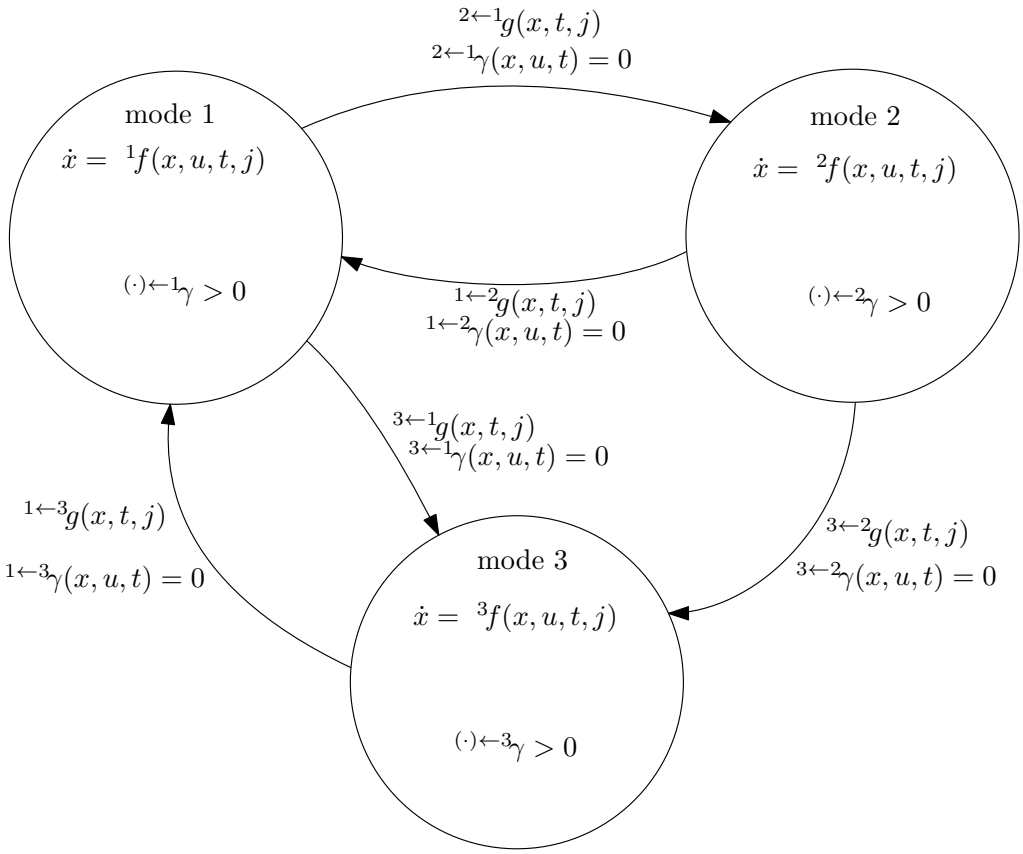

Figure 2.3: A graphical representation of the hybrid system representation as used in [15]. Three modes are observed where the arrows denote the possible transitions. The system will stay in a mode as long as the guard condition(s) is unsatisfied, i.e., when $^{(\cdot)\leftarrow(\cdot)}\gamma > 0$. When triggering any of the corresponding guard conditions by having $^{(\cdot)\leftarrow(\cdot)}\gamma = 0$, the system transitions to a new mode with a corresponding jump map $^{(\cdot)\leftarrow(\cdot)}\boldsymbol{g}$ applied to the state.

2.3 Summary

This chapter discussed the dynamics of mechanical systems with unilateral constraints in the frameworks of non-smooth mechanics and hybrid systems. In the non-smooth mechanics framework, we formulated the continuous dynamics via a constrained Euler-Lagrange equation and the impact dynamics via the combination of the impact equation and the generalized Newton's impact law. These dynamics are then used to perform numerical experiments in Chapter 5.

After, we formulated the dynamics in a hybrid system framework. The mode dynamics are described with the continuous dynamics and the jump maps with the impact dynamics. Transitions between modes occur when guards are triggered, which are described via the unilateral constraints. The hybrid system framework allows us then to describe the considered trajectories, i.e., trajectories with simultaneous impacts and no Zeno-behavior, in Chapter 3 and perform the sensitivity analysis in Chapter 4.

Chapter 3

Reference spreading for simultaneous guard activation

In this chapter, we discuss the hybrid control strategy used in this work. The first part of this chapter reviews the so-called *reference spreading hybrid control*, as in [15, 16, 17, 18, 23, 24], applied to nonlinear state-triggered hybrid systems that jump due to the activation of a single guard condition. An example of such systems are mechanical systems experiencing single-contact impacts. In the rest of the work, we refer to this strategy as *RS control for single guard activation*. The contribution of this work is to extend this control strategy to nonlinear state-triggered hybrid systems that jump due to the activation of multiple guard conditions simultaneously. Mechanical systems experiencing simultaneous impacts are an example of such systems. This new control strategy is called *RS control for simultaneous guard activation*.

3.1 Reference spreading for single guard activation

This section treats the RS control for single guard activation. First, we expand on the tracking problem of state-triggered hybrid systems with single guard activation. Here, the state and reference trajectories typically show *non-coinciding jump times*, leading to the undesired *peaking behavior*, see [12] - [25]. RS control is then introduced to solve this problem by using so-called *extended trajectories*. These extended trajectories are essential for this work, as it allows us to extend the RS Control in Section 3.2 and, additionally, to perform the sensitivity analysis, see [23], in Chapter 4. We end this section by introducing the hybrid time (t, j), as used in [15, 16, 17, 18, 24], allowing us to provide clear descriptions of trajectories with multiple jumps. One will see that the hybrid time is even more necessary for trajectories with simultaneous guard activation, i.e., trajectories jumping due to the activation of multiple guard conditions simultaneously, and this hybrid time is thus further modified in Section 3.2.

3.1.1 Tracking problem state-triggered hybrid systems with single guard activation

We consider a state-input trajectory $(\boldsymbol{\alpha}, \boldsymbol{\mu})$ with jumps, where $\boldsymbol{\alpha}(t)$ is the reference trajectory and $\boldsymbol{\mu}(t)$ the associated *nominal input*. We assume that the reference trajectory shows no Zeno behavior, and that the vector fields, jump maps, and guard conditions, are sufficiently smooth. The smoothness assumption then allows us to study the local behavior about the reference, cf. [23]. Figure 3.1 illustrates a reference trajectory $\boldsymbol{\alpha}(t)$ (blue line) and a nearby state trajectory $\boldsymbol{x}(t)$ (red line) with a different initial condition. The vertical axis represents the state in Euclidean space $\mathbb{R}^{n_\sigma}$, and the horizontal axis the time $t \in \mathbb{R}$. Furthermore, the left drawing illustrates the trajectory in an ante-event mode (σ_a), while the right drawing illustrates the trajectory in a post-event mode (σ_p). A jump to another mode (or the same mode) takes place when the guard

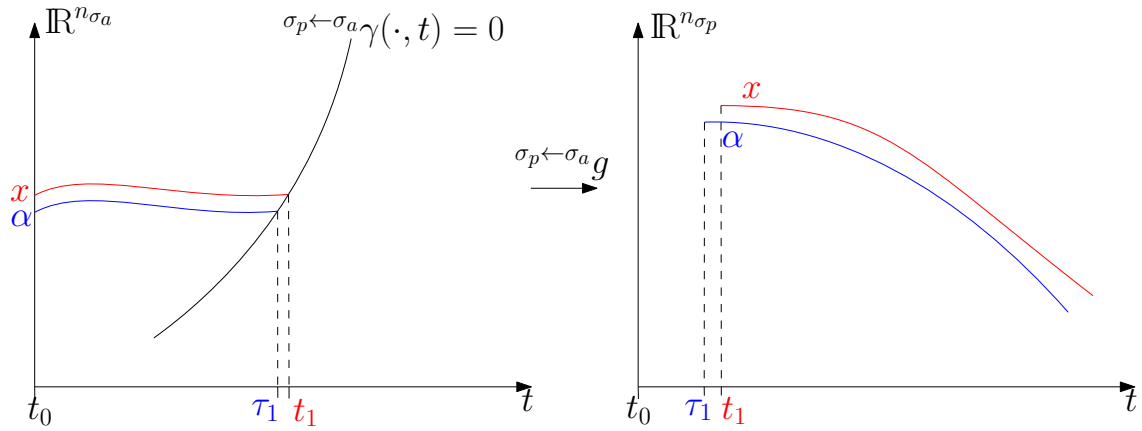

Figure 3.1: A graphical representation of the reference trajectory $\boldsymbol{\alpha}(t)$ (blue line) and a nearby trajectory $\boldsymbol{x}(t)$ (red line). The left drawing represents the ante-event mode σ_a, and the right drawing represents the post-event mode σ_p.

condition ${}^{\sigma_p\leftarrow\sigma_a}\gamma(\cdot,t)=0$ is triggered, where we furthermore assume *transversality* at time of triggering.

Assumption 3.1 (Transversality) *Given a guard function $\gamma(\boldsymbol{x}(t),t)$, then the transversality condition is fulfilled when*

$$D_1\gamma(\boldsymbol{\alpha}(t),t)\cdot{}^{\sigma}\boldsymbol{f}(\boldsymbol{\alpha}(t),\boldsymbol{\mu}(t),t)+D_2\gamma(\boldsymbol{\alpha}(t),t)\cdot 1\neq 0. \tag{3.1}$$

The transversality condition states that $\dot{\gamma}\neq 0$, and this corresponds with the occurrence of impacts. We will see in Chapter 4 that this condition is necessary for the sensitivity analysis. Note that for Assumption 3.1, we use the notation $D_b\gamma(\boldsymbol{\alpha},t)$ to denote the partial derivative of the function γ with respect to its b'th argument evaluated at the values $\boldsymbol{\alpha}$ and t, see [41, Section 2.3, p.75-83].

Recalling the left drawing of Figure 3.1, one can observe the guard condition as the black curved line. One will additionally notice that the state and reference trajectory trigger this guard condition at different time instances. These time instances are defined for the state trajectory as *event times* t_j and for the reference trajectory as *nominal event times* τ_j, with $j\in\mathbb{N}_{\geq 0}$. Here, j is the discrete time (jump counter) which increases whenever a guard condition is triggered. When triggering the guard condition, a jump map ${}^{\sigma_p\leftarrow\sigma_a}\boldsymbol{g}$ is applied, transitioning the trajectory from the left drawing to the right drawing.

The mismatch of jump times between the reference and state trajectory tend to show in tracking problems of state-triggered hybrid systems, see [12] - [25]. Using the Euclidean error

$$\boldsymbol{e}_C(t)=\boldsymbol{x}(t)-\boldsymbol{\alpha}(t), \tag{3.2}$$

will show discontinuous behavior of the error trajectory during this interval of non-coinciding jump times. Figure 3.2 illustrates a possible behavior of this error trajectory for the state and reference trajectory in Figure 3.1. One will notice a peak of high error values during the time interval $\tau_1\leq t\leq t_1$, and consequently this is defined as *peaking behavior*. For mechanical systems, this can be clarified by the opposing velocity signs of the reference and state trajectory during this time interval. This peaking phenomenon is undesired, see [12] - [25], as the error trajectory may show desirable results by converging to zero away from jump times, but can not be defined stable in, for instance, the sense of Lyapunov. This, consequently, limits the number of stabilizing control strategies that can be applied to achieve trajectory tracking. Furthermore, designing a tracking

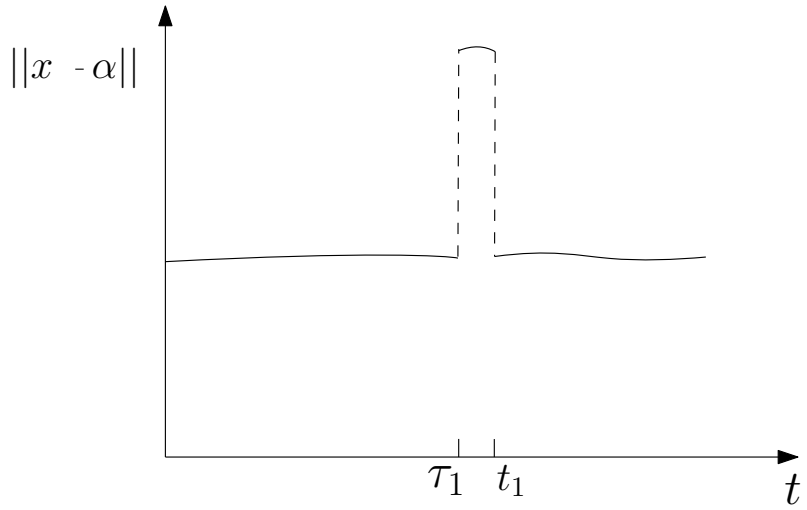

Figure 3.2: A graphical representation of a possible Euclidean error norm trajectory of Figure 3.1. During the time interval $t \in [t_1, \tau_1]$ the error norm shows the undesired peaking behavior.

controller based on the Euclidean error may result in poor performance, see [16]. In RS control, a new notion of error is defined to circumvent this peaking behavior and consecutively achieve trajectory tracking. This control strategy is discussed next.

3.1.2 Reference spreading for single guard activation: single-event

The RS control uses a new notion of error based on the concept of extended trajectories. The resulting error term has no peaking behavior and can be used to design a tracking controller, see see [15, 16, 17, 18, 23, 24]. As these extended trajectories play an important part in this control strategy (and also in the rest of this work), we first explain how one can obtain such trajectories.

The reference trajectory in Figure 3.1 may be interpreted to have two segments, i.e., an ante-event and post-event segment, giving

$$\boldsymbol{\alpha}(t) = \begin{cases} \boldsymbol{\alpha}^a(t), & t \in [t_0, \tau_1], \\ \boldsymbol{\alpha}^p(t), & t \in (\tau_1, t_f], \end{cases} \tag{3.3}$$

denoted, respectively, with upperscripts a and p. The nominal input to define (3.3) is similarly defined in two segments as

$$\boldsymbol{\mu}(t) = \begin{cases} \boldsymbol{\mu}^a(t), & t \in [t_0, \tau_1], \\ \boldsymbol{\mu}^p(t), & t \in (\tau_1, t_f]. \end{cases} \tag{3.4}$$

The extended reference trajectory, denoted with an upper bar as $\bar{\boldsymbol{\alpha}}(t)$, is then realized by the extension of the individual segments of (3.3) to a larger time interval. These segments can be extended past the point of discontinuity at $t = \tau_1$, ignoring the guard conditions, by forward or backward integration of the vectorfields in their corresponding modes. To define these extended segments, one requires vectorfields $\boldsymbol{f}^a$ and $\boldsymbol{f}^p$ to be defined past these points of discontinuity, and consequently we need extended input terms $\bar{\boldsymbol{\mu}}$. Figure 3.3 illustrates possible extended input terms for a discontinuous nominal input. Looking at the ante-event segment specifically, one could define the extended ante-event input segment as

$$\bar{\boldsymbol{\mu}}^a(t) = \begin{cases} \boldsymbol{\mu}^a(t), & t \in [t_0, \tau_1], \\ \bar{\boldsymbol{\mu}}_1^a(t), & t \in [\tau_1, t_f], \end{cases} \quad \text{or} \quad \bar{\boldsymbol{\mu}}^a(t) = \begin{cases} \boldsymbol{\mu}^a(t), & t \in [t_0, \tau_1], \\ \bar{\boldsymbol{\mu}}_2^a(t), & t \in [\tau_1, t_f]. \end{cases} \tag{3.5}$$

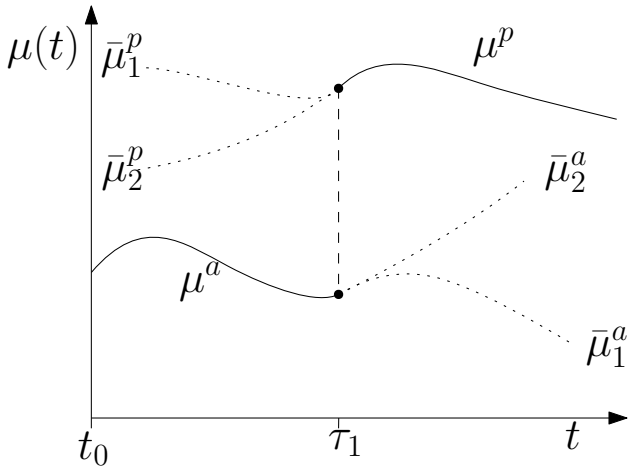

Figure 3.3: A graphical representation of possible extended input segments. The pre-event segments are denoted with upperscript a and the post-event segments with upperscript p.

These extended input terms are free to be shaped, but it is recommended to keep them continuous. Defining discontinuous extended segments may cause complications for the sensitivity analysis of state-triggered hybrid systems performed in Chapter 4. This analysis is derived from classical sensitivity analysis on nonlinear systems, see [42], which assumes continuous input terms. Note that when the nominal input is continuous, one is free to use the nominal input as an extension.

The extended reference segments $\bar{\boldsymbol{\alpha}}^a(t)$ and $\bar{\boldsymbol{\alpha}}^p(t)$ can then be defined using corresponding extended input terms $\bar{\boldsymbol{\mu}}^a(t)$ and $\bar{\boldsymbol{\mu}}^p(t)$. Note that there is only one extended reference trajectory, which is defined by the combination of all these extended segments. Figure 3.4 illustrates the extended reference segments for the reference trajectory in Figure 3.1. Looking at the left drawing, one can notice that the extended reference segment is defined past its guard triggering condition. Similarly on the right drawing, the extended reference segment is defined before the nominal event time τ_1.

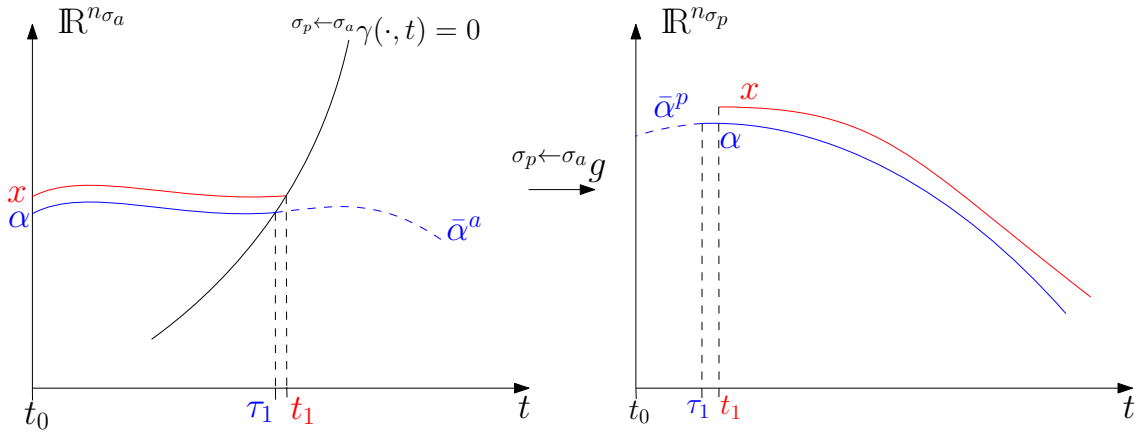

Figure 3.4: A graphical representation of the extended reference trajectory of Figure 3.1.

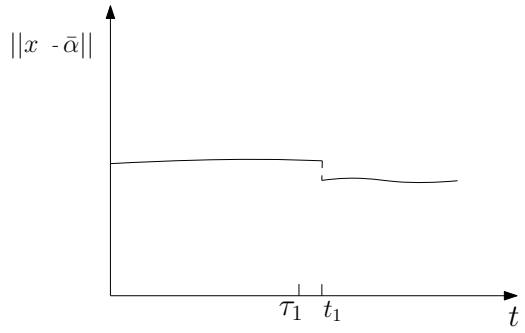

Figure 3.5: A graphical representation of a possible behavior of $||\boldsymbol{e}_R||$ for the state and extended reference trajectory in Figure 3.4. We have discontinuous behavior at $t = t_1$ (the jump time of the state trajectory), but peaking behavior is eliminated.

A new notion of error is created as

$$\boldsymbol{e}_R(t) = \begin{cases} \boldsymbol{x}(t) - \bar{\boldsymbol{\alpha}}^a(t), & \text{before event time } t_1, \\ \boldsymbol{x}(t) - \bar{\boldsymbol{\alpha}}^p(t), & \text{after event time } t_1. \end{cases} \tag{3.6}$$

This error term jumps at the same time instances as the state trajectory and uses the extended reference trajectory to always compare the state and reference trajectory for the same modes. Figure 3.5 then illustrates a possible behavior of this new error trajectory, and one can see that no peaking behavior is present. Note that the error may still show discontinuous behavior, but that the jump in this new error term is most likely not as big as for the Euclidean error. The RS control then incorporates this new error term (3.6) in its control input as

$$\boldsymbol{u}(t) = \bar{\boldsymbol{\mu}}(t) - \boldsymbol{K}(t)\boldsymbol{e}_R(t), \tag{3.7}$$

where $\boldsymbol{K} \in \mathbb{R}^{m_\sigma \times n_\sigma}$ is a (time-varying) feedback gain. Similarly, the control input consists of an ante-event and a post-event segment, switching at the jump times of the state trajectory $\boldsymbol{x}$. Next, we introduce the hybrid time (t, j). This is done to keep the notations consistent and clear, as denoting a pre-event with a letter a and the post-event with a letter p may not be that efficient when considering multiple jumps.

3.1.3 Reference spreading for single guard activation: multiple-events

An extended reference trajectory has a number of segments that equals the number of modes that it experiences. For the single-event case, one could distinguish these segments by denoting an ante- and post- event mode. When considering multiple events, such a method may become ambiguous. A solution to this, is to use the concept of hybrid time (t, j), see [43], with t denoting the continuous time and j the discrete time (jump counter). The hybrid time formalism, used in [15, 16, 17, 18, 24], allows to conveniently describe trajectories with multiple events, occurring at nominal times τ_1, τ_2, etc. The hybrid time domain of the reference is defined as

$$I_\alpha = \bigcup_{j=0}^{N} \{[\tau_j, \tau_{j+1}] \times \{j\}\}, \tag{3.8}$$

where $\tau_0 = t_0$ and $\tau_{N+1} = t_f$. The domain of the extended reference trajectory is then obtained by extending the domain I_α, see [15, 24], giving $\bar{I}_\alpha \supset I_\alpha$. One could define the reference domain at a particular discrete time j as $I_\alpha^j = [\tau_j, \tau_{j+1}]$ and consequently obtain the extended reference domain as $\bar{I}_\alpha^j = [-\delta + \tau_j, \tau_{j+1} + \delta]$ with $\delta > 0$. The extended reference segments are defined as $\bar{\boldsymbol{\alpha}}(t, j) = \boldsymbol{\alpha}(t, j)$ for $(t, j) \in I_\alpha$ and can be described pas point of discontinuity, i.e., before τ_j and past τ_{j+1}, by integrating the vectorfield, respectively, backward and forward. The result of this approach is presented in Figure 3.6.

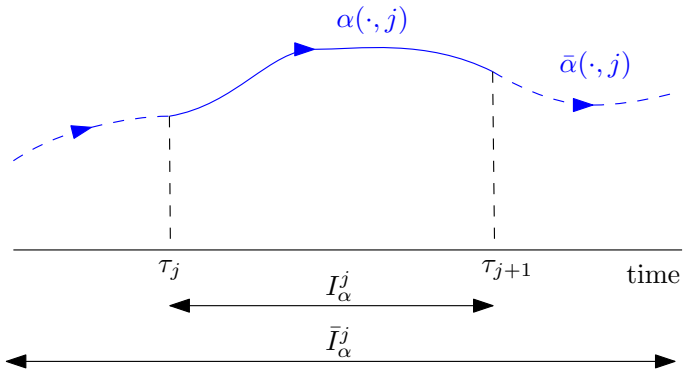

Figure 3.6: A graphical representation of a reference trajectory, with solid lines, and extended reference trajectory, with dashed lines, for discrete time j, see [24]. The nominal and extended hybrid time domains are illustrated as I_α^j and $\bar{I}_\alpha^j$.

A similar hybrid time domain can be defined for the state trajectory as

$$I_x = \bigcup_{j=0}^{N} \{[t_j, t_{j+1}] \times \{j\}\}, \tag{3.9}$$

with $t_{N+1} = t_f$. Figure 3.7 gives an illustration of an arbitrary (extended) reference and state trajectory in the hybrid time domain. By defining the hybrid time domain $\bar{I}_\alpha \supseteq I_x$, one is able to compare an extended reference trajectory to a state trajectory in the same modes. The error (3.6) can then be rewritten as a function of hybrid time as

$$\boldsymbol{e}_R(t, j) = \boldsymbol{x}(t, j) - \bar{\boldsymbol{\alpha}}(t, j). \tag{3.10}$$

The control input term likewise changes into

$$\boldsymbol{u}(t, j) = \bar{\boldsymbol{\mu}}(t, j) - \boldsymbol{K}(t, j)\boldsymbol{e}_R(t, j). \tag{3.11}$$

This concludes the RS control for single guard activation. In the next section, we continue by treating the RS control for simultaneous guard activation.

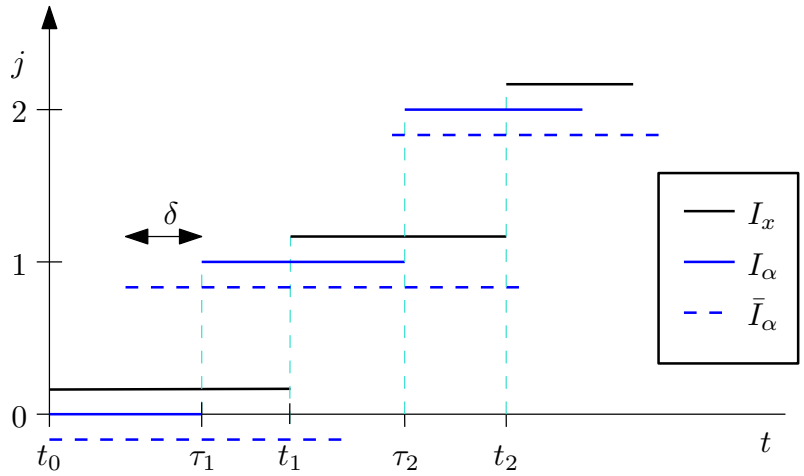

Figure 3.7: A graphical representation, in hybrid time domain, of the differences among the reference trajectory $\boldsymbol{\alpha}$, the extended reference trajectory $\bar{\boldsymbol{\alpha}}$, and the state trajectory $\boldsymbol{x}$, see [24].

3.2 Reference spreading for simultaneous guard activation

In the previous section, the RS control for single guard activation was discussed. This section focuses on the RS control for simultaneous guard activation, which has not been done in the literature before. Recall that the term *simultaneous guard activation* is used to clarify that two (or more) guard conditions are triggered at the same time instance. We start by discussing the tracking problem. A similar problem is observed as with the single-guard case, i.e., peaking phenomenons, but also new problems are observed, i.e., the perturbed system jumping more and coming into modes not specified in the reference. To solve the tracking problem, we propose the RS control for simultaneous guard activation, which also makes use of extended trajectories. Similarly as with the single-guard case, a *multi-scale hybrid time* (t, i, k) is introduced to provide clear descriptions of the trajectories. In this multi-scale hybrid time, new variables i and k denote different discrete time scales. The local stability of the system is then further analyzed in Chapter 4 via a local model, cf. [23].

3.2.1 Tracking problem state triggered hybrid systems with simultaneous guard activation

We assume just as for the single-guard case a reference trajectory that has no Zeno-behavior and sufficiently smooth guard functions, vector fields, and jump maps. The guard condition is assumed to be triggered with the transversality property, and we further assume *unidirectional event completion.*

Assumption 3.2 (Unidirectional event completion) *For a system starting in a mode with inactive guards and undergoing a transition corresponding to the nominal event, the system does not transition to modes for which already active guards become inactive.*

A guard is then deemed *active* when the system keeps satisfying the guard and *inactive* when the system can not satisfy the guard. The term *transition corresponding to the nominal event* is clarified further below. In a mechanical context, the usage of Assumption 3.2 leads to the consideration of inelastic impacts with no superfluous contacts. Relating the guard to the contact distance function being zero, we can deem the guard active after inelastic impact as the contact distance becomes zero.

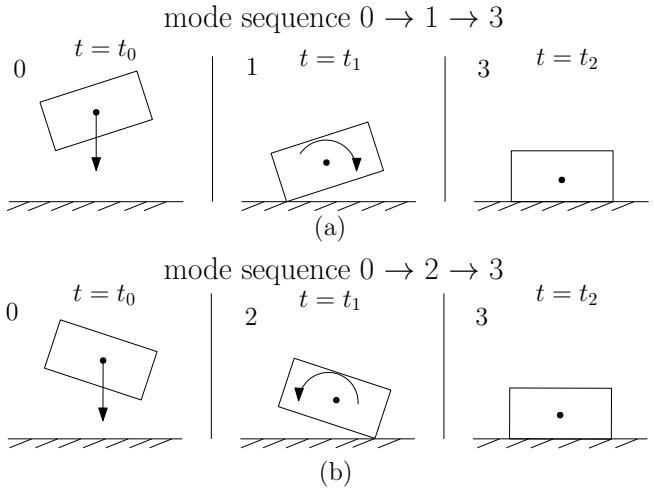

Figure 3.8: A graphical representation of a falling planar block with two contact points experiencing different impact sequences for different perturbations on its initial rotation. The impact times are given as t_1 and t_2 with $t_0 \leq t_1 \leq t_2$. In the upper drawing (a), the block impacts on its left corner first. In the lower drawing (b), the block impacts on its right corner first.

In contrast to the single-guard case, a nearby state trajectory to the reference trajectory does not solely jump sooner or later than the reference, but shows in addition more jumps. During these jumps, the system comes into modes which are not specified in the reference. To illustrate this behavior, we consider a mechanical system experiencing simultaneous impact. To this end, we treat a simplified system with two contact points as in Figure 2.1 of Chapter 2. Simultaneous impact is then characterized by the two contact points A and B impacting the horizontal surface at the same time instance.

Four modes are present, denoted as $\sigma \in \{0, 1, 2, 3\}$, where mode 0 represents *free motion*, mode 1 *single contact at point A*, mode 2 *single contact at point B*, and mode 3 *full contact*. A reference trajectory with simultaneous impact starts and stays in mode 0 until the system impacts, after which it continues in mode 3. A state trajectory with an initial condition $\boldsymbol{x}(t_0, j)$, different but close to $\boldsymbol{\alpha}(t_0, j)$, continues instead in modes which are not specified in the reference motion. Consequently, these modes are called *unspecified modes*. In addition, depending on the perturbation, the state trajectory may experience a different *mode sequence*. Figure 3.8 illustrates this, where the lower and upper drawings depict the motion of a block with a certain perturbation on its initial rotation. In the upper drawing, the block experiences the mode sequence $0 \to 1 \to 3$, whereas in the lower drawing the block experiences the mode sequence $0 \to 2 \to 3$. Notice how the initial and final modes for the state trajectories are equal as for the nominal trajectory, i.e., mode 0 and mode 3. One can thus interpret the state trajectory to undergo a transition corresponding to the nominal event, with the state trajectory *initiating the nominal event* at the first impact $t = t_1$ and *completing the nominal event* at the final impact $t = t_2$. Note that the reference trajectory can then be interpreted to initiate and complete the nominal event at the time instance $t = \tau_1$.

The perturbed block experiences thus two impacts, and Figure 3.9 illustrates this by letting the state trajectory have two jumps. Observe how the reference trajectory jumps only once, and, subsequently, one concludes that there is not only a mismatch in the jump time, but also a mismatch in the number of jumps. The influence of this is also seen in the Euclidean error (3.2), depicted in Figure 3.10, where one observes two peaks of high error values instead of one. This peaking phenomenon is unwanted for the same reasons as given for the single-guard case in Section 3.1.1. Furthermore, to our knowledge, there exist no control strategies dealing with this mismatch of number of jumps between the state and reference trajectory.

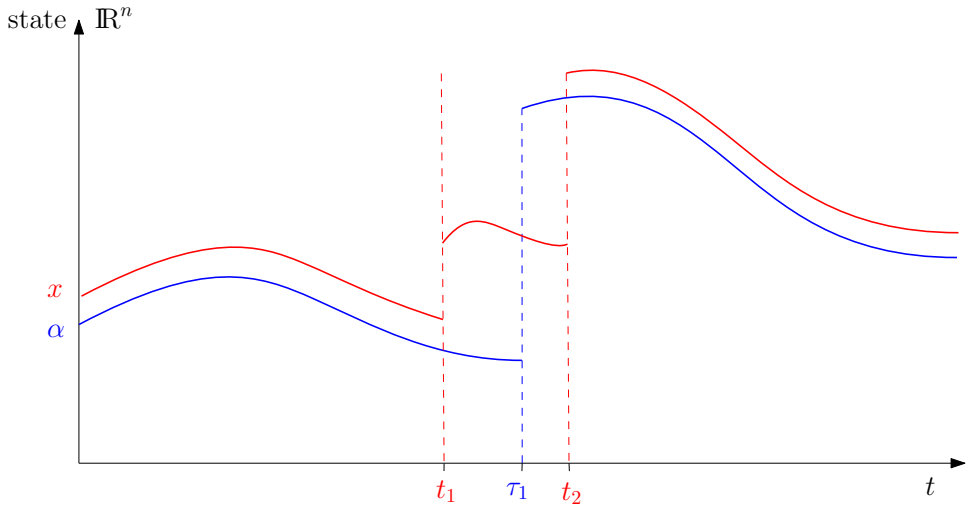

Figure 3.9: A graphical representation of a reference trajectory $\boldsymbol{\alpha}(t, j)$ with simultaneous impacts (blue line) and a nearby state trajectory $\boldsymbol{x}(t, j)$ (red line) with a short sequence of single-contact impacts. The reference trajectory jumps at $t = \tau_1$, and the perturbed trajectory at $t = t_1$ and $t = t_2$.

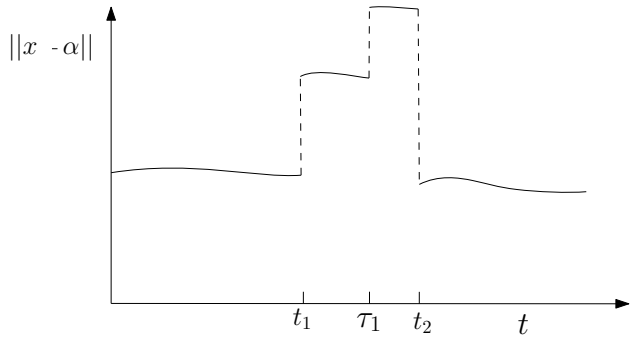

Figure 3.10: A graphical representation of the Euclidean error norm for the trajectories in Figure 3.9. The peaking behavior is seen in the time interval $t \in [t_1, t_2]$ where one observes two jumps.

Another problem, is the occurrence of unspecified modes. The state trajectory may behave vastly different, depending on its initial perturbation. Recall that Figure 3.8 illustrates this, in which the block may experience two different perturbed motions, i.e., two different mode sequences. One may consider that the number of *feasible* mode sequences, i.e., realizable in practice, is related to the number of guard conditions (participating in simultaneous guard activation). Consequently, trajectory tracking may become more difficult when increasing the number of guard conditions. We thus propose the RS control for simultaneous guard activation to deal with the more complex peaking phenomenon and, in addition, realize trajectory tracking regardless of the mode sequence of the state trajectory. The latter is done as we are uninterested in the behavior of the system in the unspecified mode(s), i.e., as long as the dynamical system is able to complete the nominal event it is fine. Before describing the control strategy, we first introduce the multi-scale hybrid time (t, i, k) to describe the considered trajectories in a less ambiguous manner, explained in detail in Section 3.2.2. From now on, the hybrid time (t, j) is referred to as *classical hybrid time*.

3.2.2 Multi-scale hybrid time (t, i, k)

We first explain the problems of using the classical hybrid time (t, j). One observes from Figure 3.9 that a mismatch of number of jumps is present between the state and reference trajectory, i.e., there are more event times t_j than nominal event times τ_j. This is due to perturbations typically destroying the occurrence of a simultaneous guard activation. The state trajectory instead activates the guards in a case-dependent sequence that involves typically no simultaneous guard activation. This leads to a short lived-continuous time evolution of the trajectory, and consequently we say that state trajectory undergoes a *short-lived sequential activation* of the single guard conditions.

Due to this mismatch of jump count, the discrete time (jump counter) of the reference j_α does not increase in the same manner as the discrete time of the state j_x. The error term (3.10) then compares the state and reference trajectory for the wrong modes. For the block example in Figure 3.8, $j_x = 1$ could indicate one of the unspecified modes *1* or *2*, while $j_\alpha = 1$ indicates mode 3. Having multiple events with simultaneous guard activation will only make the difference between j_α and j_x bigger, especially considering the possibility of having different numbers of guard conditions involved at different nominal events. To clarify the complicated behaviour of multiple simultaneous guard activated events, we consider a mechanical system experiencing simultaneous impacts, i.e., the tetrahedron in Figure 3.11 with the contact points *C*, *D*, and *E*.

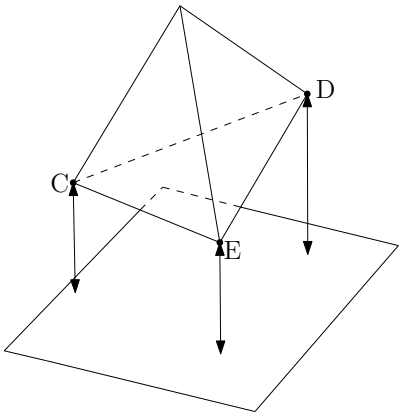

Figure 3.11: A Tetrahedal object with three contact points C, D, and E. The contact distances are represented by the double-sided arrows, and the object is in a motion where it will impact with its surface CDE.

We define a reference trajectory for this object that has the following nominal events: (1) simultaneous inelastic impact with all its contact points C, D, and E; (2) simultaneous detachment with all its contact points. The state trajectory may then behave differently, because

- at the first nominal event, the state trajectory experiences two events. The first event is the object experiencing a single-contact inelastic impact at point C, and the second event is the object experiencing simultaneous inelastic impacts at points D and E.
- At the second nominal event, the state trajectory experiences three events. Herein, the object experiences a short sequence of single-contact detachments for the three contact points.

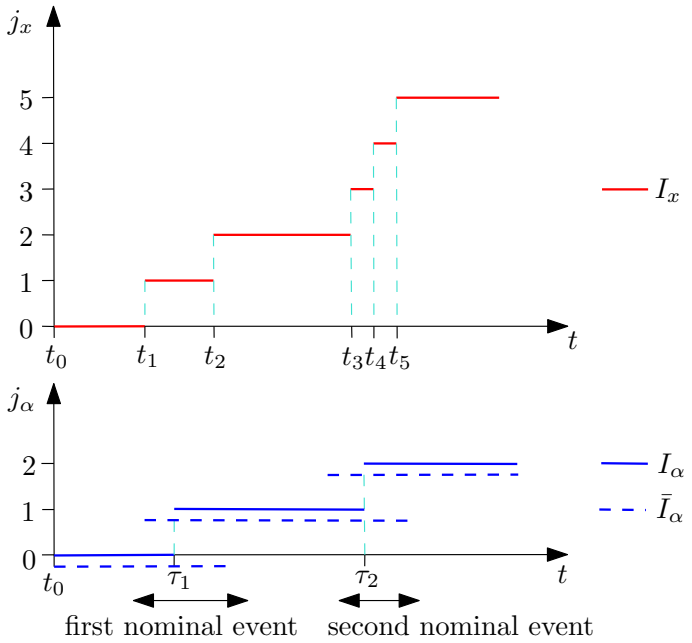

Figure 3.12: A graphical representation, in classical hybrid time domain (t, j), of the differences among the reference trajectory $\boldsymbol{\alpha}$, the extended reference trajectory $\bar{\boldsymbol{\alpha}}$, and the state trajectory $\boldsymbol{x}$ for the tetrahedal object example experiencing multi-contact nominal events.

Figure 3.12 illustrates a possible classical hybrid time domain representation of the example described above. Here, the solid blue lines represent the reference trajectory, the dashed blue lines the extended reference trajectory, and the solid red lines the state trajectory. One observes that after the first nominal event, the discrete time for both trajectories are $j_\alpha = 1$ and $j_x = 2$. This difference increases after the second nominal event where the discrete times are $j_\alpha = 2$ and $j_x = 5$. One thus concludes that using the discrete time j may result in ambiguous descriptions of the trajectories, i.e., one may not know which counters j_x and j_α should be used in (3.10) to compare the correct extended reference segment to the current state segment.

We propose the multi-scale hybrid time (t, i, k) to solve this problem. Here, $k \in \mathbb{N}_{\geq 1}$ represents a so-called *micro* counter, and $i \in \mathbb{N}_{\geq 0}$ a so-called *macro* counter. This is explained next, where we furthermore explain the relation between classical hybrid time (t, j) and multi-scale hybrid time (t, i, k).

Relation i, k and j

Considering the hybrid time domain in Figure 3.12, one may want to show that the event times t_1 and t_2 *belong* to the first nominal event, while the event times t_3 - t_5 *belong* to the second nominal event. To do so, we *split* the discrete time j in a macro counter i and micro counter k. The counter i starts at 0 for $t = t_0$ and increases with a step of one unit every time the nominal event is initiated. The micro counter k starts at 1 for $t = t_0$ and increases with a step of one unit whenever an event happens, except when the macro counter i is increased of one unit, as then k gets reset to 1. Note that the counter i increases whenever an event is initiated to completing a nominal event, and k indicates how many local events has passed during the completion of this nominal event.

Remark 3.1 *The multi-scale hybrid time (t, i, k) requires knowledge of the nominal event beforehand. It is for this reason that the reference trajectory should be known for a correct application of the multi-scale hybrid time.*

By substituting the event times t_j and τ_j as, respectively, t_i^k and τ_i^k, one can assign event times to belong to a corresponding nominal event. Interpreting the macro counter i as a nominal event counter, one can substitute the first two event times t_1 and t_2 of figure 3.12 as, respectively, t_1^1 and t_1^2. The same can be done for second set of event times t_3 - t_5, resulting in t_2^1, t_2^2, and t_2^3. In the following, we omit the upperscript k when $k = 1$, i.e., $t_i := t_i^1$. Figure 3.13 then illustrates the hybrid time domain of the trajectories in Figure 3.12 for a multi-scale hybrid time application.

The mathematical relation between (i, k) and j is defined as

$$j = (k - 1) + \sum_{p=0}^{i-1} \kappa(p) \tag{3.12}$$

with $\kappa(i)$ being the so-called *event complexity of nominal event i*. This variable denotes the total (maximum) local events that a trajectory has experienced to completing a (previous) nominal event i, i.e., the maximum micro counter k for a (previous) macro counter i. Considering Figure 3.13, we can insert $\kappa(0) = 1$, $\kappa(1) = 2$, and $k = 3$ into (3.12) resulting in $j = 5$. Note that given the context of the event, we can determine $\kappa(2) = 3$. If we did not know that the state trajectory had completed its event, then we may have also had a $k = 4$ for $i = 2$.

We can then formally describe the multi-scale hybrid time domain of the reference, similar to (3.8), as

$$I_\alpha = \bigcup_{i=0}^{N} \{ \bigcup_{k=1}^{\kappa_\alpha(i)} \{ [\tau_i^k, \tau_i^{k+1}] \times \{k\} \} \times \{i\} \}, \tag{3.13}$$

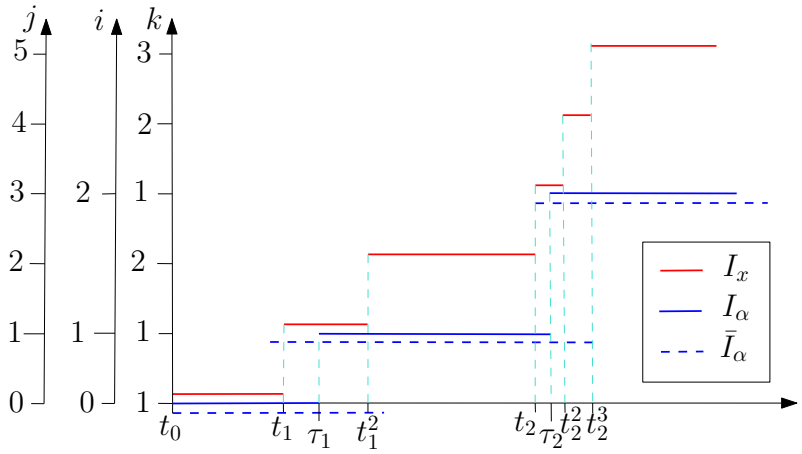

Figure 3.13: A graphical representation, in multi-scale hybrid time (t, i, k), of the differences among the reference trajectory $\boldsymbol{\alpha}$, the extended reference trajectory $\bar{\boldsymbol{\alpha}}$, and the state trajectory $\boldsymbol{x}$. A reference trajectory with simultaneous guard activation and a state trajectory with a short-lived sequential activation of (single) guard conditions is considered. This can be observed as a maximum counter $k = 1$ for the reference trajectory and a maximum counter $k > 1$ for the state trajectory.

where $\tau_0^1 = t_0$, $\tau_i^{k+1} = \tau_{i+1}^1$ when $k = \kappa_\alpha(i)$, and $\tau_N^{k+1} = t_f$ when $k = \kappa_\alpha(N)$. Note that in the rest of this chapter we always assume $\kappa_\alpha(i)$ to be 1 (without loss of generality), as trajectories with simultaneous guard activation only jumps once. The hybrid time domain for the state is similarly set up as

$$I_x = \bigcup_{i=0}^{N} \{ \bigcup_{k=1}^{\kappa_x(i)} \{ [t_i^k, t_i^{k+1}] \times \{k\} \} \times \{i\} \}, \tag{3.14}$$

where $t_0^1 = t_0$, $t_i^{k+1} = t_{i+1}^1$ when $k = \kappa_x(i)$, and $t_N^{k+1} = t_f$ when $k = \kappa_x(N)$. We distinguish the maximum micro counters of the two trajectories with a subscript as κ_α and κ_x.

For a particular discrete time i and k, the reference domain is defined as $I_\alpha^{k,i} = [\tau_i^k, \tau_i^{k+1}]$, and we obtain the extended reference domain as $\bar{I}_\alpha^{k,i} = [-\delta + \tau_i^k, \tau_i^{k+1} + \delta]$ with $\delta > 0$. Taking $\bar{\boldsymbol{\alpha}}(t, i, k) = \boldsymbol{\alpha}(t, i, k)$ for $(t, i, k) \in I_\alpha$, we obtain $\bar{\boldsymbol{\alpha}}(t, i, k)$ before or past the point of discontinuity by integrating the vectorfield forward or backward in time. Now that the multi-scale hybrid time is fully treated, we continue by explaining our control strategy.

3.2.3 Reference spreading for simultaneous impacts: single-event case

As mentioned above, a perturbation typically causes a state trajectory to come into unspecified modes. Dependent on the perturbation, the state trajectory may experience different unspecified mode(s) and thus experience different mode sequences. We are, however, not interested in the possible behaviors of the state trajectory during these unspecified mode(s) and only focus on the mode just before the nominal event has initiated and the mode just after the nominal event has concluded. Furthermore, as we perform a local analysis, we assume the perturbations to be small and consequently assume the duration of the unspecified mode(s) to be short. Due to this short time-interval, one can not assume to measure the state and thus the error. For these reasons, we thus seek a control strategy that should achieve trajectory tracking regardless of the mode sequence of the state trajectory, i.e., we do not keep track of the error during these unspecified modes.

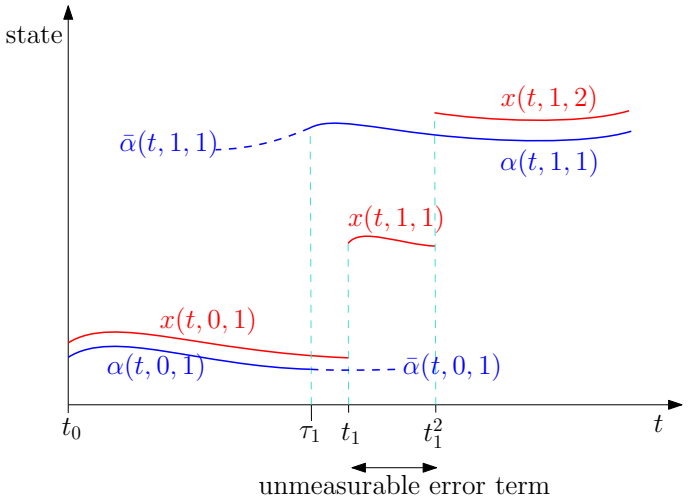

Figure 3.14: Graphical illustration of a reference trajectory with simultaneous guard activation and a nearby state trajectory with a short sequential activation of single guard conditions. The unmeasurable period is indicated as the time during these unspecified mode(s), i.e., during the time when the state trajectory *tries* to complete the nominal event.

To do so, we define the control input $\boldsymbol{u}(t,i,k)$, formulated in the same hybrid time domain as the state $\boldsymbol{x}$, for these measurable periods, i.e., before t_i^1 and past $t_i^{\kappa_x(i)}$, as

$$\boldsymbol{u}(t,i,\kappa_x(i)) = \bar{\boldsymbol{\mu}}(t,i,1) - \boldsymbol{K}(t,i,1)\boldsymbol{e}_R(t,i,\kappa_x(i)) \tag{3.15}$$

with

$$\boldsymbol{e}_R(t,i,\kappa_x(i)) = \boldsymbol{x}(t,i,\kappa_x(i)) - \bar{\boldsymbol{\alpha}}(t,i,1). \tag{3.16}$$

In (3.15) and (3.16), one should note that the micro counters k for the variables $\bar{\boldsymbol{\alpha}}$, $\bar{\boldsymbol{\mu}}$, and $\boldsymbol{K}$ are substituted with 1, corresponding to the assumed maximum micro counter $\kappa_\alpha(i) = 1$. The variables $\bar{\boldsymbol{\mu}}$ and $\boldsymbol{K}$ are thus defined in the same hybrid time domain as the reference. Equation (3.16) only defines the error when the two trajectories are in the same modes. The two trajectories are in the same modes when neither trajectories have initiated the nominal event and when both trajectories have completed the nominal event. The completion of the nominal event is characterized by the micro counter $\kappa(i)$, hence why we only compare the terms $\kappa_x(i)$ and $\kappa_\alpha(i) = 1$. To clarify this, an example is depicted in Figure 3.14 for which $i = 0$ and $k = 1$ at t_0. Furthermore, $\kappa_\alpha(0) = \kappa_\alpha(1) = 1$, $\kappa_x(0) = 1$, and $\kappa_x(1) = 2$, to which the measurable error term is defined as

$$\begin{aligned} \boldsymbol{e}_R(t,0,1) &= \boldsymbol{x}(t,0,1) - \bar{\boldsymbol{\alpha}}(t,0,1), \\ \boldsymbol{e}_R(t,1,2) &= \boldsymbol{x}(t,1,2) - \bar{\boldsymbol{\alpha}}(t,1,1). \end{aligned} \tag{3.17}$$

For the duration that the state trajectory is in the unspecified mode(s), the error can not be measured such that another control input is needed. One option is to remove feedback completely and only apply the pre-nominal event feedforward segment in the control input as

$$\boldsymbol{u}(t,i,k_x) = \bar{\boldsymbol{\mu}}(t,i-1,1), \qquad \forall\{k_x\}\times\{i\} : k_x \neq \kappa_x(i), \tag{3.18}$$

where one should recall that the macro counter i is of one step higher in the unspecified mode(s). Another option is to not remove the feedback, and keep it constant to the value determined just before the nominal event was initiated, i.e., before macro counter i had jumped. One reason is the attempt to further decrease the duration of the unspecified mode(s). Another reason is the control input getting only one jump, in contrast to the first strategy where the control input gets two jumps. This may consequently result in better performance when applying the second strategy,

which is formulated as

$$\begin{aligned}\boldsymbol{u}(t,i,k_x) = \bar{\boldsymbol{\mu}}(t,i-1,1) - \boldsymbol{K}(t_i,i-1,1)\Big(\boldsymbol{x}(t_i,i-1,\kappa_x(i-1)) - \bar{\boldsymbol{\alpha}}(t_i,i-1,1)\Big),\\ \forall\{k_x\}\times\{i\} : k_x \neq \kappa_x(i).\end{aligned} \tag{3.19}$$

The RS control for simultaneous guard activation is thus formulated as (3.15) and (3.16), i.e., the control input for the measurable periods, with either (3.18) or (3.19), i.e., the control input for the unmeasurable period.

Different methods exist to design a feedback gain $\boldsymbol{K}$. In this work, we choose to derive this via a model that predicts the local behavior of the reference trajectory. We thus continue in Chapter 4 by analyzing the stability of a reference trajectory with simultaneous guard activation. From this local analysis, a *time-triggered hybrid system* is obtained. Stability analysis on time-triggered hybrid systems are well established in the literature, cf. [16], and may be used in combination with *RS control for simultaneous guard activation* to design a tracking controller. This is proven for *RS control for single guard activation* in [16], and numerical experiments in Chapter 5 are thus performed to determine whether this may also hold for the simultaneous guard activated case. If so, then the time-triggered hybrid system may further be used to design optimal feedback gains, cf. [24].

3.2.4 Summary

In this chapter, we have discussed the RS control for single guard activation and the classical hybrid time (t, j) to, respectively, track and describe track trajectories with (multiple) jumps due to the activation of a single guard condition. For trajectories with (multiple) simultaneous guard activation, we have proposed the RS control for simultaneous guard activation and the multi-scale hybrid time (t, i, k) to, similarly, track and describe the considered trajectories in this work. For sake of brevity, we will refer to (t, i, k) as the *hybrid time* throughout the rest of the report. We now further analyze the local stability of trajectories with simultaneous guard activation in Chapter 4 via a sensitivity analysis, cf. [23]. To realize this analysis, extended trajectories are used. The resulting local model, a time-triggered hybrid system, may then help in designing stabilizing closed-loop gains for the RS control for simultaneous guard activation.

Chapter 4

Sensitivity analysis for simultaneous guard activation

In this work, we focus on mechanical systems with unilateral constraints experiencing simultaneous impacts. These systems fit well, to a certain extent, in a hybrid system framework as discussed in Section 2.2. We proposed a hybrid control strategy in Chapter 3 for these trajectories with simultaneous impacts, i.e., trajectories with simultaneous guard activation. Here, *Simultaneous guard activation* is clarified as the triggering of two (or more) guard conditions simultaneously. In this chapter, we investigate whether a local model can be built that predicts the development of such trajectories for slight perturbations in the initial condition or feedforward input. For smooth nonlinear systems this is called a sensitivity analysis, see [42]. In [23] and references therein, the authors have performed a sensitivity analysis on state-triggered hybrid systems with single-guard triggered jumps. In this work, the sensitivity analysis of [23] is extended to be applicable to trajectories with simultaneous guard activation. To our knowledge, this has not been done in the literature and the closest to what we found is [26].

This chapter starts by introducing *multi-contact hybrid notations* fitting to the multi-scale hybrid time (t, i, k) and dynamical systems experiencing simultaneous guard activation. After that, the sensitivity analysis on trajectories with simultaneous guard activation is performed, and a local model is built to analyze the influence of perturbations. We then conclude this chapter by describing how this local model can be used to analyze the stability of the dynamical system and, possibly, to design a tracking controller.

4.1 Multi-contact hybrid notations

Using conventional hybrid notations as in Section 2.2 might bring complications (e.g. non intuitive expressions) for describing state-triggered hybrid systems with jumps due to simultaneous guard activation. In this section, we discuss these complications and propose an alternative notation to describe these systems more proper. To clarify the application of these notations for the considered system in this work, examples of mechanical systems experiencing simultaneous impacts are treated. First, the mode is discussed, second the jump map, and third the guard.

4.1.1 Multi-scale mode numbering convention

The mode is commonly denoted as $\sigma = \{1, 2, \cdots, N\}$ with N being the number of discrete modes. For events with multiple guard conditions, such a notation may, however, lead to a large number of discrete modes due to the many combinations of active guards. Recall from Section 3.1.1 that a guard is deemed active when the corresponding guard condition keeps being satisfied. The interpretation of the mode may then become non-intuitive as it is unclear

which guards are active. We thus use a *base 2* representation, i.e., a binary row vector, to give a rational way to number the modes. Instead of $\sigma = \{0, 1, 2, 3, 4, 5\}$, we write, for instance, $\sigma = \{000_2, 001_2, 010_2, 011_2, 100_2, 101_2\}$, where we emphasize with the subscript 2 that it is a base 2 representation. For sake of brevity, we leave this subscript out in the rest of the report.

In a *base 2 mode numbering convention*, the number of columns is equal to the number of (participating) guards. Every column is associated a-priori to a guard, where a *0* represents an inactive guard and a *1* represents an active guard. This is clarified with the following example:

Example 4.1 *Considering an object with four contact points impacting a horizontal surface, e.g., a planar contact between a face of a 3D box and a flat surface, then one can assign four guards to be present, i.e., the contact distances between the contact points and the flat surface to equal zero. The base 2 mode numbering convention then has four columns, for which* $\sigma = 0000$ *represents the four guards being inactive, i.e., the 3D box has no contact with the flat surface, and* $\sigma = 1111$ *represents all four guards being active, i.e., the 3D box has contact with the flat surface with all its four contact points.*

A complication for this notation arises when multiple nominal events with simultaneous guard activations are considered. Assuming that the completion of separate nominal events involve the activation of different sets of guards, e.g., a mechanical system experiencing consecutive simultaneous impacts (and detachments) in different configurations, then the mode numbering convention may become unclear/unnecessary long. This is especially the case when detachments are characterized by a condition on the acceleration, cf. [24], and thus different guard conditions are needed for impacts and detachments. It is for this reason that we incorporate the hybrid time (t, i, k), introduced in Section 3.2.2, into the notation of the modes. We denote the set of modes *relevant* for a specific nominal event[1] as $\Sigma(i)$. Defining $c(i)$ as the number of guards that need to be active to complete a nominal event, we formulate the set of *relevant modes* as $\Sigma(i) = \{0, 1\}^{c(i)}$. One then only treats the relevant modes when analyzing a nominal event. To clarify this, we treat the implementation in more detail.

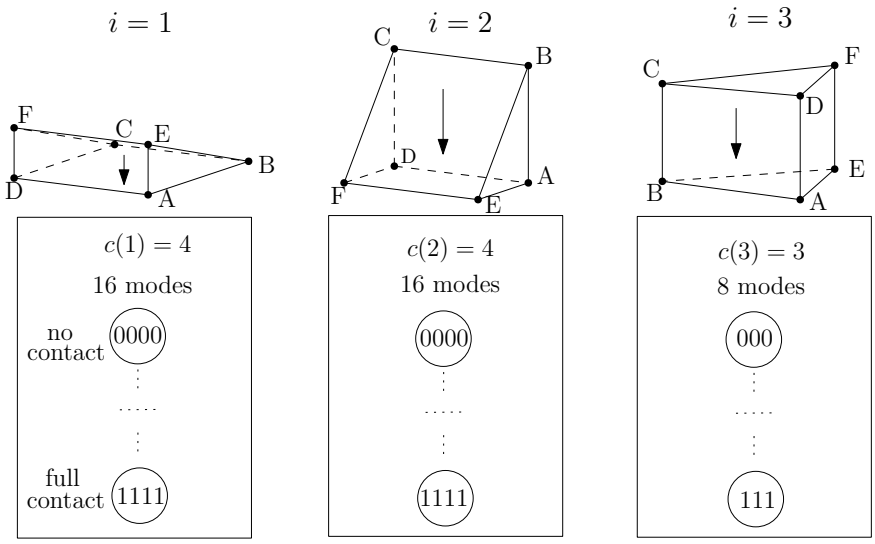

Figure 4.1: A graphical representation of a wedge with 6 contact points impacting a flat surface (in the direction of the arrow) for different configurations and its relevant modes $\Sigma(i)$. For nominal event $i = 1$ and $i = 2$, a four-contact simultaneous impact is considered for object surfaces ABCD and ADEF. For nominal event $i = 3$, a three-contact simultaneous impact is considered for object surface ABE.

[1] Recall from Section 3.2.2 that the nominal event is directly related to the macro counter i.

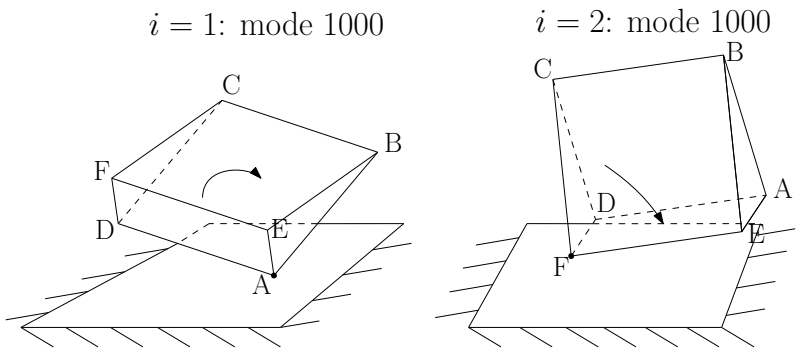

Figure 4.2: A graphical representation of the wedge configuration in mode 1000 for nominal event $i = 1$ (left drawing) and nominal event $i = 2$ (right drawing). The arrow depicts the direction in which the object falls.

Remark 4.1 *One should take into account that the terms "inactive" and "active" guards are relative with respect to the nominal event. If we would characterize a mechanical system to impact and detach by, respectively, the contact distance being zero and the contact distance being greater than zero, than an active guard for the impacting event, i.e., the contact distance being zero, is deemed as an inactive guard for a detaching event. An active guard for the detaching event would then become the contact distance being greater than zero. In this mechanical context, one may prefer to use a general mode notation with the columns denoting the contact distances, rather than the method proposed in this section.*

Figure 4.1 illustrates the relevant modes for different nominal events of a wedge impacting a flat surface in the direction of the arrow. For nominal events (macro counters) $i = 1$ and $i = 2$, the wedge experiences *four-contact simultaneous impact*, i.e., a simultaneous impact involving four contact points, on the flat surface with, respectively, the object surfaces ABCD and ADEF. Consequently, both nominal events are described with the same mode numbering convention. Although the modes are similar, e.g., mode *0000* is present for both nominal events $i = 1$ and $i = 2$, the interpretation of the mode requires knowledge of the nominal event beforehand. It is a-priori determined that the first column of the modes in $\Sigma(1)$ represents the contact between *A and the flat surface* and the first column of the modes in $\Sigma(2)$ the contact between *F and the flat surface*. Figure 4.2 clarifies this by illustrating possible wedge configurations for both nominal events with the same mode. For the last nominal event at $i = 3$, it is noticed that the mode numbering convention consists of one column less. This is due to the simultaneous impact for the surface ABE involving only three contacts, while the previous simultaneous impacts involved four contacts.

To describe the individual modes, we define a so-called *transition specific mode* $\sigma_k(i) \in \Sigma(i)$. We speak of *transition* when the system transitions from a mode of inactive guards to a mode of active guards. For sake of brevity, we will refer to $\sigma_k(i)$ as *mode* for the rest of the report. We consider Assumption 3.2, which essentially limits the set of possible post-event modes. Figure 4.3 depicts this property for an example with a three column mode, in which we observe $\Sigma(i)$ as a *partial ordered set* with $\sigma_{k+1}(i) > \sigma_k(i)$ defining a mode *greater* when it has more active guards and furthermore obeys Assumption 3.2. Note that $\sigma_{k+1}(i) = \emptyset$ when $k = \kappa(i)$, i.e., there is no post-event mode when the nominal event is completed.

A more intuitive interpretation of Figure 4.3 is obtained when we consider a mechanical system with three contacts. The reference motion of this mechanical system is a three-contact simultaneous impact on a flat surface, resulting in the mode sequence $000 \rightarrow 111$. A perturbed motion may, however, experience a different sequence, where the system experiences impact at one contact point and arrives in, for example, mode 100. As we assume inelastic impacts and no superfluous contacts, see Chapter 2, we expect the system to not detach at the impacted point, and hence

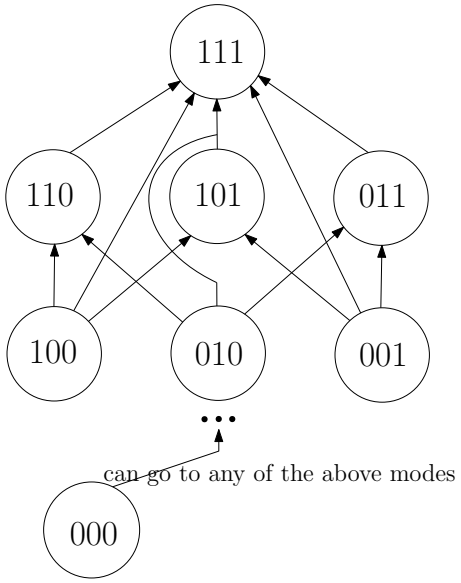

Figure 4.3: A graphical representation of the partial ordered set Σ for a mode with three columns. It depicts the limited set of modes which can take place after a (or multiple) guard condition(s) is triggered, as according to Assumption 3.2.

one can not achieve a further mode transition as, for instance, $100 \rightarrow 011$, where the first column becomes a zero. This then correlates with Assumption 3.2, where we assume that active guards can not become inactive during the transition that corresponds to a nominal event. Only modes in which extra contacts get closed, i.e., the contact distance between the corresponding contact and impacting surface becomes zero, are feasible post-event modes. Note that when $k = \kappa(i)$, the transition corresponding to the nominal event is completed, and hence all relevant guard conditions are active, resulting in $\sigma_\kappa(i) = 111$. One should furthermore take into account that $1 \leq \kappa(i) \leq c(i)$, depending on how the perturbed trajectory behaves. A perturbed trajectory may experience the mode sequence $000 \rightarrow 011 \rightarrow 111$, thus having a maximum micro counter $\kappa(i) = 2$, while the number of guard conditions $c(i) = 3$.

Example 4.2 *Considering a mechanical system with $c(i) = 4$ and its current mode being $\sigma_1(i) = 0011$, then the set of possible modes for the next impact at counter $k = 2$ is $\sigma_2(i) \in \{1111, 1011, 0111\} \subset \Sigma(i)$. The assumption of no superfluous contacts omits the possibility of having post-impact modes for which the third and fourth column become 0. The assumption of inelastic impacts then causes only post-impact modes with extra 1 in the first and/or second column.*

4.1.2 Multi-scale hybrid time jump map

In the sensitivity analysis in [15], that makes use of the classic hybrid time (t, j), the jump map from pre-event mode σ_a to post-event mode σ_p is indicated as ${}^{\sigma_p \leftarrow \sigma_a}\boldsymbol{g}(\boldsymbol{x}(t, j), t, j)$. In this work, we employ the hybrid time (t, i, k) in the jump map expression as

$$ {}^{\sigma_{k+1}(i) \leftarrow \sigma_k(i)}\boldsymbol{g}(\boldsymbol{x}(t, i, k), t, i, k), \tag{4.1} $$

for which $\sigma_{k+1}(i)$ denotes the post-event mode and $\sigma_k(i)$ the pre-event mode. For the sake of brevity, in the following we will write (4.1) simply as

$$ {}^{\sigma_{k+1} \leftarrow \sigma_k}\boldsymbol{g}(x^k, t, i) \tag{4.2} $$

with ${}^{\sigma_{k+1} \leftarrow \sigma_k}\boldsymbol{g} : \mathbb{R}^{n_{\sigma_k}} \times \mathbb{R} \times \mathbb{N} \rightarrow \mathbb{R}^{n_{\sigma_{k+1}}}$ and

$$ \boldsymbol{x}^k = \boldsymbol{x}^k(t, i) := \boldsymbol{x}(t, i, k). \tag{4.3} $$

For the first transitions at a nominal event i, we write the transition $\sigma_\kappa(i-1) \to \sigma_1(i)$ with a slight abuse of notation as $\sigma_0(i) \to \sigma_1(i)$. Note that $\sigma_\kappa(i-1)$ represents the mode before initiating a nominal event i, which is also interpreted as the mode after completing previous nominal event $i-1$, see Section 3.2.2. We introduce a virtual mode $\sigma_0(i) := \sigma_\kappa(i-1)$ which is used to keep the notation consistent. To clarify this matter, we consider a nominal event $i-1$ with three participating guard conditions, i.e., the transition is completed when these three guards are active. Completing the transition corresponding to the nominal event $i-1$ results in a mode $\sigma_\kappa(i-1) = 111$. At the next nominal event i, however, four guard conditions may be participating, and we thus have a mode numbering convention with four columns, i.e., $\sigma_k(i) \in \Sigma = \{0,1\}^4$. To keep the columns consistent for the first transition that corresponds to completing nominal event i, the choice is to denote a virtual micro counter $k = 0 := \kappa(i-1)$ for macro counter i, resulting in $\sigma_0(i) = 0000 := \sigma_\kappa(i-1)$. One could imagine the occurrence of such a situation for mechanical systems when considering a detachment with less/more number of contacts involved than the consecutive impact. We then similarly write the jump map corresponding to the first transition as

$$^{\sigma_1 \leftarrow \sigma_0}\boldsymbol{g}(\boldsymbol{x}^0, t, i) := {}^{\sigma_1(i) \leftarrow \sigma_\kappa(i-1)}\boldsymbol{g}(\boldsymbol{x}^\kappa, t, i-1) \tag{4.4}$$

with

$$\boldsymbol{x}(t, i, 0) := \boldsymbol{x}(t, i-1, \kappa). \tag{4.5}$$

With the jump map defined, we introduce the concept of *associativity* which will play an important role in the sensitivity analysis. We define this as:

Definition 4.1 (Associativity of jump maps) *The jump map of a hybrid system with a jump due to simultaneous activation of c guard conditions can be defined as*

$$^{\{1\}^c \leftarrow \{0\}^c}\boldsymbol{g}\left(x^0, t, i\right). \tag{4.6}$$

One speaks of associativity of jump maps when

$$^{\{1\}^c \leftarrow \{0\}^c}\boldsymbol{g}\left(x^0, t, i\right) = {}^{\sigma_\kappa \leftarrow \sigma_{\kappa-1}}\boldsymbol{g} \circ {}^{\sigma_{\kappa-1} \leftarrow \sigma_{\kappa-2}}\boldsymbol{g} \circ \cdots \circ {}^{\sigma_1 \leftarrow \sigma_0}\boldsymbol{g}\left(x^0, t, i\right) \tag{4.7}$$

holds for any mode sequence $\sigma_\kappa \leftarrow \sigma_{\kappa-1} \leftarrow \cdots \leftarrow \sigma_0$ with $\sigma_{k+1} > \sigma_k$ defining a mode "greater" when it has more guards active and furthermore obeys Assumption 3.2. Herein, we define $\sigma_\kappa = \{1\}^c$ and $\sigma_0 = \{0\}^c$ with $1 \leq \kappa \leq c$.

One can interpret this as a *c-simultaneous guard activated jump map*, i.e., a jump map associated with the triggering of c-guard conditions simultaneously, being decomposed into an instantaneous arbitrary sequence of *c-smaller guard activated jump maps*, i.e., jump maps associated with the triggering of less than c guard conditions (simultaneously), with the total number of unique guard conditions being equal to c and $\sigma_{k+1} > \sigma_k$ as mentioned above. This can be clarified with the following example:

Example 4.3 *Consider a mechanical system with no superfluous contacts undergoing a three-contact simultaneous inelastic impact for which the pre-impact mode is denoted as $\sigma_0(i) = 000$ and post-impact mode as $\sigma_1(i) = 111$, giving the jump map*

$$^{111 \leftarrow 000}\boldsymbol{g}(x^0, t, i). \tag{4.8}$$

Having associativity then allows us to decompose this three-contact simultaneous impact into an arbitrary instantaneous sequence of sub-impacts, i.e., impacts leading to completing the nominal simultaneous impact, as

$$\begin{aligned} {}^{111 \leftarrow 000}\boldsymbol{g}(x^0, t, i) &= {}^{111 \leftarrow 110}\boldsymbol{g} \circ {}^{110 \leftarrow 00}\boldsymbol{g}(x^0, t, i) \\ &= {}^{111 \leftarrow 011}\boldsymbol{g} \circ {}^{011 \leftarrow 00}\boldsymbol{g}(x^0, t, i) \\ &\vdots \\ &= {}^{111 \leftarrow 011}\boldsymbol{g} \circ {}^{011 \leftarrow 001}\boldsymbol{g} \circ {}^{001 \leftarrow 00}\boldsymbol{g}(x^0, t, i) \end{aligned} \tag{4.9}$$

for which the mode sequence is thus not important.

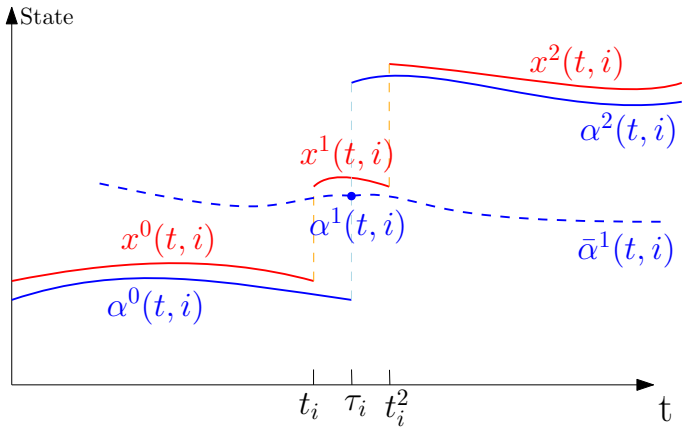

Figure 4.4: A graphical representation of the effects of using Assumption 4.1 on the reference trajectory $\boldsymbol{\alpha}$. The typical simultaneous guard activated jump from $\boldsymbol{\alpha}^0$ to $\boldsymbol{\alpha}^2$ is now decomposed into two steps with $\boldsymbol{\alpha}^1$ being an intermediate point in the unspecified mode.

We notice from Section 3.2.2 that the reference trajectory has a maximum micro counter $\kappa_\alpha(i) = 1$ and that the perturbed trajectory tends to have an unequal maximum micro counter $1 \leq \kappa_x(i) \leq c(i)$. For the sensitivity analysis performed in Section 4.2, we want to compare the two trajectories in the same modes, even for unspecified modes. We thus want to define a virtual trajectory $\boldsymbol{\alpha}$ in the same unspecified modes as the trajectory $\boldsymbol{x}$. This is achieved by using the associativity property:

Assumption 4.1 (Associativity) *We assume that associativity as in Definition 4.1 is at hand.*

Figure 4.4 illustrates the effects of using Assumption 4.1. Here, we define via the associativity property the point $\boldsymbol{\alpha}^1(t,i)$ in the unspecified mode. The point $\boldsymbol{\alpha}^1(t,i)$ is only defined at τ_i, and we need to use the concept of extended trajectories to define $\bar{\boldsymbol{\alpha}}^1(t,i)$ for a larger time interval in this unspecified mode. This consequently allows us to compare the perturbed trajectory to a matching extended reference segment in the unspecified mode. Note that without associativity, we would have an immediate jump from $\boldsymbol{\alpha}^0$ to $\boldsymbol{\alpha}^2$, thus skipping the point $\boldsymbol{\alpha}^1$ in the unspecified modes. We thus would not be able to make a logical comparison between the (extended) reference trajectory and a perturbed trajectory in the unspecified mode(s).

To make sure that we can always compare the perturbed trajectory to a matching extended reference segment, we define every mode transition as if only one guard conditions is activated. Note that every simultaneous guard activated jump is thus decomposed into an instantaneous arbitrary sequence of single guard activated jumps. This will guarantee that $\kappa_\alpha(i) = \kappa_x(i)$, such that we only need to use one maximum micro counter $\kappa(i)$. Furthermore, $\kappa(i) = c(i)$, and in the rest of the report we will often denote $c(i)$ as the maximum micro counter due to its more intuitive interpretation. Figure 4.3 changes accordingly, where post-event modes can only be of one layer higher. Consequently, mode 000 can not directly transition to mode 111, but will transition to either modes 100, 010 or 001. Note that $c(i)$ and $\kappa(i)$ do not have the same interpretation, see Section 3.2.2, and can only assumed to be equal due to Assumption 4.1.

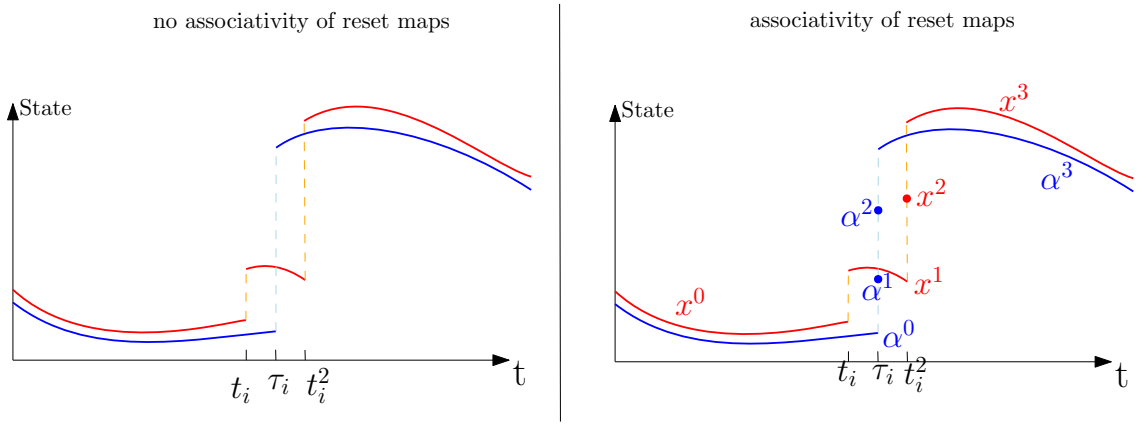

Figure 4.5: A graphical representation of the effect of associativity on the trajectories around the first nominal event of Figure 3.12. The left drawing shows the *real* behavior and the right drawing shows the effects of associativity.

To make sure that the reader understands how associativity is applied in this work, we treat Figure 4.5. The left drawing of this figure depicts an example without associativity, which is based on Figure 3.12 with event descriptions listed in Section 3.2.2. The reference trajectory experiences a mode sequence *000* $\rightarrow$ *111* at $t = \tau_i$, and the perturbed trajectory a possible mode sequence *000* $\rightarrow$ *100* at $t = t_i$ and *100* $\rightarrow$ *111* at $t = t_i^2$. On the right drawing, we apply Assumption 4.1 and define both trajectories in a mode sequence where only one contact gets closed at a time, i.e., the post-event mode $\sigma_{k+1}(i)$ for a current mode $\sigma_k(i)$ has only one extra column becoming a 1. We may then define the perturbed trajectory with a mode sequence *000* $\rightarrow$ *100* at $t = t_i$ and *100* $\rightarrow$ *101* $\rightarrow$ *111* or *100* $\rightarrow$ *110* $\rightarrow$ *111* at $t = t_2$, which are both feasible due to associativity, i.e., the post-impact state does not change experiencing either mode sequence. The reference trajectory is then defined in a similar mode sequence as the perturbed trajectory, resulting in the perturbed trajectory to always have a matching extended reference segment.

4.1.3 Multi-scale hybrid time guard

In the sensitivity analysis in [15], that makes use of the classic hybrid time (t, j), the guard is indicated as ${}^{\sigma_p \leftarrow \sigma_a}\gamma(\boldsymbol{x}, \boldsymbol{u}, t, j) = 0$. In this work, a different version is used where a clear link is made to the base 2 mode numbering convention. We use a notation which clarifies that the number of guards are equal to the number of columns in the mode numbering convention. Note that we did not take such an approach for the jump map notation, as the jump map is typically different when undergoing mode transitions. The guard, however, may be the same for different transitions. Figure 4.6 illustrates this, in which only four unique guards are observed. In it, both transitions 0000 $\rightarrow$ 1000 and 0110 $\rightarrow$ 1110 use the same guard triggering condition $\gamma^{1000} = 0$, which we explain in more detail below.

The system remains in mode $\sigma_k(i)$ as long as the following vector condition is met,

$$\boldsymbol{\Gamma}\left(\boldsymbol{x}(t, i, k), \boldsymbol{u}(t, i, k), t, i, k\right) > 0. \tag{4.10}$$

In (4.10), the inequality is to be understood element wise. For sake of brevity, (4.10) is abbreviated into

$$\boldsymbol{\Gamma}^k\left(\boldsymbol{x}^k, \boldsymbol{u}^k, t, i\right) > 0 \tag{4.11}$$

with $\boldsymbol{\Gamma}^k : \mathbb{R}^{n_{\sigma_k}} \times \mathbb{R} \times \mathbb{N} \times \mathbb{R}^{m_{\sigma_k}} \rightarrow \mathbb{R}^{c(i)-k}$, where we consider Assumption 4.1. Note that we use Assumption 4.1 to make sure that every mode transition only fulfills one guard condition.

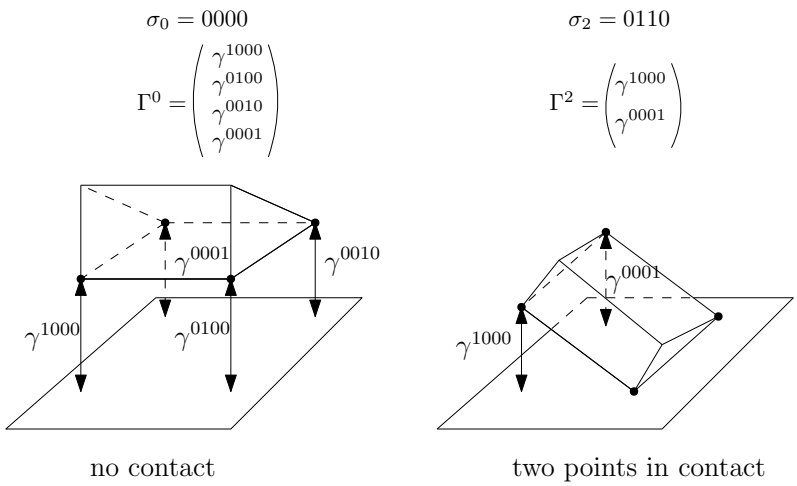

Figure 4.6: A graphical representation of the guard vector and the individual guard functions. On the left drawing, all contacts are open and therefore the total guard has four elements. On the right drawing, two contacts are closed which results in the total guard only having two elements.

Observing Figure 4.6, one notices that $\mathbf{\Gamma}^0$ shares guard functions with $\mathbf{\Gamma}^2$, showing how the number of different guard functions equals $c(i)$. The individual guard functions are denoted as

$$\gamma^{s_k}\left(\boldsymbol{x}(t,i,k), \boldsymbol{u}(t,i,k), t, i, k\right) > 0, \tag{4.12}$$

which we abbreviate as $\gamma^{s_k}\left(\boldsymbol{x}^k, t, i, \boldsymbol{u}^k\right) : \mathbb{R}^{n_{\sigma_k}} \times \mathbb{R} \times \mathbb{N} \times \mathbb{R}^{m_{\sigma_k}} \to \mathbb{R}$. The variable $s_k(i) \in S(i)$ is introduced, where we call $S(i)$ a *constraint indicator* and $s_k(i)$ a *transition specific constraint indicator*. By satisfying the guard condition $\gamma^{s_k} = 0$, one can immediately deduce the mode that follows from the current mode σ_k as s_k indicates which column of σ_k becomes a *1*. As we treat every guard seperately, $S(i)$ thus only consists of the modes of $\Sigma(i)$ that have one column being a *1*, e.g., $s_k(i) \in S(i) = \{1000, 0100, 0010, 0001\}$ for $\Sigma(i) = \{0,1\}^4$. The satisfaction of both $\gamma^{1000} = 0$ and $\gamma^{0100} = 0$, for instance, results in a post-event mode for which the first and second columns of the current mode $\sigma_k(i)$ become a *1*. Similarly, a mode transition from $0000 \to 0010$ implies the satisfaction of $\gamma^{0010} = 0$. The guard is thus formulated in such a manner that satisfying its condition reveals in an intuitive manner the post-event mode. This relation is set as

$$\sigma_{k+1}(i) = \sigma_k(i) + s_k(i), \tag{4.13}$$

where $s_k(i)$ is restricted to have no columns being a *1* that are already so for $\sigma_k(i)$, i.e., an already active guard condition can not be triggered again. Suppose $\sigma_k(i) = 0110$, then we can not have $s_k = 0100$ or $s_k = 0010$. A feasible option may then be $s_k = 1000$, resulting in $\sigma_{k+1}(i) = \sigma_k(i) + s_k(i) = 1110$.

Remark 4.2 *additions and subtractions on base 2 numbers (binary row vectors) are interpreted differently in this work and should not be interpreted as operations on the numbers that they represent, but rather as operations on the individual elements (columns). Here, we perform the additions and subtractions on each column separately and allow the outcome to go negative. Taking* $\sigma_1 = 1001$ *and* $\sigma_2 = 0101$ *results in the subtraction '*$\sigma_1 - \sigma_2 = \sigma_3 = (1, -1, 0, 0)$*'. The first column of* σ_1*, denoted as* $\sigma_{1,1}$*, gives the value* $\sigma_{1,1} = 1$*, and the first column of* σ_2*, denoted as* $\sigma_{2,1}$*, gives the value* $\sigma_{2,1} = 0$*. Subtracting both first column values then results in '*$\sigma_{1,1} - \sigma_{2,1} = 1 - 0 = 1$*', giving the first column of* σ_3 *a 1. Similarly, the second column of* σ_1 *gives* $\sigma_{1,2} = 0$*, and the second column of* σ_2 *gives* $\sigma_{2,2} = 1$*. Subtracting the second column values then results in '*$\sigma_{1,2} - \sigma_{2,2} = 0 - 1 = -1$*', giving the second column of* σ_3 *a -1 value.*

A mathematical representation of the constraint indicator can be given as

$$S(i) = \{w \in \Sigma_i \mid num1(w) = 1\} \subset \Sigma(i), \tag{4.14}$$

where the operator $num1(\cdot)$ counts the number of positive *1*'s in the base 2 mode numbering convention. For example, $num1(0001) = 1$, $num1(1001) = 2$, and $num1(1111) = 4$. Note that this operator does not count negative 1's resulting from subtractions, such that for $num1(\ (1, 1, -1, 1)\ ) = 3$. We provide some further examples to familiarize with (4.13) and (4.14).

Example 4.4 *Considering a mechanical system experiencing impact with three contact points, then the set of modes is defined as* $\Sigma(i) = \{000, 001, 010, 100, 011, 110, 101, 111\}$. *Taking the modes with only one column being 1 as in* (4.14)*, results in the set of constraint indicators* $S(i) = \{001, 010, 100\}$.

Example 4.5 *Considering the mechanical system depicted in Figure 4.6 with* $c(i) = 4$*, then the satisfaction of the guard condition* $\gamma^{0001} = 0$ *results in the post-event modes 0001 and 0111 for, respectively, the left and right drawing. One observes that the same guard can thus be used for different mode transitions.*

From Figure 4.6, one determines that $\mathbf{\Gamma}^k$ reduces in size for increasing k. With this in mind, the definition of s_k follows as

$$s_k(i) \in \{w \in S(i) \mid num1(w - \sigma_k(i)) \neq 0\}, \tag{4.15}$$

where one should recall that the subtraction is only meant in the sense of columns. Equation (4.15) is clarified with the following example.

Example 4.6 *Considering* $k = 2$ *and* $c(i) = 4$ *with the current mode* $\sigma_2 = 1100$ *and constraint indicator* $S(i) \in \{1000, 0100, 0010, 0001\}$*, then one is able to define the transition specific constraint indicator as* $s_2(i) \in \{0010, 0001\}$. *The total guard vector is then defined as*

$$\mathbf{\Gamma}^2 = \begin{pmatrix} \gamma^{0010} \\ \gamma^{0001} \end{pmatrix} \in \mathbb{R}^{c(i)-k} = \mathbb{R}^2. \tag{4.16}$$

The transition specific constraint indicators 1000 and 0100 do not occur as a possibility for s_2*, as this would indicate the triggering of an already active guard condition. Testing* (4.15) *for the transition specific constraint indicator 1000, i.e., testing whether* $w = 1000$ *satisfies the requirement in* (4.15)*, gives the subtraction '*$1000 - \sigma_2 = (0, -1, 0, 0)$*'. Inserting the result in the operator* $num1$ *results in* $num1(\ (0, -1, 0, 0)\ ) = 0$ *and shows that* $s_2 \neq 1000$*. We do the same for the transition specific constraint indicator 0010, giving the subtraction '*$0010 - \sigma_2 = (-1, -1, 1, 0)$*'. The operator then gives* $num1(\ (-1, -1, 1, 0)\ ) = 1$ *which shows that the condition in* (4.15) *is satisfied.*

We end this section with a special case which occurs when $k = \kappa(i)$, giving

$$\mathbf{\Gamma}^{\kappa}(i) = \emptyset, \tag{4.17}$$

as $s_\kappa(i) = \emptyset$. This may mislead the reader in thinking there are no mode transitions possible. To solve this ambiguity, we use the virtual mode $\sigma_0(i+1) := \sigma_\kappa(i)$ giving

$$\mathbf{\Gamma}^{\kappa}(i) = \mathbf{\Gamma}^{0}(i+1), \tag{4.18}$$

for which the elements of $\mathbf{\Gamma}^0(i+1)$ are defined as $\gamma^{s_k}(i+1)$ with $s_k(i+1) \in S(i+1)$. Now that all the important notations are adjusted and clarified, we can make intuitive descriptions of dynamical systems experiencing jumps due to simultaneous guard activation. We thus continue with the sensitivity analysis.

4.2 Sensitivity analysis for simultaneous guard activation

For single-guard triggered events, the sensitivity analysis resulted in a *linear time-triggered hybrid system*, cf. [23]. This time-triggered hybrid system jumped with a jump map, called *jump gain*, which took into account the perturbation effects due to the mismatch of jump times between the perturbed and reference trajectory, see Section 3.1.1. The resulting local model was thus able to predict the behavior of the perturbed trajectory, even though it jumped at a different time instance, i.e., at the a-priori known nominal events times. Stability analysis for time-triggered hybrid systems are well established in the literature, cf. [16], and a similar system is desired for simultaneous guard triggered events.

In this section, we perform a sensitivity analysis with respect to perturbations of the initial contions and control input to understand the behavior of a trajectory with (multiple) simultaneous guard activated events. This sensitivity analysis is performed with the hybrid system notations proposed in Section 4.1 and a *mode sequence* notation introduced in Section 4.2.1. Note that we do not treat input-dependent guard conditions, as can be used for describing detachments, cf. [15, 17]. The local model derived from the sensitivity analysis can then be used to infer stability of a trajectory with simultaneous guard activation and, possibly, to design stabilizing or closed-loop-response-shaping feedback gains, treated further in Section 4.3. Now, we introduce the *mode sequence* notation, which is necessary for a clear description of the sensitivity analysis as can be read next.

4.2.1 The potential mode sequence notation

As discussed in section 3.2.1, a perturbation of the initial condition to a reference trajectory with simultaneous guard activation may let the trajectory come into so-called unspecified modes. This phenomenon was clarified with a falling block example, see Figure 3.8, and one observed that the system may come into different unspecified modes, accordingly experiencing a different mode sequence, depending on the perturbation. To distinguish trajectories with different mode sequences, we incorporate the mode sequence in its notation. An example is

$$^{\sigma_\kappa \leftarrow \sigma_{\kappa-1} \leftarrow \cdots \leftarrow \sigma_0}\boldsymbol{x}(t,i), \tag{4.19}$$

where $\sigma_0(i)$ is a mode summarizing the full history of mode sequences as is explained further below. Note that $\sigma_0(i)$ can also be interpreted as the virtual initial mode to completing a nominal event as described in Section 4.1.2. In the sensitivity analysis, all mode sequences are considered, and thus not solely *feasible* trajectories, i.e., trajectories realizable in practice. Examples of feasible trajectories are given in example 4.7 and corresponding Figure 4.7, in which the trajectory jumps at the first guard condition that is triggered. Keep in mind that we consider Assumption 4.1 to be deployed, thus allowing us to define $\boldsymbol{\alpha}$ in the unspecified mode.

Example 4.7 *For a mechanical system with two contact points, we define the set of relevant modes* $\Sigma(i) = \{00, 01, 10, 11\}$. *Assuming that the reference motion experiences simultaneous inelastic impact, i.e., it goes from mode 00* $\rightarrow$ *11, then a perturbed motion typically experience no simultaneous inelastic impact, i.e., it experiences either mode sequence* $00 \rightarrow 01 \rightarrow 11$ *or* $00 \rightarrow 10 \rightarrow 11$, *while taking into consideration Assumption 2.1. Figure 4.7 illustrates this behaviour, where we consider (perturbed) state trajectories* $\boldsymbol{x}_{c1}$ *(orange trajectory) and* $\boldsymbol{x}_{c2}$ *(red trajectory). One observes that after each mode transition, the left upperscript of* $\boldsymbol{x}$ *gets longer by adding the mode that it currently resides in. One can determine the advantage of this notation by looking at the lowest drawing, i.e., mode 11, where the mode sequence of the considered state trajectories are instantly recognized.*

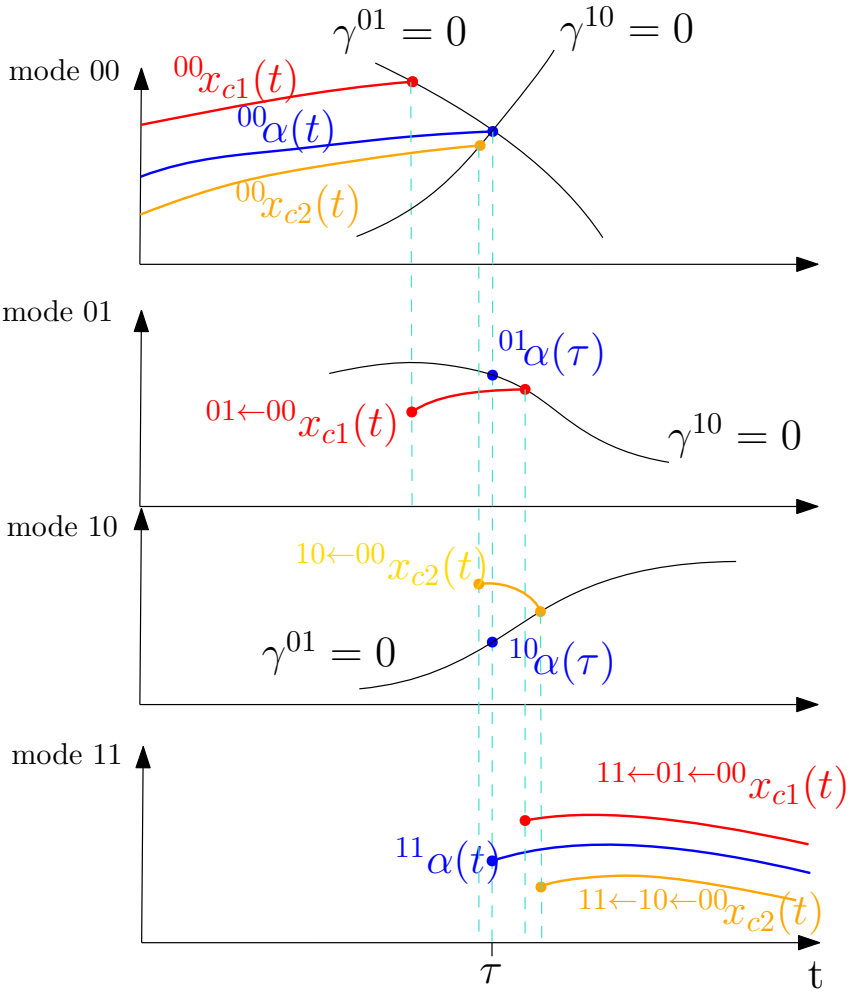

Figure 4.7: A graphical representation of a reference trajectory (blue line) with simultaneous guard activation and feasible perturbed trajectories (orange and red line) that experiences a short sequential activation of single guard conditions. One recognizes feasible trajectories by the instant jumps that occur when the first guard conditions is triggered, e.g., in the upper drawing ${}^{00}\boldsymbol{x}_{c1}$ jumps when triggering $\gamma^{01} = 0$.

Remark 4.3 *We can notice in Figure 4.7 that the mode sequence is not defined for the reference, i.e., we only denote its current mode as, e.g.,* ${}^{11}\boldsymbol{\alpha}$*. Adding the full mode sequence to a notation is only necessary when the mode sequence influences the state after the nominal event is completed. For example, we could consider* ${}^{11\leftarrow 00}\boldsymbol{\alpha}(\tau)$*, jumping via a single jump map at* τ*, and* ${}^{11\leftarrow 01\leftarrow 00}\boldsymbol{\alpha}(\tau)$*, jumping via two jump maps at* τ*, and notice that the result after jump is still the same. This is due to* $\boldsymbol{\alpha}(\tau)$ *satisfying two guard conditions at the same time instance and assuming associativity of reset maps (Assumption 4.1). One can read below that this typically does not hold for the state trajectory, such that the state trajectory does require the full mode sequence in its notation.*

We have thus treated feasible trajectories, but the sensitivity analysis also considers infeasible trajectories. An infeasible trajectory is a trajectory which does not jump when it triggers the first guard condition. The trajectory will, instead, ignore the first triggered guard condition and continue until another guard condition (that is not the first one) is triggered. After that, all remaining guard conditions are treated again (including the previous ignored first guard condition), and the trajectory continues to trigger all its remaining guard conditions in an arbitrary sequence. The infeasible trajectory is thus a trajectory that satisfies all relevant guard conditions in an arbitrary

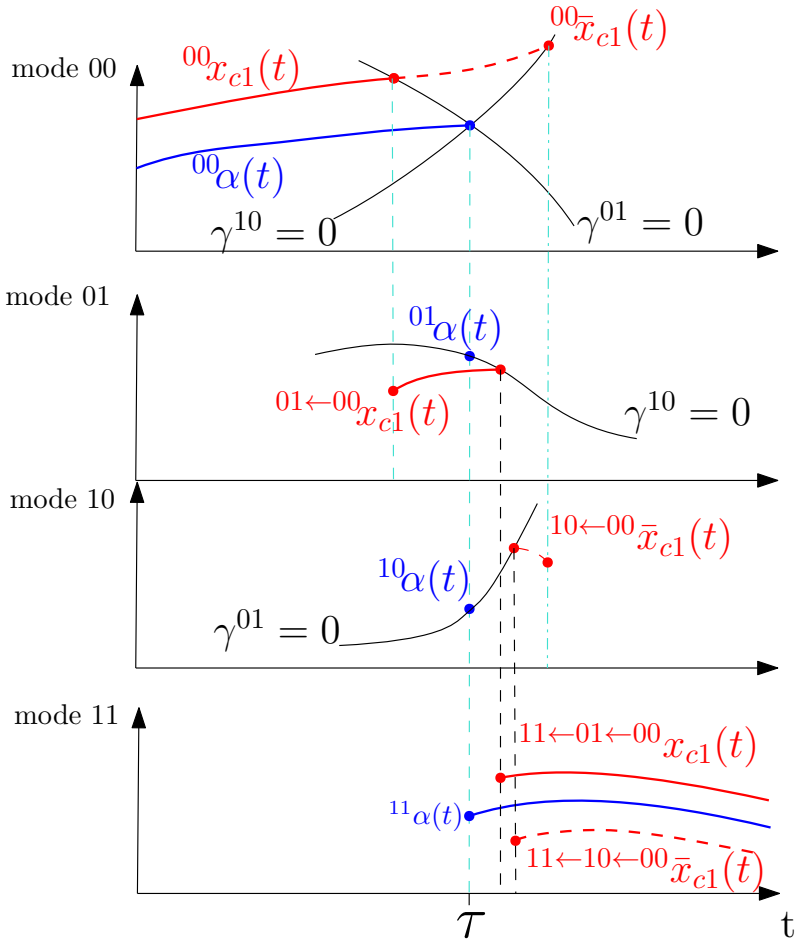

Figure 4.8: A graphical representation of a feasible and an infeasible trajectory. The feasible trajectory $\boldsymbol{x}_{c1}$ is depicted as a red solid line, and the infeasible trajectory $\bar{\boldsymbol{x}}_{c1}$ is depicted as a red dashed line.

sequence that is not the same as the feasible trajectory. This is clarified with Figure 4.8, which uses the trajectories $\boldsymbol{\alpha}$ and $\boldsymbol{x}_{c1}$ of Figure 4.7. In the following explanation, we only treat the extended trajectory ${}^{11\leftarrow 10\leftarrow 00}\bar{\boldsymbol{x}}_{c1}$.

Starting in the upper drawing for mode 00, we consider the trajectory ${}^{00}\bar{\boldsymbol{x}}_{c1}$ that *ignores* the first guard condition $\gamma^{01} = 0$ and continues until it triggers the other guard condition $\gamma^{10} = 0$. A physical interpretation of this is given via the left and middle drawing of Figure 4.9. On the left drawing, a block is seen with a slightly perturbed rotation. In practice, this block would impact at its right corner point as illustrated in Figure 3.8(b). For an infeasible trajectory, however, the unilateral constraint corresponding to the right corner point is ignored, and the right part of the block is allowed to penetrate the flat surface. The first impact then happens when the left corner point makes contact with the flat surface as depicted in the middle drawing of Figure 4.9. The infeasible trajectory in Figure 4.8 then continuous in mode 10, indicated as ${}^{10\leftarrow 00}\bar{\boldsymbol{x}}_{c1}$.

Observe that the starting point of the extended trajectory in mode 10 is past the level set $\gamma^{10}(\cdot, t, i, k) = 0$, indicating that the trajectory will not, at least locally, trigger this guard condition by forward integration of the vectorfield. This can also be observed from the middle drawing in Figure 4.9, where the block will not experience an impact soon by rotating clockwise. Naturally, if we rotate long enough, then the block eventually experiences a second impact at its right corner

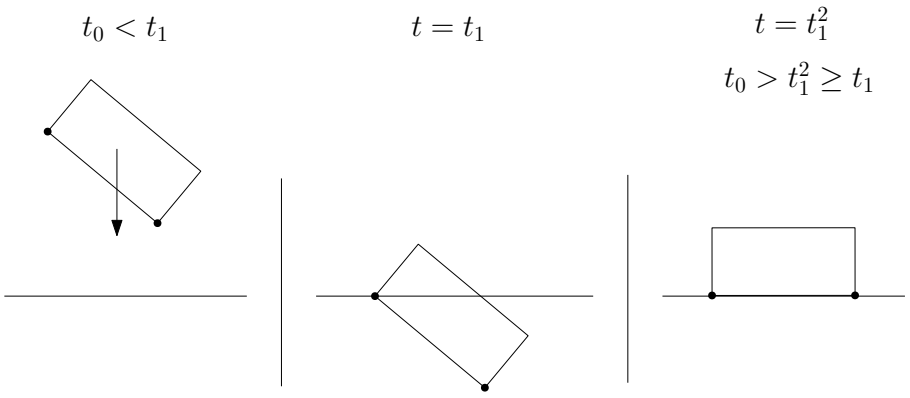

Figure 4.9: A graphical representation of how the system in figure 3.8(b) would develop for an infeasible trajectory.

point, but this happens with the block being underneath the surface (given that the guard is activated when the contact distance reduces to zero). To make sure that we keep a local analysis, and that the same nominal event is completed as for the feasible trajectory, one may need to apply backward integration of the vectorfield. By rotating the block in the middle drawing of Figure 4.9 anti-clockwise, one achieves a much sooner *impact* and a final configuration similar to the feasible trajectory (see right drawing of Figure 3.8(b)). This is thus also done for the trajectory ${}^{10\leftarrow 00}\bar{\boldsymbol{x}}_{c1}$ in Figure 4.8, in which we observe the trajectory to go backwards. The state of the feasible and infeasible trajectory in the final mode 11 may then be different due to their underlying mode sequence. This may be due to the different impacting effects, or the extended input terms, having different effects on infeasible configurations such as in the middle drawing of Figure 4.9.

One thus concludes that it is necessary to denote the mode sequence in the notation of the state trajectory, as the same trajectory with a different sequence of guard activation may give different end results. An example was given in Figure 4.8, in which the trajectories ${}^{11\leftarrow 01\leftarrow 00}\boldsymbol{x}_{c1}$ and ${}^{11\leftarrow 10\leftarrow 00}\bar{\boldsymbol{x}}_{c1}$ may end up differently, even when they started for the same conditions. Next, we perform the sensitivity analysis with the hybrid notations in Section 4.1 and the mode sequence notation in this section.

4.2.2 Positively homogeneous time-triggered hybrid system

In the sensitivity analysis, we inspect the behavior of a nominal trajectory with simultaneous guard activation under influence of a perturbation of the initial conditions and control input. An initial condition is given as

$$ {}^{\sigma_0}\boldsymbol{x}(t_0, 0) = \eta(\epsilon), \tag{4.20}$$

where it is assumed to depend smoothly on a perturbation parameter $\epsilon \in \mathbb{R}$, cf. [42, Section 10.1, p. 382-393]. Similarly, the input term also depends smoothly on ϵ giving

$$ \boldsymbol{u}(t, i, k, \epsilon). \tag{4.21}$$

Defining the state evolutions as

$$ \dot{\boldsymbol{x}}(t, i, k) = {}^{\sigma_k}\boldsymbol{f}(\boldsymbol{x}, \boldsymbol{u}, t, i), \tag{4.22}$$

where ${}^{\sigma_k}\boldsymbol{f} : \mathbb{R}^{n_{\sigma_k}} \times \mathbb{R}^{m_{\sigma_k}} \times \mathbb{R} \times \mathbb{N} \to \mathbb{R}^{n_{\sigma_k}}$, one can formulate a solution of (4.20) - (4.22) that depends continuously on the parameter ϵ, hence we write

$$ \boldsymbol{x}_\epsilon(t, i, k) := \boldsymbol{x}(t, i, k, \epsilon). \tag{4.23}$$

Note that the nominal trajectory and nominal input is then realized by setting $\epsilon = 0$ for (4.20) and (4.21), indicating zero perturbation.

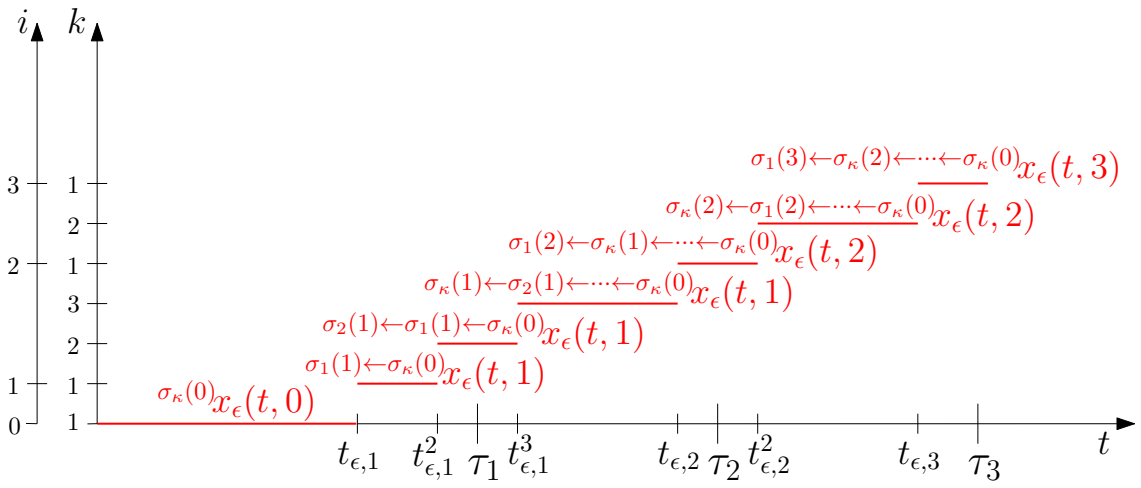

Figure 4.10: A graphical representation, in hybrid time domain (t, i, k), for a perturbed trajectory $\boldsymbol{x}_\epsilon$ experiencing three transitions corresponding to three distinct nominal events.

To present the analysis in a simple manner, we treat only one nominal event i. This consequently changes some notations, and we use Figure 4.10 to clarify this. Here, the event times of the perturbed trajectory $\boldsymbol{x}_\epsilon$ are denoted as $t^k_{\epsilon,i}$. For the sensitivity analysis, we might consider only the impacts around the second nominal event, such that we take an initial perturbed state as

$$^{\sigma_\kappa(1)\leftarrow\sigma_2(1)\leftarrow\cdots\leftarrow\sigma_\kappa(0)}\boldsymbol{x}_\epsilon(t,1). \tag{4.24}$$

The sequence $\sigma_\kappa(1) \leftarrow \sigma_2(1) \leftarrow \cdots \leftarrow \sigma_\kappa(0)$ is replaced by the virtual initial mode $\sigma_0(2)$, see Section 4.1.2, such that we rewrite (4.24) as

$$^{\sigma_0(2)}\boldsymbol{x}_\epsilon(t,2) := {}^{\sigma_\kappa(1)\leftarrow\sigma_2(1)\leftarrow\cdots\leftarrow\sigma_\kappa(0)}\boldsymbol{x}_\epsilon(t,1). \tag{4.25}$$

We can then analyze the second nominal event, where we let the perturbed trajectory go from initial setting $^{\sigma_0}\boldsymbol{x}_\epsilon(t,2)$ to final setting $^{\sigma_\kappa\leftarrow\sigma_{\kappa-1}\leftarrow\cdots\leftarrow\sigma_0}\boldsymbol{x}_\epsilon(t,2)$. In the rest of the chapter, we leave the macro counter i out of the notations to present the analysis clearer. Figure 4.11 then depicts how the notations are simplified for the sensitivity analysis. Note that any arbitrary mode sequence can be inserted here, such that we could also treat an infeasible trajectory as clarified in Section 4.2.1. We will use the notations as on the right drawing of Figure 4.11 throughout the rest of the analysis.

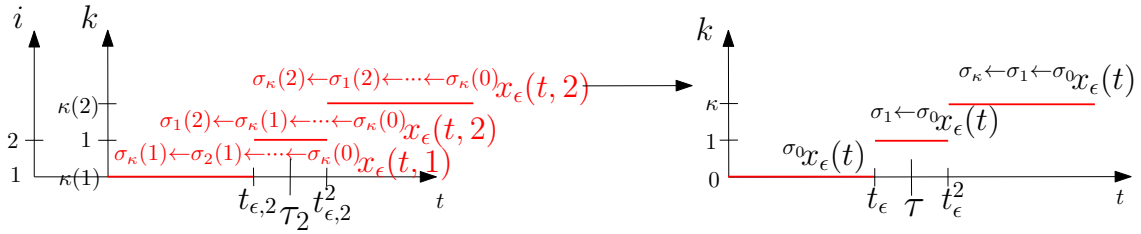

Figure 4.11: A graphical representation, in hybrid time domain, of how the perturbed trajectory $\boldsymbol{x}_\epsilon$ around the second nominal event is described for the sensitivity analysis.

A perturbed trajectory $\boldsymbol{x}_\epsilon(t)$ is expected to be close (in a sense to be made precise) to the nominal trajectory $\boldsymbol{\alpha}(t)$ for small values of ϵ. Inspired by classical perturbation analysis, a linear approximation based on a Taylor series of $\boldsymbol{x}_\epsilon(t)$ with respect to ϵ is formulated as

$$\begin{aligned}\boldsymbol{x}_\epsilon(t) = \boldsymbol{x}(t,\epsilon) &= \boldsymbol{x}(t,0) + \epsilon \frac{\partial \boldsymbol{x}(t,\epsilon)}{\partial \epsilon}|_{\epsilon=0} + o(\epsilon) \\ &= \boldsymbol{\alpha}(t) + \epsilon \boldsymbol{z}(t) + o(\epsilon),\end{aligned} \tag{4.26}$$

for which we define $\boldsymbol{z}$ as a *positively homogeneous state* (for reasons apparent later). Here, $\boldsymbol{z}$ jumps at the same time instances as the reference, as observed by the corresponding expression $\frac{\partial \boldsymbol{x}(t,\epsilon)}{\partial \epsilon}$ being evaluated at $\epsilon = 0$, i.e., evaluated at zero perturbation. As we consider state-triggered hybrid systems, we need to reformulate (4.26) in extended trajectories as the event times of the reference and perturbed trajectory generally do not coincide. Taking a hybrid system with c guard conditions, e.g., a mechanical system with c unilateral constraints, and using Assumption 4.1, allows us to set $\kappa = c$ and formulate the reference trajectory as

$$\boldsymbol{\alpha}(t) = \begin{cases} {}^{\sigma_0}\boldsymbol{\alpha}(t), & t \in [t_0, \tau], \\ {}^{\sigma_1}\boldsymbol{\alpha}(t), & t = \tau, \\ {}^{\sigma_2}\boldsymbol{\alpha}(t), & t = \tau, \\ \quad\vdots & \\ {}^{\sigma_c}\boldsymbol{\alpha}(t), & t \in [\tau, t_f], \end{cases} \tag{4.27}$$

and the perturbed trajectory as

$$\boldsymbol{x}_\epsilon(t) = \begin{cases} {}^{\sigma_0}\boldsymbol{x}_\epsilon(t), & t \in [t_0, t_\epsilon], \\ {}^{\sigma_1 \leftarrow \sigma_0}\boldsymbol{x}_\epsilon(t), & t \in [t_\epsilon, t_\epsilon^2], \\ {}^{\sigma_2 \leftarrow \sigma_1 \leftarrow \sigma_0}\boldsymbol{x}_\epsilon(t), & t \in [t_\epsilon^2, t_\epsilon^3], \\ \quad\vdots & \\ {}^{\sigma_c \leftarrow \sigma_{c-1} \leftarrow \cdots \leftarrow \sigma_0}\boldsymbol{x}_\epsilon(t), & t \in [t_\epsilon^c, t_f], \end{cases} \tag{4.28}$$

where $t_\epsilon^k = t_\epsilon^{k+1}$ implies the satisfaction of two guard conditions simultaneously. Similarly, if more event times t_ϵ^k are equal to each other, more guard conditions are satisfied simultaneously. We describe the positively homogeneous trajectory as

$$\boldsymbol{z}(t) = \begin{cases} {}^{\sigma_0}\boldsymbol{z}(t), & t \in [t_0, \tau], \\ {}^{\sigma_1 \leftarrow \sigma_0}\boldsymbol{z}(t), & t = \tau, \\ {}^{\sigma_2 \leftarrow \sigma_1 \leftarrow \sigma_0}\boldsymbol{z}(t), & t = \tau, \\ \quad\vdots & \\ {}^{\sigma_c \leftarrow \sigma_{c-1} \leftarrow \cdots \leftarrow \sigma_0}\boldsymbol{z}(t), & t \in [\tau, t_f], \end{cases} \tag{4.29}$$

which has a similar jump scheme as the reference trajectory, i.e., it jumps at nominal event time τ. Note that the positively homogeneous state is dependent on the perturbed state, see (4.26), and consequently, the mode sequence needs to be denoted, i.e., a different mode sequence of the perturbed state should imply a different positively homogeneous state after jump. We will see further below that the positively homogeneous system realizes this by jumping differently for different mode sequences.

To make (4.26) more accurate for the considered state-triggered hybrid system, extended segments of (4.27) and (4.29) are used, giving

$$\boldsymbol{x}_\epsilon(t) = \begin{cases} {}^{\sigma_0}\bar{\boldsymbol{\alpha}} + & {}^{\sigma_0}\bar{\boldsymbol{z}}\epsilon + o(\epsilon), & t \in [t_0, t_\epsilon], \\ {}^{\sigma_1}\bar{\boldsymbol{\alpha}} + & {}^{\sigma_1 \leftarrow \sigma_0}\bar{\boldsymbol{z}}\epsilon + o(\epsilon), & t \in [t_\epsilon, t_\epsilon^2], \\ & \vdots & \\ {}^{\sigma_c}\bar{\boldsymbol{\alpha}} + & {}^{\sigma_c \leftarrow \sigma_{c-1} \leftarrow \cdots \leftarrow \sigma_0}\bar{\boldsymbol{z}}\epsilon + o(\epsilon), & t \in [t_\epsilon^c, t_f]. \end{cases} \tag{4.30}$$

From (4.30), we formulate the *positively homogeneous time-triggered hybrid system*, also called *positive homogenization*, as

$$\begin{aligned} {}^{\sigma_0}\bar{\boldsymbol{z}}(t) &= \boldsymbol{z}_0, & t &= t_0, \\ {}^{\sigma_0}\dot{\bar{\boldsymbol{z}}}(t) &= {}^{\sigma_0}\boldsymbol{A}(t)\,{}^{\sigma_0}\bar{\boldsymbol{z}}(t) + {}^{\sigma_0}\boldsymbol{B}(t)\,{}^{\sigma_0}\boldsymbol{v}(t), & t &\in [t_0, t_f], \\ {}^{\sigma_s}\bar{\boldsymbol{z}}(t) &= \boldsymbol{G}(t, {}^{\sigma_0}\bar{\boldsymbol{z}}(t))\,{}^{\sigma_0}\bar{\boldsymbol{z}}(t), & t &= \tau, \\ {}^{\sigma_s}\dot{\bar{\boldsymbol{z}}}(t) &= {}^{\sigma_s}\boldsymbol{A}(t)\,{}^{\sigma_s}\bar{\boldsymbol{z}}(t) + {}^{\sigma_s}\boldsymbol{B}(t)\,{}^{\sigma_c}\boldsymbol{v}(t), & t &\in [t_0, t_f], \end{aligned} \tag{4.31}$$

with $\sigma_s = \sigma_c \leftarrow \sigma_{c-1} \leftarrow \cdots \leftarrow \sigma_0$ denoting the full mode sequence, $\boldsymbol{z}_0 = {}^{\sigma_0}\boldsymbol{z}(t_0)$ the initial condition, t_0 the initial time, t_f the final time, and ${}^{\sigma_k}\boldsymbol{v} \in \mathbb{R}^{m_{\sigma_k}}$ a perturbed input consisting, possibly, of segments for the modes σ_0 and σ_c, respectively, the initial and final mode. The matrices $\boldsymbol{A}$ and $\boldsymbol{B}$ are formulated as

$$\begin{aligned} {}^{p}\boldsymbol{A}(t) &= D_1\,{}^{p}\boldsymbol{f}({}^{p}\bar{\boldsymbol{\alpha}}(t), {}^{p}\bar{\boldsymbol{\mu}}(t), t), \\ {}^{p}\boldsymbol{B}(t) &= D_2\,{}^{p}\boldsymbol{f}({}^{p}\bar{\boldsymbol{\alpha}}(t), {}^{p}\bar{\boldsymbol{\mu}}(t), t), \end{aligned} \tag{4.32}$$

with $p \in \{\sigma_0, \sigma_c\}$, ${}^{\sigma_k}\boldsymbol{A} \in \mathbb{R}^{n_{\sigma_k} \times n_{\sigma_k}}$ and ${}^{\sigma_k}\boldsymbol{B} \in \mathbb{R}^{n_{\sigma_k} \times m_{\sigma_k}}$. We use the notation $D_b\boldsymbol{f}(\boldsymbol{\alpha}, \boldsymbol{\mu}, t)$ to denote the partial derivative of the function $\boldsymbol{f}$ with respect to its b'th argument evaluated at the values $\boldsymbol{\alpha}$, $\boldsymbol{\mu}$, and t, see [41, Section 2.3, p.75-83]. The proof of (4.31) and (4.32) are given in Appendix B.1. Note that in this work, we only consider the *simultaneous going-to-contact situation*, leaving the *simultaneous contact-release case* for further investigation, cf. [15, 17].

The jump effects of (4.31) are described with a so-called *conewise constant jump gain* $\boldsymbol{G}(t, {}^{\sigma_0}\bar{\boldsymbol{z}}(t))$. This conewise constant jump gain is realized by combining the jump and in-between flow effects of the perturbed dynamical system. Via this jump map, the positive homogenization is able to describe the local system behavior, even when the positive homogenization shows different jumping behavior than the perturbed dynamical system, i.e., it jumps effectively only once and at fixed time instances. As the perturbed dynamical system may show vastly different behavior for different perturbation, the conewise constant jump gain changes its constant jump gain according to the mode sequence that is taken by the perturbed dynamical system. The positive homogenization *knows* about this mode sequence via its own state information, hence the dependency of the conewise constant jump gain on ${}^{\sigma_0}\bar{\boldsymbol{z}}(t)$. Next, we elaborate on how the positive homogenization chooses the correct constant jump gain.

Remark 4.4 *Notice how taking into consideration rocking (superfluous contacts), see Chapter 2, complicates the behavior of the perturbed dynamical system, and subsequently the conewise constant jump gain. Therefore, it is chosen not to consider rocking behavior as via Assumption 3.2.*

4.2.3 Positively homogeneous jump mapping

The conewise constant jump gain $\boldsymbol{G}(\tau, {}^{\sigma_0}\bar{\boldsymbol{z}}(\tau))$ maps a pre-nominal event state ${}^{\sigma_0}\bar{\boldsymbol{z}}(\tau)$ to a post-nominal event state ${}^{\sigma_s}\bar{\boldsymbol{z}}(\tau)$, where σ_0 denotes the initial mode and σ_s the full mode sequence. As mentioned above, the conewise constant jump gain depends on the behavior of the perturbed dynamical system. From Figure 4.7, one observes that the system behavior varies for different mode sequences, leading to the conewise constant jump gain $\boldsymbol{G}(\tau, {}^{\sigma_0}\bar{\boldsymbol{z}}(\tau))$ to change its constant jump gain $\boldsymbol{G}(\tau)$ accordingly. The number of constant jump gains then equals the number of

possible mode sequences. For the example considered in Figure 4.8, the conewise constant jump gain is formulated as

$$\boldsymbol{G}(\tau, {}^{\sigma_0}\bar{\boldsymbol{z}}(\tau)) = \begin{cases} {}^{11\leftarrow 01\leftarrow 00}\boldsymbol{G}(\tau) & \textit{condition } 1, \\ {}^{11\leftarrow 10\leftarrow 00}\boldsymbol{G}(\tau) & \textit{condition } 2, \end{cases} \tag{4.33}$$

where $\boldsymbol{G}(\tau)$ represents the constant jump gain, and the two conditions are ${}^{00}\bar{\boldsymbol{z}}(\tau)$ dependent. These conditions are referred to as *jump shaping conditions*, shaping the conewise constant jump gain $\boldsymbol{G}(\tau, {}^{\sigma_0}\bar{\boldsymbol{z}}(\tau))$ to the correct constant jump gain $\boldsymbol{G}(\tau)$, and we now explain how to derive them.

Recall that the sensitivity analysis takes both feasible and infeasible trajectories into account, see Section 4.2.1. In practice, however, only the feasible trajectory is possible. Figure 4.7 illustrated such a feasible trajectory, experiencing a jump as soon as it satisfied a guard condition. To determine the feasible mode sequence, one thus has to figure out which guard condition is triggered first. In the following, we simply write *mode sequence* to which the user should interpret that we mean the *feasible mode sequence*.

For a given perturbed trajectory with a current mode σ_k, we deduce the next mode by

$$\sigma_{k+1} = \underset{\sigma_{k+1}}{argmin}\ {}^{\sigma_{k+1}\leftarrow\sigma_k^*\leftarrow\cdots\leftarrow\sigma_0^*} t_\epsilon^{k+1}, \tag{4.34}$$

where ${}^{\sigma_0}t_\epsilon^0$ represents t_0 as an initial time, and an upperscript *, e.g., σ_1^*, a mode that was already given (or determined via previous iterations of (4.34)). Here, we consider $\sigma_{k+1} > \sigma_k$ with a mode being *greater* when it has one guard more active, as via Assumption 4.1, and satisfies Assumption 3.2. Note that in case we have simultaneous guard activation, multiple σ_{k+1} would be possible. The upperscript * prevents (4.34) to take into account mode transitions that were concluded to be infeasible from previous iterations. To then deduce the full mode sequence, one has to iterate (4.34) from initial to final mode, respectively, σ_0 and σ_c, where we use Assumption 4.1 to state that every transition satisfies only one guard and thus that the maximum micro counter $\kappa = c$.

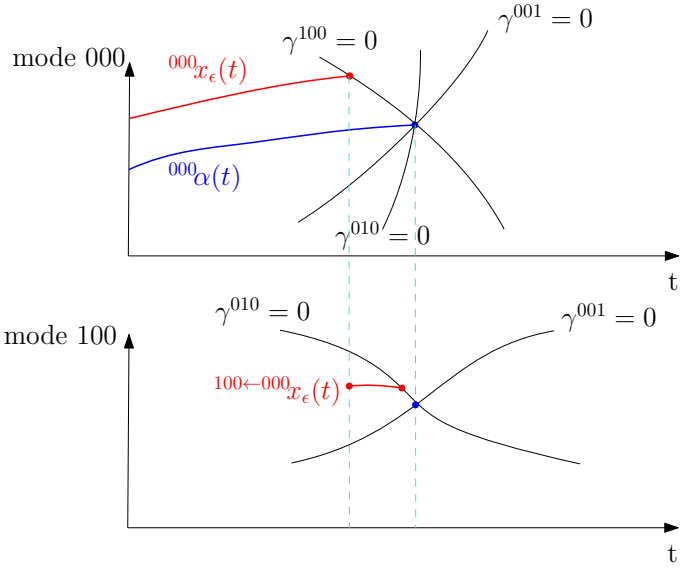

Figure 4.12: A graphical representation of a feasible trajectory $\boldsymbol{x}_\epsilon$ (red solid line) for a system with three guards. Satisfying one guard, as the system does in mode 100, immediately excludes the satisfied guard for the next transition.

To clarify the usage of (4.34), we consider Figure 4.12 with initial $k = 0$. In mode 000, we observe three guard conditions which the (extended) perturbed trajectory ${}^{000}\boldsymbol{x}_\epsilon$ could hit at different event times. The earliest event time takes place when the guard condition $\gamma^{100} = 0$ is triggered, and the trajectory transitions to mode 100. This then concludes the first iteration of (4.34), and we take $k = 1$ for the second iteration. In this iteration, we only consider the trajectories with an initial mode transition $000 \to 100$ and neglect, e.g., mode transition $000 \to 010$, as $\sigma_0^* = 000$ and $\sigma_1^* = 100$. The next transition is then determined with

$$\sigma_2 = \underset{\sigma_2 \in \{100,101\}}{argmin} \; {}^{\sigma_2 \leftarrow 100 \leftarrow 000}t_\epsilon^2. \tag{4.35}$$

From the lower drawing of Figure 4.12, one observes that the earliest event time takes place when the guard condition $\gamma^{010} = 0$ is hit. The second mode transition is then determined as $100 \to 110$, giving the full mode sequence $000 \to 100 \to 110 \to 111$.

Equation (4.34) may thus help us in designing the jump shaping conditions of (4.33). Recall, however, from Section 3.2.3, that the state can not be assumed to be measurable between the time-interval t_ϵ and t_ϵ^c, i.e., the first and final event times corresponding to the completion of a nominal event. Consequently, the event times during this time-interval can not be assumed to be known. Furthermore, we would like the positive homogenization to determine the mode sequence by itself, i.e., the positive homogenization does not require knowledge of a perturbed motion a-priori and thus the exact event times. A solution is to rewrite the event times in a Taylor series with respect to the parameter ϵ, similar as (4.26), giving

$$t_\epsilon^{k+1} = \tau + \epsilon\Delta_{k+1} + o(\epsilon), \tag{4.36}$$

where we denote $\epsilon \frac{\partial t_\epsilon^{k+1}}{\partial \epsilon}|_{\epsilon=0} = \epsilon\Delta_{k+1}$ as a local approximation of the time difference between the perturbed and nominal event time.

Remark 4.5 *Considering Assumption 3.1 to hold, then we could derive the perturbed event times implicitly via the guard condition*

$$\gamma^{s_k}(\boldsymbol{x}_\epsilon^k(t_\epsilon^k), t_\epsilon^k) = 0. \tag{4.37}$$

By taking the partial derivative of (4.37) *with respect to* ϵ*, one subsequently deduces* (4.36)*.*

We can reformulate Δ_{k+1} as

$$\Delta_{k+1} = \underset{s_k}{argmin} \; \frac{-D_1\gamma^{s_k}\left({}^{\sigma_k}\bar{\boldsymbol{\alpha}}(\tau), \tau\right) \cdot {}^{\sigma_k^* \leftarrow \sigma_{k-1}^* \leftarrow \cdots \leftarrow \sigma_0^*}\bar{\boldsymbol{z}}(\tau)}{D_1\gamma^{s_k}({}^{\sigma_k}\bar{\boldsymbol{\alpha}}(\tau), \tau) \cdot {}^{\sigma_k}\boldsymbol{f}({}^{\sigma_k}\bar{\boldsymbol{\alpha}}(\tau), {}^{\sigma_k}\bar{\boldsymbol{\mu}}(\tau), \tau) + D_2\gamma^{s_k}({}^{\sigma_k}\bar{\boldsymbol{\alpha}}(\tau), \tau) \cdot 1}, \tag{4.38}$$

where the derivation is found in Appendix B.2 for (B.21). Note that the subsequent mode is then derived as $\sigma_{k+1} = \sigma_k + s_k$, see Section 4.1.3, and that Assumption 3.1 prevents (4.38) to be not well defined. For sake of brevity, we reformulate (4.38) using a column of constants $\boldsymbol{a} \in \mathbb{R}^{n_{\sigma_k^*}}$ and a state $\bar{\boldsymbol{z}}(\tau) \in \mathbb{R}^{n_{\sigma_k^*}}$ as

$$\Delta_{k+1} = \underset{\sigma_{k+1}}{argmin} \left(({}^{\sigma_{k+1} \leftarrow \sigma_k^*}\boldsymbol{a})^T \; {}^{\sigma_k^* \leftarrow \sigma_{k-1}^* \leftarrow \cdots \leftarrow \sigma_0^*}\bar{\boldsymbol{z}}(\tau) \right), \tag{4.39}$$

where $\boldsymbol{a}$ is written with a mode sequence notation, similar to $\bar{\boldsymbol{z}}$, as to keep the notation consistent. By substituting (4.36) and (4.39) into (4.34), a more desirable format of (4.34) is obtained as

$$\sigma_{k+1} = \underset{\sigma_{k+1}}{argmin} \left(\tau + \epsilon \; ({}^{\sigma_{k+1} \leftarrow \sigma_k^*}\boldsymbol{a})^T \; {}^{\sigma_k^* \leftarrow \sigma_{k-1}^* \leftarrow \cdots \leftarrow \sigma_0^*}\bar{\boldsymbol{z}}(\tau) + o(\epsilon) \right). \tag{4.40}$$

Taking into account that τ has no influence on the mode deduction process of (4.40) and that the higher-order terms can be dismissed as we assume sufficiently small ϵ, we simplify (4.40) as

$$\sigma_{k+1} = \underset{\sigma_{k+1}}{argmin} \left(\epsilon \; ({}^{\sigma_{k+1} \leftarrow \sigma_k^*}\boldsymbol{a})^T \; {}^{\sigma_k^* \leftarrow \sigma_{k-1}^* \leftarrow \cdots \leftarrow \sigma_0^*}\bar{\boldsymbol{z}}(\tau) \right). \tag{4.41}$$

Equation (4.41) is then used to determine the jump shaping conditions of (4.33). To clarify its application, a relatively simple example is treated. Given $\sigma_0^* = 00$ for $k = 0$, then we determine in the first iteration of (4.41) whether the system transitions to mode 01 or mode 10. Inserting either mode 10 or 01 in (4.41), only results in a change of the column $\boldsymbol{a}$. Taking into account that the right-side term of (4.41) represents an approximation of the time difference between the perturbed and nominal event time, i.e., $\epsilon\Delta_k \approx t_\epsilon^k - \tau$, one concludes the subsequent mode to be the mode σ_{k+1} which results in the most negative time difference (and subsequently the smallest event time). For example, if

$$\epsilon\ ({}^{01\leftarrow 00}\boldsymbol{a})^T\ {}^{00}\bar{\boldsymbol{z}}(\tau) \leq \epsilon\ ({}^{10\leftarrow 00}\boldsymbol{a})^T\ {}^{00}\bar{\boldsymbol{z}}(\tau) \leftrightarrow \epsilon\ ({}^{01\leftarrow 00}\boldsymbol{a} - {}^{10\leftarrow 00}\boldsymbol{a})^T\ {}^{00}\bar{\boldsymbol{z}}(\tau) \leq 0 \tag{4.42}$$

holds, then a smaller event time is concluded for the subsequent mode $\sigma_{k+1} = 01$. Equation (4.42) thus can be chosen as a jump shaping condition, completing the conewise constant jump gain (4.33) as

$$\boldsymbol{G}(\tau, {}^{00}\bar{\boldsymbol{z}}(\tau)) = \begin{cases} {}^{11\leftarrow 01\leftarrow 00}\boldsymbol{G}(\tau) & \epsilon\ ({}^{01\leftarrow 00}\boldsymbol{a} - {}^{10\leftarrow 00}\boldsymbol{a})^T\ {}^{00}\bar{\boldsymbol{z}}(\tau) \leq 0, \\ {}^{11\leftarrow 10\leftarrow 00}\boldsymbol{G}(\tau) & \epsilon\ ({}^{01\leftarrow 00}\boldsymbol{a} - {}^{10\leftarrow 00}\boldsymbol{a})^T\ {}^{00}\bar{\boldsymbol{z}}(\tau) \geq 0. \end{cases} \tag{4.43}$$

Notice that if a ${}^{00}\bar{\boldsymbol{z}}(\tau)$ is found that fulfills one of the two jump shaping conditions in (4.43), that only scaling ${}^{00}\bar{\boldsymbol{z}}(\tau)$ with a non-negative parameter $\epsilon \geq 0$ results in the same jump shaping condition to be satisfied, and consequently the conewise constant jump gain $\boldsymbol{G}(\tau, {}^{00}\bar{\boldsymbol{z}}(\tau))$ becomes a similar constant jump gain $\boldsymbol{G}(\tau)$ as for the unscaled case. Therefore, the jump gain is regarded as a *positively homogeneous jump map*. The term *positively homogeneous* is deduced from the following definition in [44, Section 12.5, p. 693-703].

Definition 4.2 (positively homogeneous function) *A function $f(x_1, \cdots, x_n)$ is said to be positively homogeneous of degree p if, for every point $x_1, x_2, \cdots, x_n$ in its domain and every real number $t > 0$, we have*

$$f(tx_1, tx_2, \cdots, tx_n) = t^p f(x_1, \cdots, x_2). \tag{4.44}$$

Observe furthermore that (4.43) can also be interpreted as a *piecewise linear mapping*, differentiating the constant jump gains by the jump shaping condition(s). Figure 4.13 illustrates an example of this piecewise linear mapping for a conewise constant jump gain consisting of three constant jump gains $\boldsymbol{G}_1$, $\boldsymbol{G}_2$, and $\boldsymbol{G}_3$, formulated as

$$\boldsymbol{G}(\tau, {}^{\sigma_0}\bar{\boldsymbol{z}}(\tau)) = \begin{cases} \boldsymbol{G}_1(\tau) & \textit{condition } 1, \\ \boldsymbol{G}_2(\tau) & \textit{condition } 2, \\ \boldsymbol{G}_3(\tau) & \textit{condition } 3. \end{cases} \tag{4.45}$$

A 2-dimensional Euclidean space is considered which depicts the pre-event state ${}^{\sigma_0}\bar{\boldsymbol{z}}(\tau)$. This space is divided into three areas by the jump shaping conditions, resulting in a clear picture of when to apply one of the three constant jump gains when the pre-event state is known. One observes that the areas are divided into conelike shapes, and hence we use the term *conewise constant jump gain*. One can, for instance, see that the middle blue point $\epsilon^{\sigma_0}\bar{\boldsymbol{z}}(\tau) = 0$ lays on the intersection of these areas. This point is characterized as the unperturbed situation, and subsequently any of the three constant jump gains can be applied on it. Other examples are given by the red point $\epsilon^{\sigma_0}\bar{\boldsymbol{z}}_a(\tau)$ and purple point $\epsilon^{\sigma_0}\bar{\boldsymbol{z}}_b(\tau)$, resulting in, respectively, the application of constant jump gain $\boldsymbol{G}_3$ and constant jump gain $\boldsymbol{G}_2$. Notice that ϵ is a scalar and that the same constant jump gain can be applied as long as ϵ is non-negative.

Remark 4.6 *If all the possible constant jump gains $\boldsymbol{G}(\tau)$ of the conewise constant jump gain $\boldsymbol{G}(\tau, {}^{\sigma_0}\boldsymbol{z}(\tau))$ are equivalent to each other, the piecewise linear mapping becomes a linear mapping, and subsequently we have a linear time-triggered hybrid system.*

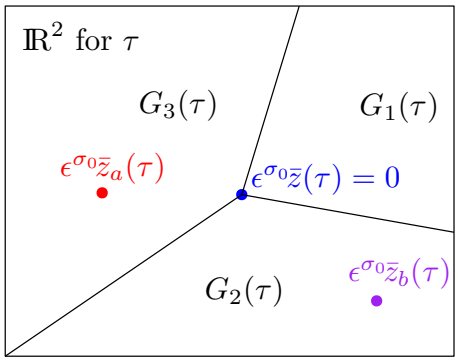

Figure 4.13: Graphical illustration of a positively homogeneous jump map that is also piecewise linear. An example is given of a conewise constant jump gain with three constant jump gains, differentiated as $\boldsymbol{G}_1$, $\boldsymbol{G}_2$, and $\boldsymbol{G}_3$. Depending on the pre-event state $\epsilon^{00}\bar{\boldsymbol{z}}(\tau)$, one of those constant jump gains is applied to the local model.

The local model thus jumps via a piecewise linear mapping that is furthermore positively homogeneous. Due to this particular mapping, the local model can not be assumed to be linear, but is rather positively homogeneous. Subsequently, the local model is termed as a positively homogeneous time-triggered hybrid system. This is proven in Appendix B.3. The advantage of our local model, is that we can get a single piecewise-linear jump map that is able to predict the total effect of a perturbation, that is sufficiently small, about simultaneous guard activation.

In the rest of the report, we assume that $\epsilon \geq 0$ such that we do not include this scaling parameter in the jump shaping conditions. To conclude the positive homogenization, a derivation of the conewise constant jump gain is given for a particular mode sequence.

4.2.4 Conewise constant jump gain for a particular mode sequence

In Figure 4.14, an example of the positively homogeneous trajectory is given. The black lines represent the extended trajectory $\bar{\boldsymbol{z}}$ as derived from the perturbed trajectory $\boldsymbol{x}_\epsilon$, i.e., via (4.30). We, however, would rather have a positively homogeneous trajectory behaving as (4.29), jumping only once at fixed time instances. To do so, the jump and in-between flow effects of the black trajectories are combined into one big jump for the red trajectory at time instance τ via a constant jump gain ${}^{\sigma_3\leftarrow\sigma_2\leftarrow\sigma_1\leftarrow\sigma_0}\boldsymbol{G}(\tau)$.

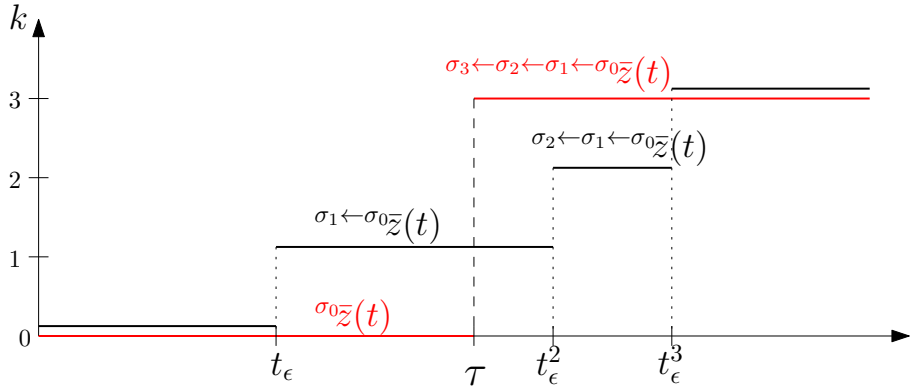

Figure 4.14: A representation of how the constant jump gain is derived for an a-priori known mode sequence.

The constant jump gain ${}^{\sigma_3\leftarrow\sigma_2\leftarrow\sigma_1\leftarrow\sigma_0}\boldsymbol{G}(\tau)$ can be built up from *individual constant jump gains* ${}^{\sigma_k\leftarrow\sigma_{k-1}}\boldsymbol{G}(\tau) \in \mathbb{R}^{n_{\sigma_k}\times n_{\sigma_{k-1}}}$, formulated and proven in [23] and Appendix B.2, with

$$\begin{aligned} \bar{\boldsymbol{z}}^+ &= \boldsymbol{G}(t)\bar{\boldsymbol{z}}^- \qquad \text{for } t=\tau \\ \boldsymbol{G}(\tau) &= \frac{\boldsymbol{f}^+ - \dot{\boldsymbol{g}}}{\dot{\gamma}} D_1\gamma + D_1\boldsymbol{g}, \end{aligned} \tag{4.46}$$

where

$$\begin{aligned} \boldsymbol{G}(\tau) &= {}^{\sigma_k\leftarrow\sigma_{k-1}}\boldsymbol{G}(\tau) \\ \bar{\boldsymbol{z}}^+ &= {}^{\sigma_k\leftarrow\sigma_{k-1}\leftarrow\cdots\leftarrow\sigma_0}\bar{\boldsymbol{z}}(t) \\ \bar{\boldsymbol{z}}^- &\begin{cases} {}^{\sigma_{k-1}\leftarrow\sigma_{k-2}\leftarrow\cdots\leftarrow\sigma_0}\bar{\boldsymbol{z}}(t) & \text{for } k>1 \\ {}^{\sigma_0}\bar{\boldsymbol{z}}(t) & \text{for } k=1 \end{cases} \\ \boldsymbol{f}^+ &= {}^{\sigma_k}\boldsymbol{f}({}^{\sigma_k}\boldsymbol{\alpha}(\tau), {}^{\sigma_k}\boldsymbol{\mu}(\tau), \tau) \\ \boldsymbol{f}^- &\begin{cases} {}^{\sigma_{k-1}}\boldsymbol{f}({}^{\sigma_{k-1}}\boldsymbol{\alpha}(\tau), {}^{\sigma_{k-1}}\boldsymbol{\mu}(\tau), \tau) & \text{for } k>1 \\ {}^{\sigma_0}\boldsymbol{f}({}^{\sigma_0}\boldsymbol{\alpha}(\tau), {}^{\sigma_0}\boldsymbol{\mu}(\tau), \tau) & \text{for } k=1 \end{cases} \\ \dot{\boldsymbol{g}} &= D_1\boldsymbol{g}\cdot\boldsymbol{f}^- + D_2\boldsymbol{g}\cdot 1 \\ \dot{\gamma} &= D_1\gamma\cdot\boldsymbol{f}^- + D_2\gamma\cdot 1 \\ D_p\boldsymbol{g} &= D_p\,{}^{\sigma_k\leftarrow\sigma_{k-1}}\boldsymbol{g}({}^{\sigma_{k-1}}\boldsymbol{\alpha}(\tau), \tau) \qquad p\in\{1,2\} \\ D_c\gamma &= D_c\gamma^{\varsigma_{k-1}}({}^{\sigma_{k-1}}\boldsymbol{\alpha}(\tau), \tau) \qquad c\in\{1,2\}. \end{aligned} \tag{4.47}$$

Note that to make sure that the individual constant jump gain (4.46) is well defined, Assumption 3.1 is considered to hold.

Assuming that the mode sequence is known, the constant jump gain is defined by multiplying the individual constant jump gains in a fixed sequence as

$$\begin{aligned} {}^{\sigma_k\leftarrow\sigma_{k-1}\leftarrow\cdots\leftarrow\sigma_0}\boldsymbol{z}(\tau) &= {}^{\sigma_k\leftarrow\sigma_{k-1}}\boldsymbol{G}(\tau)^{\sigma_{k-1}\leftarrow\sigma_{k-2}\leftarrow\cdots\leftarrow\sigma_0}\boldsymbol{z}(\tau) \\ &= {}^{\sigma_k\leftarrow\sigma_{k-1}}\boldsymbol{G}(\tau)^{\sigma_{k-1}\leftarrow\sigma_{k-2}}\boldsymbol{G}(\tau)^{\sigma_{k-2}\leftarrow\sigma_{k-3}\leftarrow\cdots\leftarrow\sigma_0}\boldsymbol{z}(\tau) \\ &= {}^{\sigma_k\leftarrow\sigma_{k-1}}\boldsymbol{G}(\tau)^{\sigma_{k-1}\leftarrow\sigma_{k-2}}\boldsymbol{G}(\tau)\cdots{}^{\sigma_1\leftarrow\sigma_0}\boldsymbol{G}(\tau)^{\sigma_0}\boldsymbol{z}(\tau) \\ &= {}^{\sigma_k\leftarrow\sigma_{k-1}\leftarrow\cdots\leftarrow\sigma_0}\boldsymbol{G}(\tau)^{\sigma_0}\boldsymbol{z}(\tau), \end{aligned} \tag{4.48}$$

which then gives

$${}^{\sigma_k\leftarrow\sigma_{k-1}\leftarrow\cdots\leftarrow\sigma_0}\boldsymbol{G}(\tau) = {}^{\sigma_k\leftarrow\sigma_{k-1}}\boldsymbol{G}(\tau)^{\sigma_{k-1}\leftarrow\sigma_{k-2}}\boldsymbol{G}(\tau)\cdots{}^{\sigma_1\leftarrow\sigma_0}\boldsymbol{G}(\tau), \tag{4.49}$$

where we denote with "$\cdots$" the other individual jump gains to complete the sequence, e.g., ${}^{\sigma_2\leftarrow\sigma_1}\boldsymbol{G}(\tau)$. Equation (4.49) is proven also in Appendix B.2.

Remark 4.7 *In this work, only the simultaneous-going-to-contact situations are considered, leaving the simultaneous contact-to-release case for future investigation. We thus do not take into account input-dependent guard functions, which possibly complicates the constant jump gain expression, cf. [17].*

With the positive homogenization defined, we continue by elaborating on how this positive homogenization is used in this work.

4.3 Stability and closed-loop analysis

The first usage of this positive homogenization is to asses the local stability of the dynamical system. This is seen from (4.30), where one can rewrite the segments of continuous dynamics as

$$\boldsymbol{x}_\epsilon - \bar{\boldsymbol{\alpha}} = \epsilon \bar{\boldsymbol{z}} + o(\epsilon). \tag{4.50}$$

Assuming the perturbation are sufficiently small, the contribution of $o(\epsilon) \approx 0$. For such cases with sufficiently small perturbations, $\epsilon\bar{\boldsymbol{z}}$ can be used to give first-order approximations of the error dynamics, i.e.,

$$\boldsymbol{e}_R = \boldsymbol{x}_\epsilon - \bar{\boldsymbol{\alpha}} \approx \epsilon \bar{\boldsymbol{z}}. \tag{4.51}$$

Numerical experiments are performed in Chapter 5 to indeed show that $\epsilon\bar{\boldsymbol{z}}$ is able to provide accurate first-order approximations of the error dynamics.

the second usage of the positive homogenization is to design a tracking controller. A closed-loop input

$$\boldsymbol{u} = \bar{\boldsymbol{\mu}} - \boldsymbol{K}(\boldsymbol{x}_\epsilon - \boldsymbol{\alpha}) \tag{4.52}$$

for the dynamical system can be interpreted by the positive homogenization as a perturbed input

$$\boldsymbol{v}(t) = -\boldsymbol{K}(t)\boldsymbol{z}(t), \tag{4.53}$$

which is proven in Appendix B.4. We may then analyze the closed-loop behavior of the positive homogenization, and see whether it can still provide accurate first-order error approximations. If so, then we could stabilize the positive homogenization to achieve trajectory tracking for the dynamical system. We use the stability definition of [16, definition 5, p.6] for the positive homogenization, stating:

Definition 4.3 (uniform assymptotic stability local model) *given t_0, the origin of the closed-loop positive homogenization* (4.31), (4.32), (4.33), (4.46)-(4.49), *and* (4.53) *is* ***uniformly asymptotically stable*** *if for every $\varepsilon > 0$ and $T_0 \geq t_0$ there exist a δ, independent of T_0, such that $||\boldsymbol{z}(T_0, i_{T_0}, k_{T_0})|| \leq \delta$ implies $||\boldsymbol{z}(t,i,k)|| \leq \varepsilon$ for all $(t,i,k) \in$ dom $\boldsymbol{\alpha}$ with $t \geq T_0$ and that $lim_{t\to\infty}||\boldsymbol{z}(t,i,k)|| = 0$. In this, i_{T_0} is the counter i corresponding to the time T_0, i.e., the largest i such that $T_0 \geq \tau_i$, and k_{T_0} the counter k corresponding to the time T_0 which is always 1.*

This is also tested via numerical experiments in Chapter 5.

4.4 Summary

In this chapter, novel hybrid notations are worked out to describe the considered hybrid system with more ease. Using these notations, a sensitivity analysis for (possibly fictious) state-triggered hybrid systems with simultaneous guard activation and fixed mode sequence is performed, resulting in a local model, i.e., a positively homogeneous time-triggered hybrid system, capable of providing first-order approximations of all the possible behavior of the nonlinear hybrid system. The positive homogenization achieves this by incorporating the jumps and in-between flow effects of the perturbed dynamical system via a so-called conewise constant jump gain, consisting of different constant jump gains corresponding to the possible mode sequences. Via a jump shaping condition, based on the smallest event time, one can determine the constant jump gain with the state of the positive homogenization. The advantage of our local model, is that we can get a single piecewise-linear jump map that is able to predict the total effect of a perturbation, that is sufficiently small, about simultaneous guard activation. This local model may then be used to analyze the open-loop and, possibly, closed-loop behavior of our non-linear state-triggered hybrid system. Numerical experiments are performed in Chapter 5 to validate this for the considered benchmark example.

Chapter 5

Numerical validation of the sensitivity analysis

In the previous chapter, a sensitivity analysis with respect to perturbations of the initial condition and control input is performed to examine the local behavior of a hybrid system about a trajectory with simultaneous guard activation, i.e., simultaneous impacts. The resulting time-triggered hybrid system, derived in Section 4.2, can be used to study the stability of the reference trajectory and, possibly, to design (time-varying) closed loop gains for stabilizing the closed-loop system response, see Section 4.3. This local model also goes by the name of *positive homogenization*.

The focus of this chapter is to numerically investigate and validate that trajectories of the positive homogenization approximate the solutions to the original nonlinear hybrid system in a local neighborhood of the reference trajectory. To do so, we introduce a planar benchmark example consisting of a fully actuated block and a hinged non-actuated plank. For each discrete mode, we detail the corresponding (constrained) continuous dynamics, the discrete dynamics describing impact, and the positive homogeneous approximation.

A reference trajectory with simultaneous impact is then designed on our benchmark example for given system parameters. A state trajectory and positively homogeneous trajectory is designed by adding a perturbation on the initial condition of the reference. To determine whether the positive homogenization is able to provide accurate first-order approximations of the behavior of our benchmark example, we further compare the results of the reference trajectory, state trajectory, and positively homogeneous trajectory. This is done both for the system in open-loop and under closed-loop conditions for different controller gains.

5.1 Benchmark example

We first describe our benchmark example and discuss some of the modeling choices/assumptions. Figure 5.1 gives a schematic representation of the considered mechanical system. It consists of a block and an unactuated plank that is secured to the origin O^0 using a revolute joint. Rotation of the plank about this joint is counteracted by both a torsional spring and a damper. For sake of brevity, this system is referred as a *plank-block system*.

To describe the mechanical and geometrical relations, we use a Cartesian frame $\{O, \vec{\boldsymbol{e}}\}$, see [33]. The origin of the frame is denoted as O and the basis as $\vec{\boldsymbol{e}} := \begin{pmatrix} \vec{e}_1, & \vec{e}_2, & \vec{e}_3 \end{pmatrix}^T$, representing a column of basis vectors with vectors characterized by the arrows on top the symbols. A right-handed frame is considered with $\vec{e}_i \cdot \vec{e}_j = \delta_{ij}$ for $i, j = \{1, 2, 3\}$ and $\vec{e}_1 \times \vec{e}_2 = \vec{e}_3$, where δ_{ij} is the Kronicker delta ($\delta_{ij} = 1$ for $i = j$ and $\delta_{ij} = 0$ otherwise). Note that $\vec{\boldsymbol{e}}_3$ is directed outwards the paper in Figure 5.1.

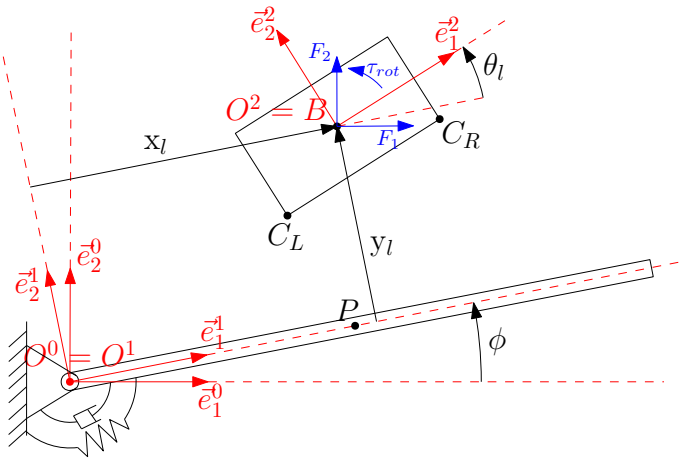

Figure 5.1: A representation of the plank-block system and the coordinates used to describe its position. The inertial frame is characterized by $\{O^0, \vec{\boldsymbol{e}}^0\}$, the plank body fixed-frame by $\{O^1, \vec{\boldsymbol{e}}^1\}$, and the block body-fixed frame by $\{O^2, \vec{\boldsymbol{e}}^2\}$. The plank with a spring and damper is unactuated, and the block with contact points C_L and C_R is actuated by actuator inputs F_1, F_2, and τ_{rot}.

A plank-block system is chosen due to the interactive dynamics during contact and impact, in which the block can, to a certain extent, influence the rotated position of the plank. An interesting situation may occur for a block impacting the plank with a perturbation in its initial condition, which will, besides having no simultaneous impact, also disturb the rotated plank position/velocity differently. Consequently, more complex behavior with respect to static cases, e.g., a block impacting the flat surface of the world, can be concluded in a neighborhood around a trajectory with simultaneous impacts. This will then also appear in the positive homogenization.

The following assumptions are made for the modeling process to make it interesting enough to demonstrate the developed theory in Chapter 3 and Chapter 4:

1. The block is assumed to be fully actuated.
2. The block impacts inelastically on a locally (dynamic) flat surface, we thus do not consider impacts on the edge of the plank. Furthermore, no superfluous contacts are considered as via Assumption 2.1.
3. The system is considered planar.
4. Contacts between the block and plank is represented using two contact points, i.e., points C_l and C_R as shown in Figure 5.1.
5. Both the plank and the block are considered rigid with uniform mass distribution.
6. There is no sliding friction between the block and plank.

The block has a mass m_B, height l_B, length L_B, and mass moment of inertia J_B. Its position and orientation (when not in contact with the plank) are described using the coordinates x_l, y_l, and θ_l as illustrated in Figure 5.1. The plank has mass m_P, height l_P, length L_P, and mass moment of inertia J_P. The rotation of the plank about point $O^0 = O^1$ is denoted ϕ and is resisted by a rotational spring with stiffness k_P and a rotational damper with damping coefficient b_P. The *generalized coordinates* for the plank-block system are chosen to be

$$\boldsymbol{q}_l = \begin{pmatrix} \mathrm{x}_l & \mathrm{y}_l & \theta_l & \phi \end{pmatrix}^T. \tag{5.1}$$

In (5.1), the subscript l is used to indicate that the configuration of the block is with respect to the moving coordinate frame $\{O^1, \vec{\boldsymbol{e}}^1\}$. We hence refer to the generalized coordinates as *local* coordinates. We choose to describe the system using local coordinates, as opposed to using coordinates with respect to the inertial frame, since this simplifies the expressions for the unilateral constraint $\boldsymbol{h}_l \geq 0$ and in turn the jump shaping conditions, see Section 4.2.3. Next, we formulate the dynamics of the plank-block system by first presenting the continuous and discrete dynamics within the framework of non-smooth mechanics and subsequently adapting and combining these to form a hybrid model representation.

5.1.1 Dynamics plank-block system in non-smooth mechanics framework

The continuous dynamics in terms of coordinates $\boldsymbol{q}_l$ and velocity $\mathbf{v}_l$ can be expressed as

$$\begin{aligned} \boldsymbol{M}_l(\boldsymbol{q}_l)\dot{\mathbf{v}}_l - \boldsymbol{H}_l(\boldsymbol{q}_l, \mathbf{v}_l) = \boldsymbol{S}_l(\boldsymbol{q}_l)\boldsymbol{u} + \boldsymbol{W}_l(\boldsymbol{q}_l)\boldsymbol{\lambda}, \\ 0 \leq \boldsymbol{h}_l \perp \boldsymbol{\lambda} \geq 0, \end{aligned} \tag{5.2}$$

see (2.4). In the above expression, the mass matrix $\boldsymbol{M}_l$ is given by

$$\boldsymbol{M}_l = \begin{pmatrix} \mathrm{m}_B & 0 & 0 & -\mathrm{m}_B \mathrm{y}_l \\ 0 & \mathrm{m}_B & 0 & \mathrm{m}_B \mathrm{x}_l \\ 0 & 0 & J_B & J_B \\ -\mathrm{m}_B \mathrm{y}_l & \mathrm{m}_B \mathrm{x}_l & J_B & 0.25\mathrm{m}_P L_P^2 + \mathrm{m}_B \mathrm{x}_l^2 + \mathrm{m}_B \mathrm{y}_l^2 + J_B + J_P \end{pmatrix}, \tag{5.3}$$

and the column $\boldsymbol{H}_l$ containing the centripedal, Coriolis and gravity terms (where g is the gravitational acceleration) is given by

$$\boldsymbol{H}_l = \begin{pmatrix} \mathrm{m}_B(\mathrm{x}_l\dot{\phi}^2 + 2\dot{\mathrm{y}}_l\dot{\phi} - \mathrm{g}\sin(\phi)) \\ -\mathrm{m}_B(-\mathrm{y}_l\dot{\phi}^2 + 2\dot{\mathrm{x}}_l\dot{\phi} + \mathrm{g}\cos(\phi)) \\ 0 \\ \mathrm{g}\mathrm{m}_B\mathrm{y}_l\sin(\phi) - \mathrm{k}_P\phi - 2\mathrm{m}_B\dot{\phi}\dot{\mathrm{x}}_l\mathrm{x}_l - 2\mathrm{m}_B\dot{\phi}\dot{\mathrm{y}}_l\mathrm{y}_l - 0.5\mathrm{g}\mathrm{m}_P L_P\cos(\phi) - \mathrm{g}\mathrm{m}_B\mathrm{x}_l\cos(\phi) - \mathrm{b}_P\dot{\phi} \end{pmatrix}. \tag{5.4}$$

The matrix of generalized force directions $\boldsymbol{S}_l$ for the input $\boldsymbol{u}$ can be expressed as

$$\boldsymbol{S}_l = \begin{pmatrix} \cos(\phi) & \sin(\phi) & 0 \\ -\sin(\phi) & \cos(\phi) & 0 \\ 0 & 0 & 1 \\ -\mathrm{y}_l\cos(\phi) - \mathrm{x}_l\sin(\phi) & \mathrm{x}_l\cos(\phi) - \mathrm{y}_l\sin(\phi) & 1 \end{pmatrix}, \tag{5.5}$$

and $\boldsymbol{u}$ as a column containing the actuation forces and torques, i.e.

$$\boldsymbol{u} = \begin{pmatrix} F_1 \\ F_2 \\ \tau_{rot} \end{pmatrix}. \tag{5.6}$$

In (5.6), F_1 represents a force acting on the block in the $\vec{e}_1^0$ direction, F_2 a force in the $\vec{e}_2^0$ direction, and τ_{rot} a torque in the positive θ_l direction. The unilateral constraints in local coordinates are formulated as $\boldsymbol{h}_l = \begin{pmatrix} h_{l,1}, & h_{l,2} \end{pmatrix}^T \geq 0$ with

$$\begin{aligned} h_{l,1} &= \left(\mathrm{y}_l - \frac{l_P}{2}\right) - \frac{l_B}{2}\cos(\theta_l) - \frac{L_B}{2}\sin(\theta_l), \\ h_{l,2} &= \left(\mathrm{y}_l - \frac{l_P}{2}\right) - \frac{l_B}{2}\cos(\theta_l) + \frac{L_B}{2}\sin(\theta_l), \end{aligned} \tag{5.7}$$

and are depicted in Figure 5.2. In formulating these contact distances, we assume that the block does not reach either of the plank's edges, i.e., that $\frac{L_B}{2} \leq \mathrm{x}_l \leq \frac{2L_P - L_B}{2}$.

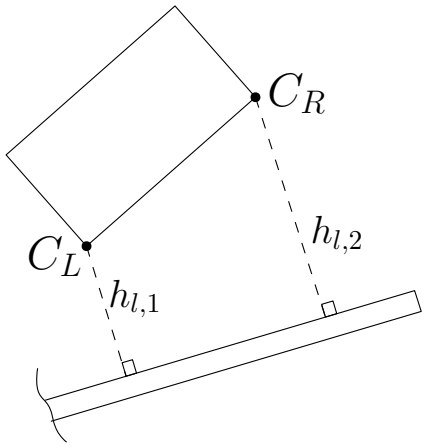

Figure 5.2: An illustration of the contact distances of the plank-block system. The distance between the left corner C_L and the plank is denoted with $h_{l,1}$, and the distance between the right corner C_R and the plank is denoted with $h_{l,2}$.

From (5.7), we derive $\boldsymbol{W}_l^T = \frac{\partial \boldsymbol{h}_l}{\partial \boldsymbol{q}_l}$ and denote the corresponding contact forces as $\boldsymbol{\lambda} = \begin{pmatrix}\lambda_1 & \lambda_2\end{pmatrix}^T$. The derivation of (5.3) - (5.7) is found in Appendix C.

For a global restitution coefficient $\varepsilon = 0$, the impact dynamics are formulated with (2.18) and Assumption 2.1 as

$$\begin{aligned} &\boldsymbol{M}_l(\boldsymbol{q}_l)(\mathbf{v}_l^+ - \mathbf{v}_l^-) = \sum_{i \in \mathcal{I}_c} \boldsymbol{W}_i(\boldsymbol{q}_l)\Lambda_i, \\ &0 \leq \xi_{l,i}^+ \perp \Lambda_i \geq 0, \quad i \in \mathcal{I}_c \end{aligned} \tag{5.8}$$

with $\mathcal{I}_c$ denoting the index set of closed contacts, $\boldsymbol{\xi}_l = \boldsymbol{W}_l^T \mathbf{v}$ the normal contact distance velocities, $\boldsymbol{W}_l = \begin{pmatrix}\boldsymbol{W}_{l,1} & \boldsymbol{W}_{l,2}\end{pmatrix}^T \in \mathbb{R}^{4\times 2}$, and $\boldsymbol{\Lambda} = \begin{pmatrix}\Lambda_1 & \Lambda_2\end{pmatrix}^T$. Note that we assume that superfluous contacts do not occur by satisfying (2.19) with

$$\nabla h_{l,i}(\boldsymbol{q}_l) = \boldsymbol{M}_l^{-1}(\boldsymbol{q}_l)\frac{\partial h_{l,i}}{\partial \boldsymbol{q}_l}, \tag{5.9}$$

and that subsequently the generalized Newton's impact law reduces to the Newton's impact law, simplifying the impact dynamics to (5.8).

The continuous and discrete (impact) dynamics are further used in this chapter to perform numerical experiments. We now formulate the dynamics of the block in hybrid system framework, see Section 2.2.

5.1.2 Dynamics plank-block in hybrid system framework

In this work, we are only interested in a simultaneous impacting motion. Therefore, the hybrid dynamics are formulated corresponding to the free-motion to two-contact transitions. Figure 5.3 illustrates the dynamics as a hybrid system with four modes. We define the state as

$$\boldsymbol{x} = \begin{pmatrix}\boldsymbol{q}_l \\ \mathbf{v}_l\end{pmatrix} \tag{5.10}$$

and the vectorfields as

$${}^{\sigma_k}\boldsymbol{f} = \begin{pmatrix}\mathbf{v}_l \\ \dot{\mathbf{v}}_l\end{pmatrix}. \tag{5.11}$$

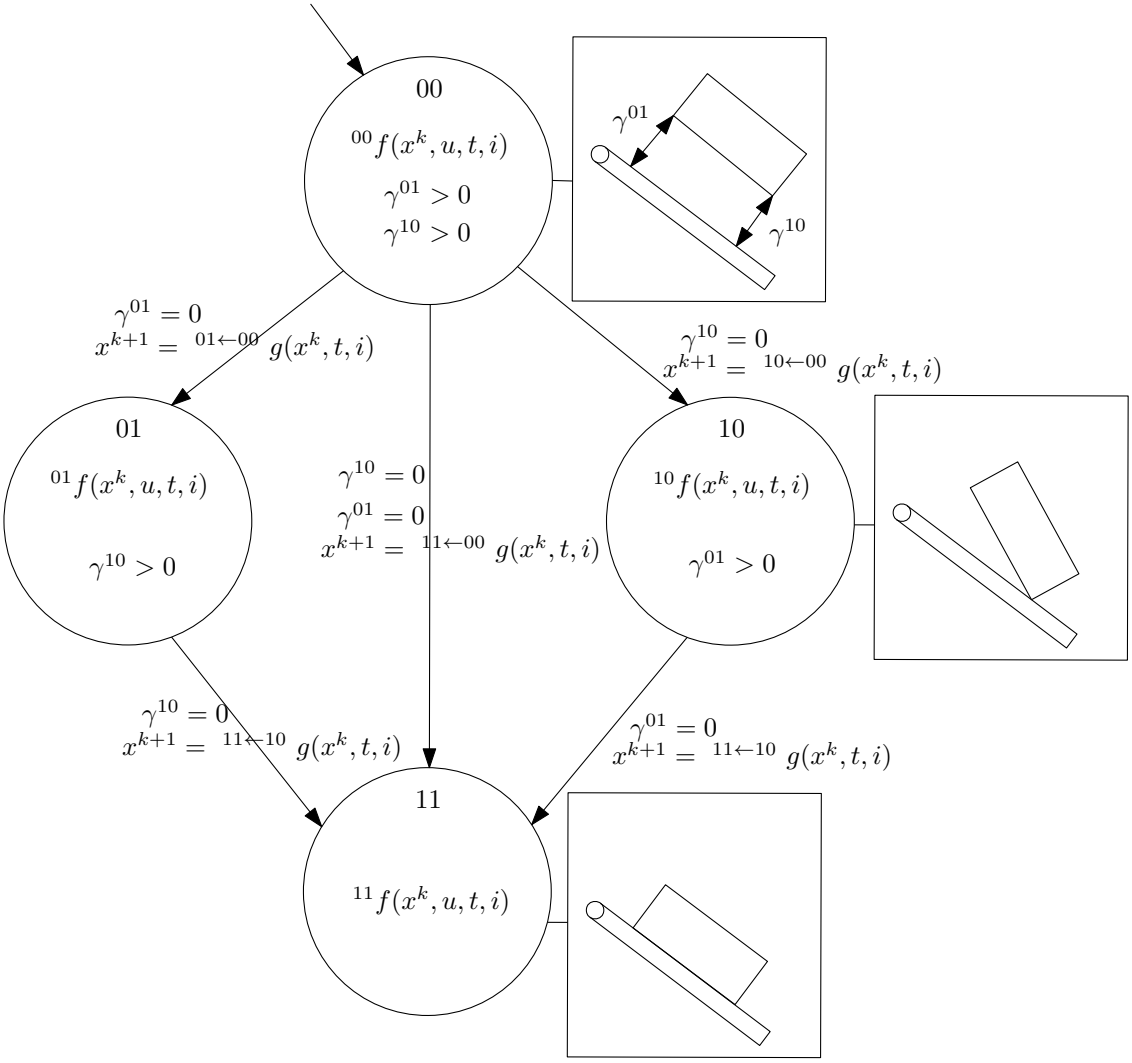

Figure 5.3: Schematic of a hybrid systems representation of the plank-block system only considering the impacting motions.

The accelerations $\dot{\mathbf{v}}_l$ in (5.11) are defined differently for each mode, where we solve the differential algebraic equation (DAE)

$$\begin{aligned} \boldsymbol{M}_l(\boldsymbol{q}_l)\dot{\mathbf{v}}_l - \boldsymbol{H}_l(\boldsymbol{q}_l, \mathbf{v}_l) &= \boldsymbol{S}_l(\boldsymbol{q}_l)\boldsymbol{u} + \sum_{i\in\mathcal{I}_c} \boldsymbol{W}_i \lambda_i, \\ \dot{\xi}_{l,i} &= 0, \quad i \in \mathcal{I}_c \end{aligned} \tag{5.12}$$

with $\dot{\xi}_{l,i} = \frac{\partial \boldsymbol{W}_{l,i}^T \mathbf{v}_l}{\partial \boldsymbol{q}_l}\mathbf{v}_l + \boldsymbol{W}_{l,i}^T \dot{\mathbf{v}}_l$ and

$$\mathcal{I}_c := \begin{cases} \emptyset & \text{for} \quad \sigma_k = 00, \\ \{1\} & \text{for} \quad \sigma_k = 01, \\ \{2\} & \text{for} \quad \sigma_k = 10, \\ \{1,2\} & \text{for} \quad \sigma_k = 11. \end{cases} \tag{5.13}$$

Note that via (5.12) an analytical expression is derived for the vectorfield in every mode, as opposed to a linear complementarity formulation. If one, however, is able to compute the derivatives of the associated vectorfields, then one does not have to go through the trouble of formulating analytical expressions as (5.12).

The modes $\Sigma \in \{00, 01, 10, 11\}$ are characterized by the number of contacts that are closed, and a contact is closed when the system satisfies the corresponding guard

$$\begin{aligned} \gamma^{01} = h_{l,1} &= \left(\mathrm{y}_l - \frac{l_P}{2}\right) - \frac{l_B}{2}\cos(\theta_l) - \frac{L_B}{2}\sin(\theta_l) = 0 \quad \text{or} \\ \gamma^{10} = h_{l,2} &= \left(\mathrm{y}_l - \frac{l_P}{2}\right) - \frac{l_B}{2}\cos(\theta_l) + \frac{L_B}{2}\sin(\theta_l) = 0. \end{aligned} \tag{5.14}$$

Taking an initial mode 00, one can describe the mode transition for $00 \to 01$ or $00 \to 10$, i.e., the *first* single contact-impact, using the reset maps

$$\begin{aligned} {}^{01\leftarrow 00}\boldsymbol{g}(x^k, t, i) &= \begin{pmatrix} \boldsymbol{q}_l^- \\ (\boldsymbol{I} - \boldsymbol{M}_l^{-1}\boldsymbol{W}_1(\boldsymbol{W}_1^T\boldsymbol{M}_l^{-1}\boldsymbol{W}_1)^{-1}\boldsymbol{W}_1^T)\mathbf{v}_l^- \end{pmatrix}, \\ {}^{10\leftarrow 00}\boldsymbol{g}(x^k, t, i) &= \begin{pmatrix} \boldsymbol{q}_l^- \\ (\boldsymbol{I} - \boldsymbol{M}_l^{-1}\boldsymbol{W}_2(\boldsymbol{W}_2^T\boldsymbol{M}_l^{-1}\boldsymbol{W}_2)^{-1}\boldsymbol{W}_2^T)\mathbf{v}_l^- \end{pmatrix}, \end{aligned} \tag{5.15}$$

that follow from (5.8). Here, $\boldsymbol{I}$ is an identity matrix, $\boldsymbol{W}_{l,i} = \boldsymbol{W}_i$ with $i \in \{1, 2\}$, and $\boldsymbol{q}_l^-$ and $\mathbf{v}_l^-$, respectively, the pre-impact position and velocity. The reset map describing simultaneous impact or the *second* single-contact impact, i.e., one contact has already impacted and is thus in contact with the flat surface, can also be derived from (5.8), giving

$${}^{11\leftarrow\sigma_k}\boldsymbol{g}(\boldsymbol{x}^k, t, i) = \begin{pmatrix} \boldsymbol{q}_l^- \\ \mathbf{v}_l^- + \boldsymbol{M}_l^{-1}(\boldsymbol{W}_1\Lambda_1 + \boldsymbol{W}_2\Lambda_2) \end{pmatrix} \tag{5.16}$$

with

$$\begin{aligned} \Lambda_1 &= -(\boldsymbol{W}_1^T\boldsymbol{M}_l^{-1}\boldsymbol{W}_1)^{-1}\left(\xi_{l,1}^- + \boldsymbol{W}_1^T\boldsymbol{M}_l^{-1}\boldsymbol{W}_2\Lambda_2\right), \\ \Lambda_2 &= \left(\boldsymbol{W}_2^T\boldsymbol{M}_l^{-1}\boldsymbol{W}_2 - \boldsymbol{W}_1(\boldsymbol{W}_1^T\boldsymbol{M}_l^{-1}\boldsymbol{W}_1)^{-1}\boldsymbol{W}_1^T\boldsymbol{M}_l^{-1}\boldsymbol{W}_2)\right)^{-1}\left(\boldsymbol{W}_2^T\boldsymbol{M}_l^{-1}\boldsymbol{W}_1(\boldsymbol{W}_1^T\boldsymbol{M}_l^{-1}\boldsymbol{W}_1)^{-1}\xi_{l,1}^- - \xi_{l,2}^-\right), \end{aligned} \tag{5.17}$$

where

$$\xi_{l,1}^- := \begin{cases} 0, \text{for} & \sigma_k = 01, \\ < 0, \text{for} & \sigma_k = 10, \\ < 0, \text{for} & \sigma_k = 00, \end{cases} \quad \text{and} \quad \xi_{l,2}^- := \begin{cases} < 0, \text{for} & \sigma_k = 01, \\ 0, \text{for} & \sigma_k = 10, \\ < 0, \text{for} & \sigma_k = 00. \end{cases} \tag{5.18}$$

In (5.18), $\boldsymbol{\xi}_l^-$ represents the pre-impact normal velocity of the contact distances, valued differently when experiencing different mode transitions. In case we have simultaneous impacts, i.e., one substitutes $\sigma_k = 00$ into (5.16), the pre-impact normal contact distance velocities $\boldsymbol{\xi}_l$ will be negative. Consequently, both $\xi_{l,1}^-$ and $\xi_{l,2}^-$ will play a role in determining the impulsive forces in (5.17). In case we do not have simultaneous impact, i.e., one substitutes $\sigma_k = 10$ or $\sigma_k = 01$ in (5.16), either $\xi_{l,1}^-$ or $\xi_{l,2}^-$ will be zero. Taking $\sigma_k = 10$, one observes from Figure 5.3 that $h_{l,2} = 0$ and consequently that $\xi_{l,2} = 0$. In turn, $\xi_{l,2}^-$ will not play a role in determining the impulsive forces in (5.17).

It is straightforward to verify numerically that the reset maps (5.15) and (5.16) are associative as they satisfy Definition 4.1, giving ${}^{11\leftarrow 00}\boldsymbol{g} = {}^{11\leftarrow 01}\boldsymbol{g} \circ {}^{01\leftarrow 00}\boldsymbol{g} = {}^{11\leftarrow 10}\boldsymbol{g} \circ {}^{10\leftarrow 00}\boldsymbol{g}$. Now that the hybrid system dynamics are defined, we further evaluate the positive homogenization.

5.1.3 Dynamics positive homogenization for plank-block

The state of the positive homogenization is defined as $\boldsymbol{z}$, see Section 4.2. We define the state as

$$\boldsymbol{z} = \begin{pmatrix} z_{\mathrm{x}_l}, & z_{\mathrm{y}_l}, & z_{\theta_l}, & z_\phi, & \dot{z}_{\mathrm{x}_l}, & \dot{z}_{\mathrm{y}_l}, & \dot{z}_{\theta_l}, & \dot{z}_\phi \end{pmatrix}^T, \tag{5.19}$$

where we emphasize with the subscripts that $\boldsymbol{z}$ is also defined in local coordinates. Trajectories $\boldsymbol{z}$ for the system of interest abide the hybrid system dynamics as (4.31), which for the plank-block system simplify to

$$\begin{aligned}
&{}^{00}\boldsymbol{z}(t) = \boldsymbol{z}_0, \qquad t = t_0, \\
&{}^{00}\dot{\boldsymbol{z}}(t) = D_1 {}^{00}\boldsymbol{f}\left({}^{00}\boldsymbol{\alpha}(t), {}^{00}\boldsymbol{\mu}(t), t\right) {}^{00}\boldsymbol{z}(t) + D_2 {}^{00}\boldsymbol{f}\left({}^{00}\boldsymbol{\alpha}(t), {}^{00}\boldsymbol{\mu}(t), t\right) {}^{00}\boldsymbol{v}(t), \qquad t \in [t_0, \tau], \\
&{}^{\sigma_s}\boldsymbol{z}(t) = \boldsymbol{G}\left(t, {}^{00}\boldsymbol{z}(t)\right) {}^{00}\boldsymbol{z}(t), \qquad t = \tau, \\
&{}^{\sigma_s}\dot{\boldsymbol{z}}(t) = D_1 {}^{11}\boldsymbol{f}\left({}^{00}\boldsymbol{\alpha}(t), {}^{11}\boldsymbol{\mu}(t), t\right) {}^{\sigma_s}\boldsymbol{z}(t) + D_2 {}^{11}\boldsymbol{f}\left({}^{00}\boldsymbol{\alpha}(t), {}^{11}\boldsymbol{\mu}(t), t\right) {}^{11}\boldsymbol{v}(t), \qquad t \in [\tau, t_f],
\end{aligned} \tag{5.20}$$

where σ_s represents the mode sequence that is either $11 \leftarrow 01 \leftarrow 00$ or $11 \leftarrow 10 \leftarrow 00$. Note that as the vectorfields $\boldsymbol{f}$ are formulated with an input $\boldsymbol{u}$ orientated in the inertial frame coordinates, see Figure 5.1, we also get a perturbed input $\boldsymbol{v}$ orientated in the same manner as $\boldsymbol{u}$; thus not in the local coordinates direction. This will slightly complicate the feedback design, as seen in Section 5.4.

The conewise constant jump gain, elaborated in Section 4.2.3, is expressed as

$$\boldsymbol{G}(\tau, {}^{00}\boldsymbol{z}(\tau)) = \begin{cases} {}^{11\leftarrow 01}\boldsymbol{G}(\tau) {}^{01\leftarrow 00}\boldsymbol{G}(\tau) & \text{for} \quad ({}^{01\leftarrow 00}\boldsymbol{a} - {}^{10\leftarrow 00}\boldsymbol{a})^T \, {}^{00}\boldsymbol{z}(\tau) \leq 0, \\ {}^{11\leftarrow 10}\boldsymbol{G}(\tau) {}^{10\leftarrow 00}\boldsymbol{G}(\tau) & \text{for} \quad ({}^{01\leftarrow 00}\boldsymbol{a} - {}^{10\leftarrow 00}\boldsymbol{a})^T \, {}^{00}\boldsymbol{z}(\tau) \geq 0 \end{cases} \tag{5.21}$$

with

$$\begin{aligned}
{}^{10\leftarrow 00}\boldsymbol{a} &= -\frac{D_1\gamma^{10}({}^{00}\boldsymbol{\alpha}(\tau), \tau)}{D_1\gamma^{10}({}^{00}\boldsymbol{\alpha}(\tau), \tau) \cdot {}^{00}\boldsymbol{f}({}^{00}\boldsymbol{\alpha}(\tau), {}^{00}\boldsymbol{\mu}(\tau), \tau)}, \\
{}^{01\leftarrow 00}\boldsymbol{a} &= -\frac{D_1\gamma^{01}({}^{00}\boldsymbol{\alpha}(\tau), \tau)}{D_1\gamma^{01}({}^{00}\boldsymbol{\alpha}(\tau), \tau) \cdot {}^{00}\boldsymbol{f}({}^{00}\boldsymbol{\alpha}(\tau), {}^{00}\boldsymbol{\mu}(\tau), \tau)},
\end{aligned} \tag{5.22}$$

where we assume inelastic impacts and deploy Assumption 2.1, i.e., closed contacts stay closed. For sake of brevity, we refer the *conewise constant jump gain* as *jump gain* in the rest of this work. Taking into account that simultaneous impact only occurs for $\theta_l = 0$ and $\mathrm{y}_l = \frac{l_P + l_B}{2}$, then we can write the jump shaping condition $({}^{01\leftarrow 00}\boldsymbol{a} - {}^{10\leftarrow 00}\boldsymbol{a})^T \, {}^{00}\boldsymbol{z}(\tau) \leq 0$ explicitly as

$$\begin{pmatrix} 0 & \frac{-L_B\dot{\theta}_l^-}{(\dot{\mathrm{y}}_l^-)^2 - 0.25L_B^2(\dot{\theta}_l^-)^2} & \frac{L_B\dot{\mathrm{y}}_l^-}{(\dot{\mathrm{y}}_l^-)^2 - 0.25L_B^2(\dot{\theta}_l^-)^2} & 0 & 0 & 0 & 0 & 0 \end{pmatrix} {}^{00}\boldsymbol{z}(\tau) \leq 0, \tag{5.23}$$

where we define $\dot{\mathrm{y}}_l^- = {}^{00}\mathrm{y}_l(\tau)$ and $\dot{\theta}_l^- = {}^{00}\theta_l(\tau)$. We can then simplify this to

$$\frac{L_B}{(\dot{y}_l^-)^2 - 0.25L_B^2(\dot{\theta}_l^-)^2}(-\dot{\theta}_l^- z_{\mathrm{y}_l} + \dot{\mathrm{y}}_l^- z_{\theta_l}) \leq 0 \tag{5.24}$$

with $z_{\mathrm{y}_l} = {}^{00}z_{\mathrm{y}_l}(\tau)$ and $z_{\theta_l} = {}^{00}z_{\theta_l}(\tau)$. Recall from Section 4.2.3 that satisfying (5.24) for a given perturbation $\boldsymbol{z}$ can be interpreted as the perturbed trajectory triggering the guard condition $\gamma^{01} = 0$ first.

Figure 5.4 then illustrates an example of the piecewise linear mapping that represents (5.21) with $\dot{\theta}_l^- = 0.5$, $\dot{y}_l^- = -1$, and $L_B > 0$. One observes that the jump map is indeed positively homogeneous as we can multiply the state $\boldsymbol{z}$ with a scalar $\epsilon \geq 0$, resulting in no change of the constant jump gain chosen in (5.21). We will furthermore show in appendix E.2 that our local model is indeed not linear for the considered benchmark example.

We now continue with the numerical experiments to validate that the local model can indeed provide accurate first-order approximations of the mechanical system behavior.

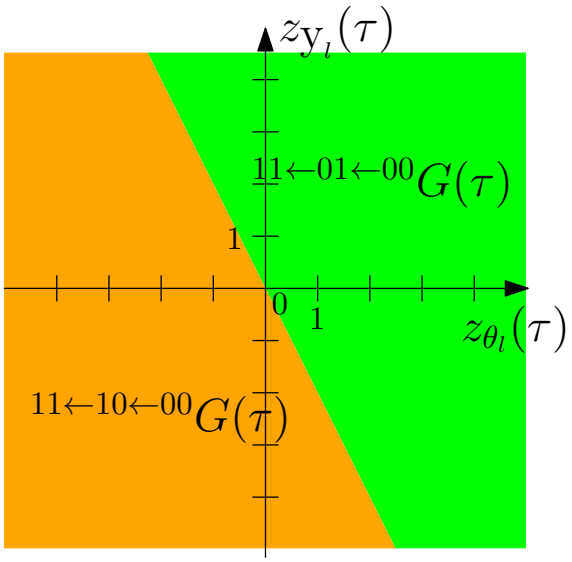

Figure 5.4: A visualization of the piecewise linear mapping (5.21) for $\dot{\theta}_l^- = 0.5$, $\dot{\mathrm{y}}_l^- = -1$, and $L_B > 0$. When a perturbation is found with the coordinates $z_{\mathrm{y}_l}(\tau)$ and $z_{\theta_l}(\tau)$ in the green area, the constant jump gain $^{11\leftarrow01\leftarrow00}\boldsymbol{G}(\tau)$ is applied.

5.2 Numerical experiment design

Before the numerical experiments are performed, certain choices have to be made. These include what type of numerical solver to use, which system parameters to consider, and which reference trajectory to choose. Regarding the numerical integration; all simulations are performed with an event-based solver within MATLAB [45]. The function ode45.m with event detection is employed, and both its absolute and relative integration tolerances are set to 10^{-3}. A Baumgarte stabilization, see [33], is further applied to guarantee stabilization of the constraint equations, see Appendix F.1. The event-based simulation model has been verified by performing equivalent simulations using a time-stepping scheme, see [34] and Appendix F.2, leading to similar results up to the order of numerical errors. Event-based simulation, in contrast to the less complex time-stepping scheme, is used as this allowed easier derivation of extended trajectories.

The plank and block parameters are given in Table 5.1 and Table 5.2. Choices are made to allow more interesting dynamic interaction, i.e., a long plank on which the block can slide and push, and prevent rocking behavior, i.e., a wide block. We consider a relatively high spring stiffness and damping coefficient of the plank to increase the impacting forces. The mass of the plank is chosen not too large, such that the plank does not solely fall downwards, and a comparable block mass is chosen to observe impacting effects that are visible in the trajectories.

Table 5.1: Block properties.

Parameter	L_B	l_B	m_B	J_B
Values	0.6 m	0.2 m	2 kg	$\frac{\mathrm{m}_B}{12}(l_B^2 + L_B^2)\mathrm{kgm}^2$

Table 5.2: Plank properties.

Parameter	L_P	l_P	m_P	J_P	b_P	k_P
Values	3 m	0.1 m	1.5 kg	$\frac{\mathrm{m}_P}{12}(l_P^2 + L_P^2)\mathrm{kgm}^2$	500 $\frac{\mathrm{Nm\ s}}{\mathrm{rad}}$	500 $\frac{\mathrm{Nm}}{rad}$

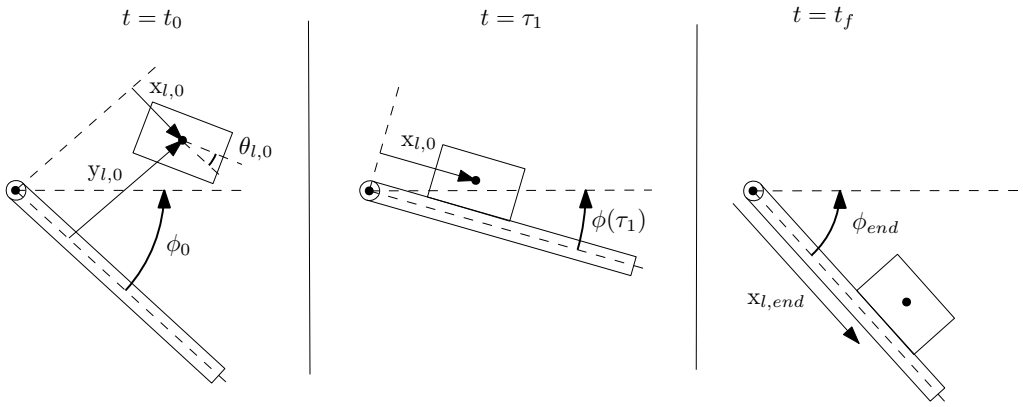

Figure 5.5: A visualization of the important steps to designing the position coordinates of the reference trajectory. On the left drawing the initial configuration is depicted, on the middle drawing the impact configuration, and on the right drawing the end configuration.

The design of the reference trajectory is visualized in Figure 5.5 and will be explained next. The motion is split in two parts, namely the *free motion phase*, i.e., the block and plank are not in contact, and the *contact phase*, i.e., the block and plank are in contact. On the left drawing, an initial configuration of the block and plank is considered in free motion at $t = t_0$. The initial block coordinates are $x_l(t_0) = x_{l,0}$, $y_l(t_0) = y_{l,0}$, and $\theta_l(t_0) = \theta_{l,0}$, and the initial plank coordinate is $\phi(t_0) = \phi_0$. We choose a ϕ_0 below its equilibrium, such that the impact will not only consist of the block velocity, but also of the plank velocity. Furthermore, the initial velocity and acceleration terms are assumed to be zero when possible, i.e., the plank acceleration can not be changed as the plank is unactuated. On the middle drawing at time $t = \tau_1$, the block is tasked to have simultaneous inelastic impact at $x_l(\tau_1) = x_{l,0}$, $y_l(\tau_1) = \frac{l_B + l_P}{2}$, and $\theta_l(\tau_1) = 0$. We let the block impact close to the hinge of the plank to derive a sliding motion during the contact phase. At time of impact, the block is assumed to only have a velocty in the y_l-direction. This will result in an easy to interpret jump shaping condition. We elaborate more on this in Section 5.3. During the contact phase, the block slides over the plank, while pushing downwards, till it reaches the position $x_{l,end}$ with the plank rotated to a desired angle ϕ_{end}. This is illustrated on the right drawing, and the velocity and acceleration terms are assumed zero again when possible. The motion of the block is created using quintic polynomials, and more details about the design of the reference trajectory can be found in Appendix D.

Table 5.3: Reference trajectory boundary conditions.

	$t_0 = 0$	(Pre) $\tau_1 = 1$	(Post) $\tau_1 = 1$	$t_f = 3$
x_l	0.8	0.8	Reset	2.6
$\dot{x}_l$	0	0	Reset	0
$\ddot{x}_l$	0	0	0	0
y_l	2	0.15	Reset	0.15
$\dot{y}_l$	0	-3	Reset	0
$\ddot{y}_l$	0	0	0	0
θ_l	0.3	0	Reset	0
$\dot{\theta}_l$	0	0	Reset	0
$\ddot{\theta}_l$	0	0	0	0
ϕ	-0.2	-	Reset	$\phi(1)^+$ - $\frac{\pi}{6}$
$\dot{\phi}$	0	-	Reset	0
$\ddot{\phi}$	-	-	0	0

The specific boundary conditions of the reference trajectory are formulated in Table 5.3. Since the plank is not actuated, its motion cannot be imposed when the block is not in contact with it. Therefore, the initial acceleration $\ddot{\phi}(t_0)$, and the impact terms $\phi(\tau_1), \dot{\phi}(\tau_1)$, and $\ddot{\phi}(\tau_1)$ cannot be imposed as illustrated with a dash in Table 5.3. Moreover, the initial conditions of the contact motion, i.e., just after impact, are related to the position and velocity terms just before impact by a reset map ${}^{11\leftarrow 00}\boldsymbol{g}$, hence the term *Reset*. The symbol $\phi(1)^+$ in Table 5.3 refers to the $\phi(\tau)$ value post-impact. The conditions formulated in this table produces a trajectory with *simultaneous impact* and also no *superfluous contacts* by fulfilling (2.19). Appendix E.1 furthermore shows that even applying small perturbations on the reference trajectory will not let superfluous contacts occur.

For the conditions in Table 5.3, Figure 5.6 and Figure 5.7 depict, respectively, the position and velocity coordinates of the reference trajectory resulting from the numerical simulation. Note that the trajectories are depicted in the local coordinates. The reference trajectory $\boldsymbol{\alpha}(t)$ is shown in solid and the extended trajectory $\bar{\boldsymbol{\alpha}}(t)$ is represented by the dashed curves. Due to the choice of describing the system in local coordinates, four of the states, i.e., y_l, $\dot{\mathrm{y}}_l$, θ_l, and $\dot{\theta}_l$ are mapped to zero by the jump map and will remain zero during contact. Due to space restrictions, in the following we typically show the Euclidean norm of the considered trajectory as opposed to depicting all of its components. An example of this representation style is seen in Figure 5.8. Note that for some figures in Sections 5.3 and 5.4, these individual components are given in Appendix F.4. These are given to the let the interested reader understand what creates the jump(s) in the norm trajectories.

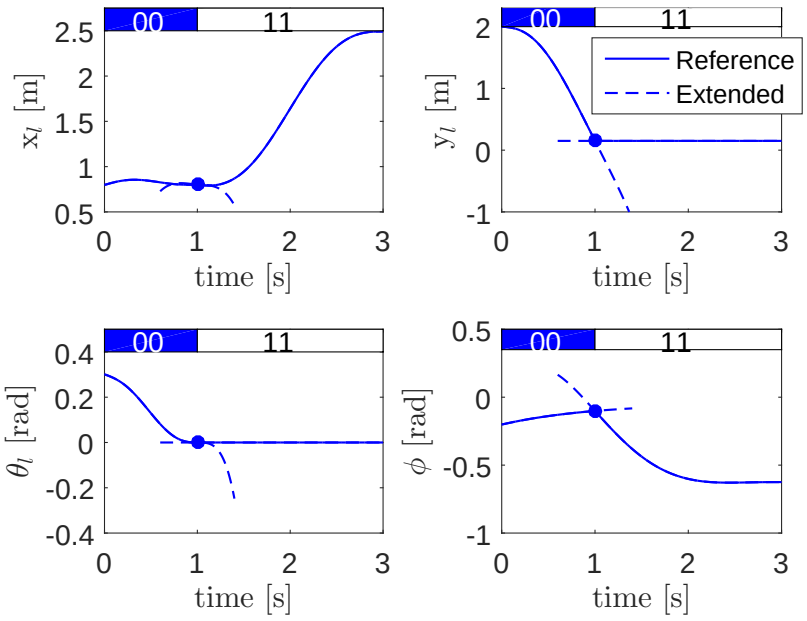

Figure 5.6: Numerical experiment results of the position coordinates of the reference trajectory, derived from the boundary conditions in Table 5.3. The solid lines represent the reference trajectory, and the dashed lines the extended reference trajectory.

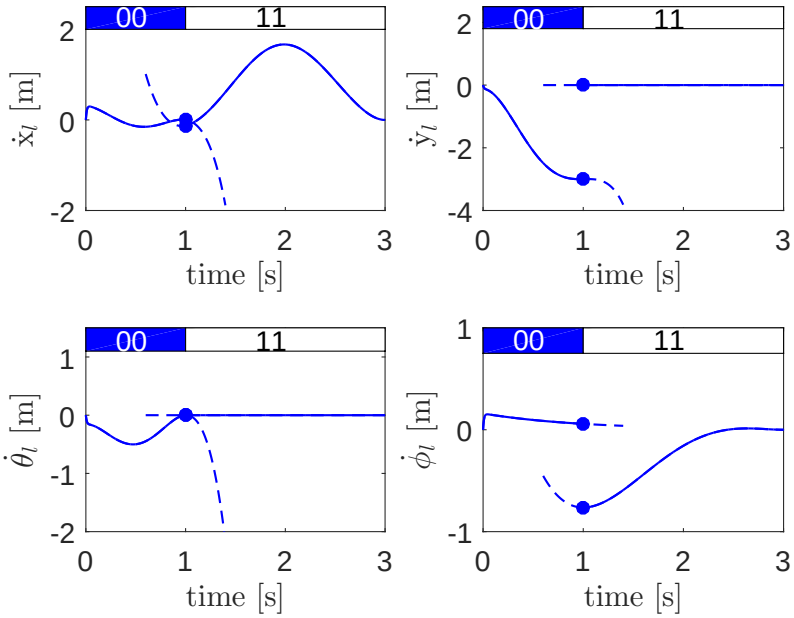

Figure 5.7: Numerical experiment results of the velocity coordinates of the reference trajectory, derived from the boundary conditions in Table 5.3. The solid lines represent the reference trajectory, and the dashed lines the extended reference trajectory.

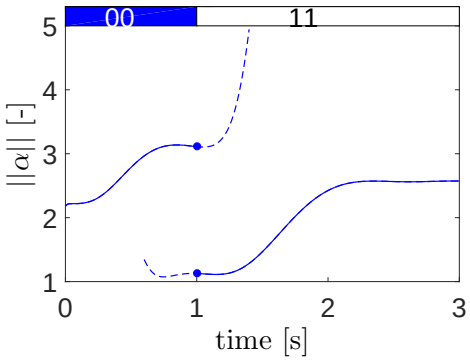

Figure 5.8: Numnerical experiment results of the Euclidean norm of the reference trajectory, derived from the boundary conditions in Table 5.3. The solid lines represent the reference trajectory, and the dashed lines the extended reference trajectory.

To realise the reference trajectory in Figure 5.8, the nominal input

$$\boldsymbol{\mu} = \begin{pmatrix} F_{1,ref} \\ F_{2,ref} \\ \tau_{rot,ref} \end{pmatrix} \tag{5.25}$$

visualized in Figure 5.9 is used. Note that $F_{1,ref}$ indicates the reference F_1 component. The solid lines represent the nominal input $\boldsymbol{\mu}$ and the dashed lines illustrate the extended version $\bar{\boldsymbol{\mu}}$. Figure 5.9 illustrates that the required forces during the contact phase are much higher than those in free motion. This is due to the high stiffness and damping of the plank in combination with a relatively small block mass.

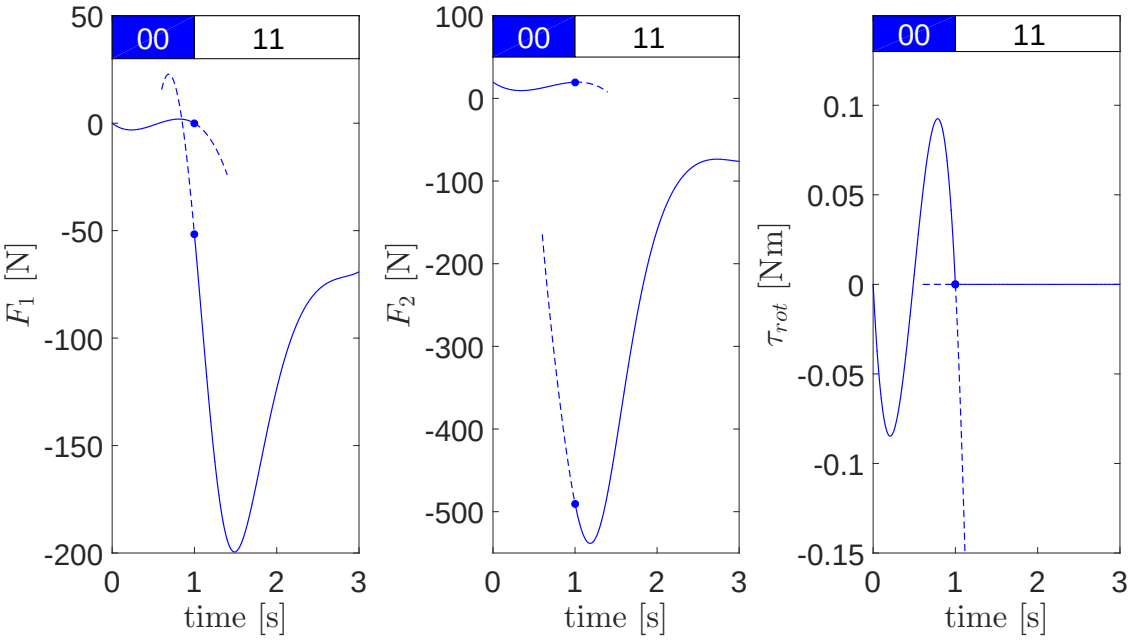

Figure 5.9: Numerical experiment results of the nominal input term $\boldsymbol{\mu}$ and its extended version $\bar{\boldsymbol{\mu}}$ to realize the reference trajectory in Figure 5.8. The nominal version is represented by the solid lines, and the extended version by the dashed lines.

Using the chosen state-input trajectory $(\boldsymbol{\alpha}(t), \boldsymbol{\mu}(t))$, the corresponding positive homogenization (4.46) is constructed. Next, numerical experiments are performed to test whether the positive homogenization can indeed provide first-order approximations of the mechanical system behavior. This is first done in open-loop, after which the closed-loop case follows.

5.3 Open-loop behaviour

In this section, we show that the positive homogenization can indeed be used to provide a first-order approximation of the error trajectory in open-loop, as deduced in Section 4.3. The conewise constant jump gain $\boldsymbol{G}(\tau, {}^{00}\boldsymbol{z}(\tau))$ plays an important role in realizing this. Due to its significance, a part of this section is also dedicated to validating (5.21) and its jump shaping conditions, e.g., (5.24). Here, we test whether (5.21) will indeed give the correct shape of the jump gain, and thus allow the positive homogenization to provide an accurate first-order open-loop approximation of the system dynamics. This is done for both the scenarios where the mechanical system experiences an impact sequence with the left-contact impacting first as an impact sequence with the right-contact impacting first. We start by analyzing the jump shaping conditions, see (5.24), and continue with the numerical experiments after.

5.3.1 Jump shaping conditions

The jump gain (5.21) changes into

$$h\boldsymbol{G}\left(\tau, {}^{00}\boldsymbol{z}(\tau)\right) = \begin{cases} {}^{11\leftarrow 01}\boldsymbol{G}(\tau)\,{}^{01\leftarrow 00}\boldsymbol{G}(\tau), & -0.2z_{\theta_l} \leq 0, \\ {}^{11\leftarrow 10}\boldsymbol{G}(\tau)\,{}^{10\leftarrow 00}\boldsymbol{G}(\tau), & -0.2z_{\theta_l} \geq 0, \end{cases} \tag{5.26}$$

with $z_{\theta_l} = {}^{00}z_{\theta_l}(\tau)$, when we insert the block parameters of Table 5.1 and the impact conditions of Table 5.3 into the jump shaping condition (5.24). One observes that the jump shaping condition is solely dependent on the sign of z_{θ_l}. Recalling from (4.51) that $\epsilon\boldsymbol{z}$ provides a first-order error approximation, one can interpret the state $\boldsymbol{z}$ as the direction of the local perturbation. That only a local perturbation in the direction of θ_l at time of impact contributes to (5.26) is, in retrospect, not surprising. Indeed, a local perturbation in x_l will only shift the impacting position along the plank, but will not prevent the occurrence of simultaneous impact. Similarly, a local perturbation in y_l will only change the impact time. This is under the assumption that $\dot{\theta}_l^-$ is 0 at time of impact. Note that (5.24) will be dependent on y_l when $\dot{\theta}_l^-$ is not 0 at time of impact. A perturbation in the direction of ϕ will similarly not prevent simultaneous impacts, as none of the coordinates x_l, y_l, and θ_l, get changed.

In the following, we describe the positive homogenization via the combination of (5.20) and (5.26). Numerical experiments are performed to analyze the accuracy of the first-order approximation by comparing either the error terms, i.e., $\boldsymbol{x}-\bar{\boldsymbol{\alpha}}$ to $\epsilon\boldsymbol{z}$, or the state terms of the real mechanical system, i.e., $\boldsymbol{x}$ to $\boldsymbol{\alpha}+\epsilon\boldsymbol{z}$. We deliberately compare two trajectories which do not jump at the same time instances, as to emphasize that the jump gain (5.26) can indeed combine the jump and flow effects of the unspecified modes well.

We simulate two cases of different initial perturbations, thus two different $\boldsymbol{z}(t_0)$. Note that in both cases the trajectory $\boldsymbol{x}$ is derived with an initial condition $\boldsymbol{x}(t_0) = \boldsymbol{\alpha}(t_0) + \epsilon\boldsymbol{z}(t_0)$. We first treat a relatively *simple* perturbation and after a more *complex* initial perturbation. We show that using (5.26) provides, for sufficiently small perturbations, accurate error approximations and that using *incorrect* jump gains of (5.26) leads to inaccurate approximations. With the term *incorrect* jump gain, we refer to the jump gain chosen in (5.26) as via reversed jump shaping conditions, i.e., we choose ${}^{11\leftarrow 10}\boldsymbol{G}(\tau){}^{10\leftarrow 00}\boldsymbol{G}(\tau)$ when $-0.2z_{\theta_l} \leq 0$.

5.3.2 Simple initial perturbation with a left-contact impacting first

The direction of initial perturbation is

$$ {}^{00}\boldsymbol{z}_{\mathrm{case1}}(t_0) = \begin{pmatrix} 0, & 0, & 0.3, & 0, & 0, & 0, & 0, & 0 \end{pmatrix}^T, \tag{5.27} $$

which remains unchanged at time of impact, i.e., ${}^{00}\boldsymbol{z}_{\mathrm{case1}}(t_0) = {}^{00}\boldsymbol{z}_{\mathrm{case1}}(\tau)$, and thus guarantees an impact sequence with the left contact-point impacting first. The trajectories $\boldsymbol{z}_{\mathrm{case1}}$ are shown in Figure 5.10 for both correct and incorrect jump gains. The influence of using an incorrect jump gain is visible, as the trajectory post-jump develops differently. In Figure 5.11, the state terms $||\boldsymbol{x}_{\mathrm{case1}}||$ and $||\boldsymbol{\alpha}+\epsilon\boldsymbol{z}_{\mathrm{case1}}||$ are compared for both jump gains. Remind that we obtain the trajectory $\boldsymbol{x}_{\mathrm{case1}}$ by taking the initial condition as $\boldsymbol{x}_{\mathrm{case1}}(t_0) = \boldsymbol{\alpha}(t_0) + \epsilon\boldsymbol{z}_{\mathrm{case1}}(t_0)$. One then sees that even using a small initial perturbation by taking $\epsilon = 0.01$, i.e., a perturbation of 0.1719 degrees in θ_l direction, does not let the two state terms coincide for an incorrect jump gain. The conclusion is that only using a correct jump gain allows the positive homogenization to provide accurate first-order approximations of the system behavior. We show further below that this also holds for an impact sequence with the right-contact impacting first. Note that in Figure 5.11, we depict the modes of the two trajectories at the top of the figure with horizontal bars characterized by their respective colors. The trajectory $\boldsymbol{x}_{\mathrm{case1}}$ has a short time period of unspecified modes, i.e., modes which do not occur in the reference, which due to its short time interval is not visible in this figure. One can notice this short time interval by the disjoint red dot at $||\boldsymbol{x}_{\mathrm{case1}}(t \approx 1)|| \approx 7$.

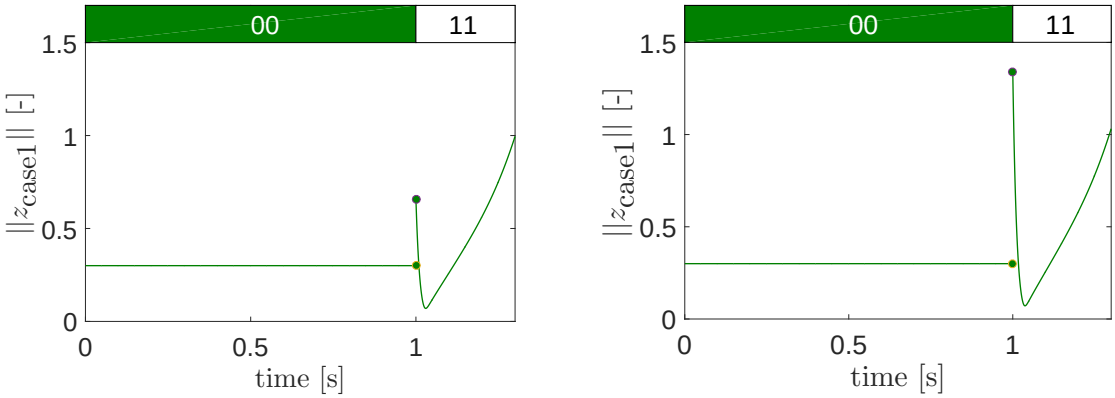

(a) Correct jump gain ${}^{11\leftarrow 01\leftarrow 00}\boldsymbol{G}(\tau)$. (b) Incorrect jump gain ${}^{11\leftarrow 10\leftarrow 00}\boldsymbol{G}(\tau)$.

Figure 5.10: Numerical experiments results of the Euclidean norm of $\boldsymbol{z}_{\text{case1}}$ (a) for correct jump gain (b) for incorrect jump gain.

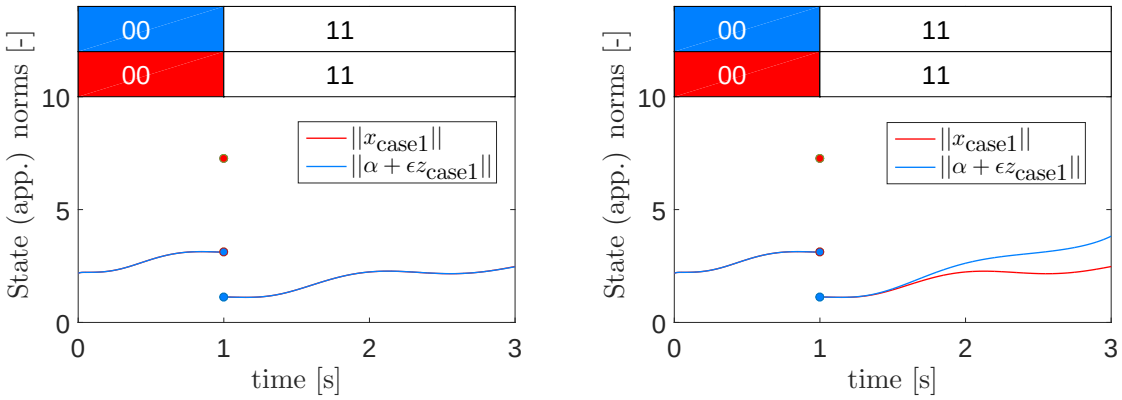

(a) Correct jump gain ${}^{11\leftarrow 01\leftarrow 00}\boldsymbol{G}(\tau)$. (b) Incorrect jump gain ${}^{11\leftarrow 10\leftarrow 00}\boldsymbol{G}(\tau)$.

Figure 5.11: Numerical experiment result of the comparison between the mechanical system $\boldsymbol{x}_{\text{case1}}$ (red line) and its approximation $\boldsymbol{\alpha} + \epsilon \boldsymbol{z}_{\text{case1}}$ (red line) with $\epsilon = 0.01$ for correct jump gain.

We further investigate the accuracy of the first-order error approximation $\epsilon \boldsymbol{z}_{\text{case1}}$ under influence of a correct jump gain. We compare the error terms $||\boldsymbol{x}_{\text{case1}} - \bar{\boldsymbol{\alpha}}||$ against $||\epsilon \boldsymbol{z}_{\text{case1}}||$ for a range of ϵ-values (and thus determine how big the error $||\boldsymbol{x}_{\text{case1}} - \bar{\boldsymbol{\alpha}}||$ can become before $||\epsilon \boldsymbol{z}_{\text{case1}}||$ is unable to provide an accurate approximation). We visualize this comparison in Figure 5.12, where we plot $||\epsilon \boldsymbol{z}_{\text{case1}}||$ (the dashed lines) and $||\boldsymbol{x}_{\text{case1}} - \bar{\boldsymbol{\alpha}}||$ (the solid lines) at different time instances against ϵ. Four time instances are considered: (1) just before the impact at $t = 0.8$ seconds (2) just after impact at $t = 1.2$ seconds (3) after short contact flow at $t = 1.8$ seconds (4) after long contact flow at $t = 3$ seconds. These four instances are shown as they each show different system contributions. At the first time instant, only the airborn flow has contributed. By inspecting the results at t = 1.2 seconds, the contribution of the jump gain to the approximation can be identified. In the results at $t = 1.8$ seconds, we can identify the effects of the contact flow for a relatively short time instance. At the end of the motion, we identify the effects of the contact flow for a relatively long time instance.

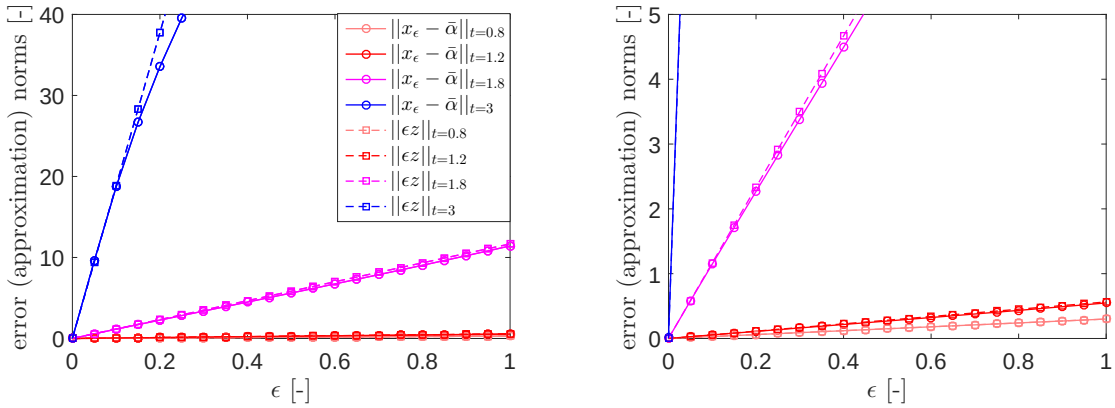

(a) Error norm range from 0 to 40.

(b) Error norm range from 0 to 5.

Figure 5.12: Numerical experiment results of $||\boldsymbol{x}_{\text{case1}} - \bar{\boldsymbol{\alpha}}||$, depicted as the solid lines, and $||\epsilon \boldsymbol{z}_{\text{case1}}||$, depicted as dashed lines and derived from correct jump gain, taken at time instances (1) $t = 0.8$ s in beige (2) $t = 1.2$ s in red (3) $t = 1.8$ s in magenta (4) $t = 3$ s in blue.

Before and just after impact (beige and red lines), one can see in Figure 5.12(b) that the solid and dashed lines coincide well for the whole range of $0 \leq \epsilon \leq 1$. One can make similar figures as Figure 5.11(a) till t=1.2 seconds and determine that the two state trajectories coincide for the whole range of ϵ-values. Looking at the short contact flow effects (the magenta line), one can determine divergent behavior between the solid and dashed lines in Figure 5.12(b) from $\epsilon \approx 0.15$ onwards. Note that the two trajectories are, however, still seemingly close, as seen in Figure 5.12(a), and will still show coinciding trajectories when comparing the state terms $||\boldsymbol{x}_{\text{case1}}||$ against $||\boldsymbol{\alpha} + \epsilon \boldsymbol{z}_{\text{case1}}||$. This point of divergence, i.e., at $\epsilon \approx 0.15$, may be seen as the point where higher-order error terms take over. Looking at the long term flow effect (blue line), one can see that from $\epsilon = 0.15$ onwards the two trajectories show different values. Figure 5.13 depicts this also, where in (a) the ϵ is small enough to still let the two trajectories coincide, while in (b) the two trajectories do not coincide at the end of the motion. Note that this conclusion may not hold for longer time durations than $t = 3$ seconds. Although the trajectories in Figure 5.13(a) do seem to coincide at first sight, one will notice when zooming in that the trajectories show signs of diverging from each other at $t = 3s$. When the error grows large enough where the higher-order error terms play a role, the two trajectories will not coincide anymore. We thus determine that the positive homogenization for our left-impacting case can be used to provide first-order error approximations as long as the perturbation is sufficiently small.

Second case : complex perturbation with a right-contact impact first

A similar analysis as above is performed, but now for a right-impacting case. Furthermore, a more *complex* initial perturbation is considered to simultaneously show how the positive homogenization performs in more challenging cases. To do so, we choose an arbitrary initial perturbation direction with the same norm as $\boldsymbol{z}_{\text{case1}}(t_0)$, resulting in

$$\boldsymbol{z}_{\text{case2}}(t_0) = -\big(0.0216, \quad 0.1384, \quad 0.1538, \quad 0.1551, \quad 0.0166, \quad 0.0473, \quad 0.1074, \quad 0.0929\big), \tag{5.28}$$

which causes a mechanical system with initial state $\boldsymbol{x}_{\text{case2}}(t_0) = \boldsymbol{\alpha}(t_0) + \epsilon \boldsymbol{z}_{\text{case2}}(t_0)$ to impact at its right corner point first (as concluded via numerical simulations). The trajectories $\boldsymbol{z}_{\text{case2}}$ for both correct and incorrect jump gains are depicted in Figure 5.14 and now also show different outcomes post-jump. What is notable in comparison to Figure 5.10, is that the pre-jump norm is not constant and that the post-jump norm increases at a much greater rate. Apart from the velocity and position perturbations of the block, a part of these differences is also due to a perturbation on the

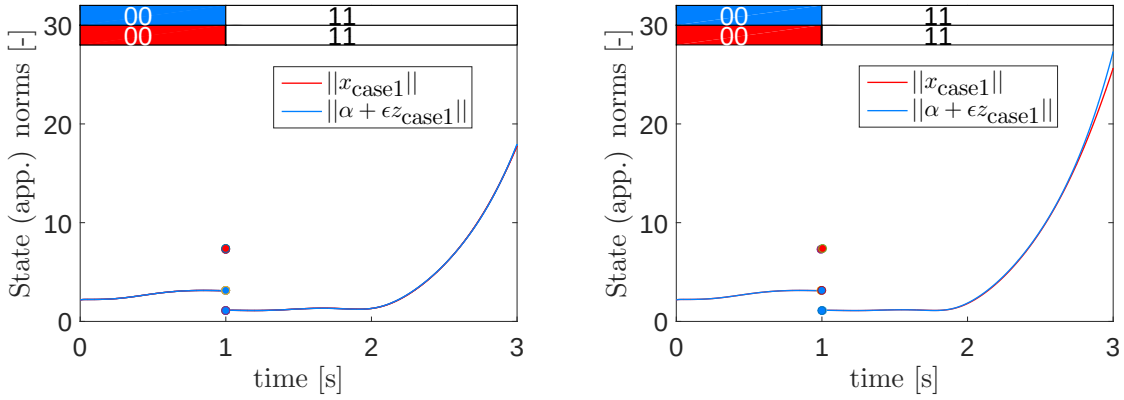

(a) $\epsilon = 0.1$. (b) $\epsilon = 0.15$.

Figure 5.13: Numerical experiment results of the comparison between $||\boldsymbol{x}_{\text{case1}}||$ (red line) and $||\boldsymbol{\alpha} + \epsilon \boldsymbol{z}_{\text{case1}}||$ (blue line) for (a) $\epsilon = 0.1$ and (b) $\epsilon = 0.15$.

plank via $z_\phi(t_0) \neq 0$ and $z_{\dot{\phi}}(t_0) \neq 0$. The plank develops differently due to the different spring and damping forces, and consequently the local coordinates experience greater changes. Subsequently, this plank perturbation influences the eventual angle at which the block will impact the plank, and thus the feedforward does not achieve its desired effect (as the feedforward is designed with a particular plank and block configuration in mind).

Before determining the accuracy of the first-order error approximation $\epsilon \boldsymbol{z}_{\text{case2}}$, we show in Figure 5.15 the influence of using a correct and incorrect jump gain. We observe that even using a small ϵ value of 0.0005 does not let the two trajectories coincide in the case of using an incorrect jump gain (Figure 5.15(b)). Note that the first-order error approximation (in the case of a correct jump gain) is accurate for much smaller ϵ-values than in the previous case. This is also seen further below.

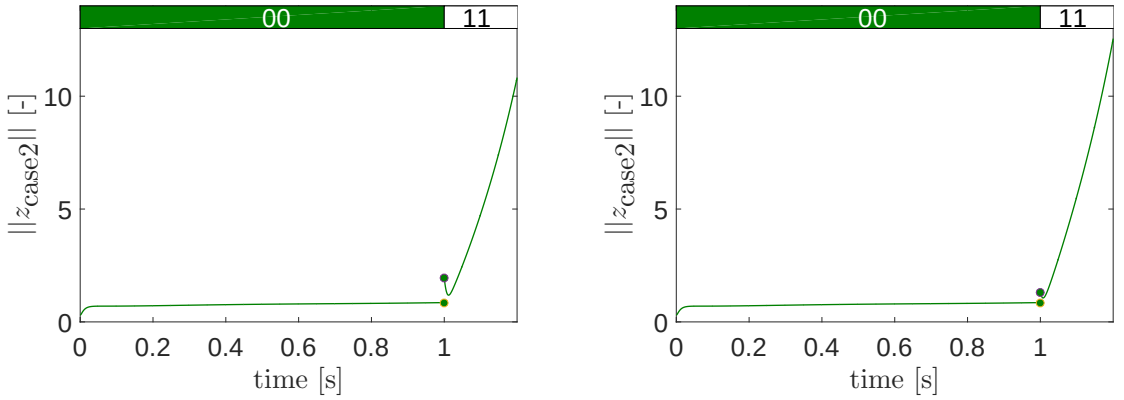

(a) Correct jump gain ${}^{11\leftarrow 10\leftarrow 00}\boldsymbol{G}(\tau)$. (b) Incorrect jump gain ${}^{11\leftarrow 01\leftarrow 00}\boldsymbol{G}(\tau)$.

Figure 5.14: Numerical experiment results of the Euclidean norm of $\boldsymbol{z}_{\text{case2}}$ (a) for correct jump gain (b) for incorrect jump gain.

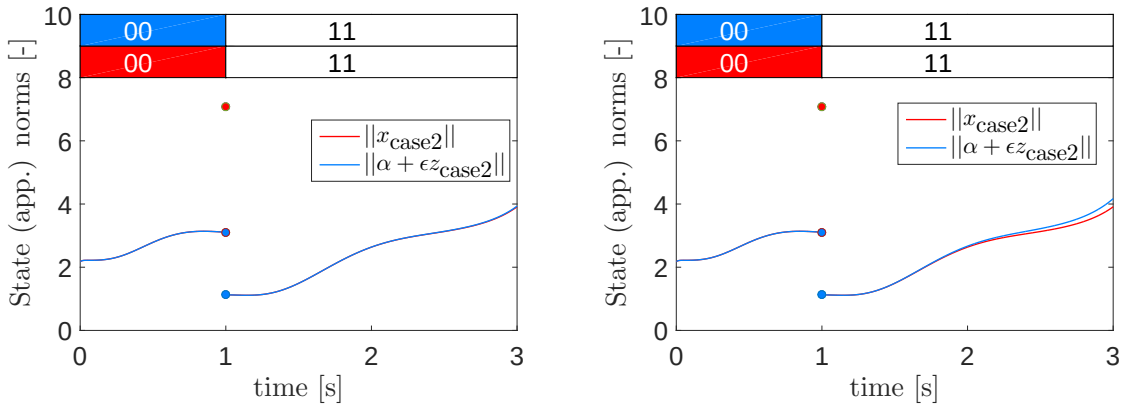

(a) Correct jump gain ${}^{11\leftarrow 10\leftarrow 00}\boldsymbol{G}(\tau)$.

(b) Incorrect jump gain ${}^{11\leftarrow 01\leftarrow 00}\boldsymbol{G}(\tau)$.

Figure 5.15: Numerical experiments results of the comparison between the mechanical system $\boldsymbol{x}_{\text{case2}}$ (red line) and its approximation $\boldsymbol{\alpha} + \epsilon \boldsymbol{z}_{\text{case2}}$ (blue line) with $\epsilon = 0.0005$ for correct jump gain.

In Figure 5.16, we plot $||\boldsymbol{x}_{\text{case2}} - \bar{\boldsymbol{\alpha}}||$ and $||\epsilon \boldsymbol{z}_{\text{case2}}||$ at four time instances against ϵ, similarly as Figure 5.12. We consider the same four time instances $t = 0.8s$ (beige), $t = 1.2s$ (red), $t = 1.8s$ (magenta), and $t = 3s$ (blue). Comparing Figure 5.16(a) to Figure 5.16(b) shows interesting differences. The most notable one, is that the first-order error approximation is only able to capture the real error effects for much smaller ϵ-values and much earlier time instances (seen by the red lines diverging from each other) than the previous case. This is not surprising when consulting Figure 5.14(a). As $\boldsymbol{z}_{\text{case2}}$ is related to the first-order error terms, we expect that a fast increment of $||\epsilon \boldsymbol{z}_{\text{case2}}||$ similarly lead to a fast increment of the real error norm $||\boldsymbol{x}_{\text{case2}} - \bar{\boldsymbol{\alpha}}||$. When the real error term becomes too big, then the higher-order error terms take over and the first-order approximation can not capture its effects. A small ϵ is then needed to let the real error term stay sufficiently small. One can see in Figure 5.16(b) that an ϵ till approximate 0.002 only gives accurate first-order error approximations for the whole time-interval, which is considerably smaller than the previous case. We thus conclude that the positive homogenization can also be used for the right-impacting case to provide accurate error approximations, as long as the real error term is sufficiently small. Furthermore, we conclude that the different initial perturbations influences the extent to how accurate the positive homogenization is.

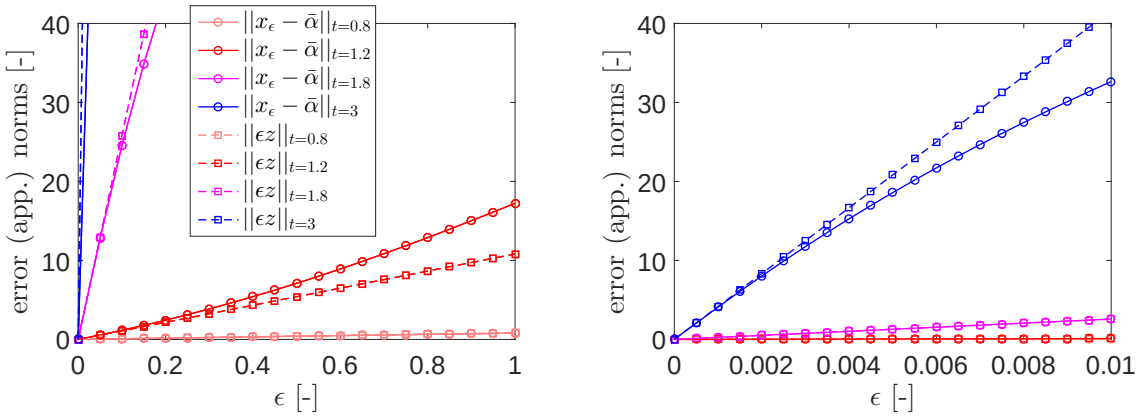

(a) ϵ range from 0 to 1.

(b) ϵ range from 0 to 0.01.

Figure 5.16: Numerical experiment results of $||\boldsymbol{x}_{\text{case2}} - \bar{\boldsymbol{\alpha}}||$, depicted as the solid lines, and $||\epsilon \boldsymbol{z}_{\text{case2}}||$, depicted as dashed lines and derived from correct jump gain, taken at time instances (1) $t = 0.8$ s in beige (2) $t = 1.2$ s in red (3) $t = 1.8$ s in magenta (4) $t = 3$ s in blue.

5.4 Closed loop

We now determine whether the closed-loop positive homogenization can be used to predict the (local) behavior of our closed-loop mechanical system. The control input (3.15) and (3.16) with either (3.18) or (3.19) is applied to steer the plank-block to the reference trajectory, and the local version $\boldsymbol{v} = -\boldsymbol{K}\boldsymbol{z}$, see (4.53), is applied to the positive homogenization. The feedback gain $\boldsymbol{K}$ is decomposed in a gain, mapping the local error to forces and torques in the corresponding directions, and a mapping between these *local* inputs and the so-called global inputs $\boldsymbol{u}$. We introduce the feedback gains for free and constrained motion,

$$
\begin{aligned}
{}^{00}\boldsymbol{K}_l &= \begin{pmatrix} K_{p,\mathrm{x}_l} & 0 & 0 & 0 & K_{d,\mathrm{x}_l} & 0 & 0 & 0 \\ 0 & K_{p,\mathrm{y}_l} & 0 & 0 & 0 & K_{d,\mathrm{y}_l} & 0 & 0 \\ 0 & 0 & K_{p,\theta_l} & 0 & 0 & 0 & K_{d,\theta_l} & 0 \end{pmatrix}, \\
{}^{11}\boldsymbol{K}_l &= \begin{pmatrix} K_{p,\mathrm{x}_l} & 0 & K_{d,\mathrm{x}_l} & 0 \\ 0 & K_{p,\phi} & 0 & K_{d,\phi} \\ 0 & 0 & 0 & 0 \end{pmatrix},
\end{aligned}
\tag{5.29}
$$

respectively, with constant gains $K_{p,\cdot}$ and $K_{d,\cdot}$. The closed-loop input, as in (5.20), is then given by

$$
\begin{aligned}
{}^{00}\boldsymbol{v} &= -\begin{pmatrix} -\cos(\phi_{ref}) & -\sin(\phi_{ref}) & 0 \\ \sin(\phi_{ref}) & \cos(\phi_{ref}) & 0 \\ 0 & 0 & 1 \end{pmatrix} {}^{00}K_l \, {}^{00}\boldsymbol{z}, \\
{}^{11}\boldsymbol{v} &= -\begin{pmatrix} -\frac{(l_B+l_P)\sin(\phi_{ref}) - 2\mathrm{X}_{l,ref}\cos(\phi_{ref})}{2\mathrm{X}_{l,ref}} & -\frac{\sin(\phi_{ref})}{\mathrm{X}_{l,ref}} & 0 \\ \frac{(l_B+l_P)\cos(\phi_{ref}) + 2\mathrm{X}_{l,ref}\sin(\phi_{ref})}{2\mathrm{X}_{l,ref}} & \frac{\cos(\phi_{ref})}{\mathrm{X}_{l,ref}} & 0 \end{pmatrix} {}^{11}K_l \, {}^{11}\boldsymbol{z},
\end{aligned}
\tag{5.30}
$$

with

$$
{}^{11}\boldsymbol{z} = \begin{pmatrix} z_{\mathrm{x}_l} \\ z_\phi \end{pmatrix}. \tag{5.31}
$$

More detail about (5.30) can be found in appendix F. For the following analysis, we consider feedback gains that result in uniform asymptotic stability of our local model, see Defintion 4.3. We then, for instance, investigate how well the state $\boldsymbol{z}$ approximates the error $\boldsymbol{x} - \bar{\boldsymbol{\alpha}}$ in closed-loop.

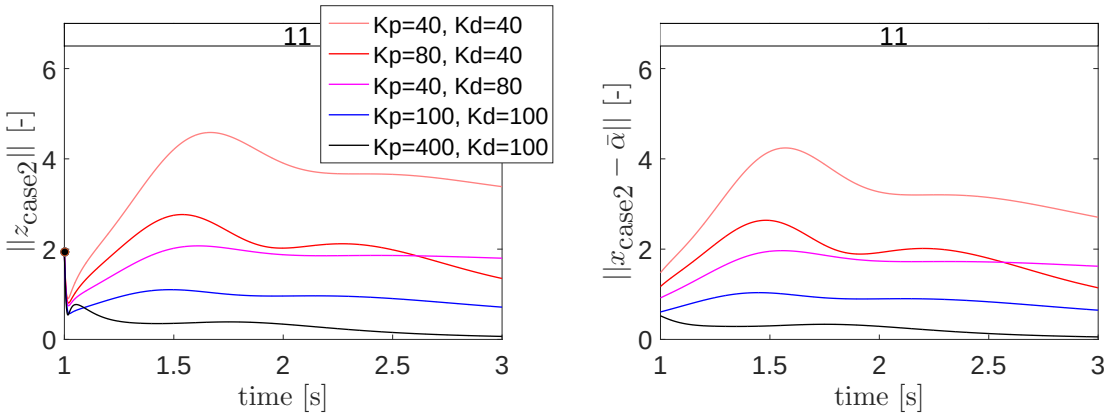

(a) Closed-loop positive homogenization $||\boldsymbol{z}_{\text{case2}}||$.

(b) Closed-loop error trajectory $||\boldsymbol{x}_{\text{case2}} - \bar{\boldsymbol{\alpha}}||$.

Figure 5.17: Numerical experiment results of the constrained motion norm development of the error as (a) $||\boldsymbol{z}_{\text{case2}}||$ and (b) $||\boldsymbol{x}_{\text{case2}} - \bar{\boldsymbol{\alpha}}||$. Free motion feedback gain is set to zero, and constrained motion feedback gain is set with the corresponding feedback gains in the legend. Here, the same feedback gain is used for all coordinates, such that, for instance, $K_{p,\text{x}_l} = K_{p,\phi} = K_p$ for ${}^{11}\boldsymbol{K}_l$ in (5.29).

First case: right contact impact first and earlier impact time

We now analyze how closed-loop gains influence the positive homogenization and mechanical system for a perturbation leading to a right-contact impact sequence and an impact time(s) before the nominal impact time. We consider the initial perturbation direction of $\boldsymbol{z}_{\text{case2}}(t_0)$, see (5.28), and set the closed-loop gains for free motion phase to zero, i.e., ${}^{00}\boldsymbol{K}_l = \boldsymbol{0}^{3\times 8}$. The latter is done to avoid the scenario where the system has already almost converged before impact, whereas the main novelty in the local approximation lies in its description of the impact phenomena. Note that by taking the free motion feedback gain equal to zero, the control strategy for these unspecified modes also reduces to just using (3.18).

Figure 5.17(a) depicts the constrained motion closed-loop trajectory of the positive homogenization and in a legend the corresponding constrained motion feedback gains. These feedback gains are the same for all coordinates, such that, for instance, $K_{p,\text{x}_l} = K_{p,\phi} = K_p$ for ${}^{11}\boldsymbol{K}_l$ in (5.29). Note that as we set the free motion closed-loop gains to zero, it is not interesting to depict the free motion part of the trajectory. Furthermore, the open-loop case can be seen in Figure 5.14(a) and in it, the constrained motion norm grows in an unbounded manner. We can observe that applying feedback thus prevents this unbounded growth. Furthermore, one observes that the positive homogenization seems to be uniform asymptotically stable.

Figure 5.17(b) depicts the closed-loop error term of the mechanical system. Remind that $\boldsymbol{x}_{\text{case2}}$ is simulated with an initial condition $\boldsymbol{x}_{\text{case2}}(t_0) = \boldsymbol{\alpha}(t_0) + \epsilon \boldsymbol{z}_{\text{case2}}$. We consider $\epsilon = 1$ and use the same constrained motion feedback terms as in the legend of Figure 5.17(a). We depict the trajectories in the same time-interval as to make the comparison between the two figures more intuitive. Note that the real error trajectory jumps at approximately 0.8439 seconds and 0.8981 seconds, and that Figure 5.17(b) does not depict the full trajectory in constrained motion.

One can see that Figure 5.17(a) and Figure 5.17(b) show similar results in closed-loop. This is interesting, as the positive homogenization, flowing in modes 00 and mode 11, experiences a jump at t=1s, while the error trajectory, flowing in mode 00, mode 10, and mode 11, experiences two jumps at t=0.8439s and t=0.8981s. Apparently, the positive homogenization can still approximate

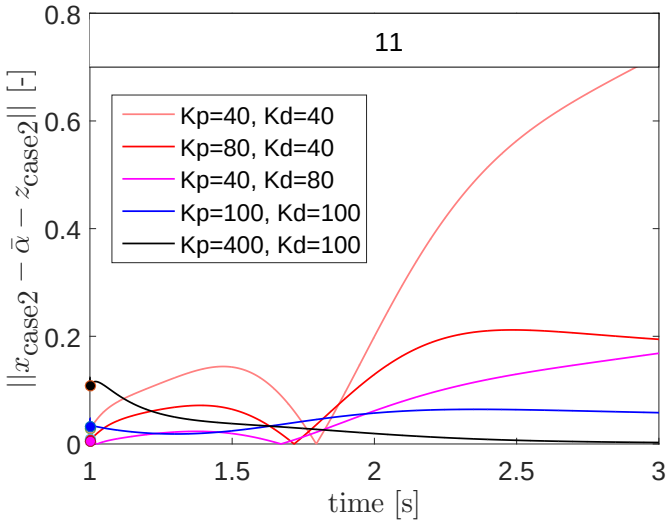

Figure 5.18: Numerical experiment results of the error accuracy by depicting the constrained motion norm of $||\boldsymbol{x}_{\text{case2}} - \bar{\boldsymbol{\alpha}} - \epsilon \boldsymbol{z}_{\text{case2}}||$. The free motion feedback gains are set to zero and the constrained motion feedback gains are formulated in the legend. These gains are the same for all coordinates.

the error trajectory well, even though it has a mismatch of jumps. Consequently, this may indicate that the positive homogenization can be used to give insight of trajectory tracking capabilities. To determine how well the positive homogenization approximates the error trajectory, we further evaluate $||\boldsymbol{x}_{\text{case2}} - \bar{\boldsymbol{\alpha}} - \epsilon \boldsymbol{z}_{\text{case2}}||$ for which a smaller value correlates with greater accuracy. Figure 5.18 depicts this, in which we similarly depict the trajectory past $t = 1$ seconds. One observes that the red, blue, and black lines converge to 0, indicating that the positive homogenization may be more accurate over time, whereas the beige and magenta lines seem to go away from zero, indicating that the positive homogenization may not be able to accurately approximate the real error in the near future. Note that for smaller perturbation parameters ϵ, we stil get similar plots where the beige and magenta line diverge from zero.

The positional error terms of the beige lines are depicted in Figure 5.19. Note that extra plots of the beige and magenta lines of Figure 5.17 are seen in Appendix F.4. From it, one observes that the positively homogeneous trajectory and error trajectory are not equal. Inspecting Figure 5.17, one observes that both trajectories still converge to zero, but that the rate of convergence differs. In this case, the real error trajectory converges faster to zero than our local model, as also seen for the positional error term in Figure 5.19. This may be due to the error trajectory being influenced by the constrained motion feedback gains much earlier than the positive homogenization, as the error trajectory finalizes its transition at approximately 0.9 seconds. Nonetheless, both the positively homogeneous trajectory and error trajectory seem to converge to zero, such that we still suspect that when the positive homogenization is uniform asymptotically stable, that we achieve trajectory tracking for our mechanical system.

Adding feedback thus allows the positive homogenization to provide accurate approximations of the system response for a significantly larger domain of initial conditions. To clarify this, we take the worst performing feedback gain of Figure 5.18, i.e., $K_p = 40$ and $K_d = 40$, and make a similar plot as Figure 5.16. For convenience, we plotted the open-loop case in Figure 5.20(a) and the closed-loop case in Figure 5.20(b). We now see an improvement in how well the approximation describes the mechanical system, as the solid and dashed lines coincide over a larger range of ϵ values, namely till $\epsilon \approx 0.3$ in comparison with the open-loop $\epsilon \approx 0.002$. Looking at the magenta

and blue lines, i.e., at time values 1.8 seconds and 3 seconds, one can notice that the solid lines are below the dashed lines. The norm of the error trajectory is thus lower than our first-order approximated error norm $\epsilon \boldsymbol{z}$. This complies with the conclusion derived above, in which we stated that the real error trajectory converges faster to zero than our approximated error trajectory. Knowing that our approximated error norm indicates to be uniform asymptotically stable, one may determine to have achieved trajectory tracking for our mechanical system for the considered perturbation.

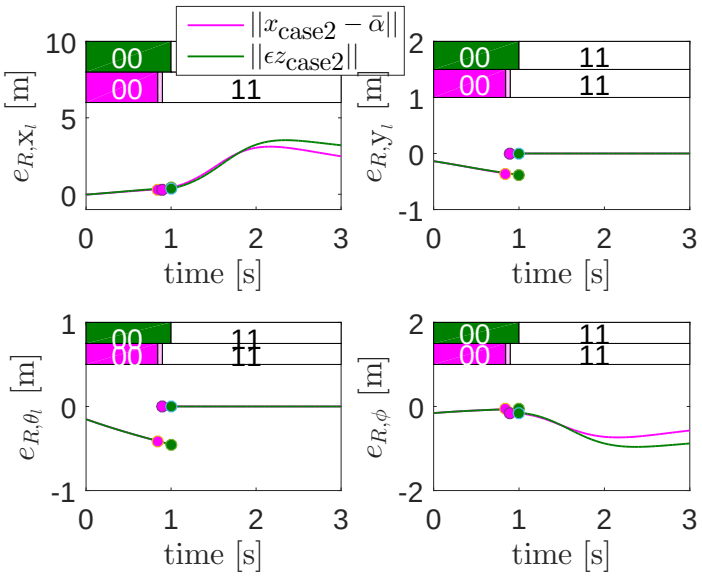

Figure 5.19: Numerical experiments results of the position trajectories of the beige lines in Figure 5.17. The green trajectory represents the closed-loop positive homogenization, and the magenta trajectory the closed-loop error trajectory.

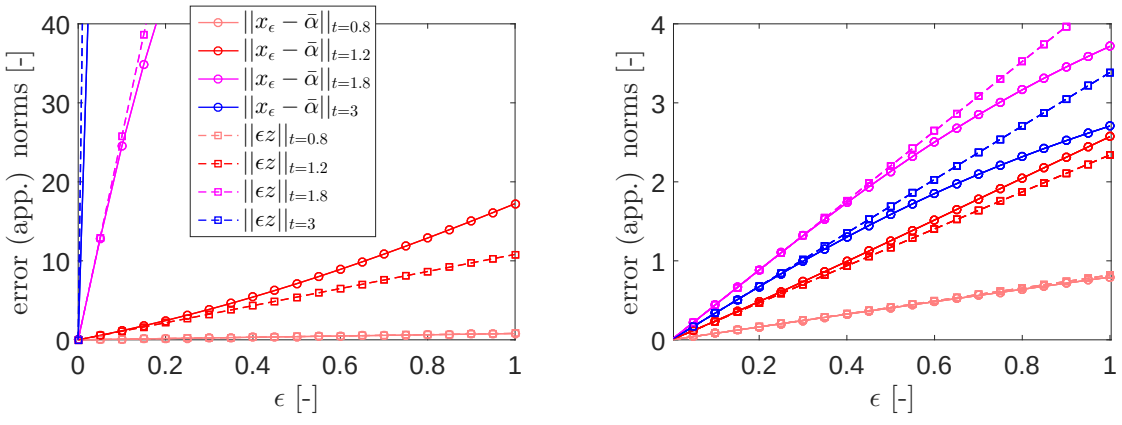

(a) Open loop.

(b) Closed-loop.

Figure 5.20: Numerical experiment results of $||\boldsymbol{x}_{\text{case2}} - \bar{\boldsymbol{\alpha}}||$, depicted as the solid lines, and $||\epsilon \boldsymbol{z}_{\text{case2}}||$, depicted as dashed lines, for open- and closed- loop conditions, taken at time instances (1) $t = 0.8$ s in beige (2) $t = 1.2$ s in red (3) $t = 1.8$ s in magenta (4) $t = 3$ s in blue. The free motion feedback gain is set to zero, and the constrained motion feedback gain is chosen to be $K_p = 40$ and $K_d = 40$ over all coordinates.

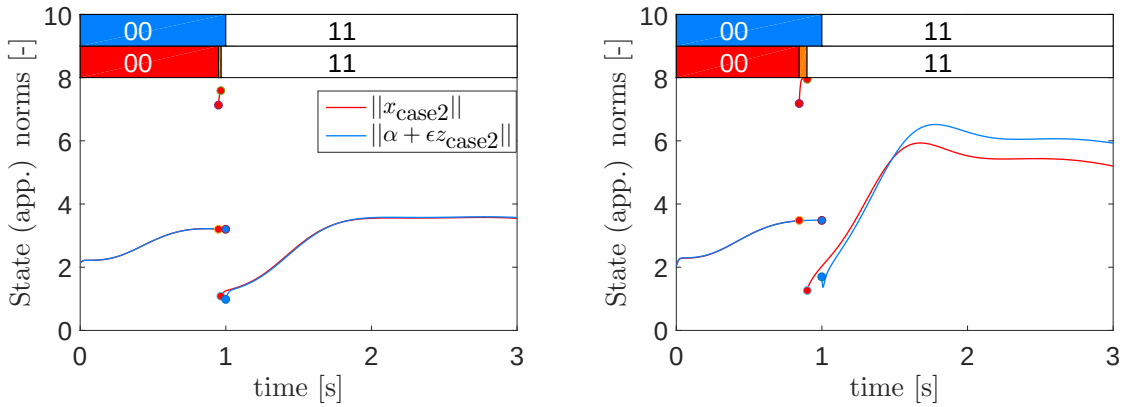

(a) Closed-loop with initial perturbation $\epsilon = 0.3$.

(b) Closed-loop with initial perturbation $\epsilon = 1$.

Figure 5.21: Numerical experiment results of the comparison between the state trajectory $\boldsymbol{x}_{\text{case2}}$ (red line) and its approximation $\boldsymbol{\alpha} + \epsilon \boldsymbol{z}_{\text{case2}}$ (blue line) in closed-loop with free motion feedback gain set to zero and constrained motion feedback gain $K_p = 40$ and $K_d = 40$.

To end this case, we visualize how the state trajectory of the mechanical system develops when applying this constrained motion feedback gain of $K_p = 40$ and $K_d = 40$ for an initial perturbation of $\epsilon = 0.3$ and an initial perturbation of $\epsilon = 1$. Note that the free motion feedback gain is still set to zero. Figure 5.21 depicts the two closed-loop trajectories for these different perturbations. We focus first on Figure 5.21(a), which according to Figure 5.20 should give an accurate approximation. One can observe that the real state trajectory $\boldsymbol{x}_{\text{case2}}$ (the red line) experiences two jumps, while the positively homogeneous approximated state trajectory $\boldsymbol{\alpha}+\epsilon\boldsymbol{z}_{\text{case2}}$ (blue line) jumps only once at the nominal event time. This is also visible in the horizontal bars above, for which the red trajectory has an extra orange block that indicates the duration of the unspecified mode. During this unspecified mode, one notices that $||\boldsymbol{\alpha} + \epsilon \boldsymbol{z}_{\text{case2}}||$ is not capable of providing accurate descriptions of the state trajectory $\boldsymbol{x}_{\text{case2}}$. This is intended, as we want to ignore this phase in the positive homogenization. One notices, that despite the fact that the positively homogeneous approximation lumps both impacts into one jump, that the response after the full impacting event is still very well described. The positive homogenization can thus describe the system locally very well. In Figure 5.21(b), an example with a bigger initial perturbation is treated, and one can observe that the positive homogenization is less capable of approximating the local system behavior. One can, however, still see that the trajectories show somewhat similar behavior. For the case considered here, we thus validate that if the perturbation is sufficiently small, that the positive homogenization can provide accurate estimates of the system behavior also in closed-loop.

Second case: left contact impact first and later impact time

The perturbations considered above all lead to the mechanical system impacting before the nominal event time. We now analyze how well the positive homogenization performs for situations where the mechanical system impacts at a later time instance than the nominal event time. The initial pertubation direction is

$$\boldsymbol{z}_{\text{case3}} = \begin{pmatrix} 0.1 & 0.2 & 0.3 & 0 & 0.05 & 0.1 & 0.2 & 0 \end{pmatrix}, \tag{5.32}$$

which via numerical simulations result in the mechanical system impacting at a later time instance and furthermore experiencing a left-impact sequence. Note that we deduce $\boldsymbol{x}_{\text{case3}}$ with an initial condition $\boldsymbol{x}_{\text{case3}}(t_0) = \boldsymbol{\alpha}(t_0) + \epsilon \boldsymbol{z}_{\text{case3}}$. We consider no perturbation on the plank, what is expected to result in less control effort to achieve uniform asymptotic stability of the positive homogenization and, possibly, trajectory tracking of the mechanical system. In the following, a similar

analysis is performed as for the previous case.

The free motion feedback gains are set to zero again, and similar constrained motion feedback gains are considered as for the previous case. Figure 5.22(a) illustrates the closed-loop trajectory of the positive homogenization and Figure 5.22(b) the closed-loop error trajectory of the mechanical system with a perturbation parameter $\epsilon = 1$. Notice that the error trajectory jumps according to $\boldsymbol{x}_{\text{case3}}$, and one can see jumps occuring at a later time instance than the nominal event time, i.e., at t=1.0515s and t=1.1253s. Note that for the error trajectory, the constrained motion feedback gain is thus only applied after the final jump has been determined, i.e., after $t = 1.1253$s. An initial perturbation with $\epsilon = 1$ is taken, and one can see that even in this case the positive homogenization can approximate the error trajectory well. One furthermore notices that less control effort is needed to reduce the error when compared to Figure 5.17. We think that a huge part of this is due to the plank perturbations. Considering the previous case, we could set the plank perturbations of $\boldsymbol{z}_{\text{case2}}$ to 0, i.e., $z_\phi = 0$ and $z_{\dot{\phi}} = 0$. In that instance, Figure 5.17(a) would change in one where the constrained motion feedback $K_p = 40$ and $K_d = 40$ results in a similar performance as the current black trajectory depicted in it. Returning to this case, we could also add a perturbation of $z_\phi = 0.1$ to $\boldsymbol{z}_{\text{case3}}$ which changes the closed-loop trajectory of the positive homogenization with constrained motion feedback $K_p = 40$ and $K_d = 40$ to end up at a value of 1.8. Changing other perturbations, e.g., $z_{\theta_l} = 0.4$, does not have such a great impact on the error trajectory.

To determine the approximation accuracy, we plot the trajectories of $||\boldsymbol{x}_{\text{case3}} - \bar{\boldsymbol{\alpha}} - \epsilon \boldsymbol{z}_{\text{case3}}||$ in which we set ϵ to 1. Figure 5.23 depicts this, in which we only visualize the part after the final jump, i.e., after $t = 1.1253s$. This is done, as we assume that the approximation is not accurate during the interval of unspecified mode, and thus does not give any further insight. One notices that the approximation is quite accurate for all feedback terms. We also notice that high K_p value result in better approximations. This is not surprising, as the plank position influences the performance of the feedforward considerably. We then achieve the same conclusion as for the previous case, that uniform assymptotic stability of our positive homogenization seems to indicate trajectory tracking of our mechanical system for the considered perturbation.

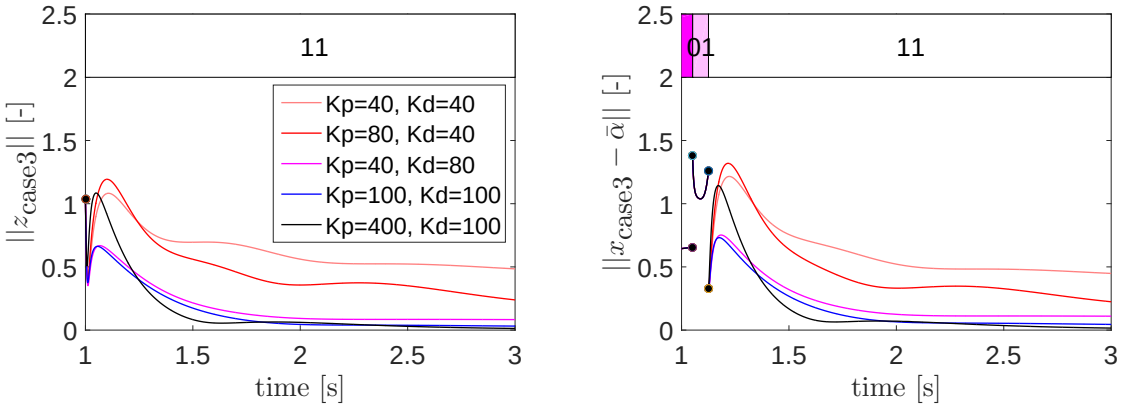

(a) Closed-loop positive homogenization.

(b) Closed-loop mechanical system error trajectory.

Figure 5.22: Numerical experiment result of the closed-loop trajectories of the positive homogenization (a) and mechanical system (b) with a perturbation direction $\boldsymbol{z}_{\text{case3}}$. The free motion feedback gains are set to zero, and the constrained motion feedback gains are mentioned in the legend. The mechanical system is simulated with a perturbation of $\epsilon = 1$.

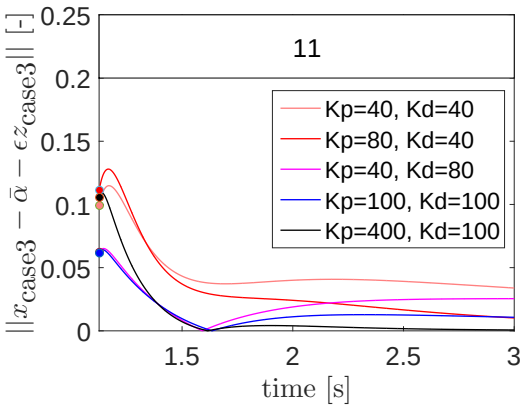

Figure 5.23: Numerical experiment results of the error accuracy by depicting the constrained motion norm of $||\boldsymbol{x}_{\text{case3}} - \bar{\boldsymbol{\alpha}} - \epsilon \boldsymbol{z}_{\text{case3}}||$. The free motion feedback gains are set to zero, and the constrained motion feedback gains are formulated in the legend. These gains are the same for all coordinates.

We thus make the following conjecture:

Conjecture 5.1 *For the cases considered in this work, simulation results seem to show that uniform asymptotic stability of the positive homogenization indicates trajectory tracking of the nonlinear state-triggered hybrid system under influence of RS control. In [16], this is proven for the single impact case. We think that the theorem in [16] can be extended to be applicable for simultaneous impacting cases.*

One also sees in this case that adding feedback allows the positive homogenization to provide more accurate approximations of the system response for a significantly larger domain of initial conditions. We clarify this with Figure 5.24 in which the error terms are compared at several time instances against ϵ. These time instances are taken again at $t = 0.8s$, t=1.2s, t=1.8s, and t=3s. One can see the open-loop case in Figure 5.24(a) and the closed-loop case in Figure 5.24(b). For the closed-loop, the free motion feedback gain is set to zero, and the constrained motion feedback is set with a $K_p = 40$ and a $K_d = 40$. One observes that the closed-loop case is quite accurate over the whole range of ϵ-values.

We end this case similarly with an example of how the state and error trajectory would behave under the constrained motion feedback $K_p = 40$ and $K_d = 40$. Figure 5.25(a) depicts the state trajectories and Figure 5.25(b) the error trajectories. Both are simulated with an ϵ value of 1. One can notice how well the two trajectories coincide, even though the two trajectories jump at different time instances. In Appendix F.4, we have furthermore provided plots of the Euclidean error and the reference spreading error $\boldsymbol{e}_R = \boldsymbol{x} - \bar{\boldsymbol{\alpha}}$ as used in this work, based on Figure 5.25(b). In it, one can observe that the Euclidean error indeed shows multiple jumps with much higher peaks, while the reference spreading error shows much more preferable behavior.

We have considered many situations for the closed-loop analysis, i.e., left-impact sequence, right-impact sequence, earlier impact time than the reference, and later impact time than the reference. All these cases showed that the RS control was able to provide trajectory tracking of the mechanical system, even when setting the free motion feedback gains to zero and using the same *low* performing constrained motion feedback gains $K_p = 40$ and $K_d = 40$. For the benchmark example considered in this work, the RS control can thus provide trajectory tracking, and additionally the positive homogenization can be used to design the tracking controller. We, however, did not determine how well the two unspecified mode strategies (3.18) and (3.19) perform. This is done next, as to conclude this chapter.

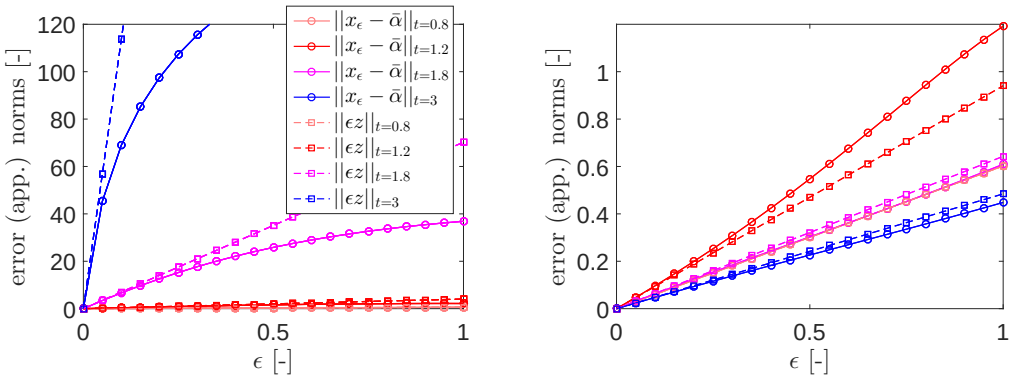

(a) Open-loop. (b) Closed-loop.

Figure 5.24: Numerical experiment results of $||\boldsymbol{x}_{\text{case3}} - \bar{\boldsymbol{\alpha}}||$, depicted as the solid lines, and $||\epsilon \boldsymbol{z}_{\text{case3}}||$, depicted as dashed lines, for open- and closed- loop conditions, taken at time instances (1) $t = 0.8$ s in beige (2) $t = 1.2$ s in red (3) $t = 1.8$ s in magenta (4) $t = 3$ s in blue. The free motion feedback gain is set to zero, and the constrained motion feedback gain is chosen to be $K_p = 40$ and $K_d = 40$ over all coordinates.

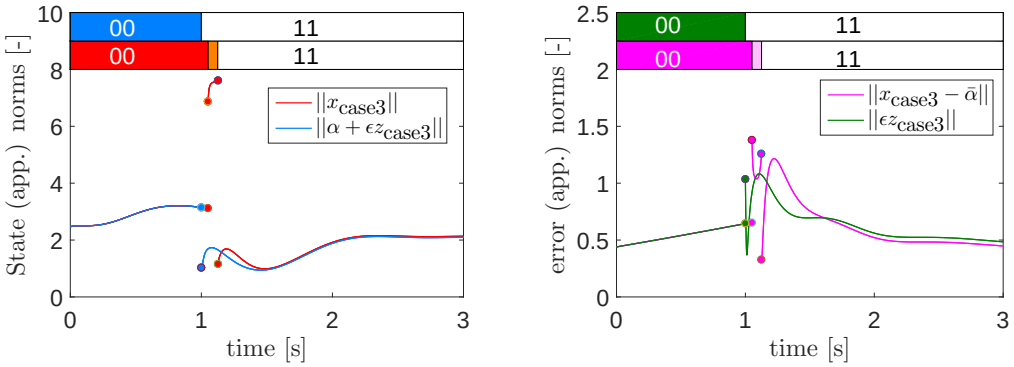

(a) Closed-loop state trajectories. (b) Closed-loop error trajectories.

Figure 5.25: Numerical experiment results of (a) the comparison between the state trajectory $\boldsymbol{x}_{\text{case3}}$ (red line) and its approximation $\boldsymbol{\alpha} + \epsilon \boldsymbol{z}_{\text{case3}}$ (blue line) in closed-loop, and (b) the comparison between the error trajectory $||\boldsymbol{x}_{\text{case3}} - \bar{\boldsymbol{\alpha}}||$ (pink line) and its approximation $||\epsilon \boldsymbol{z}_{\text{case3}}||$ (green line) in closed-loop. The free motion feedback gain is set to zero, and constrained motion feedback gain is set with $K_p = 40$ and $K_d = 40$.

RS control unspecified mode strategy

In Section 3.2.3, it was highlighted that the error is typically undefined during the short time interval of unspecified modes. We proposed two strategies for the control input during these unspecified modes, i.e., (3.18) and (3.19), as to improve performance. Both strategies use an extended version of the free motion feedforward term. The reasoning behind this, was that applying the free motion feedforward, designed to achieve impact, during unspecified modes, should only make the short sequence of unspecified modes go by faster. Now, it is shown how these two strategies influence the performance of RS control. As we did not treat feedback in the free motion phase, we were not able to compare the performance of these two unspecified mode strategies before.

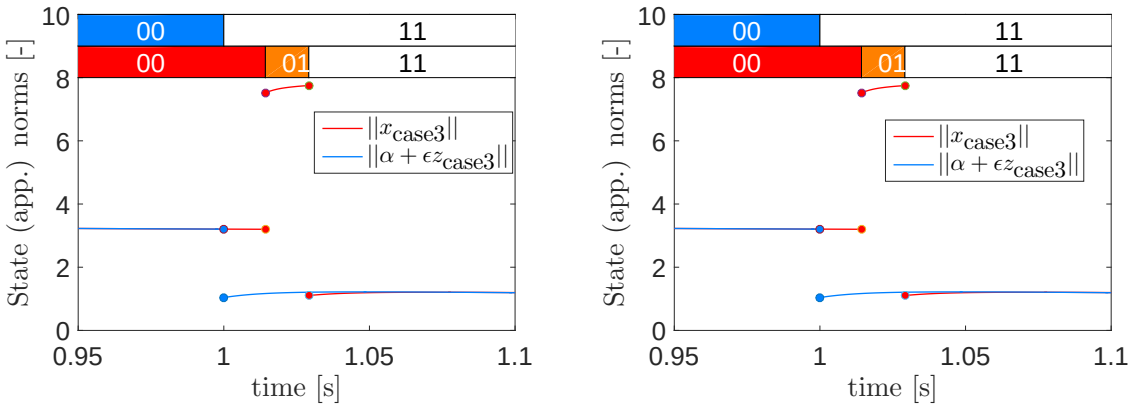

(a) Strategy 1: No feedback effort during unspecified modes.

(b) Strategy 2: keep the last determined free motion feedback term constant.

Figure 5.26: Numerical experiment results of the closed-loop state trajectory $\boldsymbol{x}_{\text{case3}}$ (red line) and its closed-loop approximation $\boldsymbol{\alpha} + \epsilon \boldsymbol{z}_{\text{case3}}$ (blue line) for an $\epsilon = 1$. The free motion feedback gain is valued with $K_p = 40$ and $K_d = 40$, and the constrained motion feedback also with $K_p = 40$ and $K_d = 40$. (a) depicts a RS control with the unspecified mode control input (3.18) and (b) depicts a RS control with the unspecified mode control input (3.19).

One strategy is to remove the feedback effort and only apply the feedforward term, which is depicted in Figure 5.26(a). The other strategy is to keep the last determined free motion feedback effort constant, which is seen in Figure 5.26(b). These two plots are created using an initial perturbation of $\epsilon \boldsymbol{z}_{\text{case3}}$ for an $\epsilon = 1$. The free motion feedback term is taken equal to the constrained motion feedback term, with $K_p = 40$ and $K_d = 40$. One notices that the two results of Figure 5.26 are indistinguishable. This could be due to the error being so small that the contribution of the closed-loop gain in (3.19) is negligible, as $-{}^{00}\boldsymbol{K}(t_1)({}^{00}\boldsymbol{x}_{\text{case3}}(t_1) - {}^{00}\tilde{\boldsymbol{\alpha}}(t_1)) = \begin{pmatrix} -0.1276, & -0.1383, & -0.0065 \end{pmatrix}^T$ with t_1 being the first impact time of the perturbed mechanical system. Taking into consideration that quite some control effort is needed to push the block, as seen from Figure 3.3, this result may not be so surprising. Lowering the plank stiffness and damping coefficient may, however, lead to a different result. Another reason may be the small time window of unspecified modes, where the feedback effort of (3.19) has no time to influence the system in a way that leads to a different outcome when applying (3.18) instead.

5.5 Summary

We have elaborated on the plank-block system that is used in this work and have derived a positive homogenization to approximate its dynamics near a chosen reference trajectory. We have shown that both in open- and closed- loop, the positive homogenization is able to provide accurate first-order approximations of the mechanical system responses. What was remarkable, was that the positive homogenization did so, while jumping differently than the perturbed mechanical system. This was only realizable due to the positive homogenization jumping with the conewise constant jump gain formulated in Chapter 4.

From the closed-loop analysis, we saw that uniform asymptotic stability of the positive homogenization might imply trajectory tracking of the mechanical system. At least for the benchmark example considered in this work, the positive homogenization can be used to derive a tracking controller, and the RS control can be used to achieve trajectory tracking.

Chapter 6

Conclusions and recommendations

6.1 Conclusions

We have concluded from Chapter 5 that the local approximation can be used to stabilize the plank-block system, thus giving a positive indication for the research objective mentioned in Section 1.5: *we may indeed be able to use the RS control and the positive homogenization to stabilize motions with simultaneous impact.* This conclusion has been reached by taking the following steps.

First, we formulated the dynamics of mechanical systems with unilateral constraints in Chapter 2. To do so, we used the theory of non-smooth mechanics and the generalized Newton's impact law to model inelastic impacts. A condition for avoiding superfluous impacts, depending on the mass and inertia properties of the system, and considering constraint equations, has subsequently been formulated. These contacts lead to rocking behavior of a mechanical system and are undesired due to the more complicated dynamics that arise. We then reformulated the mechanical system into a hybrid system framework to which we applied RS control.

Second, we introduced RS control for single guard activation in Chapter 3 and showed how it has been applied in literature as in [15, 16, 17, 18, 23, 24]. The notion of classical hybrid time (t, j) was introduced and extended for a multi-contact mechanical system, resulting in a multi-scale hybrid time (t, i, k). For this, we introduced a macro counter i, related to the nominal events, and micro counter k, related to the local events. The control strategy is then extended to the so-called RS control for simultaneous guard activation. Via a sensitivity analysis, the stability of trajectories with simultaneous impacts are analyzed and a tracking controller is designed.

Third, we performed the sensitivity analysis in Chapter 4 where we introduced new hybrid system notations to facilitate the presentation of the analysis. This sensitivity analysis resulted in a positively homogeneous time-triggered hybrid system, capable of describing the local behaviour of the mechanical system in a neighborhood of a reference trajectory with simultaneous inelastic impacts. One of the contributions of this work is then the extension of the sensitivity analysis, in which we incorporated the perturbed jumps and in-between flow effects of the multi-contact mechanical system into a conewise constant jump gain that describes the jumping behavior of the positive homogenization. As the mechanical system can undergo a different sequence of impacts for different perturbations, the conewise constant jump gain changes its shape accordingly to make the positive homogenization provide accurate first-order approximations of the mechanical system behavior. This is validated numerically for a plank-block system.

Finally, we introduced a plank-block system - chosen due to the interactive dynamics between the two bodies - in Chapter 5. A reference trajectory with simultaneous impact is formulated, for which the corresponding positive homogenization is derived. We then validated the performance

of the positive homogenization by verifying that it can provide accurate first-order approximations of the error dynamics of the mechanical system, given that the perturbations are sufficiently small. This is done both in open- and closed- loop conditions. for the given benchmark example and a given perturbation, we observed that uniform asymptotic stability of the positive homogenization indicates trajectory tracking of the mechanical system via RS control for simultaneous guard activation. Additionally, we observed that applying the RS control for simultaneous guard activation on the plank-block system indeed results in tracking control regardless of the perturbation, i.e., the different mode sequences that the mechanical system can undertake. This then indicates that the RS control for simultaneous guard activation and the underlying sensitivity analysis may indeed be used to achieve trajectory tracking for a mechanical system experiencing simultaneous inelastic impacts in general.

6.2 Recommendations

Many assumptions and simplifications of reality were made in composing a benchmark test-case in this work. It is therefore recommended to test the derived control strategy and perform the sensitivity analysis also for a more comprehensive multi-contact mechanical system that models reality more accurately. One can consider a 3-D model, in which the perturbed system could experience more than two jumps. Consequently, the conewise constant jump gain will get more complex, i.e., it consists of more constant jump gains. Determining whether this more complex conewise constant jump gain still gives accurate first-order approximations of the real perturbed jump and in-between flow dynamics, is an interesting experiment.

One can also consider to make the (impacting) environment more challenging. In this work, we have already extended the static flat impacting surface to a more dynamic flat impacting surface. A more interesting direction is then to consider non-flat surfaces as in [5], where we could consider impacts on edges. Furthermore, we have ignored the occurrence of friction and considered a symmetric object with uniform mass distribution, which also simplified our model considerably. It thus is interesting to determine whether the positive homogenization can still approximate the error dynamics well for these cases.

Also, in this work, superfluous contacts have been avoided. These superfluous contacts result in the perturbed system to have more possible transitions, and consequently the conewise constant jump gain gets more complex as it consists of more constant jump gains. Furthermore, the constant jump gains most likely also get more complex, as the constant jump gain needs to incorporate the detachment phases into it. This, however, may easily be solved by taking a similar approach as in this work, where we multiply the individual constant jump gains in a sequence as (4.49). The difficult part then lies in the formulation of an individual constant jump gain that corresponds to the detachment. The extension of the theory to cases where a single impact at one point leads to a detachment of another contact is thus recommended for future research.

Another recommendation, is to extend the considered trajectory. We have only considered a single simultaneous impact in this work, but one can also derive a conewise constant jump gain for detachments. We then can test more challenging reference trajectories with multiple impacts and detachments, possibly interchanging simultaneous and single impacts. Furthermore, we would like to recommend to analyze the control framework in the presence of actuator saturation and to find optimal time-varying feedback gains (cf. [24]) for improving performance.

A final recommendation is to extend the theory in [16], by formulating a proof that uniform asymptotic stability of the positive homogenization similarly leads to tracking control of the mechanical system experiencing simultaneous impacts.

Bibliography

[1] H. Park, S. Park, and S. Kim. Variable-speed quadrupedal bounding using impulse planning: Untethered high-speed 3d running of mit cheetah 2. In *Robotics and automation (ICRA), 2015 IEEE international conference on*, pages 5163–5170. IEEE, 2015.

[2] M.H. Raibert. Trotting, pacing and bounding by a quadruped robot. *Journal of biomechanics*, 23:79–81, 83–98, 1990.

[3] S. Kajita, F. Kanehiro, K. Kaneko, K. Fujiwara, K. Harada, K. Yokoi, and H. Hirukawa. Biped walking pattern generation by using preview control of zero-moment point. In *Robotics and Automation, 2003. Proceedings. ICRA'03. IEEE International Conference on*, volume 2, pages 1620–1626. IEEE, 2003.

[4] P. Sardain and G. Bessonnet. Forces acting on a biped robot. center of pressure-zero moment point. *IEEE Transactions on Systems, Man, and Cybernetics-Part A: Systems and Humans*, 34(5):630–637, 2004.

[5] G. Wiedebach, S. Bertrand, T. Wu, L. Fiorio, S. McCrory, R. Griffin, F. Nori, and J. Pratt. Walking on partial footholds including line contacts with the humanoid robot atlas. In *Humanoid Robots (Humanoids), 2016 IEEE-RAS 16th International Conference on*, pages 1312–1319. IEEE, 2016.

[6] H. Zhao, J. Reher, J. Horn, V. Paredes, and A.D. Ames. Realization of nonlinear real-time optimization based controllers on self-contained transfemoral prosthesis. In *Proceedings of the ACM/IEEE Sixth International Conference on Cyber-Physical Systems*, pages 130–138. ACM, 2015.

[7] A.D. Ames. First steps toward automatically generating bipedal robotic walking from human data. In *Robot Motion and Control 2011*, pages 89–116. Springer, 2012.

[8] Y. Hurmuzlu and D.B. Marghitu. Rigid body collisions of planar kinematic chains with multiple contact points. *The international journal of robotics research*, 13(1):82–92, 1994.

[9] H. Zhao, J. Horn, J. Reher, V. Paredes, and A.D. Ames. Multicontact locomotion on transfemoral prostheses via hybrid system models and optimization-based control. *IEEE Transactions on Automation Science and Engineering*, 13(2):502–513, 2016.

[10] A. Stemmer, A. Albu-Schaffer, and G. Hirzinger. An analytical method for the planning of robust assembly tasks of complex shaped planar parts. In *Robotics and Automation, 2007 IEEE International Conference on*, pages 317–323. IEEE, 2007.

[11] P.R. Giordano, A. Stemmer, K. Arbter, and A. Albu-Schaffer. Robotic assembly of complex planar parts: An experimental evaluation. In *Intelligent Robots and Systems, 2008. IROS 2008. IEEE/RSJ International Conference on*, pages 3775–3782. IEEE, 2008.

[12] J.J.B. Biemond, N. van de Wouw, W.P.M.H. Heemels, and H. Nijmeijer. Tracking control of mechanical systems with impacts. In *American Control Conference (ACC), 2012*, pages 258–263. IEEE, 2012.

[13] J.J.B. Biemond, N. van de Wouw, W.P.M.H. Heemels, R.G. Sanfelice, and H. Nijmeijer. Tracking control of mechanical systems with a unilateral position constraint inducing dissipative impacts. In *Decision and Control (CDC), 2012 IEEE 51st Annual Conference on*, pages 4223–4228. IEEE, 2012.

[14] J.J.B. Biemond, W.P.M.H. Heemels, R.G. Sanfelice, and N. van de Wouw. Distance function design and lyapunov techniques for the stability of hybrid trajectories. *Automatica*, 73:38–46, 2016.

[15] M.W.L.M. Rijnen, A.T. van Rijn, H. Dallali, A. Saccon, and H. Nijmeijer. Hybrid trajectory tracking for a hopping robotic leg. *IFAC-PapersOnLine*, 49(14):107–112, 2016.

[16] M.W.L.M. Rijnen, J.J.B. Biemond, N. van de Wouw, A. Saccon, and H. Nijmeijer. Hybrid systems with state-triggered jumps: sensitivity-based stability analysis with application to trajectory tracking. Submitted to IEEE Transactions on Automatic Control for review, 2017.

[17] A.T. van Rijn. Hybrid trajectory tracking for hopping robots. Master's thesis, Eindhoven University of Technology, 2016.

[18] E.B.C. De Mooij. Hybrid trajectory tracking for impact motions of humanoid robots. Master's thesis, Eindhoven University of Technology, 2016.

[19] R.G. Sanfelice, A.R. Teel, and R. Sepulchre. A hybrid systems approach to trajectory tracking control for juggling systems. In *Decision and Control, 2007 46th IEEE Conference on*, pages 5282–5287. IEEE, 2007.

[20] L. Menini and A. Tornambè. Asymptotic tracking of periodic trajectories for a simple mechanical system subject to nonsmooth impacts. *IEEE Transactions on Automatic Control*, 46(7):1122–1126, 2001.

[21] F. Forni, A.R. Teel, and L. Zaccarian. Follow the bouncing ball: Global results on tracking and state estimation with impacts. *IEEE Transactions on Automatic Control*, 58(6):1470–1485, 2013.

[22] J.J.B. Biemond, N. van de Wouw, W.P.M.H. Heemels, and H. Nijmeijer. Tracking control for hybrid systems with state-triggered jumps. *IEEE Transactions on Automatic Control*, 58(4):876–890, 2013.

[23] A. Saccon, N. van de Wouw, and H. Nijmeijer. Sensitivity analysis of hybrid systems with state jumps with application to trajectory tracking. In *Decision and Control (CDC), 2014 IEEE 53rd Annual Conference on*, pages 3065–3070. IEEE, 2014.

[24] M.W.L.M. Rijnen, A. Saccon, and H. Nijmeijer. On optimal trajectory tracking for mechanical systems with unilateral constraints. In *Decision and Control (CDC), 2015 IEEE 54th Annual Conference on*, pages 2561–2566. IEEE, 2015.

[25] R.I. Leine and N. Van de Wouw. *Stability and convergence of mechanical systems with unilateral constraints*, volume 36. Springer Science & Business Media, 2007.

[26] S.A. Burden, S.S. Sastry, D.E. Koditschek, and S. Revzen. Event–selected vector field discontinuities yield piecewise–differentiable flows. *SIAM Journal on Applied Dynamical Systems*, 15(2):1227–1267, 2016.

[27] M. Baumann, J.J.B. Biemond, R.I. Leine, and N. van de Wouw. Synchronization of impacting mechanical systems with a single constraint. *Physica D: Nonlinear Phenomena*, 362:9–23, 2018.

[28] H. Zhang, B. Brogliato, and C. Liu. Dynamics of planar rocking-blocks with coulomb friction and unilateral constraints: comparisons between experimental and numerical data. *Multibody System Dynamics*, 32(1):1–25, 2014.

[29] J. Wang, C. Liu, and D. Ma. Experimental study of transport of a dimer on a vertically oscillating plate. In *Proceedings of the Royal Society of London A: Mathematical, Physical and Engineering Sciences*, volume 470 (2171), page 20140439. The Royal Society, 2014.

[30] C. Liu, H. Zhang, Z. Zhao, and B. Brogliato. Impact–contact dynamics in a disc–ball system. In *Proc. R. Soc. A*, volume 469 (2152), page 20120741. The Royal Society, 2013.

[31] R.I. Leine and N. Van De Wouw. Uniform convergence of monotone measure differential inclusions: with application to the control of mechanical systems with unilateral constraints. *International Journal of Bifurcation and Chaos*, 18(05):1435–1457, 2008.

[32] R.I. Leine and N. Van De Wouw. Stability properties of equilibrium sets of non-linear mechanical systems with dry friction and impact. *Nonlinear Dynamics*, 51(4):551–583, 2008.

[33] N. van de Wouw. Lecture notes and exercises for the part on multibody dynamics 2015. Eindhoven University of Technology.

[34] N. van de Wouw. An introduction to time-stepping: a numerical technique for mechanical systems with unilateral constraints. Eindhoven University of Technology.

[35] M. Baumann. *Synchronization of Nonsmooth Mechanical Systems with Impulsive Motion*. PhD thesis, ETH Zürich, 2017.

[36] R.I. Leine and M. Baumann. Variational analysis of inequality impact laws. In *Proceedings of the ENOC 2014 Conference, Vienna*, 2014.

[37] C. Glocker. *Set-valued force laws: dynamics of non-smooth systems*, volume 1. Springer Science & Business Media, 2013.

[38] L. Caishan, Z. Zhen, and B. Brogliato. Frictionless multiple impacts in multibody systems. *Proceedings of Royal Society A*, 464:3193–3211, 2008.

[39] B. Brogliato, H. Zhang, and C. Liu. Analysis of a generalized kinematic impact law for multibody-multicontact systems, with application to the planar rocking block and chains of balls. *Multibody System Dynamics*, 27(3):351–382, 2012.

[40] W.P.M.H. Heemels and B. De Schutter. Hybrid systems and control (lecture notes 2015). Eindhoven University of Technology.

[41] R. Abraham, J.E. Marsden, and T. Ratiu. *Manifolds, tensor analysis, and applications*, volume 75. Springer Science & Business Media, 2012.

[42] H.K. Khalil. *Nonlinear Systems: Pearson New International Edition.*, volume Third Edition. Pearson Education, Limited, 2013.

[43] R. Goebel, R.G. Sanfelice, and A.R. Teel. *Hybrid Dynamical Systems: modeling, stability, and robustness*. Princeton University Press, 2012.

[44] R.A. Adams and C. Essex. *Calculus: a complete course*, volume Seventh Edition. Pearson Canada Toronto, 2009.

[45] Matlab version 8.6 (r2015b). The MathWorks inc., 2015. https://nl.mathworks.com/?s_tid=gn_logo.

[46] J. Haslinger and G.E. Stavroulakis. *Nonsmooth mechanics of solids*, volume 485. Springer Science & Business Media, 2007.

[47] J.J. Moreau. Standard inelastic shocks and the dynamics of unilateral constraints. In *Unilateral problems in structural analysis*, pages 173–221. Springer, 1985.

Appendix A

Superfluous contact analysis

In this appendix, we work (2.19) out and show that satisfaction of this condition should give no superfluous contacts for a planar two-contact mechanical system. Before doing so, we introduce some mathematical concepts used to perform this analysis.

A.1 Preliminaries

This section introduces the mathematical concepts employed in Appendix A.2 (and other appendices). The reader can skip it at the first reading, returning to it when clarification is needed. Note that the definitions are taken from [25, Section 2, p.21-41] unless stated otherwise.

Definition A.1 (Cone) *A subset $G \subset \mathbb{R}^n$ is called a cone if for any $\boldsymbol{x} \in G$ and $\lambda > 0$ also $\lambda \boldsymbol{x} \in G$ holds. A cone is convex if the subset $G \subset \mathbb{R}^n$ is convex.*

Definition A.2 (Contingent cone) *Let C be a closed set and let $\boldsymbol{x}$ be a point in C. The contingent cone is defined as*

$$\mathcal{K}_C(\boldsymbol{x}) = \{\boldsymbol{y} \mid \exists t_k \downarrow 0 \ , \ \boldsymbol{y}_k \to \boldsymbol{y}, \ \textit{with } \boldsymbol{x} + t_k \boldsymbol{y}_k \in C\}. \tag{A.1}$$

The contingent cone is also referred to as *tangent cone of Bouligand.*

Definition A.3 (Convex set) *A set $C \subset \mathbb{R}^n$ is convex if for each $\boldsymbol{x} \in C$ and $\boldsymbol{y} \in C$ also (1-a)$\boldsymbol{x}$ + a$\boldsymbol{y} \in C$ for arbitrary a with $0 \leq a \leq 1$.*

Definition A.4 (Closed set) *A set $C \subset \mathbb{R}^n$ is closed if it contains all its limit points. Every limit point of a set C is the limit of some sequence $\{\boldsymbol{x}_k\}$ with $\boldsymbol{x}_k \in C$ for all $k \in \mathbb{N}$.*

Definition A.5 (Set-valued function) *A set-valued function $\boldsymbol{\mathcal{F}} : \mathbb{R}^n \to \mathbb{R}^n$ is a map that associates with any $\boldsymbol{x} \in \mathbb{R}^n$ a set $\boldsymbol{\mathcal{F}}(\boldsymbol{x}) \subset \mathbb{R}^n$.*

Definition A.6 (Monotone Set-valued Function) *A set-valued map $\boldsymbol{\mathcal{F}}(\boldsymbol{x})$ is called monotone if its graph is monotone in the sense that*

$$\forall (\boldsymbol{x}, \boldsymbol{y}) \in Graph(\boldsymbol{\mathcal{F}}), \quad \forall (\boldsymbol{x}^*, \boldsymbol{y}^*) \in Graph(\boldsymbol{\mathcal{F}}), \quad (\boldsymbol{y} - \boldsymbol{y}^*)^T (\boldsymbol{x} - \boldsymbol{x}^*) \geq 0. \tag{A.2}$$

In addition, if

$$(\boldsymbol{y} - \boldsymbol{y}^*)^T (\boldsymbol{x} - \boldsymbol{x}^*) \geq a ||\boldsymbol{x} - \boldsymbol{x}^*||^2 \tag{A.3}$$

for some $a > 0$, then the set-valued map is strictly monotone.

Definition A.7 (Maximal monotone set-valued function) *A monotone set-valued function $\boldsymbol{\mathcal{F}}(\boldsymbol{x})$ is called maximal monotone if there exists no other monotone set-valued function whose graph strictly contains the graph of $\boldsymbol{\mathcal{F}}$. If $\boldsymbol{\mathcal{F}}$ is strictly monotone and maximal, then it is called strictly maximal monotone.*

Definition A.8 (Metric) *[41, Section 1.2, p.9 -12] : Let M be a set. A metric (also called a topological metric) on M is a function $d : M \times M \to \mathbb{R}$ such that for all $m_1, m_2, m_3 \in M$,*

- $d(m_1, m_2) = 0$ *iff* $m_1 = m_2$ *(definiteness);*
- $d(m_1, m_2) = d(m_2, m_1)$ *(symmetry); and*
- $d(m_1, m_3) \leq d(m_1, m_2) + d(m_2, m_3)$ *(triangle inequality).*

A metric space is the pair (M, d); if there is no danger of confustion, just write M for (M, d).

Note that on $\mathbb{R}^n$ this metric is given by

$$d(\boldsymbol{x}, \boldsymbol{y}) = \sqrt{\sum_{i=1}^{n} (x_i - y_i)^2} = ||\boldsymbol{x} - \boldsymbol{y}|| \tag{A.4}$$

when referring to the Euclidean Norm. A set with a metric induced by a matrix $\boldsymbol{M}$ can then be interpreted as a set with the metric

$$d(\boldsymbol{x}, \boldsymbol{y}) = \sqrt{(\boldsymbol{x} - \boldsymbol{y})^T \boldsymbol{M} (\boldsymbol{x} - \boldsymbol{y})} = ||\boldsymbol{x} - \boldsymbol{y}||_{\boldsymbol{M}}. \tag{A.5}$$

Definition A.9 (Normal Cone) *Let $C \subset \mathbb{R}^n$ be a convex set and $\boldsymbol{x} \in C$. The set of vectors $\boldsymbol{y} \in \mathbb{R}^n$ that are normal vectors of C at $\boldsymbol{x} \in C$ form the normal cone of C in $\boldsymbol{x}$:*

$$\mathcal{N}_C(\boldsymbol{x}) = \{\boldsymbol{y} \mid \boldsymbol{y}^T (\boldsymbol{x}^* - \boldsymbol{x}) \leq 0, \quad \boldsymbol{x} \in C, \forall \boldsymbol{x}^* \in C\}. \tag{A.6}$$

Definition A.10 (Proximal point) *The proximal point of a closed convex set $C \subset \mathbb{R}^n$ to a point $\boldsymbol{z}$ is the closest point in C to $\boldsymbol{z}$:*

$$prox_C(\boldsymbol{z}) = \arg\min_{\boldsymbol{x}^* \in C} ||\boldsymbol{z} - \boldsymbol{x}^*||, \qquad \boldsymbol{z} \in \mathbb{R}^n. \tag{A.7}$$

Note that when we have a metric induced by a matrix $\boldsymbol{M}$, that the proximal point function becomes

$$\text{prox}_C^{\boldsymbol{M}}(\boldsymbol{z}) = \arg\min_{\boldsymbol{x}^* \in C} ||\boldsymbol{z} - \boldsymbol{x}^*||_{\boldsymbol{M}} = \arg\min_{\boldsymbol{x}^* \in C} \sqrt{(\boldsymbol{z} - \boldsymbol{x}^*)^T \boldsymbol{M} (\boldsymbol{z} - \boldsymbol{x}^*)}, \qquad \boldsymbol{z} \in \mathbb{R}^n. \tag{A.8}$$

Figure A.1 illustrates the proximal point function $\text{prox}_C(\boldsymbol{z})$ for $\boldsymbol{z} \in \mathbb{R}^n$ and closed convex set C. From the figure we notice three properties:

- if $\boldsymbol{q} \in \text{bdry} C$, denoting the boundary of set C, and the boundary is smooth at the point $\boldsymbol{q}$, then there exists a line of arguments $\boldsymbol{z}$ resulting in the same outcome. This can be seen at $\boldsymbol{q}_1$ where a dashed line (ray) is seen extending from C towards the bottom right. Every point $\boldsymbol{z}$ on that line then results in the same proximal point.
- if $\boldsymbol{q} \in \text{bdry} C$ and the boundary is non-smooth at $\boldsymbol{q}$, then there exists a cone of arguments which have the same proximal point of C. Looking at $\boldsymbol{q}_2$, a green cone is formulated in which for every point in this green cone, the same outcome $\boldsymbol{q}_2$ is obtained.
- if $\boldsymbol{q} \in C$, we find $\boldsymbol{z} = \text{prox}_C(\boldsymbol{z}) = \boldsymbol{q}$. An example is $\boldsymbol{q}_3 = \boldsymbol{z}_3$.

Definition A.11 (Tangent cone) *Let C be a closed set and let $\boldsymbol{x}$ be a point in C. The tangent cone is defined as*

$$\mathcal{T}_C(\boldsymbol{x}) = \{\boldsymbol{y} \mid \forall t_k \downarrow 0 \ , \ \boldsymbol{x}_k \to \boldsymbol{x} \text{ with } \boldsymbol{x}_k \in C \ , \ \exists \ \boldsymbol{y}_k \to \boldsymbol{y} \ , \text{ with } \boldsymbol{x}_k + t_k \boldsymbol{y}_k \in C\}. \tag{A.9}$$

The tangent cone is also called *circatangent cone* or *tangent cone of Clarke.*

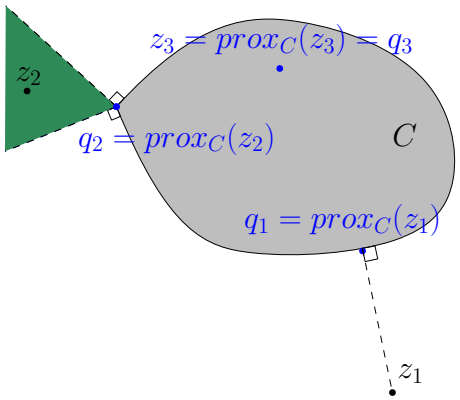

Figure A.1: A graphical representation of the proximal point in the closed convex set $\mathcal{C}$ to the points $\boldsymbol{z}_1 \notin \mathcal{C}$, $\boldsymbol{z}_2 \notin C$, and $\boldsymbol{z}_3 \in C$, cf. [25].

Inner product

We use the inner product defined in [46, Section 4.1, p. 72-73]. If we define two vectors $\vec{v} \in \mathcal{L}$ and $\vec{w} \in \mathcal{L}$, with $\mathcal{L}$ being an n-dimensional linear space over the field of real numbers $\mathbb{R}$, then we can define the inner product as

$$\vec{x} \cdot \vec{w} = \boldsymbol{v}^T \boldsymbol{M} \boldsymbol{w}, \tag{A.10}$$

where $\boldsymbol{v} \in \mathbb{R}^n$ and $\boldsymbol{w} \in \mathbb{R}^n$ are coordinate representations in Euclidean space, and $\boldsymbol{M} \in \mathbb{R}^{n \times n}$ a symmetric and positive definite matrix derived from the basis vectors. Note that using the left-sided notation of (A.10) assumes the reader to know the basis and thus the matrix $\boldsymbol{M}$. From the inner product we derive the norm and angle between two vectors as, respectively,

$$||\vec{v}||_{\boldsymbol{M}} = \sqrt{\vec{v} \cdot \vec{v}} = \sqrt{\boldsymbol{v}^T \boldsymbol{M} \boldsymbol{W}} \tag{A.11}$$

and

$$\cos(\phi) = \frac{\vec{v} \cdot \vec{w}}{||\vec{v}||_{\boldsymbol{M}} ||\vec{w}||_{\boldsymbol{M}}}. \tag{A.12}$$

Derivative

The time derivative of a function $\boldsymbol{a}(t) \in \mathbb{R}^n$ is denoted as

$$\dot{\boldsymbol{a}}(t) = \frac{d\boldsymbol{a}(t)}{dt} \in \mathbb{R}^n. \tag{A.13}$$

When multiple arguments are involved, we use the notation in [41, Section 2.3, p.75-83]. We write the derivative of a function f as a linear map Df. Suppose we have a function $\boldsymbol{f}(\boldsymbol{x}, \boldsymbol{u}) : \mathbb{R}^n \times \mathbb{R}^m \to \mathbb{R}^n$, then we can define the partial derivatives at point $\boldsymbol{x}_0$ and $\boldsymbol{u}_0$ as

$$\frac{\partial \boldsymbol{f}(\boldsymbol{x}_0, \boldsymbol{u}_0)}{\partial \boldsymbol{x}} = D_1 \boldsymbol{f}(x_0, u_0) \in \mathbb{R}^{n \times n} \tag{A.14}$$

and

$$\frac{\partial \boldsymbol{f}(\boldsymbol{x}_0, \boldsymbol{u}_0)}{\partial \boldsymbol{u}} = D_2 \boldsymbol{f}(x_0, u_0) \in \mathbb{R}^{n \times m}, \tag{A.15}$$

where we denote $D_i \boldsymbol{h}$ as the partial derivative of the function $\boldsymbol{h}(\cdot)$ with respect to its i'th argument.

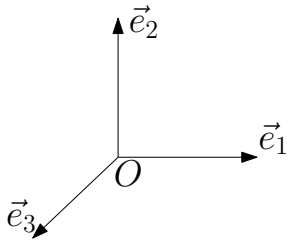

Figure A.2: Cartesian frame $\{O, \vec{\boldsymbol{e}}\}$ [33, Section 1.1, p.1].

Cartesian frame

Mechanical systems are described in Euclidean 3-dimensional space, where a Cartesian frame $\{O, \vec{\boldsymbol{e}}\}$ as in Figure A.2 is used to describe geometrical and mechanical relations in this space, see [33]. The origin of the frame is denoted as O and the basis as $\vec{\boldsymbol{e}} := \begin{pmatrix} \vec{e}_1 & \vec{e}_2 & \vec{e}_3 \end{pmatrix}^T$, representing a column of basis vectors.

A right-handed frame, seen in Figure A.2, is considered with $\vec{e}_i \cdot \vec{e}_j = \delta_{ij}$ for $i, j = \{1, 2, 3\}$ and $\vec{e}_1 \times \vec{e}_2 = \vec{e}_3$, where δ_{ij} is the Kronicker delta ($\delta_{ij} = 1$ for $i = j$ and $\delta_{ij} = 0$ otherwise). The $\boldsymbol{M}$ matrix in the inner product formulation, see (A.10), changes for the Cartesian frame to an identity matrix. This then results in the standard inner product and the standard norm.

Position vector

In Figure A.3, an inertial frame $\{O^0, \vec{\boldsymbol{e}}^0\}$ is attached to the world, and a body-fixed frame $\{O^1, \vec{\boldsymbol{e}}^1\}$ is attached to the center of mass of a rigid body. The vector $\vec{r}_{CM}$ indicates the position of the mass center of the rigid body with respect to the inertial frame and can be denoted as

$$\vec{r}_{CM} = (\boldsymbol{r}^0_{CM})^T \vec{\boldsymbol{e}}^0 = (\boldsymbol{r}^1_{CM})^T \vec{\boldsymbol{e}}^1 \tag{A.16}$$

with, e.g., $\boldsymbol{r}^0_{CM}$ denoting the column of coordinates of $\vec{r}_{CM}$ with respect to frame 0.

Rotation matrix

The rotation of frame 1 with respect to frame 0 is written as

$$\vec{\boldsymbol{e}}^1 = \boldsymbol{A}^{10} \vec{\boldsymbol{e}}^0, \tag{A.17}$$

for which the matrix $\boldsymbol{A}$ is a so-called direction cosine matrix.

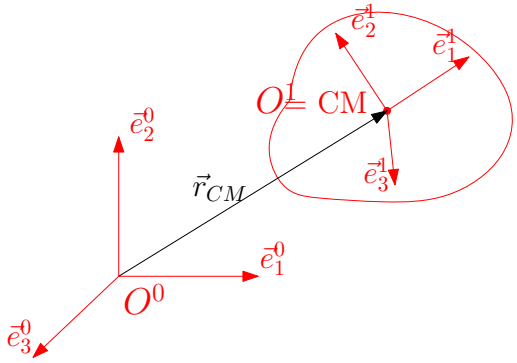

Figure A.3: Inertial and body-fixed Cartesian frames [33].

Angular velocity

The angular velocity of frame 1 with respect to frame 0 is given as

$$^{10}\vec{\omega} = (^{10}\boldsymbol{\omega}^1)^T \vec{\boldsymbol{e}}^1 \tag{A.18}$$

with

$$^{10}\boldsymbol{\omega}^1 = \begin{pmatrix} ^{10}\omega_1^1 \\ ^{10}\omega_2^1 \\ ^{10}\omega_3^1 \end{pmatrix}. \tag{A.19}$$

The angular velocity vector can be derived from the Poisson equation

$$^{10}\tilde{\boldsymbol{\omega}}^1 = \boldsymbol{A}^{10}(\dot{\boldsymbol{A}}^{10})^T = \begin{pmatrix} 0 & -^{10}\omega_3^1 & ^{10}\omega_2^1 \\ ^{10}\omega_3^1 & 0 & -^{10}\omega_1^1 \\ -^{10}\omega_2^1 & ^{10}\omega_1^1 & 0 \end{pmatrix}. \tag{A.20}$$

A.2 Analysis

As mentioned in Section 2.1.2, the impact dynamics (2.18), based on the impact equation and generalized Newton's impact law, are not formulated in a manner for which we can analyze superfluous contacts analytically. We thus reformulate the generalized Newton's impact law in a more intuitive format, which we use to find conditions to exclude cases of superfluous contacts. To do so, a variational analysis for impact laws is performed as in [36] and [35, Section 3.3, 42-48]. The generalized Newton's impact law with global restitution coefficient $\varepsilon = 0$ is rewritten as

$$-\boldsymbol{\Lambda} \in \mathcal{H}(\bar{\boldsymbol{\xi}}) = -2\text{prox}^{\boldsymbol{G}}_{\mathbb{R}^+_0}(-\boldsymbol{G}^{-1}\bar{\boldsymbol{\xi}}), \tag{A.21}$$

where $\mathcal{H}$ is a *maximal monotone set-valued function*, $\boldsymbol{G} = \boldsymbol{W}^T\boldsymbol{M}^{-1}\boldsymbol{W}$ a *Delassus* matrix, and $\bar{\boldsymbol{\xi}} = \frac{1}{2}(\boldsymbol{\xi}^+ - \boldsymbol{\xi}^-)$ the difference of the normal contact velocity terms between pre- and post- impact. From (2.15) and (A.21), one derives the explicit mapping between pre- and post- impact velocities

$$\mathbf{v}^+ = \text{prox}^{\boldsymbol{M}}_{\mathcal{T}_C(\boldsymbol{q})}(\mathbf{v}^-), \qquad \text{with } \mathcal{T}_C(\boldsymbol{q}) = \{\mathbf{v} | \boldsymbol{W}^T\mathbf{v} \geq 0\}, \tag{A.22}$$

where $\mathcal{T}_C(\boldsymbol{q})$ is a *tangential cone* to the *closed set* of possible configurations $C \subset \mathbb{R}^n$ at configuration $\boldsymbol{q}$, cf. [46, Section 4.6, p. 80-81], and $\text{prox}^{\boldsymbol{M}}_{\mathcal{T}_C(\boldsymbol{q})}(\cdot)$ a *proximal point function* to the set $\mathcal{T}_C(\boldsymbol{q})$ in the metric induced by a matrix $\boldsymbol{M}$. For sake of brevity, we will mention the latter as *in the metric* $\boldsymbol{M}$ in the rest of the work.

Equation (A.22) is similar to *Moreau's impact law* for global restitution coefficient $\varepsilon = 0$, and we thus use the geometrical approach in [46, Section 4 + 5, p.70-101] to describe this mapping in more detail and simultaneously deduce the occurrence of superfluous contacts. For mechanical systems with unilateral constraint functions $\boldsymbol{h}(\boldsymbol{q}) \geq 0$, the closed (convex) set C is defined by the unilateral constraints (see [46, Section 4.6, p. 80-81]) as

$$C := \{\boldsymbol{q} \mid h_i(\boldsymbol{q}) \geq 0, \quad i \in \mathcal{I}\}, \tag{A.23}$$

where it is assumed that the level curves $h_i(\boldsymbol{q}) = 0$ intersect each other transversally and the functions $h_i(\cdot)$ are continuously differentiable. Figure A.4 illustrates an example of the closed set C defined by four unilateral constraints. Here, we are interested in the configurations at which the level curves $h_i(\cdot) = 0$ intersect each other, e.g., at the configuration $\boldsymbol{q}_4$. These configurations are interpreted as the configuration of the system where two or more pairs of contact points are closed, and consequently superfluous contacts are analyzed at these configurations. We will from now on just mention that *contacts are closed* or *contacts are open* when talking about a pair of contact points.

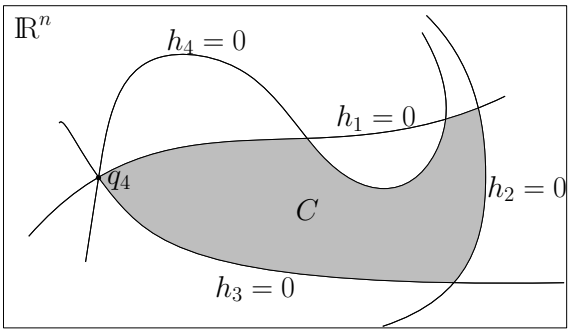

Figure A.4: Example of a closed set C defined by the four level curves $h_i = 0$ with $i = \{1, 2, 3, 4\}$ [46]. The level curves can be interpreted as the configurations for which the corresponding contact is closed. The intersection of the level curves $h_1 = 0$, $h_2 = 0$, and $h_3 = 0$ is denoted by the point $\boldsymbol{q}_4$. This point can then be interpreted as the configuration where three contacts are closed.

Figure A.5 then gives an intuitive interpretation of the analysis performed further below. Considering the set C in Figure A.4 as the admissable configurations of a system, then we could consider the system to be in an arbitrary initial boundary configuration $\boldsymbol{q} \in bdry(C)$ at initial time $t = t_0$. This configuration is depicted in the left drawing of Figure A.5 as an orange dot, where we denote with an arrow how the configuration changes. Here, the system has a contact closed corresponding to the constraint $h_3 = 0$. At time t_i the system experiences a simultaneous inelastic impact at $\boldsymbol{q}_4$ which is depicted in the middle drawing of Figure A.5. Note that $\boldsymbol{q}_4$ is the point where three level curves $h_1 = 0$, $h_3 = 0$, and $h_4 = 0$ intersect each other, and consequently two more contacts are closed. One may then conclude that if for $t > t_i$ the system moves away from the configuration $\boldsymbol{q}_4$ to a configuration satifying $h_3 \neq 0$, then the originally closed contact opens, and subsequently the system has a superfluous contact. This is depicted in the right drawing of Figure A.5, where the system after inelastic impact appears in a configuration where the initially closed contact $h_3 = 0$ re-opens as $h_3 \neq 0$. If, however, for $t > t_i$ we conclude that $\boldsymbol{q} = \boldsymbol{q}_4$, then the initially closed contact stays closed, and we thus have no occurrence of superfluous contacts.

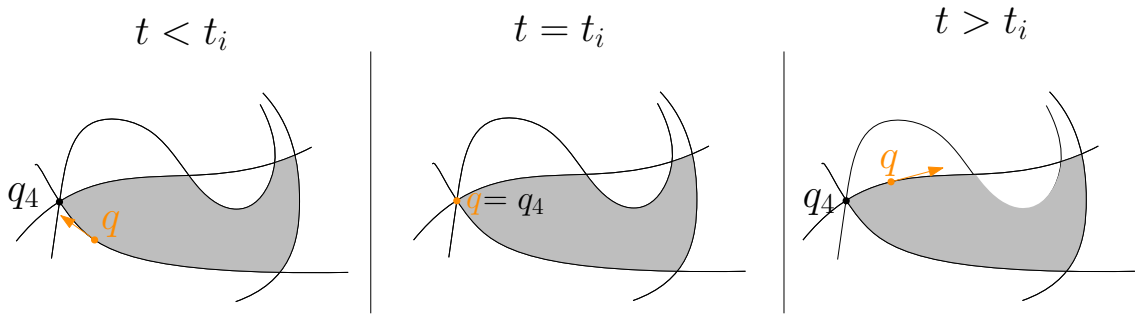

Figure A.5: Example of the analysis of superfluous contacts. At $t < t_i$, with t_i denoting an impact time, there is an initial configuration of $\boldsymbol{q}$ (in orange) on the level set $h_3 = 0$. This indicates that one of the contacts is already closed. The configuration evolves along the level set $h_3 = 0$ till inelastic impact is determined at $t = t_i$ for the configuration $\boldsymbol{q} = \boldsymbol{q}_4$. For $t > t_i$ (post-impact) the configuration evolves along the level set $h_1 = 0$, indicating that the previously closed contact for $h_3 = 0$ opens, and the corresponding contact is thus deemed a superfluous contact.

This may better be explained with a physical example. Figure A.6 illustrates an example where we re-interpret the area around $\boldsymbol{q}_4$ of Figure A.4 as a valley. We consider the level curves $h_1 = 0$ and $h_3 = 0$ as respectively the left and right slopes of the valley and $\boldsymbol{q}_4$ the lowest point of the valley. In this case, the level curve $h_4 = 0$ thus does not play a role. We could then depict an initial $\boldsymbol{q}$ on $h_3 = 0$ as a ball which rolls towards the lowest point $\boldsymbol{q}_4$. Due to properties such as the speed of the ball, mass of the ball, and steepness of the valley, the ball may not stay in the lowest point of the valley at $\boldsymbol{q}_4$, but will roll out of the valley over the left slope. One could think of the ball overcoming the impacting effects when it collides with the left slope. This could then be interpreted as the presence of superfluous contact, and is depicted on the upper drawing of Figure A.6. The lower drawing of Figure A.6 depicts the opposite case, where the steepness of the valley is so big, that the mass and speed of the ball is unable to get out of the valley. This can then be interpreted as a situation with no superfluous contacts.

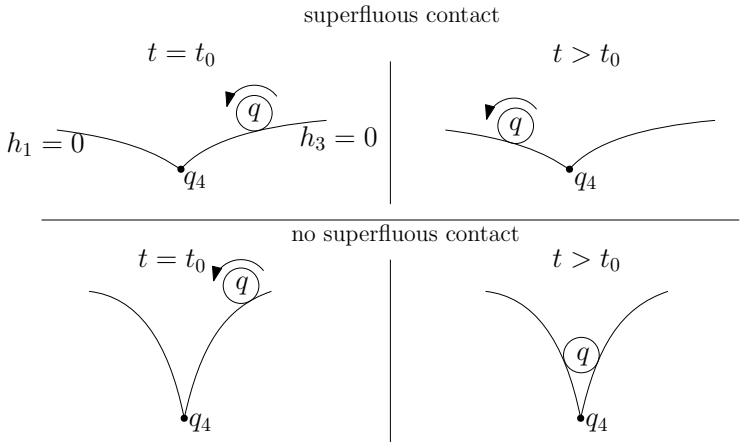

Figure A.6: Example of interpretation of superfluous contact. The area around $\boldsymbol{q}_4$ in Figure A.4 is re-interpreted as a valley, where $h_1 = 0$ depicts the left slope, $h_3 = 0$ the right slope, and $\boldsymbol{q}_4$ the lowest point of the valley. Here, $h_4 = 0$ is neglected. The ball is interpreted as a configuration $\boldsymbol{q}$ on $h_3 = 0$, where the upper drawing depicts an interpretation of superfluous contact, and the lower drawing depicts an interpretation of no superfluous contact.

The proximal point function $\text{prox}^{\boldsymbol{M}}_{\mathcal{T}_C(\boldsymbol{q})}(\cdot)$ (A.22) can distinguish under which conditions superfluous contacts happen. We can analyze these conditions by analyzing the cone formulations at the impact configuration $\boldsymbol{q}$ in the closed set C. We focus on the tangent and *normal cone*[1] which are depicted in Figure A.7 as respectively $\mathcal{T}_C$ and $\mathcal{N}_C$ for both the situation with and without *re-entrant corner*. Note that for example $\mathcal{T}_C$ should be interpreted as $\mathcal{T}_C(\boldsymbol{q})$. A re-entrant corner is defined as $\mathcal{T}_C \subset \mathcal{K}_C$, where $\mathcal{K}_C$ is the contingent cone, and one should be aware that (A.22) is not applicable when this is present. The issue of re-entrant corners is treated in [Section 5.4, p. 90-91][46] where it is described that re-entrant corners may lead to a set of post-impact velocity solutions instead of only one solution of post-impact velocities. Furthermore, one can not define an admissable domain with (A.23). A famous physical example for this re-entrant corner is the situation where an impact occurs between two cornors of two rigid bodies.

In [46], the normal cone for mechanical systems with unilateral constraints - remind that it is defined as polar tangent cone in [46] - can also be formulated as

$$\mathcal{N}_C(\boldsymbol{q}) = \{\boldsymbol{y} \mid \boldsymbol{y} = -\sum_{i \in I_c} \lambda_i \nabla h_i(\boldsymbol{q}), \quad \lambda_i \geq 0, \qquad \forall i \in \mathcal{I}_c\}, \tag{A.24}$$

[1]The normal cone is defined differently in [25] and [46]. In this work we define the normal cone as in [25] and this can be interpreted as the polar tangent cone in [46].

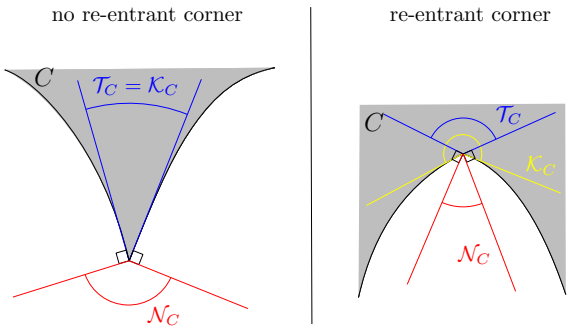

Figure A.7: Difference between tangent (Clarke's), contingent (Boulingard's), and normal cones, for a re-entrant and non re-entrant corner.

with $\mathcal{I}_c$ being the closed contacts index and $\nabla h_i(\boldsymbol{q}) = \boldsymbol{M}^{-1}(\boldsymbol{q})\frac{\partial h_i}{\partial \boldsymbol{q}}$ representing a velocity component. Note that the latter can be deduced when rewriting the impact equation (2.15) by taking the mass matrix $\boldsymbol{M}$ from the left side to the right side, giving

$$\mathrm{v}^+ - \mathrm{v}^- = \boldsymbol{M}^{-1}(\boldsymbol{q})\boldsymbol{W}(\boldsymbol{q}, t)\boldsymbol{\Lambda}, \tag{A.25}$$

where the right term represents $\nabla \boldsymbol{h}(\boldsymbol{q})$. Taking into account that the boundary lines of $\mathcal{T}_C$ are perpendicular to the boundary lines of $\mathcal{N}_C$ in terms of the metric $\boldsymbol{M}$, allows us to interpret the tangent cone as

$$\mathcal{T}_C(\boldsymbol{q}) = \{\boldsymbol{q}^* | (\boldsymbol{q}^* - \boldsymbol{q})^T \boldsymbol{M}(\boldsymbol{q}) \nabla h_i(\boldsymbol{q}) \leq 0, \quad \forall i \in \mathcal{I}_c, \text{ with } \boldsymbol{q}, \boldsymbol{q}^* \in C\}. \tag{A.26}$$

A pair of orthogonal closed convex cones $\mathcal{N}_C$ and $\mathcal{T}_C$ are now defined. We can then use theorem 4.1 in [46, Section 4.3, p.74-75] which in essence says that for a pair of orthogonal closed convex cones $\mathcal{T}_C$ and $\mathcal{N}_C$, any vector $\vec{w}$ in a n-dimensional inner product space can be decomposed as the sum $\vec{w} = \vec{v}^{\mathcal{T}} + \vec{v}^{\mathcal{N}}$ with

$$\boldsymbol{v}^{\mathcal{T}} \in \mathcal{T}_C, \qquad \boldsymbol{v}^{\mathcal{N}} \in \mathcal{N}_C, \qquad \vec{v}^{\mathcal{T}} \cdot \vec{v}^{\mathcal{N}} = 0. \tag{A.27}$$

The proof of this can be found in [46] and [47].

We can now depict the geometrical interpretation of $\mathrm{prox}_{\mathcal{T}_C}^{\boldsymbol{M}}(\cdot)$ in vector space, where we draw the cones $\mathcal{T}_C$ and $\mathcal{N}_C$ as subset of the n-dimensional linear inner product space $\mathcal{L}$. A planar two contact example is considered, where two unilateral constraints $h_1(\boldsymbol{q}) \geq 0$ and $h_2(\boldsymbol{q}) \geq 0$ are present. These unilateral constraints result in a closed convex set $\mathcal{C}$ of admissible configurations, to which we treat a similar set $\mathcal{C}$ as in the left drawing of Figure A.7. Figure A.8 depicts the possible cone formulations at the point of discontinuity, i.e., at the point where the level surfaces $h_1 = 0$ and $h_2 = 0$ intersect. We then perform a cone analysis using theorem 4.1 of [46, Section 4.3, p.74-75] at the point of discontinuity. Note that this cone analysis is a local analysis and thus only predicts the behavior in a neighborhood around the impacting point.

On the left drawing, the pair of orthogonal cones are derived with (A.24) and (A.26). Applying the proximal point function (A.22) to a vector $\vec{w}$, results in the projection of $\vec{w}$ on the tangent cone $\mathcal{T}_C$. Reminded of the example in Figure A.6, the vector $\vec{w}$ can be understood as the pre-impact velocity of the ball at the corner $\boldsymbol{q}_4$. By looking at the projection of $\vec{w}$ on $\mathcal{T}_C$, i.e., $\vec{v}^{\mathcal{T}}$, one can analyze whether superfluous contacts are present. We observe $\vec{w} \notin \mathcal{N}_C$, and see that the projection on $\mathcal{T}_C$ results in a vector $\vec{v}^{\mathcal{T}}$ pointing outwards the considered point of discontinuity. Recalling that $\mathcal{T}_C$ is a local approximation of the level surfaces $h_i = 0$, with $i = \{1, 2\}$, one can relate the vector $\vec{v}^{\mathcal{T}}$ to the post-impacting velocity of the ball at $\boldsymbol{q}_4$ in Figure A.6.

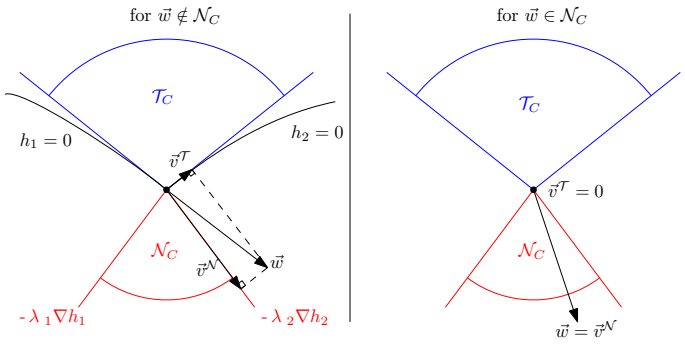

Figure A.8: Geometrical interpretation of generalized Newton's impact law [46, Figure 19, p.75] with global restitution coefficient $\varepsilon = 0$. The left drawing depicts a case with superfluous contacts, while the right drawing depicts a case with no superfluous contacts.

We then assume to prevent the occurrence of superfluous contacts when $\vec{v}^{\mathcal{T}} = 0$ for any $\vec{w} \in -\mathcal{T}_C$. For the example of the ball depicted in Figure A.6, a vector $\vec{v}^{\mathcal{T}} = 0$ may then indicate that the ball will lay still in corner $\boldsymbol{q}_4$. On the right drawing of Figure A.8, one can see a case for which $\vec{v}^{\mathcal{T}}$ is zero, namely when $\vec{w} \in \mathcal{N}_C$. We thus assume that we can prevent the occurrence of superfluous contacts by satisfying $-\mathcal{T}_C \subseteq N_C$. For the cone analysis, this will then always result in $\vec{w} \in \mathcal{N}_C$, resulting in $\vec{v}^{\mathcal{T}} = 0$.

As $\mathcal{N}_C$ and $\mathcal{T}_C$ are a pair of orthogonal cones, we can make one cone *smaller* by making the other cone *bigger*. By making the normal cone $\mathcal{N}_C$ have an angle bigger than 90 degrees in the metric $\boldsymbol{M}$, guarantees that $\mathcal{T}_C$ is of an angle smaller than 90 degrees. This in turn will make sure that $-\mathcal{T}_C \subseteq \mathcal{N}_C$, and we thus assume to have prevented the occurance of superfluous contacts and rocking for the two-contact planar mechanical system. Taking into account that the outer lines of $\mathcal{N}_C$ are defined as $-\lambda \nabla h_i$ for $i \in \mathcal{I}_C$, see (A.24), we satisfy $-T_C \subseteq \mathcal{N}_C$ by fulfilling

$$\arccos\left(\frac{\nabla h_1^T \boldsymbol{M} \nabla h_2}{\sqrt{\nabla h_1^T \boldsymbol{M} \nabla h_1}\sqrt{\nabla h_2^T \boldsymbol{M} \nabla h_2}}\right) \geq \frac{\pi}{2}. \tag{A.28}$$

Appendix B

Positive homogenization

In this appendix, the positive homogenization, as discussed in Chapter 4, is worked out. The following topics are treated:

- The formulation of the continuous dynamics.
- The formulation of the conewise constant jump gain for a particular mode sequence.
- A proof that a positively homogeneous jump mapping also results in a positively homogeneous model.
- How the application of a feedback gain $\boldsymbol{K}$ on the nonlinear hybrid system can be interpreted for the positive homogenization.

B.1 Continuous dynamics of the positive homogenization

We show how the continuous dynamics of (4.31) are worked out. We only treat one mode and thus leave the multi-scale hybrid time (t, i, k) and mode sequence notation out of the analysis. The method applied is based on the sensitivity analysis for nonlinear smooth dynamical system, cf. [42, Chapter 3.3, p.99-102 and Chapter 10.1 p. 382-393].

We characterize a perturbation via a parameter ϵ. We then assume the initial state $\boldsymbol{x}(t_0)$ and the input $\boldsymbol{u}(t)$ to depend continuously on this parameter ϵ, such that we define $\boldsymbol{x}(t_0, \epsilon)$ and $\boldsymbol{u}(t, \epsilon)$. The nominal values of the state and input are realized by setting $\epsilon = 0$. We furthermore have a vectorfield $\boldsymbol{f}(t, \boldsymbol{x}, \boldsymbol{u})$ depending continuously on its arguments and having continuous first partial derivatives with respect to its arguments. The perturbed state is then defined as

$$\boldsymbol{x}(t, \epsilon) = \boldsymbol{x}(t_0, \epsilon) + \int_{t_0}^{t} \boldsymbol{f}\left(s, \boldsymbol{x}(s, \epsilon), \boldsymbol{u}(s, \epsilon)\right) ds, \tag{B.1}$$

and taking the partial derivative of (B.1) with respect to ϵ results in

$$\frac{\partial \boldsymbol{x}(t, \epsilon)}{\partial \epsilon} = \frac{\partial \boldsymbol{x}(t_0, \epsilon)}{\partial \epsilon} + \int_{t_0}^{t} \left[\frac{\partial \boldsymbol{f}}{\partial \boldsymbol{x}}(s, \boldsymbol{x}\left(s, \epsilon\right), \boldsymbol{u}(s, \epsilon)) \frac{\partial \boldsymbol{x}}{\partial \epsilon}(s, \epsilon) + \frac{\partial \boldsymbol{f}}{\partial \boldsymbol{u}}(s, \boldsymbol{x}\left(s, \epsilon\right), \boldsymbol{u}(s, \epsilon)) \frac{\partial \boldsymbol{u}}{\partial \epsilon}(s, \epsilon) \right] ds. \tag{B.2}$$

Differentiating (B.2) further with respect to time t gives

$$\frac{\partial^2 \boldsymbol{x}(t, \epsilon)}{\partial t \partial \epsilon} = D_1 \boldsymbol{f}\left(t, \boldsymbol{x}(t, \epsilon), \boldsymbol{u}(t, \epsilon)\right) \frac{\partial \boldsymbol{x}}{\partial \epsilon}(t, \epsilon) + D_2 \boldsymbol{f}\left(t, \boldsymbol{x}(t, \epsilon), \boldsymbol{u}(t, \epsilon)\right) \frac{\partial \boldsymbol{u}}{\partial \epsilon}(t, \epsilon), \tag{B.3}$$

where $\frac{\partial^2 \boldsymbol{x}(t_0, \epsilon)}{\partial t \partial \epsilon} = 0$. Note that the notations $D_1 \boldsymbol{f}$ and $D_2 \boldsymbol{f}$ are used to denote the partial derivative of $\boldsymbol{f}$ with respect to the first and second arguments, and is detailed more in Appendix A.1.

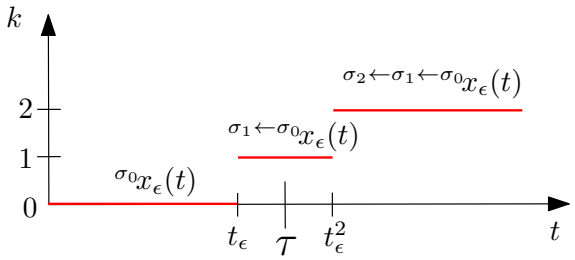

Figure B.1: A graphical illustration of a perturbed trajectory experiencing two jumps at the times t_ϵ and t_ϵ^2. The time τ is the jump time of the nominal trajectory, and one can observe that the perturbed trajectory does not have coinciding jump times with the nominal trajectory.

Evaluiating (B.3) at $\epsilon = \epsilon_0 := 0$ gives the continuous dynamics of our positive homogenization as

$$\dot{\boldsymbol{z}} = D_1\boldsymbol{f}(t, \boldsymbol{\alpha}(t), \boldsymbol{\mu})\boldsymbol{z}(t) + D_2\boldsymbol{f}(t, \boldsymbol{\alpha}(t), \boldsymbol{\mu})\boldsymbol{v}(t) \tag{B.4}$$

with $\boldsymbol{z} = \frac{\partial \boldsymbol{x}(t,\epsilon)}{\partial \epsilon}|_{\epsilon=0}$ and $\boldsymbol{v} = \frac{\partial \boldsymbol{u}(t,\epsilon)}{\partial \epsilon}|_{\epsilon=0}$. One can interpret (B.4) as the evolution of the perturbed trajectory $\boldsymbol{x}(t,\epsilon)$ with respect to the nominal trajectory $\boldsymbol{x}(t,0) := \boldsymbol{\alpha}(t)$. Getting $\boldsymbol{z} = 0$ then results in the perturbed trajectory being equal to the nominal trajectory.

B.2 Proof conewise constant jump gain

In this section, we prove that for an a-priori known mode sequence the conewise constant jump gain can be derived as (4.49), i.e., from individual jump gains (4.46) as in [23][1]. We only treat a perturbed trajectory with two jumps, see Figure B.1, but the approach can be extended to trajectories with multiple jumps. We have chosen for a relatively simple example as it is easy to present on paper. Note that we consider sufficiently small perturbations, such that a first-order approximation of the dynamics is valid. Furthermore, we assume that the guard functions, vectorfields, and jump maps are sufficiently smooth and that Assumption 4.1 holds.

Figure B.1 illustrates an example of a perturbed dynamical system experiencing two jumps at t_ϵ and t_ϵ^2 instead of one jump at nominal time τ. We want to combine the perturbed jumps and in-between flow effects of the dynamical system, i.e., the dynamics for the time-interval $t_\epsilon \leq t \leq t_\epsilon^2$, into one jump for the positive homogenization as

$$^{\sigma_2\leftarrow\sigma_1\leftarrow\sigma_0}\boldsymbol{z}(\tau) = {}^{\sigma_2\leftarrow\sigma_1\leftarrow\sigma_0}\boldsymbol{G}(\tau)\,{}^{\sigma_0}\boldsymbol{z}(\tau). \tag{B.5}$$

Note that the positive homogenization forms a local approximation of the behavior of the dynamical system and jumps only once at the nominal event time τ.

To realize (B.5), we make first-order approximations of the behavior of the dynamical system, evaluated at the perturbed event times, and express them in variables for nominal time τ. The state after the last jump of the dynamical system at t_ϵ^2 is described as

$$^{\sigma_2\leftarrow\sigma_1\leftarrow\sigma_0}\bar{\boldsymbol{x}}_\epsilon(t_\epsilon^2) = {}^{\sigma_2\leftarrow\sigma_1}\boldsymbol{g}({}^{\sigma_1\leftarrow\sigma_0}\bar{\boldsymbol{x}}_\epsilon(t_\epsilon^2), t_\epsilon^2), \tag{B.6}$$

where the pre-jump variable $^{\sigma_1\leftarrow\sigma_0}\bar{\boldsymbol{x}}(t_\epsilon^2)$ is further defined as

$$^{\sigma_1\leftarrow\sigma_0}\bar{\boldsymbol{x}}_\epsilon(t_\epsilon^2) = \int_{t_\epsilon}^{t_\epsilon^2} {}^{\sigma_1}\boldsymbol{f}(\,{}^{\sigma_1\leftarrow\sigma_0}\bar{\boldsymbol{x}}_\epsilon(t), {}^{\sigma_1}\bar{\boldsymbol{u}}(t,\epsilon), t)dt + {}^{\sigma_1\leftarrow\sigma_0}\boldsymbol{g}({}^{\sigma_0}\bar{\boldsymbol{x}}_\epsilon(t_\epsilon), t_\epsilon), \tag{B.7}$$

consisting of the flow during the unspecified mode (in-between t_ϵ and t_ϵ^2) and the first jump effects.

[1]The jump gain however does differ a bit in comparison with the one derived in [23]. This is due to the reset map being defined differently in this work

First single jump

We start by making a first-order approximation of the first jump effects solely, thus

$$^{\sigma_1\leftarrow\sigma_0}\bar{\boldsymbol{x}}_\epsilon(t_\epsilon) = {}^{\sigma_1\leftarrow\sigma_0}\boldsymbol{g}({}^{\sigma_0}\bar{\boldsymbol{x}}_\epsilon(t_\epsilon), t_\epsilon), \tag{B.8}$$

and do not treat the flow and last jump effects yet. This thus reduces in proving (4.46), cf. [23]. To keep a clear overview of all the steps in this analysis, the following notational simplifications are made

$$\begin{aligned} \bar{\boldsymbol{x}}^k_\epsilon(t) &= {}^{\sigma_k\leftarrow\cdots\leftarrow\sigma_1\leftarrow\sigma_0}\bar{\boldsymbol{x}}_\epsilon(t), \\ \bar{\boldsymbol{z}}^k(t) &= {}^{\sigma_k\leftarrow\cdots\leftarrow\sigma_1\leftarrow\sigma_0}\bar{\boldsymbol{z}}(t), \\ \bar{\boldsymbol{\alpha}}^k(t) &= {}^{\sigma_k}\bar{\boldsymbol{\alpha}}(t), \end{aligned} \tag{B.9}$$

where we indicate the current mode with a micro counter k. Following from (4.30), the left-term of (B.8) can be rewritten as

$$\bar{\boldsymbol{x}}^1_\epsilon(t_\epsilon) = \bar{\boldsymbol{\alpha}}^1(t_\epsilon) + \epsilon\bar{\boldsymbol{z}}^1(t_\epsilon) + o(\epsilon), \tag{B.10}$$

and one observes that the terms are evaluated at t_ϵ. Taking into account Assumption 3.1 and that the perturbed event times implicitly follow from the guard conditions, i.e.,

$$\gamma^{s_0}(\boldsymbol{x}^0_\epsilon(t_\epsilon), t_\epsilon) = 0, \tag{B.11}$$

we can obtain via the partial derivative of (B.11) with respect to ϵ a linear approximation of t_ϵ as a function of ϵ, cf. [23], giving

$$\begin{aligned} t_\epsilon := t^1(\epsilon) &= \tau + \epsilon\frac{dt_\epsilon}{d\epsilon}|_{\epsilon=0} + o(\epsilon), \\ &= \tau + \epsilon\Delta_1 + o(\epsilon), \end{aligned} \tag{B.12}$$

where we abbreviate the partial derivative with respect to ϵ as Δ_k. Note that Assumption 3.1 allows us to conclude the existence of an unique event time t_ϵ for sufficiently small values of ϵ, and that (B.11) only holds for perturbations that are sufficiently small.

We can then further evaluate the right-side terms of (B.10) by expanding the variables in series with respect to ϵ, rewriting the reference as

$$\begin{aligned} \bar{\boldsymbol{\alpha}}^1(t_\epsilon) &= \boldsymbol{\alpha}^1(\tau) + \epsilon\left[\frac{d\bar{\boldsymbol{\alpha}}^1}{dt}\frac{dt_\epsilon}{d\epsilon}\right]_{\epsilon=0} + o(\epsilon) \\ &= \boldsymbol{\alpha}^1(\tau) + \epsilon\dot{\boldsymbol{\alpha}}^1(\tau)\Delta_1 + o(\epsilon), \end{aligned} \tag{B.13}$$

and the positive homogenization as

$$\begin{aligned} \bar{\boldsymbol{z}}^1(t_\epsilon) &= \bar{\boldsymbol{z}}^1(\tau) + \epsilon\left[\frac{d\bar{\boldsymbol{z}}^1}{dt}\frac{dt_\epsilon}{d\epsilon}\right]_{\epsilon=0} + o(\epsilon) \\ &= \bar{\boldsymbol{z}}^2(\tau) + \epsilon\dot{\bar{\boldsymbol{z}}}^1(\tau)\Delta_1 + o(\epsilon). \end{aligned} \tag{B.14}$$

Combining (B.10), (B.13), and (B.14) results in the left-side term of (B.8) as

$$\bar{\boldsymbol{x}}^1_\epsilon(t_\epsilon) = \boldsymbol{\alpha}^1(\tau) + \epsilon(\dot{\boldsymbol{\alpha}}^1(\tau)\Delta_1 + \bar{\boldsymbol{z}}^1(\tau)) + o(\epsilon). \tag{B.15}$$

We generalize (B.15) for the post-impact state with counter k as

$$\bar{\boldsymbol{x}}^k_\epsilon(t^k_\epsilon) = \boldsymbol{\alpha}^k(\tau) + \epsilon(\dot{\boldsymbol{\alpha}}^k(\tau)\Delta_k + \bar{\boldsymbol{z}}^k(\tau)) + o(\epsilon) \tag{B.16}$$

and the pre-impact state with counter $k-1$ as

$$\bar{\boldsymbol{x}}^{k-1}_\epsilon(t^k_\epsilon) = \boldsymbol{\alpha}^{k-1}(\tau) + \epsilon(\dot{\boldsymbol{\alpha}}^{k-1}(\tau)\Delta_k + \bar{\boldsymbol{z}}^{k-1}(\tau)) + o(\epsilon). \tag{B.17}$$

To determine the unknown variable Δ_2, the pre-impact guard condition

$$\gamma^{s_0}(\boldsymbol{x}_\epsilon^0(t_\epsilon), t_\epsilon) = 0 \tag{B.18}$$

is evaluated. Note that $\sigma_{k-1} + s_{k-1} = \sigma_k$ as determined in Section 4.1.3. Similarly, we expand (B.18) in series with respect to ϵ giving

$$\begin{aligned}\gamma^{s_0}(\boldsymbol{x}_\epsilon^0(t_\epsilon), t_\epsilon) &= \gamma^{s_0}(\boldsymbol{\alpha}^0(\tau), \tau) + \epsilon \left[\frac{\partial \gamma^{s_0}}{\partial \boldsymbol{x}}(\frac{\partial \bar{\boldsymbol{x}}_\epsilon^0}{\partial \epsilon} + \frac{\partial \bar{\boldsymbol{x}}_\epsilon^0}{\partial t}\frac{dt_\epsilon}{d\epsilon}) + \frac{\partial \gamma^{s_0}}{\partial t}\frac{dt_\epsilon}{d\epsilon}\right]_{\epsilon=0} + o(\epsilon),\\ &= \epsilon D_1\gamma_1 \cdot \left(\dot{\boldsymbol{\alpha}}^0(\tau)\Delta_1 + \bar{\boldsymbol{z}}^0(\tau)\right) + \epsilon D_2\gamma_1 \cdot \Delta_1 + o(\epsilon),\\ &= 0,\end{aligned} \tag{B.19}$$

where $\gamma^{s_0}(\boldsymbol{\alpha}^0(\tau), \tau) = 0$ and

$$D_c\gamma_1 = D_c\gamma^{s_0}(\boldsymbol{\alpha}^0(\tau), \tau), \qquad c \in \{1, 2\}. \tag{B.20}$$

From (B.19), one determines the generalized expression

$$\Delta_k = \frac{dt_\epsilon^k}{d\epsilon}|_{\epsilon=0} = -\frac{D_1\gamma_k \cdot \bar{\boldsymbol{z}}^{k-1}(\tau)}{\dot{\gamma}_k}, \tag{B.21}$$

where

$$\begin{aligned} D_c\gamma_k &= D_c\gamma^{s_{k-1}}(\boldsymbol{\alpha}^{k-1}(\tau), \tau), \qquad c \in \{1, 2\}.\\ \dot{\gamma}_k &= D_1\gamma_k \cdot \boldsymbol{f}^{k-1} + D_2\gamma_k \cdot 1\\ \boldsymbol{f}^k &= {}^{\sigma_k}\boldsymbol{f}(\boldsymbol{\alpha}^k(\tau), {}^{\sigma_k}\boldsymbol{\mu}(\tau), \tau).\end{aligned} \tag{B.22}$$

Note that the notation $D_c\gamma$ in (B.22) indicates the partial derivative of γ with respect to its c'th argument. This notation is further detailed in Appendix A.1.

To determine the right-side of (B.8), we also expand the jump map in series with respect to ϵ resulting in

$$\begin{aligned}{}^{\sigma_1\leftarrow\sigma_0}\boldsymbol{g}(\bar{\boldsymbol{x}}_\epsilon^0(t_\epsilon), t_\epsilon) &= {}^{\sigma_1\leftarrow\sigma_0}\boldsymbol{g}(\boldsymbol{\alpha}^0(\tau), \tau) + \epsilon \left[\frac{\partial \boldsymbol{g}_1}{\partial \boldsymbol{x}}(\frac{\partial \bar{\boldsymbol{x}}_\epsilon^0}{\partial \epsilon} + \frac{\partial \bar{\boldsymbol{x}}_\epsilon^0}{\partial t}\frac{dt_\epsilon}{d\epsilon}) + \frac{\partial \boldsymbol{g}_1}{\partial t}\frac{dt_\epsilon}{d\epsilon}\right]_{\epsilon=0} + o(\epsilon)\\ &= \boldsymbol{\alpha}^1(\tau) + \epsilon D_1\boldsymbol{g}_1 \cdot \left(\dot{\boldsymbol{\alpha}}^0(\tau)\Delta_1 + \bar{\boldsymbol{z}}^0(\tau)\right) + \epsilon D_2\boldsymbol{g}_1 \cdot \Delta_1 + o(\epsilon),\end{aligned} \tag{B.23}$$

where

$$\begin{aligned}\boldsymbol{g}_k &= {}^{\sigma_k\leftarrow\sigma_{k-1}}\boldsymbol{g}(\boldsymbol{x}_\epsilon^{k-1}(t_\epsilon^k), t_\epsilon^k),\\ D_c\boldsymbol{g}_k &= D_c\,{}^{\sigma_k\leftarrow\sigma_{k-1}}\boldsymbol{g}(\boldsymbol{\alpha}^{k-1}(\tau), \tau), \qquad c \in \{1, 2\}.\end{aligned} \tag{B.24}$$

Inserting (B.15) and (B.23) into (B.8) and assuming that perturbations are sufficiently small, i.e., we neglect higher-order terms $o(\epsilon)$, gives the individual jump gain (4.46) as

$$\begin{aligned}\bar{\boldsymbol{z}}^k(\tau) &= {}^{\sigma_k\leftarrow\sigma_{k-1}}\boldsymbol{G}(\tau)\bar{\boldsymbol{z}}^{k-1}(\tau)\\ {}^{\sigma_k\leftarrow\sigma_{k-1}}\boldsymbol{G}(\tau) &= \frac{\boldsymbol{f}^k - \dot{\boldsymbol{g}}_k}{\dot{\gamma}_k}D_1\gamma_k + D_1\boldsymbol{g}_k,\end{aligned} \tag{B.25}$$

where

$$\dot{\boldsymbol{g}}_k = D_1\boldsymbol{g}_k \cdot \boldsymbol{f}^{k-1} + D_2\boldsymbol{g}_k \cdot 1. \tag{B.26}$$

Perturbed flow effects and total jump

We now derive the first-order approximation of the right term of (B.6), which incorporates a novel flow term as seen as the integral in (B.7). This integral is rewritten as

$$\int_{t_\epsilon}^{t_\epsilon^2} {}^{\sigma_1}\boldsymbol{f}(t,\epsilon)dt = \boldsymbol{F}(t_\epsilon^2,\epsilon) - \boldsymbol{F}(t_\epsilon,\epsilon) = \boldsymbol{\Phi}(t_\epsilon, t_\epsilon^2, \epsilon), \tag{B.27}$$

where we simplify the arguments of ${}^{\sigma_1}\boldsymbol{f}$ to (t,ϵ) as the terms $\boldsymbol{x}$ and $\boldsymbol{u}$ are solely dependent on t and ϵ. The input is defined as

$${}^{\sigma_k}\bar{\boldsymbol{u}}(t,\epsilon) = {}^{\sigma_k}\bar{\boldsymbol{\mu}}(t) + \epsilon^{\sigma_k}\bar{\boldsymbol{v}}(t), \tag{B.28}$$

where ${}^{\sigma_0}\bar{\boldsymbol{u}} = {}^{\sigma_1}\bar{\boldsymbol{u}}$ as we keep using the same pre-nominal event input during these unspecified modes. We expand $\boldsymbol{\Phi}$ in series with respect to ϵ, giving

$$\boldsymbol{\Phi}(t^1(\epsilon), t^2(\epsilon), \epsilon) = \boldsymbol{\Phi}(t^1(0), t^2(0), 0) + \epsilon\frac{d\boldsymbol{\Phi}}{d\epsilon}|_{\epsilon=0} + o(\epsilon), \tag{B.29}$$

where $t^1(\epsilon)$ and $t^2(\epsilon)$ denote, respectively, the first and second perturbed event times. Note that we assume the perturbations to be sufficiently small such that we can write the event times as a function of ϵ, see (B.12).

The first term of (B.29) results in

$$\boldsymbol{\Phi}(t^1(0), t^2(0), 0) = \int_\tau^\tau {}^{\sigma_1}\boldsymbol{f}(s,0)dt = \boldsymbol{F}(\tau,0) - \boldsymbol{F}(\tau,0) = 0, \tag{B.30}$$

where $t^1(0) = t^2(0) = \tau$. The second term of (B.29) is derived via *Leibniz integral rule*, resulting in

$$\frac{d\boldsymbol{\Phi}}{d\epsilon} := \frac{d}{d\epsilon}\int_{t(\epsilon)}^{t^2(\epsilon)} {}^{\sigma_1}\boldsymbol{f}(t,\epsilon)dt = {}^{\sigma_1}\boldsymbol{f}(t^2(\epsilon),\epsilon)\frac{dt^2(\epsilon)}{d\epsilon} - {}^{\sigma_1}\boldsymbol{f}(t(\epsilon),\epsilon)\frac{dt(\epsilon)}{d\epsilon} + \int_{t(\epsilon)}^{t^2(\epsilon)}\frac{\partial {}^{\sigma_1}\boldsymbol{f}(t,\epsilon)}{\partial\epsilon}dt, \tag{B.31}$$

which evaluated at $\epsilon = 0$ turns into

$$\frac{d\boldsymbol{\Phi}}{d\epsilon}|_{\epsilon=0} = \boldsymbol{f}^1\Delta_2 - \boldsymbol{f}^1\Delta_1, \tag{B.32}$$

where we use the simplification $\boldsymbol{f}^k$ as stated in (B.22).

We can then approximate the right term of (B.6) with a series expansion with respect to ϵ as

$${}^{\sigma_2\leftarrow\sigma_1}\boldsymbol{g}({}^{\sigma_1\leftarrow\sigma_0}\bar{\boldsymbol{x}}_\epsilon(t_\epsilon^2), t_\epsilon^2) = \bar{\boldsymbol{\alpha}}^2(\tau) + \epsilon\frac{\partial {}^{\sigma_2\leftarrow\sigma_1}\boldsymbol{g}({}^{\sigma_1\leftarrow\sigma_0}\bar{\boldsymbol{x}}_\epsilon(t_\epsilon^2), t_\epsilon^2)}{\partial\epsilon}|_{\epsilon=0} + o(\epsilon) \tag{B.33}$$

with, while substituting (B.7),

$$\begin{aligned}\frac{\partial {}^{\sigma_2\leftarrow\sigma_1}\boldsymbol{g}({}^{\sigma_1\leftarrow\sigma_0}\bar{\boldsymbol{x}}_\epsilon(t_\epsilon^2), t_\epsilon^2)}{\partial\epsilon}|_{\epsilon=0} &= \left[\frac{\partial\boldsymbol{g}_2}{\partial\boldsymbol{x}}\left(\frac{d\boldsymbol{\Phi}}{d\epsilon} + \frac{\partial\boldsymbol{g}_1}{\partial\boldsymbol{x}}(\frac{\partial\bar{\boldsymbol{x}}^0}{\partial\epsilon} + \frac{\partial\bar{\boldsymbol{x}}^0}{\partial t}\frac{dt(\epsilon)}{d\epsilon}) + \frac{\partial\boldsymbol{g}_1}{\partial t}\frac{dt(\epsilon)}{d\epsilon}\right) + \frac{\partial\boldsymbol{g}_2}{\partial t}\frac{dt^2(\epsilon)}{d\epsilon}\right]_{\epsilon=0} \\ &= D_1\boldsymbol{g}_2\cdot\left(\boldsymbol{f}^1(\Delta_2-\Delta_1) + D_1\boldsymbol{g}_1\cdot(\bar{\boldsymbol{z}}^0 + \boldsymbol{f}^0\Delta_1) + D_2\boldsymbol{g}_1\cdot\Delta_1\right) + D_2\boldsymbol{g}_2\cdot\Delta_2,\end{aligned} \tag{B.34}$$

where we use the notational simplifications in (B.22) and (B.24).

We then provide the first-order approximation of the total jump effects, expressed at the time τ, by inserting (B.15), (B.33), and (B.34) into (B.6), giving

$$\bar{\boldsymbol{z}}^2(\tau) = D_1\boldsymbol{g}_2\cdot\left(\boldsymbol{f}^1(\Delta_2-\Delta_1) + D_1\boldsymbol{g}_1\cdot(\bar{\boldsymbol{z}}^0(\tau) + \boldsymbol{f}^0\Delta_1) + D_2\boldsymbol{g}_1\cdot\Delta_1\right) + D_2\boldsymbol{g}_2\cdot\Delta_2 - \boldsymbol{f}^2\Delta_2. \tag{B.35}$$

All that is left, is to prove that the right side of (B.35) is equal to the right side of (B.5). To give more insight about this comparison, equation (B.35) is rearranged into four grouped terms as

$$\bar{\boldsymbol{z}}^2(\tau) = D_1\boldsymbol{g}_2\cdot\boldsymbol{f}^1\Delta_2+D_1\boldsymbol{g}_2\cdot(-\boldsymbol{f}^1\Delta_1)+D_1\boldsymbol{g}_2\cdot\Big(D_1\boldsymbol{g}_1\cdot(\bar{\boldsymbol{z}}^0(\tau)+\boldsymbol{f}^0\Delta_1)+D_2\boldsymbol{g}_1\cdot\Delta_1\Big)+(D_2\boldsymbol{g}_2\cdot 1-\boldsymbol{f}^2)\Delta_2. \tag{B.36}$$

Taking into account that $\bar{\boldsymbol{z}}^1(\tau) = {}^{\sigma_1\leftarrow\sigma_0}\boldsymbol{G}(\tau)\bar{\boldsymbol{z}}^0(\tau)$ as via (B.25), the four grouped terms, from left to right, are worked out as

$$\begin{aligned}
D_1\boldsymbol{g}_2\cdot(\boldsymbol{f}^1\Delta_2) &= \left(\frac{-D_1\boldsymbol{g}_2\cdot\boldsymbol{f}^1}{\dot{\gamma}_2}D_1\gamma_2\right){}^{\sigma_1\leftarrow\sigma_0}\boldsymbol{G}(\tau)\bar{\boldsymbol{z}}^0(\tau),\\
D_1\boldsymbol{g}_2\cdot(-\boldsymbol{f}^1\Delta_1) &= D_1\boldsymbol{g}_2\left(\frac{\boldsymbol{f}^1}{\dot{\gamma}_1}D_1\gamma_1\right)\bar{\boldsymbol{z}}^0(\tau),\\
D_1\boldsymbol{g}_2\cdot\Big(D_1\boldsymbol{g}_1\cdot(\bar{\boldsymbol{z}}^0(\tau)+\boldsymbol{f}^0\Delta_1)+D_2\boldsymbol{g}_1\cdot\Delta_1\Big) &= D_1\boldsymbol{g}_2\left(\frac{-D_1\boldsymbol{g}_1\cdot\boldsymbol{f}^0-D_2\boldsymbol{g}_1\cdot 1}{\dot{\gamma}_1}D_1\gamma_1+D_1\boldsymbol{g}_1\right)\bar{\boldsymbol{z}}^0(\tau)\\
(D_2\boldsymbol{g}_2\cdot 1-\boldsymbol{f}^2)\Delta_2 &= \left(\frac{\boldsymbol{f}^2-D_2\boldsymbol{g}_2\cdot 1}{\dot{\gamma}_2}D_1\gamma_2\right){}^{\sigma_1\leftarrow\sigma_0}\boldsymbol{G}(\tau)\bar{\boldsymbol{z}}^0(\tau).
\end{aligned} \tag{B.37}$$

Inserting (B.37) into (B.36) then gives

$$\bar{\boldsymbol{z}}^2(\tau) = \left(\frac{\boldsymbol{f}^2-D_1\boldsymbol{g}_2\cdot\boldsymbol{f}^1-D_2\boldsymbol{g}_2\cdot 1}{\dot{\gamma}_2}D_1\gamma_2+D_1\boldsymbol{g}_2\right){}^{\sigma_1\leftarrow\sigma_0}\boldsymbol{G}(\tau)\bar{\boldsymbol{z}}^0(\tau), \tag{B.38}$$

where the first part can be summarized as ${}^{\sigma_2\leftarrow\sigma_1}\boldsymbol{G}(\tau)$ according to (B.25). This will then change (B.38) into (B.5). Note that adding more jumps to the perturbed trajectory will still lead the conewise constant jump gain to take a format as (4.49).

B.3 Proof positively homogeneous system

In this section, we prove that the typically positively homogeneous jump mapping $\boldsymbol{G}(\tau,{}^{\sigma_0}\boldsymbol{z}(\tau))$ makes our local model positively homogeneous, and consequently we have a positively homogeneous time-triggered hybrid system. The solution of our local model before the jump is given as

$${}^{\sigma_0}\bar{\boldsymbol{z}}(t) = e^{{}^{\sigma_0}\boldsymbol{A}(t-t_0)}\boldsymbol{z}_0+\int_{t_0}^{t}e^{{}^{\sigma_0}\boldsymbol{A}(t-s){}^{\sigma_0}}\boldsymbol{B}(s)\boldsymbol{v}(s)ds. \tag{B.39}$$

Before the jump, the local model shows linear behavior. To show this, one could define two states ${}^{\sigma_0}\boldsymbol{z}_{c1}(t)$ and ${}^{\sigma_0}\boldsymbol{z}_{c2}(t)$, realized with initial conditions ${}^{\sigma_0}\boldsymbol{z}_{c1}(t_0)$ and ${}^{\sigma_0}\boldsymbol{z}_{c2}(t_0)$ and input terms $\boldsymbol{v}_{c1}(t)=\boldsymbol{v}_{c2}(t)=\boldsymbol{v}(t)$. Scaling the initial condition and input term with a scalar ϵ, results in a similarly scaled ouput as can be deduced from (B.39). Performing additions with these states, while assuming that no jump takes place, results in

$$\epsilon_1{}^{\sigma_0}\boldsymbol{z}_{c1}(t)+\epsilon_2{}^{\sigma_0}\boldsymbol{z}_{c2}(t) = e^{{}^{\sigma_0}\boldsymbol{A}(t-t_0)}\left(\epsilon_1{}^{\sigma_0}\boldsymbol{z}_{c1}(t_0)+\epsilon_2{}^{\sigma_0}\boldsymbol{z}_{c2}(t_0)\right)+(\epsilon_1+\epsilon_2)\int_{t_0}^{t}e^{{}^{\sigma_0}\boldsymbol{A}(t-s){}^{\sigma_0}}\boldsymbol{B}(s)\boldsymbol{v}(s)ds, \tag{B.40}$$

where $\epsilon_1\in\mathbb{R}$ and $\epsilon_2\in\mathbb{R}$.

Taking into account jumping effects, however, typically destroys the linearity property. Assuming we have N number of possible mode sequences, we define the conewise constant jump gain as

$$\boldsymbol{G}(\tau,{}^{\sigma_0}\bar{\boldsymbol{z}}(\tau)) = \begin{cases}\boldsymbol{G}_1(\tau) & \text{condition 1,}\\ \boldsymbol{G}_2(\tau) & \text{condition 2,}\\ \quad\vdots & \\ \boldsymbol{G}_N(\tau) & \text{condition N,}\end{cases} \tag{B.41}$$

where we assume all N constant jump gains and jump shaping conditions to be different from each other. Assuming that

$$ {}^{\sigma_0}\boldsymbol{z}_{c1}(\tau) = e^{{}^{\sigma_0}\boldsymbol{A}(\tau-t_0){}^{\sigma_0}} \boldsymbol{z}_{c1}(t_0) + \int_{t_0}^{\tau} e^{{}^{\sigma_0}\boldsymbol{A}(t-s){}^{\sigma_0}} \boldsymbol{B}(s)\boldsymbol{v}(s)ds \tag{B.42} $$

jumps with a jump gain $\boldsymbol{G}_1(\tau)$ and

$$ {}^{\sigma_0}\boldsymbol{z}_{c2}(\tau) = e^{{}^{\sigma_0}\boldsymbol{A}(\tau-t_0){}^{\sigma_0}} \boldsymbol{z}_{c2}(t_0) + \int_{t_0}^{\tau} e^{{}^{\sigma_0}\boldsymbol{A}(t-s){}^{\sigma_0}} \boldsymbol{B}(s)\boldsymbol{v}(s)ds \tag{B.43} $$

jumps with a jump gain $\boldsymbol{G}_2(\tau)$, then we can define the solution of the local model after jump as

$$ \begin{aligned} {}^{\sigma_{s,1}}\boldsymbol{z}_{c1}(t) &= e^{{}^{\sigma_{s,1}}\boldsymbol{A}(t-\tau)}\boldsymbol{G}_1(\tau){}^{\sigma_0}\boldsymbol{z}_{c1}(\tau) + \int_{\tau}^{t} e^{{}^{\sigma_{s,1}}\boldsymbol{A}(t-s){}^{\sigma_{s,1}}} \boldsymbol{B}(s)\boldsymbol{v}(s)ds, \\ {}^{\sigma_{s,2}}\boldsymbol{z}_{c2}(t) &= e^{{}^{\sigma_{s,2}}\boldsymbol{A}(t-\tau)}\boldsymbol{G}_2(\tau){}^{\sigma_0}\boldsymbol{z}_{c2}(\tau) + \int_{\tau}^{t} e^{{}^{\sigma_{s,2}}\boldsymbol{A}(t-s){}^{\sigma_{s,2}}} \boldsymbol{B}(s)\boldsymbol{v}(s)ds, \end{aligned} \tag{B.44} $$

where $\sigma_{s,1}$ and $\sigma_{s,2}$ are two different mode sequences. We can deduce two differences in comparison with a model with no jumps. First, scaling the initial condition and input term with a scalar will result in a similarly scaled output, only if it is scaled with a non-negative number. Consequently, we term the system positively homogeneous. The second difference, is that the linearity property may not hold. We could add the two solutions of (B.44) together as

$$ {}^{\sigma_{s,1}}\boldsymbol{z}_{c1}(t) + {}^{\sigma_{s,2}}\boldsymbol{z}_{c2}(t) = e^{{}^{\sigma_s}\boldsymbol{A}(t-\tau)} \left(\boldsymbol{G}_1(\tau){}^{\sigma_0}\boldsymbol{z}_{c1}(\tau) + \boldsymbol{G}_2(\tau){}^{\sigma_0}\boldsymbol{z}_{c2}(\tau)\right) + 2\int_{\tau}^{t} e^{{}^{\sigma_s}\boldsymbol{A}(t-s){}^{\sigma_s}} \boldsymbol{B}(s)\boldsymbol{v}(s)ds, \tag{B.45} $$

where one observes that the two jump gains $\boldsymbol{G}_1$ and $\boldsymbol{G}_2$ are present in the right side. Taking, however, an initial condition ${}^{\sigma_0}\boldsymbol{z}_{c3}(t_0) = {}^{\sigma_0}\boldsymbol{z}_{c1}(t_0) + {}^{\sigma_0}\boldsymbol{z}_{c2}(t_0)$ and input term $\boldsymbol{v}_{c3}(t) = 2\boldsymbol{v}(t)$, will only let the system experience a jump via one of the jump gains formulated in (B.41). A solution may then look like

$$ {}^{\sigma_{s,3}}\boldsymbol{z}_{c3}(t) = e^{{}^{\sigma_s}\boldsymbol{A}(t-\tau)} G_N(\tau){}^{\sigma_0}\boldsymbol{z}_{c3}(\tau) + \int_{\tau}^{t} e^{{}^{\sigma_s}\boldsymbol{A}(t-s){}^{\sigma_s}} \boldsymbol{B}(s)\boldsymbol{v}_3(s)ds, \tag{B.46} $$

which does not correspond with (B.45) as it has neither jump gains $\boldsymbol{G}_1(\tau)$ and $\boldsymbol{G}_2(\tau)$ in its expression, even though it used the same initial conditions. We thus have a positively homogeneous time-triggered hybrid system. Note that when all possible shapes of (B.41) are equal, we will have a linear time-triggered hybrid system instead.

B.4 Closed-loop continuous dynamics positive homogenization

In this section, we show how a closed-loop input term for the nonlinear hybrid system influences the positive homogenization, cf. [23]. The vectorfield of the closed-loop continuous dynamics can be specified as

$$\boldsymbol{f}_{cl}(t,\boldsymbol{x}(t,\epsilon)) := \boldsymbol{f}\left(t,\boldsymbol{x}(t,\epsilon),\boldsymbol{u}\left(t,\boldsymbol{x}(t,\epsilon)\right)\right), \tag{B.47}$$

where we define the closed-loop input as $\boldsymbol{u}(t,\boldsymbol{x}(t,\epsilon)) = \boldsymbol{\mu}(t) - \boldsymbol{K}(t)\left(\boldsymbol{x}(t,\epsilon) - \boldsymbol{\alpha}(t)\right)$. We take the same approach as in Appendix B.1, where we define the state as

$$\boldsymbol{x}(t,\epsilon) = \boldsymbol{x}(t_0,\epsilon) + \int_{t_0}^{t} \boldsymbol{f}\left(s,\boldsymbol{x}(s,\epsilon),\boldsymbol{u}\left(s,\boldsymbol{x}(s,\epsilon)\right)\right) ds. \tag{B.48}$$

We then take the partial derivative with respect to ϵ resulting in

$$\begin{aligned}\frac{\partial \boldsymbol{x}(t,\epsilon)}{\partial \epsilon} = \frac{\partial \boldsymbol{x}(t_0,\epsilon)}{\partial \epsilon} + \int_{t_0}^{t} \Bigg[&\frac{\partial \boldsymbol{f}}{\partial \boldsymbol{x}}(s,\boldsymbol{x}\left(s,\epsilon\right),\boldsymbol{u}(s,\boldsymbol{x}(s,\epsilon)))\,\frac{\partial \boldsymbol{x}}{\partial \epsilon}(s,\epsilon)\cdots \\ &+ \frac{\partial \boldsymbol{f}}{\partial \boldsymbol{u}}(s,\boldsymbol{x}\left(s,\epsilon\right),\boldsymbol{u}(s,\boldsymbol{x}(s,\epsilon)))\,\frac{\partial \boldsymbol{u}}{\partial \boldsymbol{x}}(s,\boldsymbol{x}(s,\epsilon))\frac{\partial \boldsymbol{x}}{\partial \epsilon}(s,\epsilon) ds.\end{aligned} \tag{B.49}$$

We then take the derivative with respect to time t to obtain

$$\frac{\partial^2 \boldsymbol{x}(t,\epsilon)}{\partial t \partial \epsilon} = \left(D_1\boldsymbol{f}\left(t,\boldsymbol{x}(t,\epsilon),\boldsymbol{u}(t,\boldsymbol{x}(t,\epsilon)\right) - \boldsymbol{K}(t)D_2\boldsymbol{f}\left(t,\boldsymbol{x}(t,\epsilon),\boldsymbol{u}(t,\boldsymbol{x}(t,\epsilon)\right)\right)\right)\frac{\partial \boldsymbol{x}}{\partial \epsilon}(t,\epsilon), \tag{B.50}$$

where $\frac{\partial^2 \boldsymbol{x}(t_0,\epsilon)}{\partial t \partial \epsilon} = 0$. Evaluating (B.50) at $\epsilon = \epsilon_0 := 0$ results in the closed-loop continuous dynamics of the positive homogenization as

$$\dot{\boldsymbol{z}} = \left(D_1\boldsymbol{f}(t,\boldsymbol{\alpha}(t),\boldsymbol{\mu}(t)) - \boldsymbol{K}(t)D_2\boldsymbol{f}(t,\boldsymbol{\alpha}(t),\boldsymbol{\mu}(t))\right)\boldsymbol{z}(t) \tag{B.51}$$

with $\boldsymbol{z} = \frac{\partial \boldsymbol{x}(t,\epsilon)}{\partial \epsilon}|_{\epsilon=0}$. One will notice that (B.4) changes into (B.51) when $\boldsymbol{v}(t) = -\boldsymbol{K}(t)\boldsymbol{z}(t)$, and consequently we may analyze the influence of the control law in Section 3.2.3 via the closed-loop dynamics (B.51). Note that the conewise constant jump gain does not change in closed-loop, as one can observe by performing the analysis in Appendix B.2 with the perturbed input $\boldsymbol{v}(t) = -\boldsymbol{K}(t)\boldsymbol{z}(t)$.

Appendix C

Continuous dynamics plank-block system

In this appendix, the continuous dynamics of the plank-block system are derived both in local and in *global* coordinates (i.e. position and orientation of the block with respect to frame $\{O^0, \vec{\boldsymbol{e}}^0\}$, see Figure 5.1). The unconstrained dynamics in global coordinates are formulated first. We then apply a transformation of coordinates, see [33, Section 5.2.3, p.111-114], to derive the unconstrained local coordinate dynamics. At the end, expressions for the contact distances $\boldsymbol{h}_l$ are derived. Note that more information about the notations used in this appendix can be found in Appendix A.1.

C.1 Unconstrained continuous dynamics in global coordinates

We consider the system in Figure 5.1 and use Lagrange's equation, see Section 2.1.1, to describe our unconstrained model. We now describe the block coordinates w.r.t. frame 0, giving the so-called global coordinates

$$\boldsymbol{q}_g = \begin{pmatrix} \mathrm{x}_g & \mathrm{y}_g & \theta_g & \phi \end{pmatrix}^T, \tag{C.1}$$

and global velocities terms

$$\mathbf{v}_g = \begin{pmatrix} \dot{\mathrm{x}}_g & \dot{\mathrm{y}}_g & \dot{\theta}_g & \dot{\phi} \end{pmatrix}^T, \tag{C.2}$$

to which we solve

$$\frac{d}{dt}(T_{,\mathbf{v}_g}) - T_{,\boldsymbol{q}_g} + V_{,\boldsymbol{q}_g} = (\boldsymbol{Q}^{nc})^T. \tag{C.3}$$

The total kinetic energy T is the sum of the kinetic energies of the two rigid bodies. Denoting the kinetic energy of the block T_B and of the plank T_P, it follows that $T = T_B + T_P$ with

$$T_i = \frac{1}{2}\mathrm{m}_i \dot{\vec{r}}_i \cdot \dot{\vec{r}}_i + \frac{1}{2}\vec{w}_i \cdot \vec{\Omega}_i \ , \qquad i \in \{B, P\}. \tag{C.4}$$

The positions are expressed as

$$\begin{aligned} \vec{r}_B &= \begin{pmatrix} \mathrm{x}_g & \mathrm{y}_g & 0 \end{pmatrix} \vec{\boldsymbol{e}}^0, \\ \vec{r}_P &= \begin{pmatrix} \frac{\cos(\phi) L_p}{2} & \frac{\sin(\phi) L_p}{2} & 0 \end{pmatrix} \vec{\boldsymbol{e}}^0, \end{aligned} \tag{C.5}$$

and the angular velocities as

$$\begin{aligned} \vec{\omega}_B &= {}^{20}\boldsymbol{w}_B^2 \vec{\boldsymbol{e}}^2 = \dot{\theta}_g \vec{e}_3^{\,2} = \dot{\theta}_g \vec{e}_3^{\,0}, \\ \vec{\omega}_P &= {}^{10}\boldsymbol{w}_B^1 \vec{\boldsymbol{e}}^1 = \dot{\phi} \vec{e}_3^{\,1} = \dot{\phi} \vec{e}_3^{\,0}. \end{aligned} \tag{C.6}$$

The angular momentum is defined as

$$\vec{\Omega}_i = {}_i\underline{\boldsymbol{J}} \cdot \vec{w}_i, \qquad i \in \{B, P\}, \tag{C.7}$$

with the inertia tensor

$${}_i\underline{\boldsymbol{J}} = (\vec{\boldsymbol{e}}^o)^T \, {}^0_i\boldsymbol{J} \, \vec{\boldsymbol{e}}^0, \qquad i \in \{B, P\}. \tag{C.8}$$

Combining (C.4)-(C.8) gives

$$\begin{aligned} T_B &= \frac{1}{2}(\mathrm{m}_B(\dot{\mathrm{x}}_g^2 + \dot{\mathrm{y}}_g^2) + J_B\dot{\theta}_g^2), \\ T_P &= \frac{1}{2}(\mathrm{m}_P\frac{L_p^2}{4} + J_p)\dot{\phi}^2, \end{aligned} \tag{C.9}$$

where J_B and J_P represent the moment of inertia of, respectively, block and plank around the $\vec{e}_3$ axis. The potential energy for the two rigid bodies, together forming the total potential energy of the system, is formulated as

$$\begin{aligned} V_B &= -\mathrm{m}_B\vec{\mathrm{g}} \cdot \vec{r}_B = \mathrm{m}_B\mathrm{g}\mathrm{y}_g, \\ V_P &= -\mathrm{m}_P\vec{\mathrm{g}} \cdot \vec{r}_P + \int_0^\phi \mathrm{k}_P \; s \; ds = \mathrm{m}_P\mathrm{g}\frac{L_P}{2}\sin(\phi) + \frac{1}{2}\mathrm{k}_P\phi^2, \end{aligned} \tag{C.10}$$

where $\vec{\mathrm{g}} = -\mathrm{g}e_2^0$ is the gravitational acceleration. We observe that the sole contribution to the potential energy of the block is due to gravitational forces, while the plank also gets the contribution of internal energy due to the spring.

For the non-conservative forces, we have two contributions. One due to the damping of the plank and the other due to the actuation of the block. It follows that

$$\boldsymbol{Q}_{nc} = \boldsymbol{Q}_d + \boldsymbol{S}_g(\boldsymbol{q}_g)\boldsymbol{u} = \begin{pmatrix} 0 \\ 0 \\ 0 \\ -\mathrm{b}_P\phi^2 \end{pmatrix} + \begin{pmatrix} 1 & 0 & 0 \\ 0 & 1 & 0 \\ 0 & 0 & 1 \\ 0 & 0 & 0 \end{pmatrix} \begin{pmatrix} F_1 \\ F_2 \\ \tau_{rot} \end{pmatrix}, \tag{C.11}$$

where we assume to be able to actuate the block in the three directions $\mathrm{x}_g, \mathrm{y}_g$, and θ_g. Substituting (C.9), (C.10) and (C.11) in (C.3), gives the equations of motion

$$\boldsymbol{M}_g(\boldsymbol{q}_g)\dot{\mathbf{v}}_g - \boldsymbol{H}_g(\boldsymbol{q}_g, \mathbf{v}_g) = \boldsymbol{S}_g(\boldsymbol{q}_g)\boldsymbol{u}, \tag{C.12}$$

with

$$\boldsymbol{M}_g(\boldsymbol{q}_g) = \begin{pmatrix} \mathrm{m}_B & 0 & 0 & 0 \\ 0 & \mathrm{m}_B & 0 & 0 \\ 0 & 0 & J_B & 0 \\ 0 & 0 & 0 & \frac{\mathrm{m}_P L_P^2}{4} + J_P \end{pmatrix}, \tag{C.13}$$

$$\boldsymbol{H}_g(\boldsymbol{q}_g, \mathbf{v}_g) = \begin{pmatrix} 0 \\ -\mathrm{m}_B g \\ 0 \\ -\mathrm{m}_P\dot{\phi}^2 - \frac{L_P\mathrm{g}\mathrm{m}_P\cos(\phi)}{2} - \mathrm{k}_P\phi \end{pmatrix}, \tag{C.14}$$

$$\boldsymbol{S}_g(\boldsymbol{q}_g) = \begin{pmatrix} 1 & 0 & 0 \\ 0 & 1 & 0 \\ 0 & 0 & 1 \\ 0 & 0 & 0 \end{pmatrix}. \tag{C.15}$$

C.2 Unconstrained continuous dynamics in local coordinates

We now derive the continuous dynamics in local coordinates. We do this by applying a coordinate transformation from the global coordinates $\boldsymbol{q}_g$ into local coordinates $\boldsymbol{q}_l$, see (5.1), via the principle of virtual work, see [33, Section 5.2.3, p.111-114]. We thus formulate the virtual work as

$$\delta \boldsymbol{q}_g^T \Big(\boldsymbol{M}_g(\boldsymbol{q}_g)\dot{\mathbf{v}}_g - \boldsymbol{H}_g(\boldsymbol{q}_g, \mathbf{v}_g) - \boldsymbol{S}_g(\boldsymbol{q}_g)\boldsymbol{u} \Big) = \delta \boldsymbol{q}_l^T \Big(\boldsymbol{M}_l(\boldsymbol{q}_l)\dot{\mathbf{v}}_l - \boldsymbol{H}_l(\boldsymbol{q}_l, \mathbf{v}_l) - \boldsymbol{S}_l(\boldsymbol{q}_l)\boldsymbol{u} \Big), \tag{C.16}$$

where on the left the global coordinate terms and on the right the local coordinate terms are formulated. The coordinates $\boldsymbol{q}_g$ and $\boldsymbol{q}_l$ are related to each other by the expression

$$\boldsymbol{q}_g(\boldsymbol{q}_l) = \begin{pmatrix} \cos(\phi)\mathrm{x}_l - \sin(\phi)\mathrm{y}_l \\ \sin(\phi)\mathrm{x}_l + \cos(\phi)\mathrm{y}_l \\ \theta_l + \phi \\ \phi \end{pmatrix}, \tag{C.17}$$

from which we can find the derivatives

$$\begin{aligned} \mathbf{v}_g(\boldsymbol{q}_l, \mathbf{v}_l) &= \frac{\partial \boldsymbol{q}_g(\boldsymbol{q}_l)}{\partial \boldsymbol{q}_l}\mathbf{v}_l = \mathbf{T}_l(\boldsymbol{q}_l)\mathbf{v}_l, \\ \dot{\mathbf{v}}_g(\boldsymbol{q}_l, \mathbf{v}_l, \dot{\mathbf{v}}_l) &= \mathbf{T}_l(\boldsymbol{q}_l)\dot{\mathbf{v}}_l + \dot{\mathbf{T}}_l(\boldsymbol{q}_l, \mathbf{v}_l)\mathbf{v}_l. \end{aligned} \tag{C.18}$$

Taking into account that $\delta \boldsymbol{q}_g = \mathbf{T}_l(\boldsymbol{q}_l)\delta \boldsymbol{q}_l$, we transform the left side of (C.16) into

$$\delta \boldsymbol{q}_l^T \Big(\mathbf{T}_l^T \boldsymbol{M}_g\Big(\boldsymbol{q}_g(\boldsymbol{q}_l)\Big)\mathbf{T}_l\dot{\mathbf{v}}_l + \mathbf{T}_l^T \boldsymbol{M}_g\Big(\boldsymbol{q}_g(\boldsymbol{q}_l)\Big)\dot{\mathbf{T}}_l\mathbf{v}_l - \mathbf{T}_l^T \boldsymbol{H}_g\Big(\boldsymbol{q}_g(\boldsymbol{q}_l), \mathbf{v}_g(\boldsymbol{q}_l, \mathbf{v}_l)\Big)\Big) - \mathbf{T}_l^T \boldsymbol{S}_g\Big(\boldsymbol{q}_g(\boldsymbol{q}_l)\Big)\boldsymbol{u}\Big), \tag{C.19}$$

from which, considering (C.16), follows that

$$\begin{aligned} \boldsymbol{M}_l(\boldsymbol{q}_l) &= \mathbf{T}_l^T \boldsymbol{M}_g\Big(\boldsymbol{q}_g(\boldsymbol{q}_l)\Big)\mathbf{T}_l, \\ \boldsymbol{H}_l(\boldsymbol{q}_l, \dot{\boldsymbol{q}}_l) &= \mathbf{T}_l^T \boldsymbol{H}_g\Big(\boldsymbol{q}_g(\boldsymbol{q}_l), \mathbf{v}_g(\boldsymbol{q}_l, \mathbf{v}_l)\Big)\Big) - \mathbf{T}_l^T \boldsymbol{M}_g\Big(\boldsymbol{q}_g(\boldsymbol{q}_l)\Big)\dot{\mathbf{T}}_l\mathbf{v}_l, \\ \boldsymbol{S}_l(\boldsymbol{q}_l) &= \mathbf{T}_l^T \boldsymbol{S}_g\Big(\boldsymbol{q}_g(\boldsymbol{q}_l)\Big). \end{aligned} \tag{C.20}$$

We then have our unconstrained local dynamics as

$$\boldsymbol{M}_l(\boldsymbol{q}_l)\dot{\mathbf{v}}_l - \boldsymbol{H}_l(\boldsymbol{q}_l, \mathbf{v}_l) = \boldsymbol{S}_l(\boldsymbol{q}_l)\boldsymbol{u}. \tag{C.21}$$

Note that same result is achieved by deriving the kinetic and potential energy, and nonconservative forces in terms of local coordinates and applying (C.3).

C.3 Contact distances in local coordinates

We now derive the contact distances $h_{l,1}$ and $h_{l,2}$, see Figure C.1, in local coordinates. These contact distances are formulated as

$$\begin{aligned} h_{l,1} &= (\mathrm{y}_l - \frac{l_p}{2}) - D_1, \\ h_{l,2} &= (\mathrm{y}_l - \frac{l_p}{2}) - D_2, \end{aligned} \tag{C.22}$$

in which l_P is the height of the plank, D_1 the distance $C_L - O^2$ in the $\vec{e}_2^1$ direction, and D_2 the distance $C_R - O^2$ in the $\vec{e}_2^1$ direction.

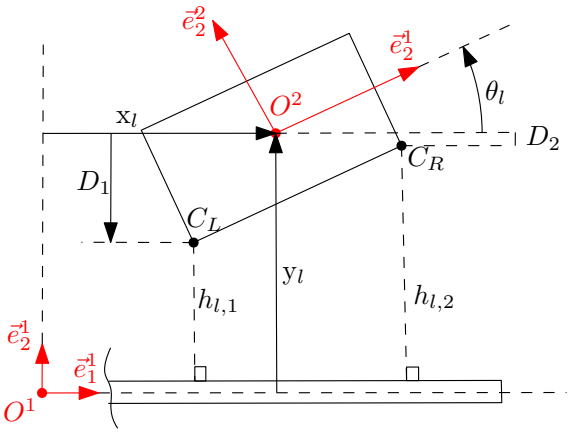

Figure C.1: A graphical representation of the contact distances of the plank-block system and the variables used to describe these contact distances.

We elaborate on the derivation of D_1, to which we use Figure C.2. The variable D_1 can be observed as the length BL. Taking into account that the point O^2 represents the geometrical center of the block, it follows that $EL = \frac{l_B}{2}$ and $EO^2 = \frac{L_B}{2}$. Here, l_b represents the block height and L_B the block width. It then follows that the length of AE is

$$AE = \tan(\theta_l) EO^2 = \frac{L_B}{2} \tan(\theta_l). \tag{C.23}$$

Noticing the similarity between $\triangle ABL$ and $\triangle AEO^2$, we derive $\angle ALB = \theta_l$ and subsequently

$$BL = \cos(\theta_l) AL = \cos(\theta_l) \frac{l_b}{2} + \sin(\theta_l) \frac{L_b}{2} = D_1. \tag{C.24}$$

The contact distance for the left contact point is then formulated as

$$h_{l,1} = (\mathrm{y}_l - \frac{l_P}{2}) - \cos(\theta_l) \frac{l_B}{2} - \sin(\theta_l) \frac{L_B}{2}. \tag{C.25}$$

A similar approach can then be taken for the right contact distance $h_{l,2}$, resulting in

$$h_{l,2} = (\mathrm{y}_l - \frac{l_P}{2}) - \cos(\theta_l) \frac{l_B}{2} + \sin(\theta_l) \frac{L_B}{2}. \tag{C.26}$$

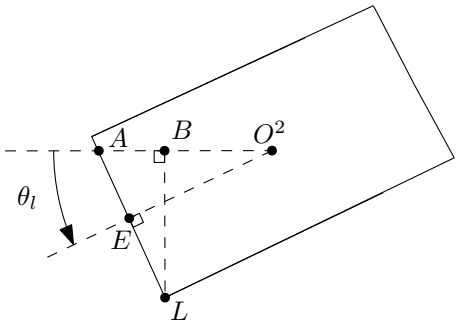

Figure C.2: A planar block used to analyze the distance D_1 of Figure C.1.

Appendix D

Reference trajectory design

In this appendix, we discuss the formulation of a feedforward, or nominal input term $\boldsymbol{\mu}(t)$, to realize the reference trajectory in Section 5.2. We consider two phases: (1) free motion, i.e., block and plank are detached (2) constrained motion, i.e., block and plank are in contact.

D.1 Free motion phase

We derive the feedforward with global coordinates $\boldsymbol{q}_g$ and thus consider the dynamics in (C.12). The reason for using $\boldsymbol{q}_g$ instead of $\boldsymbol{q}_l$ will be explained further below. By designing a reference trajectory $\boldsymbol{q}_{g,ref}$, one is able to gain feedforward expressions by taking the inverse of the considered dynamics. We start by pointing out that the matrix $\boldsymbol{S}_g(\boldsymbol{q}_g)$ is not of full rank. This is due to the system being underactuated, as the plank can not be controlled (in free motion at least). To find a reference trajectory that complies with the dynamics, we split (C.12) into an actuated part and an unactuated part, corresponding to, respectively, the block and plank dynamics. The block dynamics are formulated as

$$\boldsymbol{M}_B(\boldsymbol{q}_B)\dot{\mathbf{v}}_B - \boldsymbol{H}_B(\boldsymbol{q}_B, \mathbf{v}_B) = \boldsymbol{S}_B\boldsymbol{u} \tag{D.1}$$

with

$$\boldsymbol{q}_B = \begin{pmatrix} \mathrm{x}_g \\ \mathrm{y}_g \\ \theta_g \end{pmatrix}, \quad \mathbf{v}_B = \begin{pmatrix} \dot{\mathrm{x}}_g \\ \dot{\mathrm{y}}_g \\ \dot{\theta}_g \end{pmatrix}, \quad \boldsymbol{M}_B = \begin{pmatrix} \mathrm{m}_B & 0 & 0 \\ 0 & \mathrm{m}_B & 0 \\ 0 & 0 & J_B \end{pmatrix}, \quad \boldsymbol{H}_B = \begin{pmatrix} 0 \\ -\mathrm{m}_B\mathrm{g} \\ 0 \end{pmatrix}, \quad \boldsymbol{S}_B = \begin{pmatrix} 1 & 0 & 0 \\ 0 & 1 & 0 \\ 0 & 0 & 1 \end{pmatrix}, \tag{D.2}$$

and the plank dynamics as

$$(\frac{\mathrm{m}_P L_P^2}{4} + J_P)\ddot{\phi} + \mathrm{b}_P\dot{\phi}^2 + \frac{L_P \mathrm{g} \mathrm{m}_P \cos(\phi)}{2} + \mathrm{k}_P\phi = 0. \tag{D.3}$$

Observe that $\boldsymbol{S}_B$ is of full rank, and that the block can be controlled via

$$\boldsymbol{u} = \boldsymbol{\mu} = \boldsymbol{S}_B^{-1}\Big(\boldsymbol{M}_B(\boldsymbol{q}_B)\dot{\mathbf{v}}_{B,ref} - \boldsymbol{H}_B(\boldsymbol{q}_B, \mathbf{v}_B)\Big) \tag{D.4}$$

with a twice differentiable trajectory

$$\boldsymbol{q}_{B,ref} = \begin{pmatrix} \mathrm{x}_{g,ref} \\ \mathrm{y}_{g,ref} \\ \theta_{g,ref} \end{pmatrix}. \tag{D.5}$$

Substituting (D.4) into (D.1), results in

$$\boldsymbol{M}_B(\boldsymbol{q}_B)\dot{\mathbf{v}}_B = \boldsymbol{M}_B(\boldsymbol{q}_B)\dot{\mathbf{v}}_{B,ref} \rightarrow \dot{\mathbf{v}}_B = \dot{\mathbf{v}}_{B,ref}, \tag{D.6}$$

realizing tracking of the designed reference trajectory under the assumptions that $\boldsymbol{q}_B(t_0) = \boldsymbol{q}_{B,ref}(t_0)$ and no external disturbances are present. The individual components of (D.5) are defined with quintic polynomials, e.g.,

$$\mathrm{x}_{g,ref}(t) = a_0 + a_1 t + a_2 t^2 + a_3 t^3 + a_4 t^4 + a_5 t^5 \tag{D.7}$$

with $a_i \in \mathbb{R}$, for $i \in \mathbb{N}_{>0}$, being coefficients. These coefficients are realised when initial- and end-conditions are known, i.e.,

$$\begin{pmatrix} a_0 \\ a_1 \\ a_2 \\ a_3 \\ a_4 \\ a_5 \end{pmatrix} = \begin{pmatrix} 1 & t_0 & t_0^2 & t_0^3 & t_0^4 & t_0^5 \\ 0 & 1 & 2t_0 & 3t_0^2 & 4t_0^4 & 5t_0^4 \\ 0 & 0 & 2 & 6t_0 & 12t_0^2 & 20t_0^3 \\ 1 & t_f & t_f^2 & t_f^3 & t_f^4 & t_f^5 \\ 0 & 1 & 2t_f & 3t_f^2 & 4t_f^4 & 5t_f^4 \\ 0 & 0 & 2 & 6t_f & 12t_f^2 & 20t_f^3 \end{pmatrix} \begin{pmatrix} \mathrm{x}_{g,0} \\ \dot{\mathrm{x}}_{g,0} \\ \ddot{\mathrm{x}}_{g,0} \\ \mathrm{x}_{g,f} \\ \dot{\mathrm{x}}_{g,f} \\ \ddot{\mathrm{x}}_{g,f} \end{pmatrix} \tag{D.8}$$

with $\mathrm{x}_{g,0}$ denoting the initial condition and $\mathrm{x}_{g,f}$ the final condition. By putting constraints on the acceleration, we can prevent the occurrence of discontinuities in the feedforward when attaching reference trajectories to each other.

We can now also explain why we design in global coordinates, rather than local coordinates. By only stating an initial- and end- condition for the design of the reference trajectory as in (D.8), we expect the frame to which the coordinates are defined to not change. In local coordinates, we thus expect frame $\{O^1, \vec{\boldsymbol{e}}^1\}$, or the plank, to remain static. The plank, however, does move, and we can thus not define a good reference trajectory.

The design of the reference trajectory is thus done via (D.5), (D.7), and (D.8), which can be used when the initial- and end- conditions are formulated in global coordinates. For the given reference trajectory detailed in Section 5.2 , the initial conditions (specified in local coordinates) are formulated as

$$\begin{aligned} \boldsymbol{q}_l(t_0) &= \begin{pmatrix} \mathrm{x}_{l,0} & \mathrm{y}_{l,0} & \theta_{l,0} & \phi_0 \end{pmatrix}^T, \\ \dot{\boldsymbol{q}}_l(t_0) &= \begin{pmatrix} \dot{\mathrm{x}}_{l,0} & \dot{\mathrm{y}}_{l,0} & \dot{\theta}_{l,0} & \dot{\phi}_0 \end{pmatrix}^T, \\ \ddot{\boldsymbol{q}}_l(t_0) &= \begin{pmatrix} \ddot{\mathrm{x}}_{l,0} & \ddot{\mathrm{y}}_{l,0} & \ddot{\theta}_{l,0} & \frac{1}{\frac{\mathrm{m}_P L_P^2}{4} + J_P}(-\mathrm{b}_P \dot{\phi}_0^2 - \frac{L_P \mathrm{g} \mathrm{m}_P \cos(\phi_0)}{2} - k_P \phi_0) \end{pmatrix}^T, \end{aligned} \tag{D.9}$$

where $\ddot{\phi}_0$ is replaced with (D.3) since the plank is unactuated. The block on the contrary is fully actuated, and thus all corresponding acceleration terms can be defined as desired. The end-condition, which is pre-impact, is given as

$$\begin{aligned} \boldsymbol{q}_l(\tau_1)^- &= \begin{pmatrix} \mathrm{x}_{l,0} & \frac{l_P + l_B}{2} & 0 & \int_{t_0}^{\tau_1} \dot{\phi} dt \end{pmatrix}^T, \\ \dot{\boldsymbol{q}}_l(\tau_1)^- &= \begin{pmatrix} \dot{\mathrm{x}}_{l,f} & \dot{\mathrm{y}}_{l,f} & \dot{\theta}_{l,f} & \int_{t_0}^{\tau_1} \frac{1}{\frac{\mathrm{m}_P L_P^2}{4} + J_P}(-\mathrm{b}_P \dot{\phi}^2 - \frac{L_P \mathrm{g} \mathrm{m}_P \cos(\phi)}{2} - \mathrm{k}_P \phi) dt \end{pmatrix}^T, \\ \ddot{\boldsymbol{q}}_l(\tau_1)^- &= \begin{pmatrix} \ddot{\mathrm{x}}_{l,f} & \ddot{\mathrm{y}}_{l,f} & \ddot{\theta}_{l,f} & \frac{1}{\frac{\mathrm{m}_P L_P^2}{4} + J_P}(-\mathrm{b}_P \dot{\phi}_f^2 - \frac{L_P \mathrm{g} \mathrm{m}_P \cos(\phi_f)}{2} - \mathrm{k}_P \phi_f) \end{pmatrix}^T, \end{aligned} \tag{D.10}$$

where we define ϕ related end-conditions via (D.3). We then transform the local coordinates to global coordinates via (C.17) and (C.18), and subsequently define our reference trajectory in (D.5). The feedforward is then formulated in (D.4) via this reference trajectory.

D.2 Constrained motion phase

In this section, the second part of the feedforward is described, i.e., after impact. During constrained motion phase, the block experiences constrained dynamics as it is unable to penetrate the

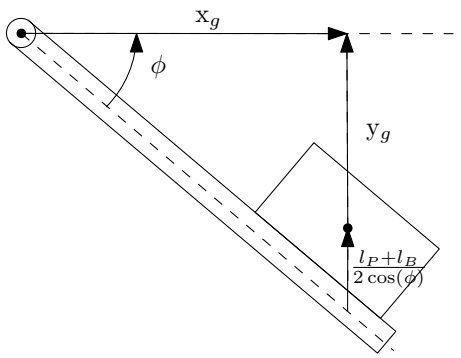

Figure D.1: A graphical representation of the global coordinates ϕ, x_l, and y_l during contact phase.

plank. As only holonomic constraints are considered, one can take a similar approach as in Appendix C.2 to now formulate the dynamics in a reduced manner, cf. [33, Section 5.2.3, p.111-114]. To do so, reduced terms

$$\boldsymbol{q}_R = \begin{pmatrix} \mathrm{x}_g \\ \phi \end{pmatrix} \text{ and } \mathbf{v}_R = \begin{pmatrix} \dot{\mathrm{x}}_g \\ \dot{\phi} \end{pmatrix} \tag{D.11}$$

are considered. The relation between the unreduced and reduced coordinates is deduced from Figure D.1 and is given as

$$\boldsymbol{q}_g(\boldsymbol{q}_R) = \begin{pmatrix} \mathrm{x}_g \\ \mathrm{x}_g \tan(\phi) + \frac{l_P+l_B}{2\cos(\phi)} \\ \phi \\ \phi \end{pmatrix}. \tag{D.12}$$

Performing similar steps as in (C.16)-(C.21) with the principle of virtual work, results in the reduced dynamics

$$\boldsymbol{M}_R(\boldsymbol{q}_R)\dot{\mathbf{v}}_R = \boldsymbol{H}_R(\boldsymbol{q}_R, \mathbf{v}_R) + \boldsymbol{S}_R(\boldsymbol{q}_R)\boldsymbol{u} \tag{D.13}$$

with $\boldsymbol{M}_R \in \mathbb{R}^{2\times 2}$, $\boldsymbol{H}_R \in \mathbb{R}^{2\times 1}$ and $\boldsymbol{S}_R \in \mathbb{R}^{2\times 3}$. Notice that instead of an underactuated system (as was the case for free motion), an overactuated system is obtained as there are more input terms than degrees of freedom. Consequently, the plank can also be controlled to a certain extent. To eliminate the overactuated nature of the system, we simply impose $\tau_{rot} = 0$, effectively reducing our input to

$$\boldsymbol{u}_{red} = \begin{pmatrix} F_1 \\ F_2 \end{pmatrix}. \tag{D.14}$$

We then change our $\boldsymbol{S}_R$ matrix to $\boldsymbol{S}_{R,red} \in \mathbb{R}^{2\times 2}$, essentially removing the third column of $\boldsymbol{S}_R$. The dynamics change to

$$\boldsymbol{M}_R(\boldsymbol{q}_R)\ddot{\boldsymbol{q}}_R = \boldsymbol{H}_R(\boldsymbol{q}_R, \dot{\boldsymbol{q}}_R) + \boldsymbol{S}_{R,red}(\boldsymbol{q}_R)\boldsymbol{u}_{red}, \tag{D.15}$$

for which a reference trajectory

$$\boldsymbol{q}_{R,ref} = \begin{pmatrix} \mathrm{x}_{g,ref} \\ \phi_{ref} \end{pmatrix} \tag{D.16}$$

is designed. This reference trajectory is constructed in the same manner as the reference trajectory for the free motion phase, i.e., using quintic polynomials. Note that this is the post-impact phase, such that the initial conditions are the conditions of (D.10) with a jump map ${}^{11\leftarrow 00}\boldsymbol{g}$ applied to it. The feedforward is formulated as

$$\boldsymbol{u} = \boldsymbol{\mu} = \begin{pmatrix} \boldsymbol{\mathcal{S}}_{R,red}^{-1}(\boldsymbol{q}_R)\Big(-\boldsymbol{H}_R(\boldsymbol{q}_R, \mathbf{v}_R) + \boldsymbol{M}_R(\boldsymbol{q}_R)\dot{\mathbf{v}}_{R,ref} \Big) \\ 0 \end{pmatrix}. \tag{D.17}$$

Appendix E

Reference trajectory extra properties

In this appendix, we show that the plank-block system discussed in Chapter 5 indeed does not have a superfluous impact about the considered reference trajectory, and that the local model for the considered benchmark example is not linear.

E.1 Superfluous contacts

In this section, we consider the non-superfluous impact condition (2.19) in a neighborhood of the simultaneous impact for the reference trajectory used in Chapter 5. If one concludes that (2.19) is still valid for this neighborhood, then we assume that even a small perturbed trajectory does not experience superfluous contacts. Equation (2.19) gives

$$\psi = \arccos\left(\frac{\nabla h_1^T \boldsymbol{M}_l \nabla h_2}{\sqrt{\nabla h_1^T \boldsymbol{M}_l \nabla h_1}\sqrt{\nabla h_2^T \boldsymbol{M}_l \nabla h_2}}\right) = 1.9843 \tag{E.1}$$

for the considered impact conditions of the reference trajectory, i.e., block an plank values of Tables 5.1 and 5.2, and impact configuration of Table 5.3. As the constraint angle ψ is larger than $\frac{\pi}{2}$, no superfluous impact is concluded for the reference motion. We now have to check if this will still be valid under small perturbations. Assuming we only have small perturbations, the local trend of ψ in a neighborhood of the reference event can be analyzed using the Jacobian of (E.1). Taking rows

$$\begin{aligned} \boldsymbol{p} &= \begin{pmatrix} \mathrm{m}_B, & \mathrm{m}_P, & L_B, & l_B, & L_P, & l_p, & J_B, & J_P \end{pmatrix} \quad \text{and} \\ \boldsymbol{d} &= \begin{pmatrix} \mathrm{x}_l, & \mathrm{y}_l, & \theta_l, & \phi, & \dot{\mathrm{x}}_l, & \dot{\mathrm{y}}_l, & \dot{\theta}_l, & \dot{\phi} \end{pmatrix}, \end{aligned} \tag{E.2}$$

we can define the Jacobian evaluated at pre-impact state ${}^{00}\boldsymbol{\alpha}(\tau)$ as

$$\begin{aligned} \frac{\partial \psi}{\partial \boldsymbol{p}} &= \begin{pmatrix} -0.0299, & 0.0399, & 0.1649, & -0.4540, & 0.0399, & 0.0002, & 0, & 0 \end{pmatrix} \quad \text{and} \\ \frac{\partial \psi}{\partial \boldsymbol{d}} &= \begin{pmatrix} -0.1596, & 0, & -0.0096, & 0, & 0, & 0, & 0, & 0 \end{pmatrix}, \end{aligned} \tag{E.3}$$

which shows that if we do not change any values of $\boldsymbol{p}$, that only x_l and θ_l can influence the value of ψ locally. Taking into account that θ_l can not be changed as simultaneous impact only occurs at $\theta_l = 0$, the only influence on ψ comes from x_l. Impacting the block further away from the hinge of the plank, thus decreases the value of ψ, increasing subsequently the chance of superfluous contacts. This is not surprising, as the plank is relatively *stiff* close to hinge, and *looser* further away from it. We, however, can conclude that for small perturbations on x_l, condition (2.19) is

still satisfied, and thus that a small perturbation on the reference trajectory does not experience superfluous impacts.

E.2 Positively homogeneous jump mapping

In this section, we analyze if the conewise constant jump gain $\boldsymbol{G}(\tau, {}^{00}\boldsymbol{z}(\tau))$, see (5.21), consists of constant jump gains $\boldsymbol{G}(\tau)$ that are all equal to each other for the reference trajectory designed in Chapter 5. From Appendix B.3 it follows that if this is indeed the case, then we would have a linear time-triggered hybrid system, instead of a positively homogeneous time-triggered hybrid system. To do so, we analyze whether or not the following holds

$$ {}^{11\leftarrow 01}\boldsymbol{G}(\tau)\,{}^{01\leftarrow 00}\boldsymbol{G}(\tau) = {}^{11\leftarrow 10}\boldsymbol{G}(\tau)\,{}^{10\leftarrow 00}\boldsymbol{G}(\tau). \tag{E.4} $$

If (E.4) holds, then our local model is linear, while if (E.4) does not hold, then our local model is positively homogeneous. For the reference impact values given in Table 5.3, we obtain the constant jump gains (see Appendix B.2) as

$$ {}^{11\leftarrow 01\leftarrow 00}\boldsymbol{G}(\tau) = \begin{pmatrix} 1 & 0.041 & 0.0017 & 0 & 0 & 0 & 0 & 0 \\ 0 & 0 & 0 & 0 & 0 & 0 & 0 & 0 \\ 0 & 0 & 0 & 0 & 0 & 0 & 0 & 0 \\ 0 & 0.2736 & 0.0114 & 1 & 0 & 0 & 0 & 0 \\ -0.0865 & -0.2688 & 0.3579 & 0 & 1 & 0.0410 & 0.0017 & 0 \\ 0 & 0 & 0 & 0 & 0 & 0 & 0 & 0 \\ 0 & 0 & 0 & 0 & 0 & 0 & 0 & 0 \\ -0.5769 & -0.0150 & 2.1631 & 0 & 0 & 0.2736 & 0.0114 & 1 \end{pmatrix}, \tag{E.5} $$

$$ {}^{11\leftarrow 10\leftarrow 00}\boldsymbol{G}(\tau) = \begin{pmatrix} 1 & 0.041 & 0.0017 & 0 & 0 & 0 & 0 & 0 \\ 0 & 0 & 0 & 0 & 0 & 0 & 0 & 0 \\ 0 & 0 & 0 & 0 & 0 & 0 & 0 & 0 \\ 0 & -0.2736 & 0.0114 & 1 & 0 & 0 & 0 & 0 \\ -0.0865 & -0.2688 & -0.7518 & 0 & 1 & 0.0410 & 0.0017 & 0 \\ 0 & 0 & 0 & 0 & 0 & 0 & 0 & 0 \\ 0 & 0 & 0 & 0 & 0 & 0 & 0 & 0 \\ -0.5769 & -0.0150 & -4.4044 & 0 & 0 & 0.2736 & 0.0114 & 1 \end{pmatrix}, \tag{E.6} $$

where we observe a difference to be present in the third columns. This can easily be explained by inspecting (5.24), which for the considered reference trajectory simplifies to

$$ -\frac{{}^{00}z_\theta(\tau)}{5} \leq 0. \tag{E.7} $$

Only a ${}^{00}z_\theta(\tau)$ value thus differentiates the two jump gains from each other, and this is also observed from (E.5) and (E.6); the third column represents a multiplication with ${}^{00}z_\theta(\tau)$. Intuitively, this is not surprising, as we expect an impact closer to the plank hinge to have less influence on the plank than an impact further away from the plank hinge. Taking into account that z_θ is related to the perturbation in θ_l direction, one can deduce that a perturbation on the block rotation causes either the left or right contact to impact first. Naturally, the block lenghth L_b plays an important role, where we expect the differences between the two jump gains to become smaller for smaller L_B. When looking at (5.24), we can see this also by setting $L_B = 0$, which results in an outcome of 0; thus it does not matter which jump gain is chosen.

We thus conclude that the local model of the plank-block system is not linear. We further illustrate this using an example. Assuming we have two-pre-impact state conditions

$$ \begin{aligned} \boldsymbol{z}_1^- &= \begin{pmatrix} 0, & 0, & 0.5, & 0, & 0, & 0, & 0, & 0 \end{pmatrix}^T \quad \text{and} \\ \boldsymbol{z}_2^- &= \begin{pmatrix} 0, & 0, & -0.3, & 0, & 0, & 0, & 0, & 0 \end{pmatrix}^T, \end{aligned} \tag{E.8} $$

then we can deduce that $\boldsymbol{z}_1^-$ jumps according to (E.5) and $\boldsymbol{z}_2^-$ according to (E.6) as indicated by condition (E.7). We then have the post-impact states

$$\begin{aligned}\boldsymbol{z}_1^+ &= \begin{pmatrix}8.5\cdot 10^{-4}, & 0, & 0, & 0.0057, & 0.179, & 0, & 0, & 1.0816\end{pmatrix}^T \quad \text{and} \\ \boldsymbol{z}_2^+ &= \begin{pmatrix}-5.1\cdot 10^{-4}, & 0, & 0, & -0.0034, & 0.2255, & 0, & 0, & 1.3213\end{pmatrix}^T\end{aligned} \tag{E.9}$$

with their sum given by

$$\boldsymbol{z}_{sum}^+ = \boldsymbol{z}_1^+ + \boldsymbol{z}_2^+ = \begin{pmatrix}3.4\cdot 10^{-4}, & 0, & 0, & 0.0023, & 0.4045, & 0, & 0, & 2.4029\end{pmatrix}. \tag{E.10}$$

We can then define another pre-impact state condition

$$\boldsymbol{z}_3^- = \boldsymbol{z}_1^- + \boldsymbol{z}_2^- = \begin{pmatrix}0, & 0, & 0.2, & 0, & 0, & 0, & 0, & 0\end{pmatrix}^T, \tag{E.11}$$

which jumps according to (E.5), and thus gives a post-impact state

$$\boldsymbol{z}_3^+ = \begin{pmatrix}3.4\cdot 10^{-3}, & 0, & 0, & 0.0023, & 0.0716, & 0, & 0, & 0.4326\end{pmatrix}^T \tag{E.12}$$

which on velocity level is not equal to (E.10); thus linearity property is not present.

It should be noted that deriving a condition as (5.24) is not sufficient for guaranteeing no linearity for our local model. If we replace the plank with a flat planar ground, see Figure E.1, while assuming no friction, then we have a similar condition as (5.24) with the constant jump gains defined as

$$\boldsymbol{G}(\tau) = {}^{11\leftarrow 01\leftarrow 00}\boldsymbol{G}(\tau) = {}^{11\leftarrow 10\leftarrow 00}\boldsymbol{G}(\tau) = \begin{pmatrix}1 & 0 & 0 & 0 & 0 & 0\\ 0 & 0 & 0 & 0 & 0 & 0\\ 0 & 0 & 0 & 0 & 0 & 0\\ 0 & 0 & 0 & 1 & 0 & 0\\ 0 & 0 & 0 & 0 & 0 & 0\\ 0 & 0 & 0 & 0 & 0 & 0\end{pmatrix}, \tag{E.13}$$

thus indicating that whatever transition we take, the post-impact state $\boldsymbol{z}^+$ will always be the same. this can be clarified by the physical interpretation of the impacts itself, where a different impact for the block-ground case, assuming we consider no friction, results in no different post-impact state terms whether we impact right or left first. For the plank-block system, having a different impact sequence results in different velocity behavior of the plank and subsequently also for the block.

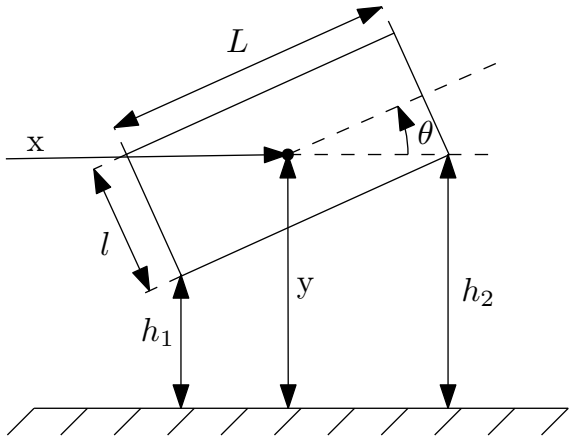

Figure E.1: A Graphical representation of the block-ground model.

Appendix F

Simulation

In this appendix, we provide extra information for the numerical experiments. The following topics are discussed:

- The constraint stabilization method is discussed.
- A comparison is made between time-stepping results and event-based results.
- The control gain for the positive homogenization in Section 5.4 is discussed in more detail.
- Extra plots are given for the individual terms of some norm figures in Sections 5.3 and 5.4.

F.1 Baumgarte stabilization

When bodies are in contact, e.g., after the block has experienced inelastic impact, one needs to provide adequate contact forces which prevent the bodies from penetrating each other. In [33, Chapter 5, p.99-127], it is mentioned that these contact forces (Lagrange multipliers) can not be assumed to fulfill the constraint equations due to numerical errors. The satisfaction of the constraint equation can detoriate when the simulation proceeds.

A solution to this problem is to apply a technique called *Baumgarte stabiization*. For this, we derive the contact forces via

$$\begin{aligned} \boldsymbol{M}_l(\boldsymbol{q}_l)\ddot{\boldsymbol{q}}_l - \boldsymbol{H}_l(\boldsymbol{q}_l,\dot{\boldsymbol{q}}_l) &= \boldsymbol{S}_l(\boldsymbol{q}_l)\boldsymbol{u} + \sum_{i\in\mathcal{I}_c} \boldsymbol{W}_i\boldsymbol{\lambda}_i, \\ \dot{\xi}_i + 2\eta\beta\xi_i + \eta^2 h_i &= 0, \qquad i \in \mathcal{I}_c, \end{aligned} \tag{F.1}$$

where we define new parameters $\eta, \beta \in \mathbb{R}$. We take $\beta = 1$ (as is usual done) and determine η from the highest frequency of the system when the plank and block are in contact. We ignore the damping of the plank and determine the natural frequency of the undamped plank with a block on top of it as

$$J_{total}(\mathrm{x}_l)\ddot{\phi} + \mathrm{k}_P\phi = 0 \tag{F.2}$$

with

$$J_{total}(\mathrm{x}_l) = J_P + \mathrm{m}_P\frac{L_P^2}{4} + J_B + \mathrm{m}_B(\mathrm{x}_l^2 + (0.5(l_P + l_B)^2) \tag{F.3}$$

being the inertia for the total plank-block system with respect to the hinge of the plank. We then determine

$$\eta = \underset{\mathrm{x}_l}{argmin}\sqrt{\frac{\mathrm{k}_P}{J_{total}(\mathrm{x}_l)}}. \tag{F.4}$$

Note that for the numerical experiments of the positive homogenization, the positive homogenization is derived from the dynamics in (F.1). This, however, does not influence the positive homogenization, as reformulating the dynamics in reduced format (see Appendix D.2) and deriving the positive homogenization from it, results in similar results as using the dynamics specified in (F.1).

F.2 Time-stepping vs event-based

In this section, we compare the results of the event-based simulation to the time-stepping scheme, see [34], in order to validate the simulation results in Chapter 5. The event-based simulation settings are the same as given in Section 5.2. For the time-stepping scheme, a fixed point-iteration is used for which we use an error tolerance of 10^{-8}. Furthermore, a proximal point description of the set-valued force laws is used, for which we use the corresponding parameter value as 0.5.

The open-loop situation is considered with a block falling without any feedforward, i.e., $\boldsymbol{\mu} = \mathbf{0}^{3\times 1}$. Taking an initial condition as

$$\boldsymbol{x} = \begin{pmatrix} 0.8, & 2, & 0.4, & -0.2, & 0, & 0, & 0, & 0 \end{pmatrix}, \tag{F.5}$$

will let the block impact in a sequence in which the right corner is touched first. We now show simulation results using this initial condition, where we compare the event-based simulation to the time-stepping scheme for different time-steps. We depict this for the time-steps 0.01s, 0.001s, and 0.0005s in, respectively, Figures F.1, F.2, and F.3. Reducing the time-step shows that the results of the time-stepping scheme and event-based simulation converge to each other. We thus determine that the event-based simulation provides accurate results.

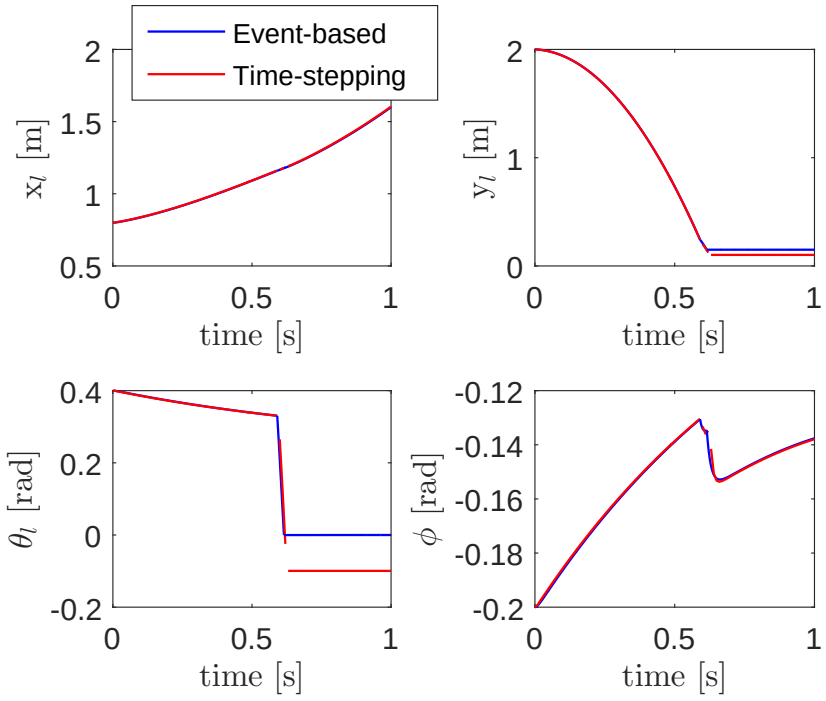

(a) Position comparison.

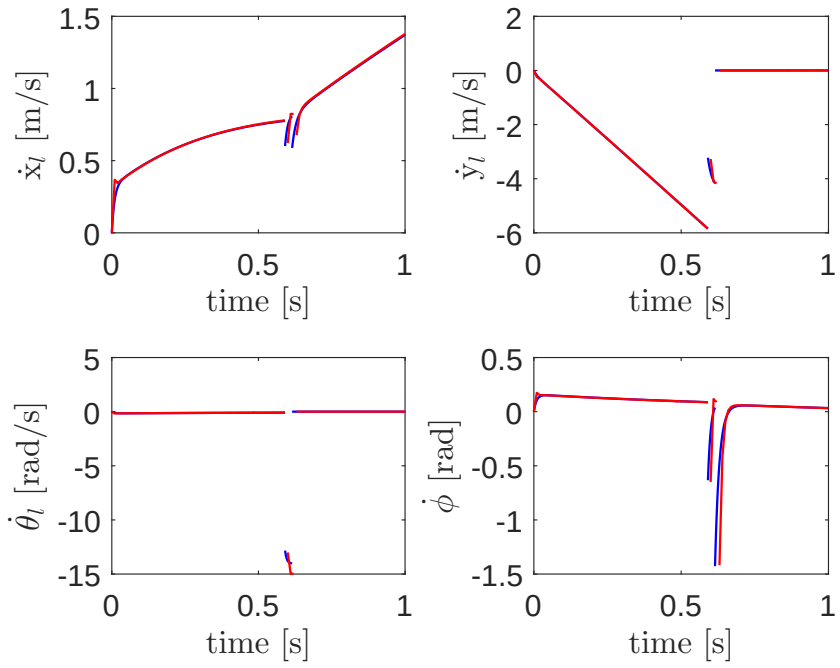

(b) Velocity comparison.

Figure F.1: Numerical experiment results of the comparison between the output of the event-based simulation and the output of time-stepping scheme with time-step 0.01s.

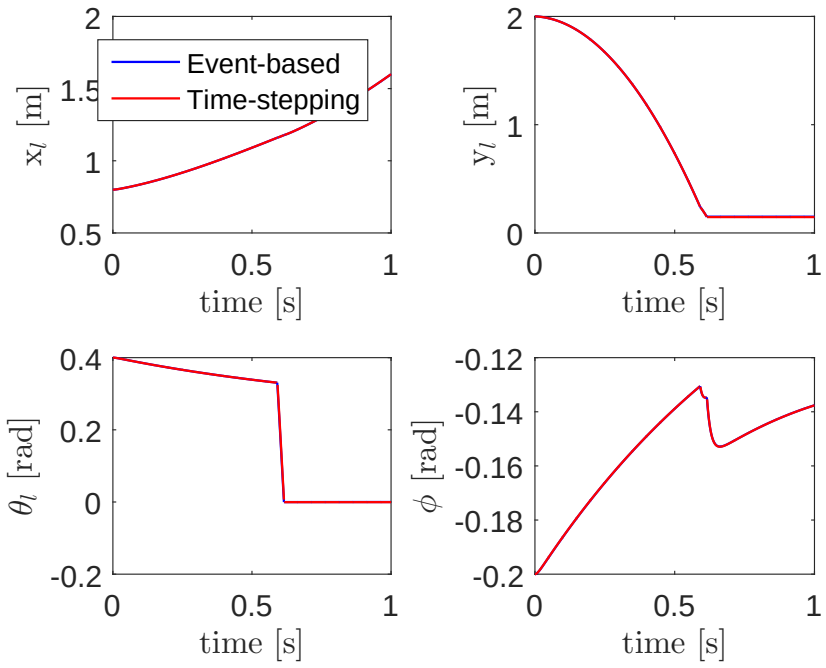

(a) Position comparison.

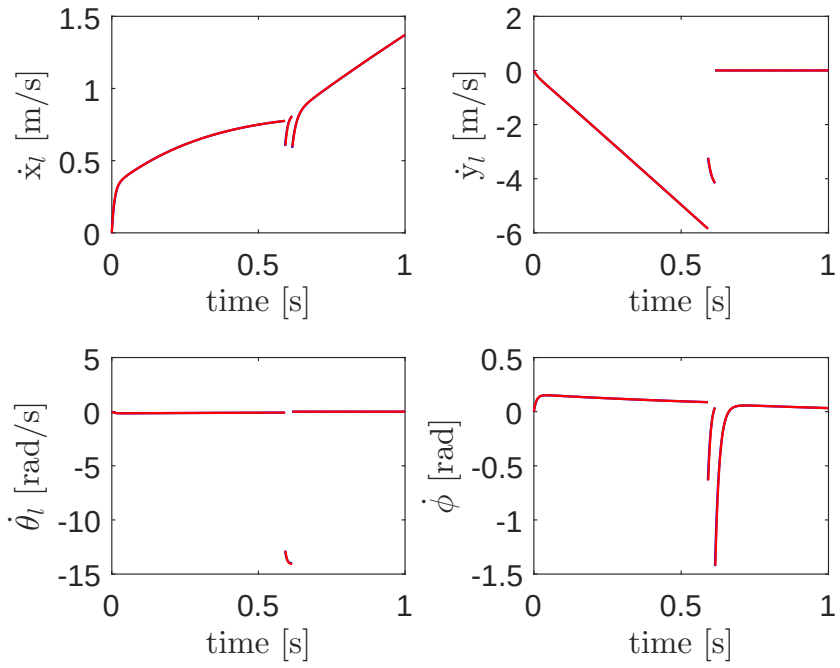

(b) Velocity comparison.

Figure F.2: Numerical experiment results of the comparison between the output of the event-based simulation and the output of time-stepping scheme with time-step 0.001s.

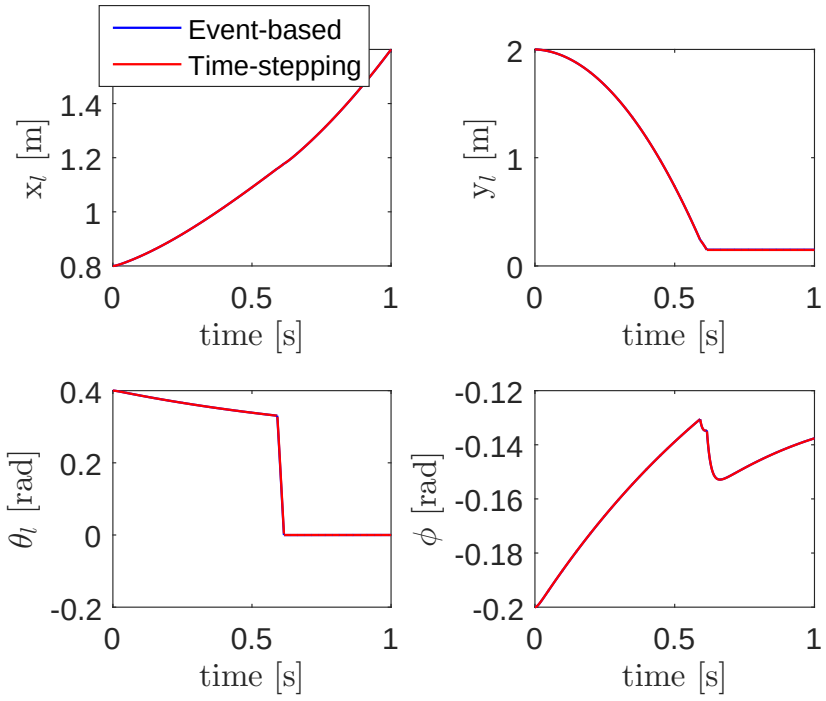

(a) Position comparison.

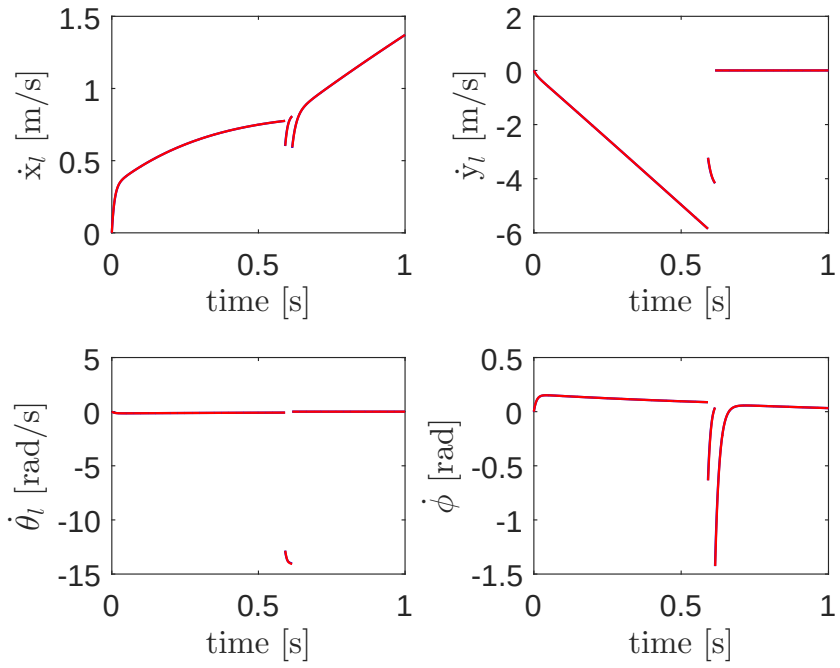

(b) Velocity comparison.

Figure F.3: Numerical experiment results of the comparison between the output of the event-based simulation and the output of time-stepping scheme with time-step 0.0005s.

F.3 Control gain positive homogenization

In this section, we discuss the closed-loop gain for the positive homogenization, i.e., (5.30). We consider two phases of system dynamics, namely free motion (mode 00) and constrained motion (mode 11). For both phases the closed-loop gains gains are described in this appendix.

Free motion

The local approximation of the continuous part of the system dynamics in free motion is given by

$$^{00}\dot{\boldsymbol{z}} = {}^{00}\boldsymbol{A}\,{}^{00}\boldsymbol{z} + {}^{00}\boldsymbol{B}\,{}^{00}\boldsymbol{v} \tag{F.6}$$

with

$$^{00}\boldsymbol{z} = \begin{pmatrix} z_{\mathrm{x}_l}, & z_{\mathrm{y}_l}, & z_{\theta_l}, & z_{\phi}, & \dot{z}_{\mathrm{x}_l}, & \dot{z}_{\mathrm{y}_l}, & \dot{z}_{\theta_l}, & \dot{z}_{\phi} \end{pmatrix}^T, \tag{F.7}$$

for which we want to design a stabilizing feedback with $^{00}\boldsymbol{v} = -{}^{00}\boldsymbol{K}\,{}^{00}\boldsymbol{z}$. A simple structure for the feedback gain $^{00}\boldsymbol{K}_l$ would be

$$^{00}\boldsymbol{K}_l = \begin{pmatrix} K_{p,\mathrm{x}_l} & 0 & 0 & 0 & K_{d,\mathrm{x}_l} & 0 & 0 & 0 \\ 0 & K_{p,\mathrm{y}_l} & 0 & 0 & 0 & K_{d,\mathrm{y}_l} & 0 & 0 \\ 0 & 0 & K_{p,\theta_l} & 0 & 0 & 0 & K_{d,\theta_l} & 0 \end{pmatrix}, \tag{F.8}$$

where $K_{p,\cdot}$ and $K_{d,\cdot}$ are scalar values. The problem with this choice, is that $\boldsymbol{v}$ is not directed along the local coordinates, but rather in global coordinates, see Appendix C.1, such that defining

$$^{00}\boldsymbol{v} = -{}^{00}\boldsymbol{K}_l\,{}^{00}\boldsymbol{z} \tag{F.9}$$

makes intuitively no sense. This can be better clarified with an example, to which we consider a perturbation solely in the x_l direction, i.e.,

$$^{00}\boldsymbol{z} = \begin{pmatrix} z_{\mathrm{x}_l}, & 0, & 0, & 0, & 0, & 0, & 0, & 0 \end{pmatrix}^T. \tag{F.10}$$

Using (F.9), it follows that the input would only have a nonzero component in the $\vec{\boldsymbol{e}}_1^0$ direction, equal to

$$F_1 = -K_{p,\mathrm{x}_l} z_{\mathrm{x}_l} \tag{F.11}$$

as illustrated in Figure F.4. We want a feedback force acting in the x_l direction, but rather get a feedback in the F_1 direction. Consequently, instead of using (F.8), (F.9), a more intuitive feedback strategy is looked for.

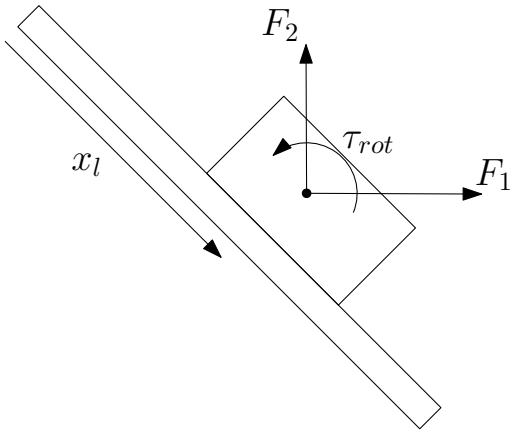

Figure F.4: Relation ϕ, x_l and y_l.

To solve this issue of non-intuitive feedback term $\boldsymbol{v}$, we link the input term $\boldsymbol{v}$ to actuator forces working in the same direction as the local coordinates. To do so, we look at the continuous dynamics in the free motion phase, see (5.2). Via the matrix multiplication

$$\boldsymbol{S}_l\boldsymbol{u} = \begin{pmatrix} \cos(\phi) & \sin(\phi) & 0 \\ -\sin(\phi) & \cos(\phi) & 0 \\ 0 & 0 & 1 \\ -y_l\cos(\phi) - x_l\sin(\phi) & x_l\cos(\phi) - y_l\sin(\phi) & 1 \end{pmatrix} \boldsymbol{u}, \tag{F.12}$$

one is able to determine the input terms $\boldsymbol{u}$ directed in the generalized coordinates $\boldsymbol{q}_l$. As we are only interested in the actuation of the block, the first three rows of $\boldsymbol{S}_l$ suffice to determine the *virtual local input*

$$\boldsymbol{u}_l = \begin{pmatrix} \cos(\phi) & \sin(\phi) & 0 \\ -\sin(\phi) & \cos(\phi) & 0 \\ 0 & 0 & 1 \end{pmatrix} \boldsymbol{u} \tag{F.13}$$

in the directions of the local block coordinates. Taking into account that $\boldsymbol{v}$ is derived in a similar manner as $\boldsymbol{z}$, see (4.26), namely from

$$\boldsymbol{u} = \boldsymbol{\mu} + \epsilon\boldsymbol{v} + o(\epsilon), \tag{F.14}$$

we can set up the same transformation for the perturbed input as

$$\boldsymbol{v}_l = \begin{pmatrix} \cos(\phi) & \sin(\phi) & 0 \\ -\sin(\phi) & \cos(\phi) & 0 \\ 0 & 0 & 1 \end{pmatrix} \boldsymbol{v} \leftrightarrow \boldsymbol{v} = \begin{pmatrix} \cos(\phi) & -\sin(\phi) & 0 \\ \sin(\phi) & \cos(\phi) & 0 \\ 0 & 0 & 1 \end{pmatrix} \boldsymbol{v}_l, \tag{F.15}$$

to which we redefine our perturbed feedback (F.9) as

$${}^{00}\boldsymbol{v} = -\begin{pmatrix} \cos(\phi_{ref}) & -\sin(\phi_{ref}) & 0 \\ \sin(\phi_{ref}) & \cos(\phi_{ref}) & 0 \\ 0 & 0 & 1 \end{pmatrix} {}^{00}\boldsymbol{K}_l{}^{00}\boldsymbol{z}. \tag{F.16}$$

On a side note, one may wonder why we do not define the whole dynamics of the mechanical system, see (5.2), orientated in local coordinates, as we can define virtual local input terms via (F.12). We then do not have to transform the local input to global input as in (F.15). The reason for this, is that it was found that, for the considered system, the open-loop dynamics of the positive homogenization with $\boldsymbol{v} = 0$ give a better approximation when the feedforward is applied in the directions of the global coordinates, then when the feedforward is specified in local directions. This is due to the $\boldsymbol{A}$ matrix of the positive homogenization to incorporate $\boldsymbol{u}$ terms in it when considering the global coordinated input, which influences the constrained motion part considerably as the nominal input becomes enormous (see figure 3.3). Note that (F.12) consists of ϕ terms multiplied with the input, e.g., $\cos(\phi)\boldsymbol{u}$.

Constrained motion

For the constrained motion, we also need to derive a similar relation as (F.15). In this phase, we assume that y_l and θ_l will stay constant such that feedback for these directions is unnecessary. The only perturbations that are present can be found in x_l or ϕ direction, and we thus only require feedback gains for these components. As we have constrained dynamics, the influence of input $\boldsymbol{u}$ on the coordinates x_l and ϕ may not be the same as stated in (F.12). It is for this reason that we seek a representation of the dynamics in a reduced set of coordinates. We will use a similar process as in Appendix D.2, but now in reduced local coordinates

$$\boldsymbol{q}_{l,R} = \begin{pmatrix} \mathrm{x}_l \\ \phi \end{pmatrix} \tag{F.17}$$

with

$$\boldsymbol{q}_l(\boldsymbol{q}_{l,R}) = \begin{pmatrix} \mathrm{x}_l \\ \frac{l_P+l_B}{2} \\ 0 \\ \phi \end{pmatrix}, \tag{F.18}$$

obtaining

$$\boldsymbol{M}_{l,R}(\boldsymbol{q}_{l,R})\dot{\mathbf{v}}_{l,R} = \boldsymbol{H}_{l,R}(\boldsymbol{q}_{l,R}, \mathbf{v}_{l,R}) + \boldsymbol{S}_{l,R}(\boldsymbol{q}_{l,R})\boldsymbol{u} \tag{F.19}$$

with

$$\boldsymbol{S}_{l,R} = \begin{pmatrix} \cos(\phi) & \sin(\phi) & 0 \\ -\frac{l_B+l_P}{2}\cos(\phi) - \mathrm{x}_l \sin(\phi) & -\frac{l_P+l_B}{2}\sin(\phi) + \mathrm{x}_l \cos(\phi) & 1 \end{pmatrix}. \tag{F.20}$$

Assuming that we apply no torques on the body, i.e., $\tau_{rot} = 0$, then we can get an expression for local input as a force in the directions of x_l and a torque in the direction of ϕ as

$${}^{11}\boldsymbol{v}_l = \begin{pmatrix} \cos(\phi_{ref}) & \sin(\phi_{ref}) \\ -\frac{l_B+l_P}{2}\cos(\phi_{ref}) - \mathrm{x}_{l,ref}\sin(\phi_{ref}) & -\frac{l_P+l_B}{2}\sin(\phi_{ref}) + \mathrm{x}_{l,ref}\cos(\phi_{ref}) \end{pmatrix} {}^{11}\boldsymbol{v}, \tag{F.21}$$

where we thus leave the third column of $\boldsymbol{S}_{l,R}$ out. We then define the input as

$${}^{11}\boldsymbol{v} = \begin{pmatrix} -\frac{(l_B+l_P)\sin(\phi_{ref}) - 2\mathrm{X}_{l,ref}\cos(\phi_{ref})}{2\mathrm{X}_{l,ref}} & -\frac{\sin(\phi_{ref})}{\mathrm{X}_{l,ref}} \\ \frac{(l_B+l_P)\cos(\phi_{ref}) + 2\mathrm{X}_{l,ref}\sin(\phi_{ref})}{2\mathrm{X}_{l,ref}} & \frac{\cos(\phi_{ref})}{\mathrm{X}_{l,ref}} \end{pmatrix} {}^{11}\boldsymbol{v}_l \tag{F.22}$$

with

$${}^{11}\boldsymbol{v}_l = -{}^{11}\boldsymbol{K}_l {}^{11}\boldsymbol{z}, \tag{F.23}$$

where we define

$${}^{11}\boldsymbol{z} = \begin{pmatrix} z_{\mathrm{x}_l} \\ z_\phi \\ \dot{z}_{\mathrm{x}_l} \\ \dot{z}_\phi \end{pmatrix}, \tag{F.24}$$

leaving z_{y_l} and z_{θ_l} out, and

$${}^{11}\boldsymbol{K}_l = \begin{pmatrix} K_{p,\mathrm{x}_l} & 0 & K_{d,\mathrm{x}_l} & 0 \\ 0 & K_{p,\phi} & 0 & K_{d,\phi} \end{pmatrix}. \tag{F.25}$$

F.4 Extra plots numerical experiments

In Sections 5.3 and 5.4, only the norm figures are presented. The reader may, however, be interested in the individual components, and this section is dedicated to this. to navigate in a simple manner through the figures, Table F.1 is provided below. On the left, the appendix figure is denoted, and on the right the corresponding figure that can be found in the main report.

Table F.1: Relating the appendix figures to the main report figures.

Appendix figure	Main report figure(s)
Figure F.5	Figure 5.10(a)
Figure F.6	Figure 5.14(a)
Figure F.7	Figure 5.13(b)
Figure F.8	Beige lines Figure 5.17.
Figure F.9	Magenta lines Figure 5.17
Figure F.10	Euclidean and reference spreading error for Figure 5.25

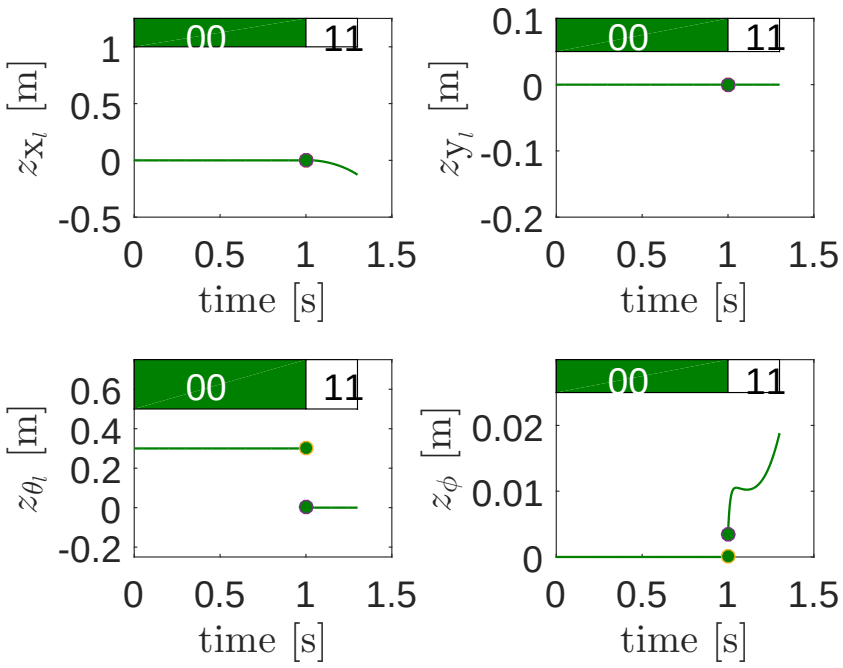

(a) Position.

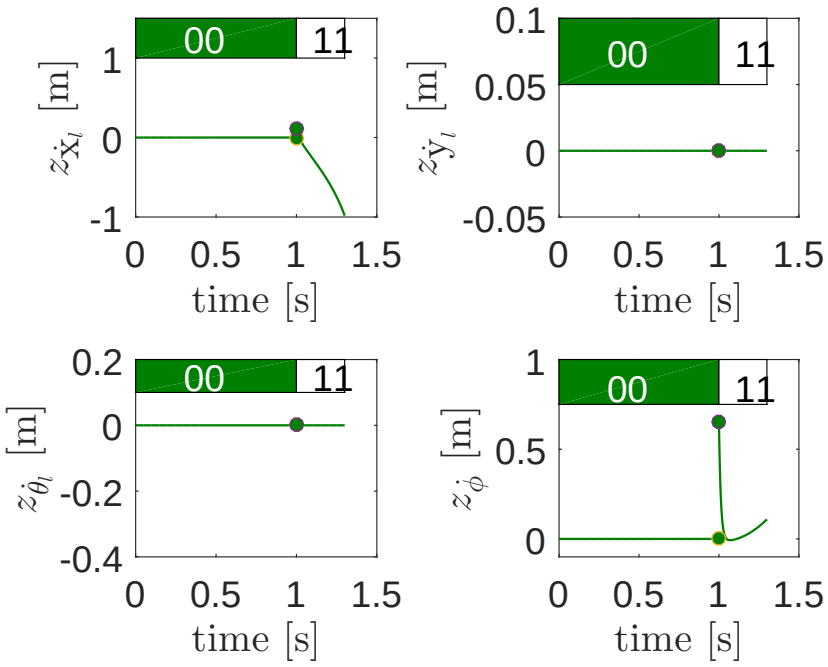

(b) Velocity.

Figure F.5: Individual plots Figure 5.10(a).

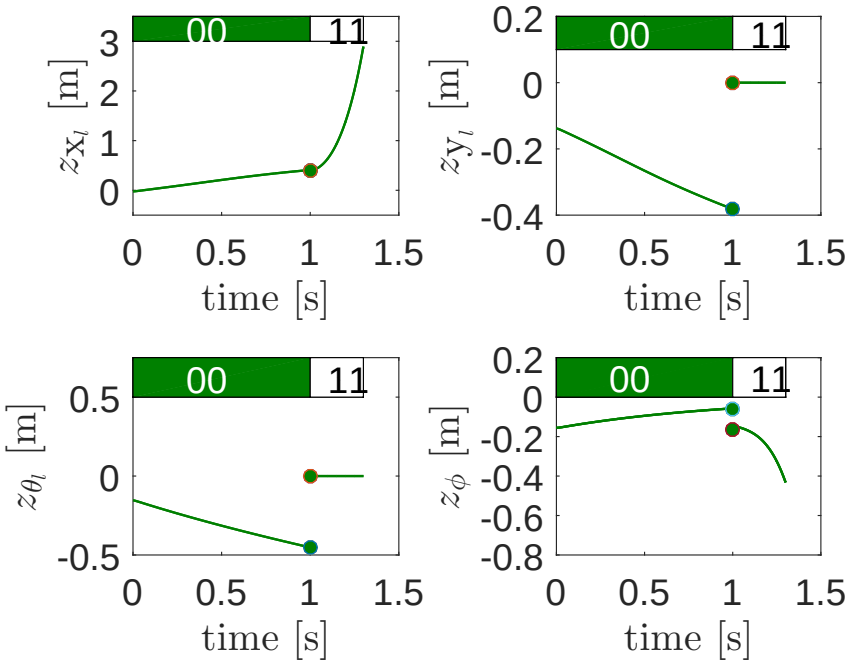

(a) Position.

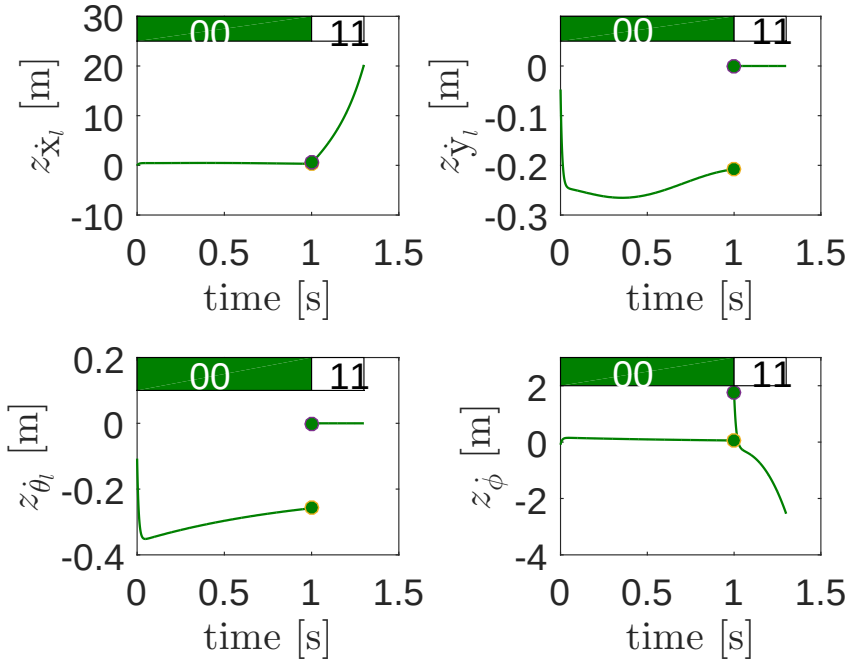

(b) Velocity.

Figure F.6: Individual plots Figure 5.14(a).

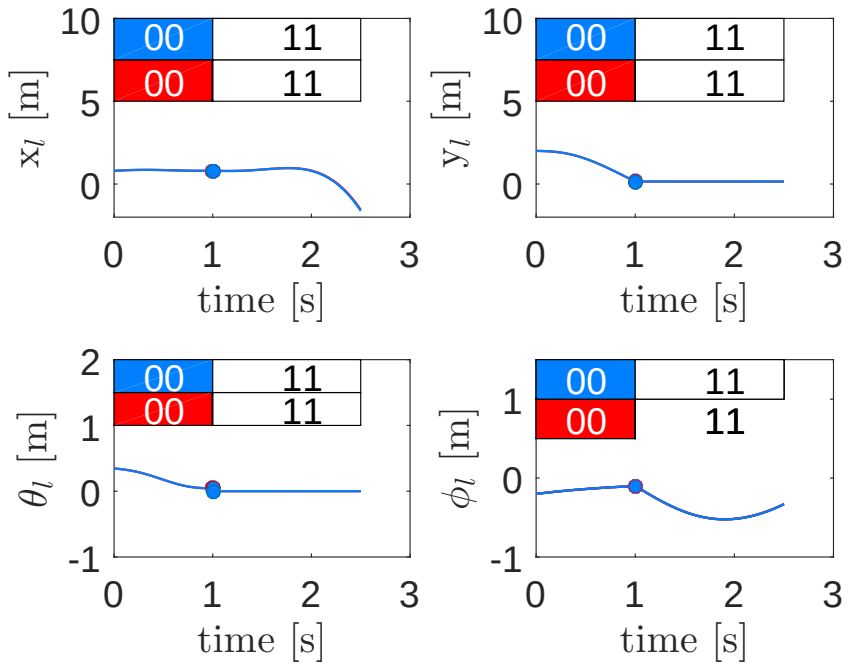

(a) Position.

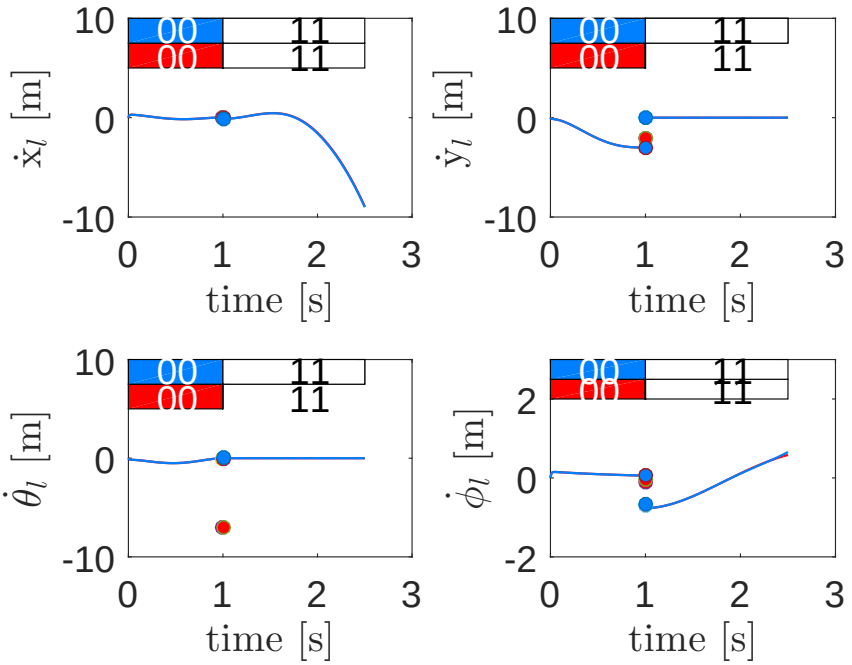

(b) Velocity.

Figure F.7: Individual plots Figure 5.13(b). The state trajectory in red, and the approximation in blue.

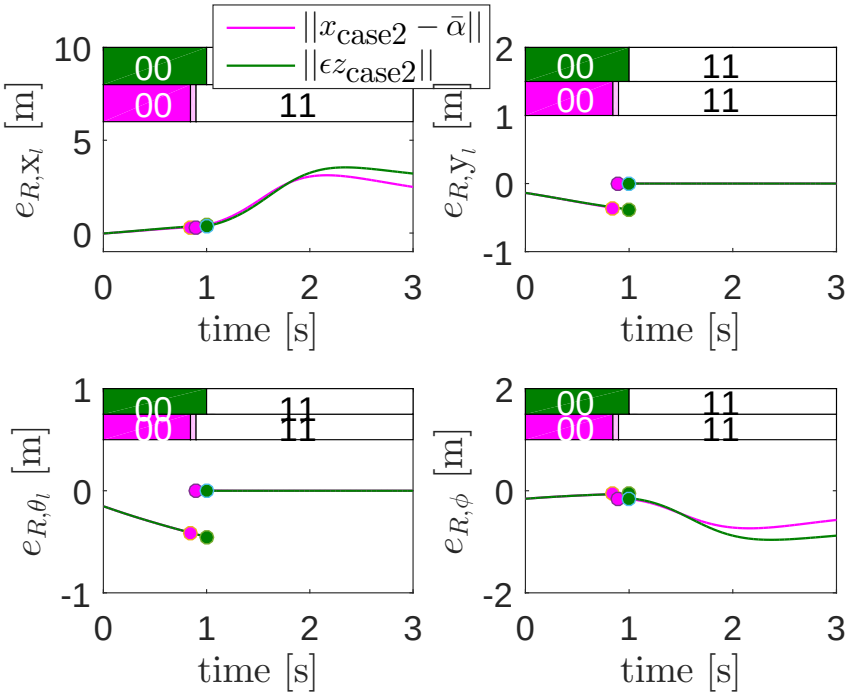

(a) Position errors.

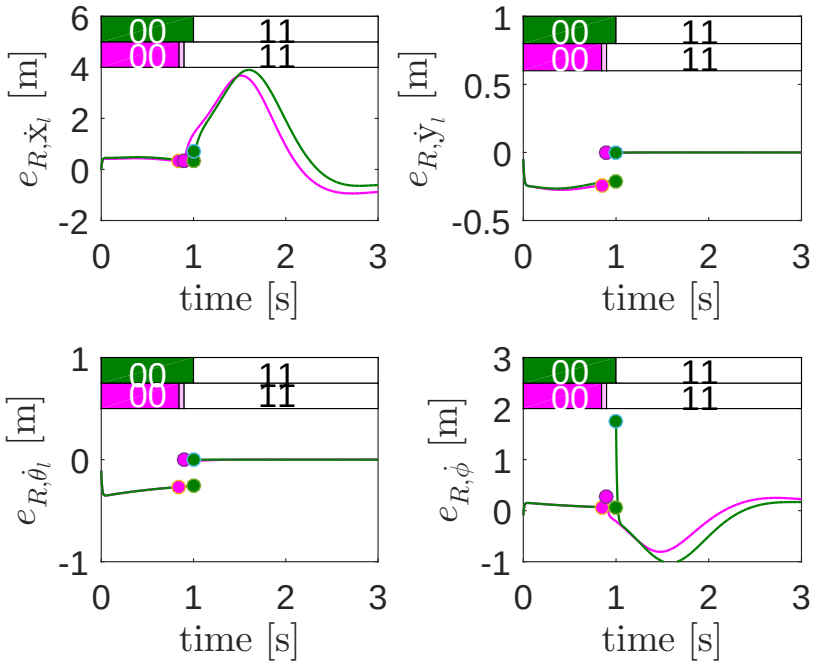

(b) Velocity errors.

Figure F.8: Individual error plots of the beige lines of Figure 5.17 (a) and (b).

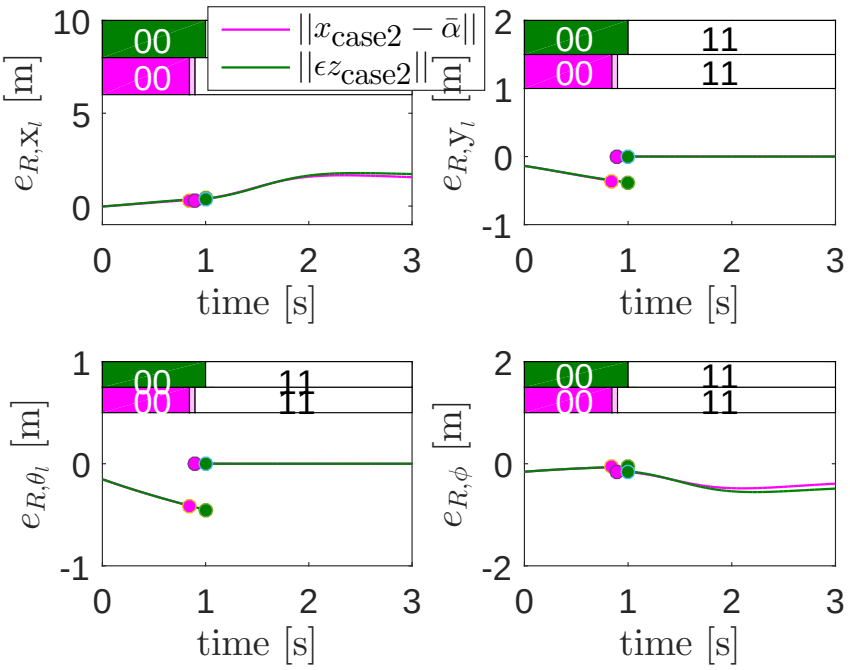

(a) Position errors.

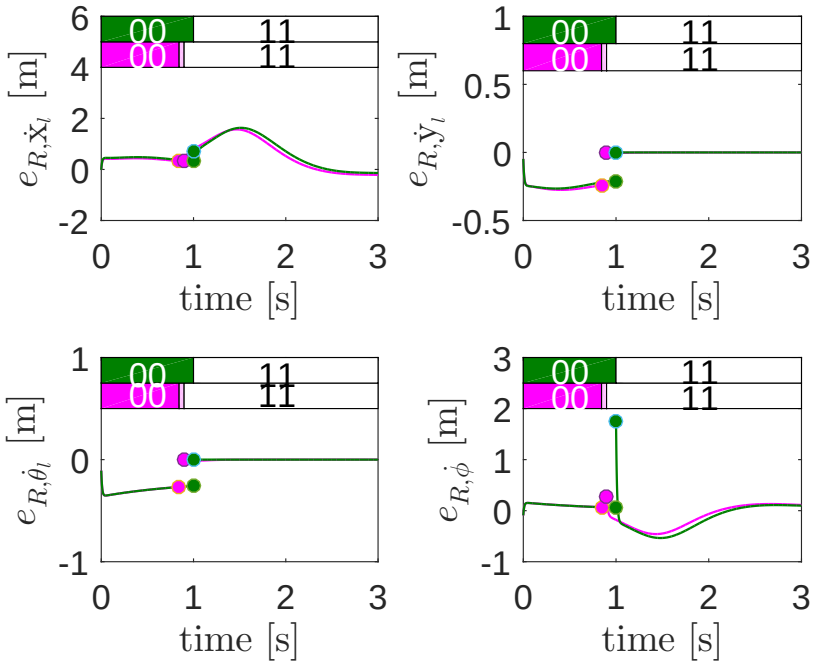

(b) Velocity errors.

Figure F.9: Individual error plots of the magenta lines of Figure 5.17 (a) and (b).

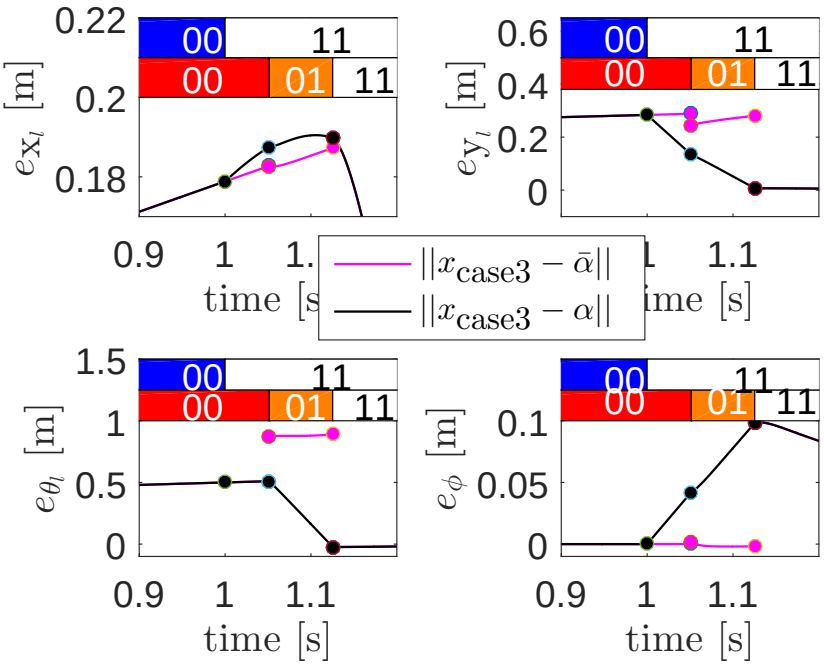

(a) Position errors.

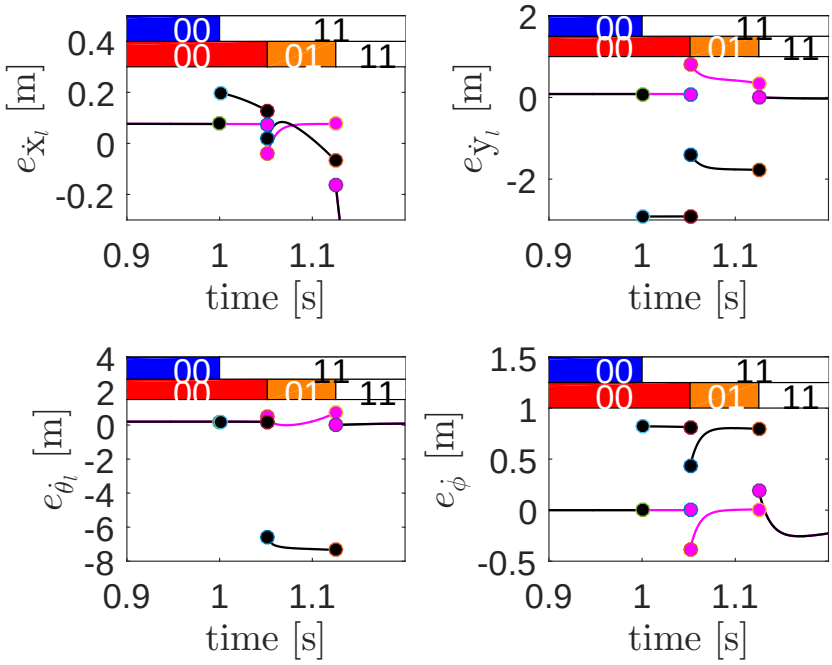

(b) Velocity errors.

Figure F.10: Individual error plots of Euclidean error (in black line) and Reference spreading error (purple line) of Figure 5.25(b). The blue bar represents the reference trajectory jumps and the red bar represents the perturbed trajectory jumps.